THE EFFECT OF STOICHIOMETRY ON THE THERMAL BEHAVIOUR OF SYNTHETIC IRON-NICKEL SULFIDES

Anthony Charles Chamberlain

This thesis is presented in fulfilment of the

requirements for the award of

Doctor of Philosophy

Curtin University of Technology

November 1996

To
Mum and Dad

ABSTRACT

The effect of stoichiometry on the pyrolytic decomposition, oxidation and ignition behaviour of synthetic violarite and pentlandite has been established. These minerals, of general formula $(Fe,Ni)_3S_4$ and $(Fe,Ni)_9S_8$ respectively, may vary considerably in Fe:Ni ratio. Pentlandite can also show some variation in metal:sulfur ratio. A series of samples, ranging in stoichiometry from $Fe_{0.96}Ni_{1.97}S_4$ to $Fe_{0.20}Ni_{2.72}S_4$ and $Fe_{5.80}Ni_{3.15}S_8$ to $Fe_{3.40}Ni_{5.55}S_8$, were synthesised and characterised using wet chemical analysis, electron probe micro-analysis (EPMA), scanning electron microscopy (SEM), X-ray diffraction (XRD), and Brunauer, Emmett and Teller (BET) surface area analysis.

The thermal behaviour of these sulfides was examined using simultaneous Thermogravimetry-Differential Thermal Analysis (TG-DTA) at different heating rates and in different atmospheres. Partially reacted samples were collected at various temperatures and analysed using XRD, EPMA, SEM, optical microscopy (OM), and Fourier transform infrared (FTIR) spectroscopy. The endmembers of the violarite and pentlandite series were examined in detail to determine the effect of stoichiometry on the reaction mechanism. In this study the reaction mechanism refers to the sequence of reactions occurring during pyrolytic decomposition or oxidation of the sulfide minerals. Samples were sieved into four particle size fractions, 125-90, 90-63, 63-45 and 45-20 μm, to determine the effect of particle size on the reaction mechanism.

When violarite was heated in an inert atmosphere at 10°C min^{-1}, it initially decomposed to a monosulfide solid solution (mss), $(Fe,Ni)_{1-x}S$, and vaesite, $(Ni,Fe)S_2$, indicated by a sharp endothermic peak in the DTA trace. The decomposition temperature was found to be linearly dependent on the iron:nickel ratio, decreasing from 495°C to 450°C as the iron:nickel ratio decreased from 0.49 to 0.07. This was followed by a broader endothermic peak coinciding with a rapid mass loss,

which was associated with the decomposition of vaesite to mss with the loss of sulfur. Between 615-805°C the mss was converted to a high temperature form of heazlewoodite, $(Fe,Ni)_{3\pm x}S_2$,which melted incongruently at 835°C and 805°C for $Fe_{0.96}Ni_{1.97}S_4$ and $Fe_{0.20}Ni_{2.72}S_4$ respectively, with further loss of sulfur vapour forming a central sulfide liquid of general formula $(Fe,Ni)_{1+x}S$.

Under similar experimental conditions, pentlandite pyrolytically decomposed forming mss and heazlewoodite with no associated loss of sulfur. The decomposition temperature decreased as the iron:nickel ratio deviated from the ideal value of 1:1. A maximum decomposition temperature of 610°C was found at an iron:nickel ratio of 1.00, decreasing to 580°C at a ratio of 1.84 and 0.61. Sulfur was evolved slowly at temperatures in excess of 760°C as mss was converted to heazlewoodite, indicated by a gradual mass loss. The heazlewoodite then melted incongruently in excess of 840°C, indicated by a sharp endothermic peak, resulting in a further loss of sulfur.

The oxidation of violarite and pentlandite was investigated at a heating rate of 10°C min^{-1} in an air atmosphere. The oxidation of violarite was initiated by decomposition to mss resulting in a rapid mass loss associated with the evolution of sulfur vapour, and an exothermic peak due to the gas phase oxidation of the sulfur. The iron sulfide component of the mss was then preferentially oxidised to iron(II) sulfate between 485-575°C, upon which the sulfate decomposed and the remaining iron sulfide was preferentially oxidised to hematite. The mss core was then converted to $(Fe,Ni)_{3\pm x}S_2$ between 635-715°C, resulting in the loss of further sulfur which was oxidised. The sulfide core, which consisted of predominantly $Ni_{3\pm x}S_2$ with a minor amount of iron still remaining in solid solution, incongruently melted at a constant temperature of 795°C regardless of the initial stoichiometry of the violarite sample. This was followed by the rapid oxidation of the liquid sulfide resulting in a sharp exothermic peak in the DTA trace.

For pentlandite, the TG-DTA curve exhibited an initial mass gain commencing at approximately 400°C, which was attributed to the preferential oxidation of iron. Evidence from SEM indicated that iron migrated towards the oxygen interface, where it was oxidised to hematite. During this process the metal:sulfur ratio decreased and pentlandite was converted to mss. The iron sulfide component of the mss phase was then preferentially oxidised to hematite as indicated by a major exotherm, which occurred in the temperature range 575-665°C, forming an oxide product layer around a nickel sulfide core. The oxidation of the remaining nickel sulfide followed the same reaction sequence to that of violarite.

By increasing the heating rate to 40°C min^{-1}, and carrying out the oxidation in pure oxygen, the tendency of the sulfides to ignite was established. Ignition was characterised by a highly exothermic reaction which coincided with a rapid mass loss over a short time period. Overheating of the samples above the programmed furnace temperature was also observed. Violarite exhibited ignition behaviour while pentlandite did not.

Both sulfides were subjected to shock heating conditions (heating rate = 1500 - 5000°C min^{-1}, oxygen atmosphere) using isothermal thermogravimetry (TG). This method produces heating rates analogous to those which are experienced in the reaction shaft of an industrial flash smelter. The effect of stoichiometry on ignition temperature and extent of oxidation for the entire series of synthetic violarites and pentlandites was determined. Partially ignited and ignited products were collected from isothermal TG experiments and were examined by OM, SEM and EPMA to establish the ignition mechanism.

Both violarite and pentlandite ignited using the isothermal TG technique. A clear relationship was found between the stoichiometry of violarite and pentlandite and the ignition temperature, with an increase in the iron:nickel ratio causing a decrease in the ignition temperature. The ignition temperature also decreased as the size of the particles decreased.

The extent of oxidation increased as the iron:nickel ratio increased, and also increased as the particle size decreased.

ACKNOWLEDGEMENTS

I would like to thank sincerely my supervisor, Professor J G Dunn, for his invaluable support throughout the course of this project. I would like to acknowledge the assistance of my associate supervisor and former PhD colleague, Dr L C Mackey, for her support and supervision during Professor Dunn's sabbatical leave.

This work would not have been possible without the assistance of the staff of the CSIRO Division of Exploration Geoscience, Floreat Park. I would like to thank Dr G Hitchen and Mr B Robinson for their technical assistance in collecting and processing the EPMA results. I also wish to thank Mr R Blitz for allowing me to use the sample preparation facilities and Dr E Nickel for training me in the finer aspects of mineral characterisation using optical microscopy.

To the staff of Applied Chemistry, in particular Mr I Sills of the Thermal Characterisation Laboratory and Mr P Chapman of the Vibrational Spectroscopy Facility, thank you for your oustanding expertise and technical assistance. I also extend my thanks to Mr G Whiting of the Glass Blowing Workshop for sealing the quartz reaction tubes, and Mr D Walton of the Workshop.

Thank you to Dr G Pooley and Dr A Van Reissen of the Centre for Microscopy and Microanalysis for their assistance with the scanning electron microscopy and quantitative analysis.

I would like to acknowledge gratefully financial support from Western Mining Corporation's Kalgoorlie Nickel Smelter and the Minerals and Energy Research Institute of Western Australia, and the Australian Postgraduate Research Award (Industry) Scheme for providing a PhD scholarship.

To my fellow PhD colleages, Dr Lisa Mackey, Dr Peter Weissenborn, Dr. Amal Ginting and Mrs Veronica Howes, most of whom have graduated and left the group, thank you for your assitance and entertaining discussions.

Finally, a very special thanks to my Mother and Father for their support and understanding throughout my years of study, and to Tamara Ingram for her loving support and time spent in proofreading my thesis.

TABLE OF CONTENTS

CHAPTER 2. EXPERIMENTAL

CHAPTER 3. CHARACTERISATION OF SYNTHETIC VIOLARITE AND PENTLANDITE

CHAPTER 5. THE PYROLYTIC DECOMPOSITION AND OXIDATION OF SYNTHETIC PENTLANDITE

LIST OF SYMBOLS

h - hematite Fe_2O_3

hz - heazlewoodite $(Fe,Ni)_{3\pm x}S_2$

ml - millerite Ni_7S_6

mss - monosulfide solid solution $(Fe,Ni)_{1-x}S$

pn - pentlandite $(Fe,Ni)_9S_8$

po - pyrrhotite $Fe_{1-x}S$

tv - trevorite $(Fe,Ni)_3O_4$

vl - violarite $(Fe,Ni)_3S_4$

vs - vaesite $(Ni,Fe)S_2$

LIST OF FIGURES

LIST OF TABLES

CHAPTER 1

INTRODUCTION

1.0 INTRODUCTION

The mining and processing of nickel ores is of major economic importance to Australia, and accounts for a total of 1.7% of the commodity exports from Australia (Cutifani, 1994). Australia is currently ranked sixth in Economic Demonstrated Resources (EDR) behind Russia, Cuba, Canada, Indonesia and New Caledonia with reserves of 2.9 million tonnes of contained metal accounting for approximately 6% of the world's total 47 million tonnes. However, it ranks as the fifth largest nickel producing country behind more established producers Russia and Canada, as well as New Caledonia and Indonesia (Cutifani, 1994).

In 1966, the first major nickel strike was announced by Western Mining Corporation at Kambalda some 570 km east of Perth. Since the discovery at Kambalda other major nickel sulfide deposits have subsequently been developed within the Yilgarn Block around the Kalgoorlie/Kambalda region including Leinster, Mount Keith, Silver Swan and Forrestania nickel mines. The deposits contain pentlandite, $(Fe,Ni)_9S_8$, and violarite, $(Fe,Ni)_3S_4$, as the major nickel bearing minerals, and are usually associated with pyrite, FeS_2, and/or pyrrhotite, $Fe_{1-x}S$. The relative quantities of each mineral can vary from deposit to deposit. Also the nickel bearing minerals can exhibit considerable variation in iron:nickel ratio.

During processing the nickel sulfide ore is concentrated by flotation and then flash smelted to produce a nickel matte which is further processed by a hydrometallurgical route to give nickel metal.

1.1 Genesis of Iron-Nickel Sulfides

Nickel sulfide deposits in the Kambalda/Kalgoorlie region occur within ultramafic volcanic rocks known as komatiites. Large volumes of very hot komatiite lava were rapidly erupted and channelled into topographic lows. As the lava flowed it thermally

eroded and assimilated the rocks underneath it. Some of these rocks were sulfide-rich sediments, and by assimilating with these the magma became saturated in sulfur. An immiscible sulfide melt, which scavenged chalcophile elements from the magma, was formed, and this separated from the komatiite melt by flow segregation and gravitational separation. The sulfide melt crystalised at the base of the komatiite pile to form massive stratiform ore, overlain by matrix and disseminated ore which are mixtures of both sulfide and silicate minerals (Marston *et al.*, 1981).

The first sulfide phase to crystalise is a monosulfide solid solution (mss) phase, $(Fe,Ni)_{1-x}S$, which is formed at approximately 1100°C. On further cooling various sulfide minerals may be exsolved from the mss depending on its composition. In the Kambalda region the primary or hypogene sulfides consist predominantly of pyrrhotite and pentlandite assemblages, associated with small quantities of pyrite, chalcopyrite and spinel phases.

Violarite can also be found as a primary mineral in the hypogene zone. Primary violarites are thought to have exsolved from mss and their compositions range from the ideal violarite endmember, $FeNi_2S_4$, to polydymite, Ni_3S_4, with considerable cobalt substitution. Primary violarite is found in association with vaesite, NiS_2, pyrite, FeS_2, and millerite, NiS. Violarite coexisting with millerite or pyrite-vaesite tends to be nickel-rich whereas violarites found in association with pyrite-millerite may vary in composition between iron-rich polydymite and cobalt-rich violarite (Hudson and Groves, 1974).

1.1.1 Supergene Enrichment

The majority of the sulfide deposits located in the Yilgarn Block have been subjected to supergene alteration and weathering. Weathered sulfide orebodies can be divided into four zones: primary, transition, supergene and oxide.

Supergene enrichment occurs during the weathering and decomposition of the primary sulfide deposits. When rain or ground water containing dissolved oxygen comes into contact with the primary sulfide orebody, the sulfide minerals are oxidised to form gossanous material and soluble metal sulfates. The metal sulfate species produced in the oxide zone are carried deeper into the lode by descending waters. In the transition zone, between the weathered outcrop and the unaltered sulfides, chemical reactions take place between the descending water, bearing metal sulfate species, and the unaltered sulfides. The metal sulfates are precipitated in the form of secondary sulfides. This gives rise to a zone of secondary or supergene sulfide enrichment. The lower region of the primary or hypogene zone remains intact.

Violarite normally occurs as a secondary mineral in the supergene zone. Due to the deep weathering profiles in Western Australia, violarite may be the predominant nickel-bearing mineral (Nickel, 1973). Three distinct mechanisms have been identified for the formation of violarite through supergene enrichment. They are:

(i) alteration of pyrrhotite-pentlandite assemblages

(ii) alteration of millerite-pentlandite assemblages

(iii) alteration of millerite

(i) Supergene alteration of pyrrhotite-pentlandite assemblages

The first reaction process involves supergene alteration of both pentlandite and pyrrhotite, which occurs via a range of redox reactions (Keele and Nickel, 1974; Nickel, Ross and Thornber, 1974). The replacement of the pyrrhotite-pentlandite assemblage with violarite and pyrite can be represented by the following general equations (Keele and Nickel, 1974):

$$Fe_{4.1}Ni_{4.9}S_8 \rightarrow 2\ Fe_{1.3}Ni_{1.9}S_4 + 1.1\ Ni^{2+} + 1.5\ Fe^{2+} + 5.2\ e^-$$

$$0.33\ Fe_7S_8 + 1.1\ Ni^{2+} \rightarrow 0.66\ Fe_{1.5}Ni_{1.7}S_4 + 1.3\ Fe^{2+} + 0.4\ e^-$$

$$Fe_7S_8 \rightarrow 4\ FeS_2 + 3\ Fe^{2+} + 6\ e^-$$

The majority of violarite occurring in the Kambalda region in Western Australia is the product of the above reactions. The driving force for the above anodic reactions is the cathodic reduction of oxygen and water at the water table.

$$2\ H_2O + O_2 + 4\ e^- \rightarrow 4\ OH^-$$

In the case of massive ore deposits the electrons form a current through the entire orebody from the anodic region at depth to the cathodic region near the surface (Thornber, 1975). In desseminated ores the electron flow will be largely restricted to the individual grains. Pyrrhotite, which is the most reactive mineral, will undergo oxidative changes first, allowing electrons to conduct to an adjacent more noble mineral such as pentlandite.

(ii) Supergene alteration of millerite-pentlandite assemblages

The second reaction process occurs when the deposit contains a millerite-pentlandite assemblage. The oxidation of the millerite is limited by the quantity of iron available from the oxidation of pentlandite.

$$Fe_{3.6}Ni_{5.4}S_8 \rightarrow 2\ Fe_{0.5}Ni_{2.7}S_4 + 2.6\ Fe^{2+} + 5.2\ e^-$$

$$20.8\ NiS + 2.6\ Fe^{2+} \rightarrow 5.2\ Fe_{0.5}Ni_{2.7}S_4 + 6.8\ Fe^{2+} + 8.4\ e^-$$

Both violarites formed tend to be more nickel-rich than those formed from pyrrhotite-pentlandite assemblages.

(iii) Supergene alteration of millerite

A third type reaction process occurs in the later stages of millerite replacement, and gives a product which exhibits an extremely high nickel content with a composition approaching that of polydymite, Ni_3S_4. The relative abundance is only very small (Keele and Nickel, 1974; Thornber, 1975).

$$4\ Ni_{0.98}Fe_{0.02}S\ +\ 0.16\ Fe^{2+} \rightarrow\ Ni_{2.76}Fe_{0.24}S_4\ +\ 1.16\ Ni^{2+}\ +\ 2\ e^-$$

1.2 Flash Smelting

In order to recover the contained nickel in a nickel sulfide concentrate the iron sulfide components must be oxidised. This is primarily achieved by using pyrometallurgical methods. Conventional pyrometallurgical processing of sulfide ores involves two main stages, smelting and converting. Smelting has traditionally been performed in reverberatory furnaces, but these have been gradually replaced by flash smelting and other smelting processes. Flash smelting incorporates the controlled oxidation and smelting of the sulfides in one unit operation, using the heat released in the oxidation reactions to smelt the sulfides.

Flash smelting was independently developed during the 1940's by Outokumpu Oy in Finland and the International Nickel Company of Canada (INCO). The Outokumpu Oy flash furnace was originally designed for treatment of copper concentrates, however the process was applied to nickel concentrates in 1959 (Stromberg *et al.*, 1995). The two processes are fundamentally different in both the design of the furnace and the introduction of the sulfide concentrate into the furnace. The INCO process uses a small hearth furnace where the dry particulate feed, consisting of sulfide concentrate and flux, is mixed with industrial oxygen (~95-98 volume % O_2)

and blown horizontally from either end of the furnace (Biswas and Davenport, 1994, pp.123-134; Davenport and Partelpoeg, 1987, pp.38-48). The heat generated from the oxidation of the iron and sulfur is sufficient to melt the sulfide particles and form a matte and slag layer at the base of the furnace. The use of pure oxygen makes the oxidation very intensive, so that generally no additional fuel is required.

The Outokumpu process uses a vertical reaction shaft where the sulfide concentrate, flux and air enter the top of the shaft. Typical residence time of particles in the reaction shaft is between 1-3 seconds. The iron and sulfur are oxidised forming molten particles which fall into the matte/slag bath, known as the settler, situated directly below the reaction shaft. The molten matte and slag droplets collect in the settler zone to form separate layers. The Outokumpu Oy process differs from the INCO process in that it uses preheated air or oxygen enriched air rather than oxygen at ambient temperature. The process is not autogenous and combustion of fossil fuels, either oil or pulverised coal, is required to supplement the heat balance of the furnace (Davenport and Partelpoeg, 1987, pp. 24-25).

The primary function of the smelting process is to preferentially oxidise the iron and sulfur components of the concentrate and produce two immiscible layers. The oxidised species combine with the silicate flux to form a slag layer which is discarded. The molten sulfides form a matte layer which is tapped and transferred to the conversion stage.

During the conversion process air or oxygen enriched air is blown through submerged tuyeres into the liquid matte, oxidising any remaining iron sulfide. Flux is added to the converter to remove the iron oxides as slag. The nickel and copper remain in the matte phase along with their associated sulfur. During processing of nickel ores the conversion stage is stopped after the matte reaches a composition of approximately 70% nickel, 22% sulfur and 1-6% iron. In the case of copper, converting air is blown

into the converters until the sulfur is completely oxidised producing blister copper. This is due to favourable thermodynamic equilibria when converting copper (see Table 1.1). At a temperature of 1500K (1227°C), chalcocite (Cu_2S) may reduce copper (I) oxide to copper metal, however in the case of nickel sulfide the temperature must reach approximately 1800K (1527°C) before heazlewoodite (Ni_3S_2) will reduce nickel oxide at partial pressures of SO_2 near one atmosphere (Themelis and Kellogg, 1983). The final blister copper contains 99% copper, 0.001-0.03% sulfur and 0.1-0.8% oxygen reporting as oxides (Biswas and Davenport, 1994, p.197).

The flash smelting process has a number of advantages over traditional roasting and smelting processes. Short reaction times during flash smelting enable high feed rates in excess of 2500 tonnes per day, resulting in higher productivity for a smelter of similar size. Large reductions in the fuel requirement have been obtained by efficiently utilising the heat produced by the combustion of the sulfide minerals. Also the continuous production of concentrated sulfur dioxide combustion gases, suitable for sulfuric acid production, have seen an increasing preference for flash smelting over traditional roasting and smelting techniques (Juusela, Harkki and Anderson, 1975; Stevenson *et al.*, 1994, p.80). The attractiveness of flash smelting has greatly

	1500K (kJ mol^{-1})		1800K (kJ mol^{-1})	
Reaction	ΔH°	ΔG°	ΔH°	ΔG°
Cu2S(l) + 2Cu2O(l) = 6Cu(l) + SO2 (g)	30.418	-53.890	-	-
Ni3S2 (l) + 4NiO(l) = 7Ni (l) + 2SO2 (g)	218.321	33.179	269.659	-5.606

Table 1.1 Free energy and enthalpy at 1500K and 1800K for the reaction of copper sulfide with copper oxide and nickel sulfide with nickel oxide (Themelis and Kellogg, 1983).

increased in recent times, for the following reasons (Harkki, Aaltonen and Tuominen, 1976; Anderson, Hanniala and Harkki, 1982):

- the availability of inexpensive tonnage oxygen has resulted in an increase in the capacity,
- the flexibility of processing complex concentrates autogeneously,
- production of higher grade mattes,
- considerable reduction in capital investment and operating costs.

1.3 Ignition Reactions and the Smelting of Sulfides

The oxidation of sulfides in a flash smelter proceeds by an ignition reaction. Ignition can be defined as corresponding to the establishment of a self-sustaining combustion reaction after the termination of heat supply from an external source (Vilyunov and Zarko, 1989, p.320). This definition assumes that there is a continuous supply of reactants for combustion to occur. In the case of sulfide minerals, where the reactants are gaseous sulfur and oxygen, the initial temperature experienced by the sample may be sufficient to cause the particle to ignite. To sustain the reaction to completion, however, the energy released by the reaction needs to heat the particle sufficiently to cause a continuous evolution of sulfur vapour. If the concentration of sulfur diminishes below some critical value, the reaction will be extinguished. In this work the ignition temperature is defined as the minimum temperature to initiate ignition, rather than the one defined by Vilyunov and Zarko (1989, p.320).

In practical terms, the sulfide concentrate is mixed with air preheated to 450-500°C and presented to a hot furnace. Under these conditions, heat generated by chemical reaction is used primarily to heat the particle rather than the environment. This

produces a rapid escalation in particle temperature accompanied by an accelerating rate of reaction, and further oxidation provides more heat which further increases the rate of reaction. The reaction process is now self sustaining, and will proceed to completion independent of the external environment providing sufficient quantities of oxidant are available (Dunn, Jayaweera and Davies, 1985). Ignition reactions are very fast, and for sulfides often complete in less than 0.1 second (Jorgensen, 1979). The chemical energy is thus released in a very short time span.

In order to ensure that the optimum performance is obtained from an industrial flash smelter it is necessary to investigate the ignition process. Two parameters of fundamental importance have been identified (Jorgensen, 1978):

(i) The ignition temperature - this is defined as the minimum temperature required to initiate an ignition reaction. This can be related to the temperature of the preheated process gas fed to the flash smelter.

(ii) The extent of reaction or oxidation of the concentrate at different temperatures of preheated process gas.

The ignition temperature is not a thermodynamic constant. The value may vary between different types of apparatus used to determine the ignition temperature (Medard, 1989, p.258). In order to obtain reproducible results all experimental variables must be strictly controlled.

1.4 Techniques for the Study of Flash Smelting Reactions

Although flash smelting has been established since the 1940's, the complexity of the reactions occurring in the reaction shaft and the short residence time of the particles has made it difficult for researchers to examine the behaviour of process variables directly.

There are strong incentives to better understand the mechanism and rate phenomena occurring in the reaction shaft. Sampling directly from the flash furnace is difficult due to the particles falling into the matte/slag bath. Hence, laboratory and pilot scale equipment have been designed so that the effect of process variables on the feedstock can be investigated.

Laboratory methods have several advantages in that they are simple to operate, rapid and cost effective. They also usually only require small quantities of samples. Variables such as particle size, oxygen concentration, residence times and heating rates can be easily controlled and their effects on reactivity determined. Pilot scale systems are generally used to simulate mass and heat transfer analogous to those found in the reaction shaft in order to accurately simulate smelting conditions. Several techniques have been used to study the flash smelting process. Their advantages and ability to simulate flash smelting conditions will be discussed.

1.4.1 Thermal Methods of Analysis

The thermal behaviour of sulfides has been extensively studied using thermal analysis techniques, under inert and oxidising atmospheres. Studies on the oxidation behaviour of sulfides are generally carried out under two sets of conditions:

(i) under mild oxidising conditions, so that the sulfide oxidises in a stepwise reaction sequence via the formation of various intermediate products, some of which may react at higher temperatures;

(ii) under vigorous oxidising conditions, so that the sulfide is ignited.

The results of experiments performed under these sets of conditions can be used to derive the reaction mechanism that occurs during the pyrometallurgical processing of sulfide minerals. Mild oxidising conditions are analogous to roasting operations,

where the sulfide mineral undergoes a set of sequential reactions. Vigorous oxidising conditions are analogous to the flash smelting process, where the oxidation of the sulfides proceeds via an ignition reaction.

Themogravimetric-Differential Thermal Analysis (TG-DTA)

TG-DTA can be used to observe changes in a sample when heated. Such changes may include crystal transformations, melting, sublimation, evaporation, decomposition, oxidation, reduction and solid-solid reactions. During these reactions the TG trace may exhibit a change in mass due to the chemical reaction as in the case of a decomposition or oxidation reaction, although crystal transformations do not exhibit any mass change. The DTA trace records the difference in the temperature between the sample and a reference. Both the sample and the reference crucibles have identical heat capacities and absorb equal amounts of heat from the surroundings. The sample mass used is sufficiently small that the difference in heat conductivity between the sample and reference is considered to have a negligible effect on the DTA. If the sample does not undergo any physical or chemical changes the temperature of the sample and reference are identical resulting in a straight DTA baseline. When the sample temperature is higher than the reference, due to a physical or chemical reaction that releases heat, then the DTA curve will deflect from the baseline in a positive direction representing an exothermic process. If the sample absorbs energy during a physical or chemical reaction then the DTA curve will deflect from the baseline in a negative direction representing an endothermic process. As the process ceases the DTA curve returns to the baseline.

Heating sulfides in an inert atmosphere will permit decomposition of the solid, with the evolution of sulfur vapour. Any phase changes will also be evident.

At moderate heating rates and under mild oxidising conditions, e.g. 5-20°C min^{-1} in air, the oxidation of sulfides occurs by a stepwise reaction mechanism. The resulting TG-DTA curve may consist of a number of mass gains and losses, and exothermic and endothermic peaks, over a wide temperature range. An example of this is shown in Figure 1.1a, where the oxidation of pyrite proceeds in several stages with both decomposition and oxidation reactions evident in the TG-DTA curve.

Under more vigorous oxidising conditions, achieved by increasing oxygen partial pressure and increasing the heating rate to 40°C min^{-1}, the sulfide sample may ignite (Dunn, Jayaweera and Davies, 1985; Dunn, De and O'Connor, 1989a; Dunn and Mackey, 1993). An ignition reaction may be characterised using TG-DTA by a single exothermic peak occurring over a relatively short time period coinciding with a rapid mass loss. The sample temperature rapidly increases well in excess of the programmed furnace temperature. A typical TG-DTA trace illustrating the ignition of pyrite is shown in Figure 1.1b. Note that the heat generated by the ignition reaction is sufficient to distort the linear heating rate profile. The relative reactivity between sulfide minerals may be established by the onset temperature of the major exotherm, with more reactive samples exhibiting a lower onset temperature.

Isothermal Thermogravimetric Analysis

This technique was developed to simulate the rapid heating rate experienced in the flash smelting process (Dunn, Jayaweera and Davies, 1985). Samples are weighed into a platinum crucible suspended from one arm of a thermobalance above a preheated furnace. The furnace is normally operated in the temperature range of 400-900°C. Once an oxygen flow is established the furnace is raised on a cam shaft around the sample, producing sample heating rates in the order of 2500-5000°C min^{-1}. If no rapid mass loss or overheating of the sample above the furnace temperature occurs, then the furnace is lowered and a fresh sample weighed into the crucible. The

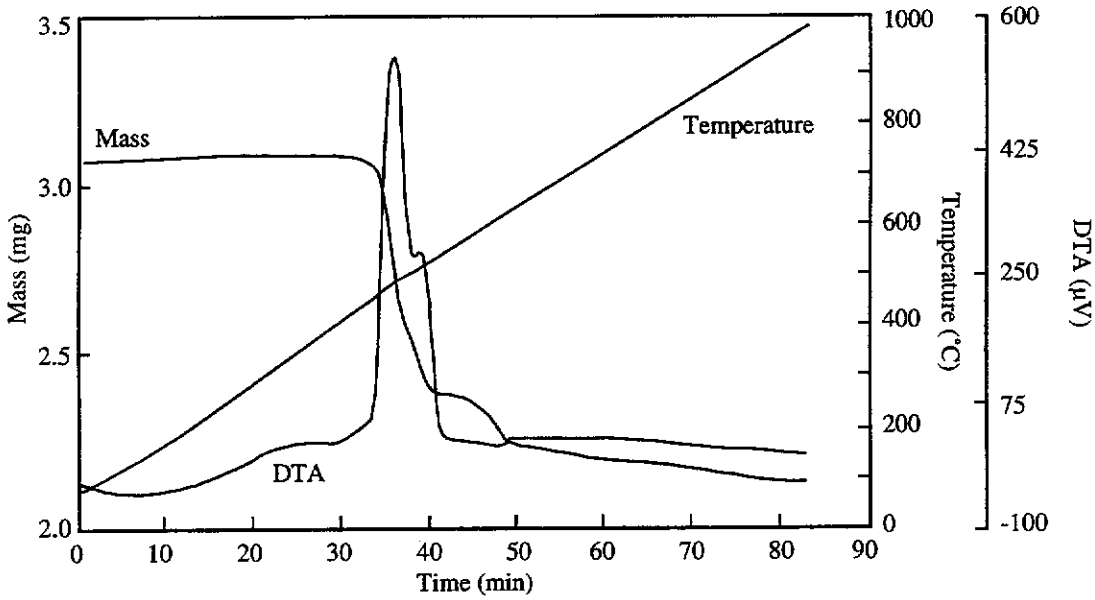

Figure 1.1a Typical TG-DTA trace of pyrite with a particle size range of 75-45 μm heated at 10°C min^{-1} in air (Dunn and Mackay, 1993).

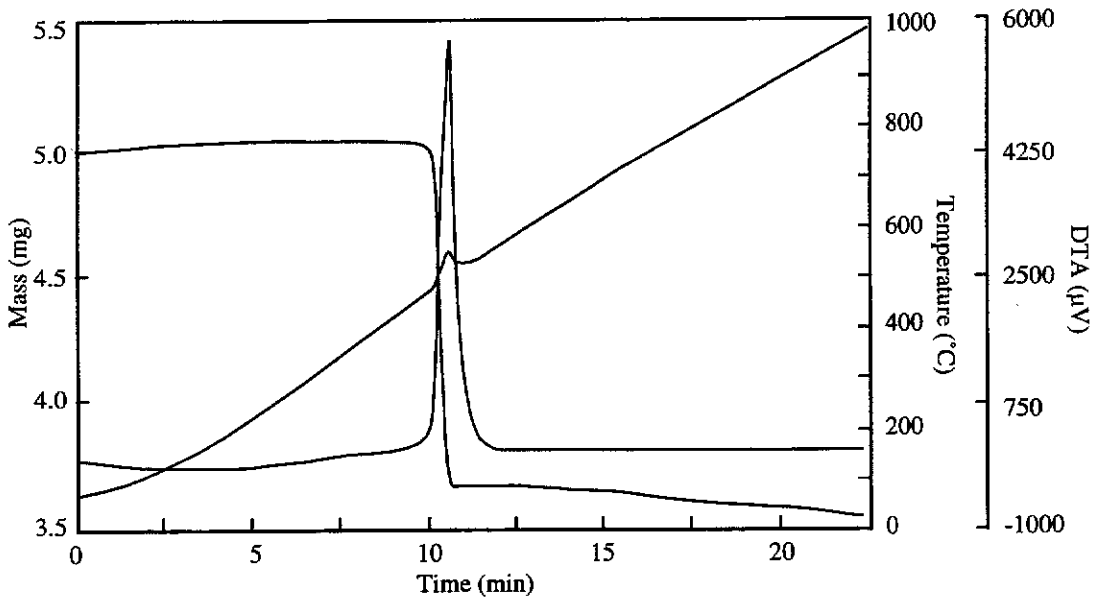

Figure 1.1b TG-DTA trace of pyrite heated at 40°C min^{-1} in an oxygen atmosphere (Dunn and Mackay, 1993).

temperature of the furnace is increased and the process repeated until rapid oxidation typical of an ignition reaction is evident. This temperature is known as the ignition temperature and is normally reproducible to within ±5°C. The mass loss upon ignition is directly proportional to the extent of oxidation. By increasing the temperature beyond the ignition temperature the extent of oxidation can be calculated against temperature.

The advantage of this technique is that it is fast and experimental conditions can be accurately controlled. This is evident by the precise values for the determination of ignition temperatures and extent of oxidation obtained. However, thermal analytical techniques have been criticised in the past for not accurately simulating heat and mass transfer conditions experienced under flash smelting. An oxygen atmosphere is usually required in order for ignition to occur. Also the gas flow to the smelter is preheated, while the oxygen gas stream entering the thermal analyser is at ambient temperature, and finally the sample is present as a packed bed rather than a gas-solid suspension. Therefore, heat transfer mechanisms in the thermal analyser will differ substantially from that existing in the flash furnace. The ignited particles still exhibit an angular morphology typical of the unreacted material. Hence, the overheating effect is not large enough to cause melting characterised by their rounded shapes found in products isolated from the flash furnace. Smaller samples sizes are used to minimise particle-particle interactions (Jorgensen, 1978). Despite these differences the results obtained by thermal analytical techniques show the same general trends as those observed using pilot scale systems (Mackey, 1991).

1.4.2 Laminar Flow Furnace

The laminar flow furnace was originally designed to study the decomposition reactions of pulverised fuel particles (Sainsbury *et al.*, 1966), but it has since been used to study the ignition of sulfides (Jorgensen and Segnit, 1977; Otsuka and Soma, 1980;

Chaubal, 1986; Jorgensen 1986 and 1987; Asaki *et al.* 1985; Huffman *et al.*, 1989; Stromberg *et al.*, 1995). A laminar flow furnace consists of a vertical tube heated by a furnace element. The sulfide feed enters the top of furnace with a small amount of cold carrier gas via a water cooled feeder. As the solid is introduced into the top of the tube it combines with the preheated gas stream. The solids and carrier gas rapidly heat to the preset furnace temperature. The furnace and preheated gas temperature may be individually set, however they are normally maintained at the same temperature. The particles are collected by a water cooled probe. Typical residence time in the furnace is approximately 0.1 s, although this may be adjusted by moving the collection probe accordingly to increase or decrease the residence time. The dimensions of the furnace, feed rate of the sulfide, gas and furnace temperatures, and composition of the combustion gas can vary in each study.

It has been recognised that conditions within a laminar flow furnace do not resemble the turbulent conditions observed in an industrial flash smelter. However, it was argued that the minimum scale of microturbulence is 10 to 100 times the diameter of the particles. Hence, the gas within this distance can be considered non-turbulent relative to the particle and mass transport between the particle and gas occurs by molecular diffusion. Therefore, the processes at the surface of the particle are essentially the same for both laminar flow and turbulent reactors (Jorgensen, 1978). Another criticism focused at laminar furnaces is their low particle densities in the gas stream compared to industrial flash smelters. As sulfur dioxide is evolved from the sulfide particles the composition of the gas stream will remain relatively unaltered along the length of the furnace. This differs from industrial flash furnaces where the stoichiometric requirement of oxygen is calculated for complete combustion of the feed. Consequently the concentration of oxygen will decrease down the reaction shaft (Themelis and Kellogg, 1983). Therefore, the conditions in a laminar flow furnace tend to be more oxidising and will drive the reaction to completion.

Finally the determination of the ignition temperature is not very precise, with temperatures in general quoted to no better than ±50°C. Hence, it is difficult to differentiate between sulfides with similar ignition temperatures (Dunn and Mackey, 1992).

1.4.3 Pilot Scale Reactors

There have been a limited number of studies conducted on nickel and copper concentrates using a pilot scale reactor. A one tenth scale model of the Kalgoorlie Nickel Smelter (KNS) reaction shaft was used to investigate the effects of mineralogical composition of the concentrate, particle size distribution of the feed, and the effect of oxygen enrichment (Mackey, 1991). The reaction products were quenched at the base of the reaction shaft with nitrogen and the solids separated from the exit gas stream by a cyclone. Examination of the ignition products revealed five main product types: unreacted or unignited particles, partially oxidised nickel-iron sulfides, partially oxidised iron sulfides, oxide/nickel sulfide particles and completely oxidised particles (Dunn *et al.*, 1993)

The majority of the particles had exceeded their melting point (>1000°C) and had formed molten hollow oxide spheres or cenospheres. Cenospheres are thought to be formed by the evolution of sulfur dioxide from the molten particles, with the gas acting as a blowing agent causing the molten particles to expand (Jorgensen, 1980a). While some particles experienced sufficiently intense conditions to allow complete oxidation others did not react at all or had only partially oxidised. The extent of oxidation was reported to be dependent on the mineralogy of the sulfide concentrate entering the furnace. Unreacted or unignited particles were found to consist primarily of pyrrhotite and pentlandite particles. The amount of unreacted particles increased as the particle size increased. Once sufficiently oxidising conditions were achieved, by increasing the oxygen content from 21% to 35%, the pyrrhotite was found to be oxidised to

completion while the pentlandite particles melted and formed partially oxidised nickel-iron sulfide species. Concentrates containing pyrite and violarite were found to be much more reactive than those consisting of pyrrhotite and pentlandite. Violarite and pyrite were very reactive under all conditions with the majority of particles forming either molten spherical oxide particles or oxide/nickel sulfide particles. During ignition the oxide/nickel sulfide particles separated into two discrete phases in the liquid state due to differences in surface tension and density between the oxide and sulfide phases.

A subsidiary aim of this work was to measure the ignition temperature of the concentrates to see whether they support earlier laboratory scale work reported (Mackey, 1991). It was found that the ignition temperature was difficult to measure directly, and the relative reactivities of the concentrates were inferred by microscopic examination of the products.

Another pilot scale reactor model again based on the Outokumpu Oy flash furnace, including the matte/slag bath, was used to study the flash smelting of copper concentrates (Kimura *et al.*, 1986; Kemori, Ojima and Kondo, 1988). Several sampling ports were located along the length of the reaction shaft to collect the ignition products prior to settling into the molten bath. The composition and size distribution of the reaction shaft product were examined at various points from the burner. Particles collected along the reaction shaft and in the settler zone showed that the oxidation of the copper concentrate was not completed by the end of the reaction shaft and continued to oxidise in the settler zone. Examination of the products showed that the size of the particles increased from 50 μm at the entry point to the reaction shaft to 250 μm just above the matte/slag bath. Mathematical modelling showed that collisions between less oxidised particles and excessively oxidised particles increased as the particles fell down the reaction shaft (Kemori *et al.*, 1987). Since the combustion air is blown into the reaction shaft around the furnace charge, the outer particles of the furnace charge experience more vigorous oxidising conditions compared to the inner

particles. As the outer particles proceed down the reaction shaft they melted due to the heat evolved from the oxidation of the particles and may collide with the inner solid particles forming agglomerates.

Other pilot scale studies have used dispersed particle jet reaction systems consisting of a feeding system and a concentrate burner (Kang, Steinhauser and Wuth, 1983; Kang and Pyun, 1988; Wuth, 1984). The gas and concentrate are dispersed through an accelerator nozzle forming a particle jet stream which is heated to its ignition temperature by a pilot burner located at the exit of the nozzle. The products were quenched in a water filled crucible. Temperature measurements of the particle jet stream showed the particles may achieve temperatures in excess of 1550°C with a residence time of approximately 29 ms.

While the majority of the research effort has been focused on flash smelting some work has been performed using a cyclone smelting pilot plant (Barin and Sauert, 1980; Barin, Modigell and Sauert, 1983). Cyclone smelting is based on the principle of suspension smelting. The sulfide is fed into the top of a cyclone while oxygen enters the cyclone tangentially. The sulfide particles ignite within the cyclone and exit into the matte/slag bath. Residence times have been estimated to be in the order of approximately 80 ms for particles with a diameter smaller than 1000 μm. The particles may reach a temperature of up to 1830°C during this time with the average temperature in the cyclone being approximately 1630°C.

Pilot scale studies and operational experience are essential for smelter design. However, pilot scale reactors are expensive to operate, require large amounts of sample and are labour intensive to maintain and operate.

1.4.4 Mathematical Modelling

There has been a substantial effort in this area recently to model the flash smelting process in an attempt to better understand the fundamental aspects occurring in the reaction shaft. Mathematical models which represent the thermodynamic and rate phenomena occurring in the reaction shaft have been developed. Validation of these models have been conducted by comparing the model with experimental observations (Themelis and Kellogg, 1983; Themelis, Makinen and Munroe, 1985; Chaubal, 1986; Hahn and Sohn, 1987; Kim, 1987; Munroe, 1987; Themelis, Wu and Jiao, 1988; Hahn and Sohn, 1990). There are two basic types of models which have been developed to simulate the industrial reaction shaft: a uni-dimensional and a two-dimensional model. The uni-dimensional model assumes the particles only move in the axial direction of the gas flow. The model is limited as it assumes uniform velocity, temperature and particle density at a given distance from the entry point. The two-dimensional model is a more sophisticated model which accounts for both axial and radial distributions (Hahn and Sohn, 1987). The model accounts for heat and material balances, including momentum transfer and the generation and dissipation of turbulent energy within the gas-particle stream near the entry zone (Themelis, Wu and Jiao, 1988).

The models were successful in calculating the axial temperature profile in the reaction shaft and the degree of sulfur removal with distance travelled by the particles (Kim, 1987). The effects of oxygen enrichment, preheated temperature of the gas and the addition of dust, flux and slag concentrates have also been established.

1.5 Mechanistic Studies on Ignition Reactions

Although the reaction mechanism of sulfide minerals has been the subject of several studies, a conclusive reaction mechanism has not been established. Earlier studies

considered that the oxidation of solid particles in an oxygen gas stream proceeded by the gaseous diffusion of oxygen to the reaction interface. This reaction mechanism is commonly referred to as the "Shrinking-Unreacted Core" model (Mohan, Mckinley and Douglas, 1979).

The shrinking-unreacted core model is a surface oxidation process controlled by the rate of both chemical reaction and mass transport. The reaction is initiated at the surface of the particle resulting in the formation of a porous, inert product layer. For the reaction to proceed the oxygen must diffuse through the product layer to the reaction interface. The gaseous products formed by the oxidation reaction must diffuse back out through the product layer into the gas stream. As the reaction progresses the reaction interface moves into the particle forming an ever thickening product layer surrounding an unreacted shrinking core.

Mechanistic studies on the ignition of coal have shown that ignition is the result of reaction between oxygen and volatile material released as the particle temperature rapidly increases.

1.5.1 Ignition of Coal Particles

When pulverised coal particles are injected into a preheated furnace the particles exhibit a rapid heating rate resulting in the ignition and combustion of the volatile matter evolved from the coal. Three factors which affect the rate of oxidation and ignition reaction of the coal have been identified (Howard and Essenhigh, 1966; Merrill, 1973; Annamalai and Durbetaki, 1977; Wall *et al.*, 1991):

(i) the volatile content of the coal
(ii) the particle size distribution of the coal
(iii) oxygen concentration of the process gas

It is generally well accepted that coals which contain a high volatile content are more susceptible to ignition than coals with a low volatile content (Juntgen, 1977; Nettleton and Stirling, 1967). Ignition studies have shown that the gas temperature required to ignite the coal particles is related to the particle temperature at which appreciable rates of loss of volatile matter occur (Nettleton and Stirling, 1967). The evolution of volatile matter from the coal particle results in a porous char which may oxidise further.

The reaction mechanism for ignition of coal particles proceeds via homogeneous combustion or heterogeneous combustion. Homogeneous combustion is when volatiles, evolved from the coal particle during heating, ignite and combust within the gas boundary layer surrounding the particle. The combustion of the volatiles causes the particle temperature to accelerate by conductive heat transfer from the flame. This causes further pyrolysis of volatiles and pyrolytic decomposition of high molecular weight volatiles. Oxygen is consumed in the flame and does not react with the char during the process. The combustion flame gradually moves towards the surface of the particle as the rate of volatilisation decreases. The reaction ceases and the char begins to oxidise by the diffusion of oxygen to the particle surface, which is now heterogeneous combustion. The heterogeneous combustion of coals may also occur below the ignition temperature. However the combustion reaction may be extinguished when the rate of volatilisation increases as the temperature approaches the ignition temperature causing the mechanism to change from heterogeneous to homogeneous combustion. The relative importance of each reaction scheme is dependent on the size of the coal particles, sample heating rate and the volatile content of the coal (Howard and Essenhigh, 1966; Annamali and Dubetaki, 1977; Shadman and Cavendish, 1980)

The variation in homogeneous and heterogeneous combustion with particle size has been attributed to the surface flux of volatile pyrolysis products evolved during heating

(Howard and Essenhigh, 1966). A large surface flux apparently forces the combustion reaction away from the solid surface, thereby protecting the solid surface from oxidation. Pyrolysis of coal particles is a volumetric reaction and the surface flux is directly proportional to the particle size. A critical particle size of 65 μm has been reported where the volatile flux is sufficient to prevent oxygen from reaching the solid surface (Howard and Essenhigh, 1966). Below this particle size gas-phase and heterogeneous combustion occur simultaneously on the solid surface, but the latter process is small during the rapid evolution of volatiles unless the particle size is less than 15 μm.

1.5.2 Ignition of Ternary Sulfides

As with coal particle ignition, the sulfur vapour produced by the thermal decomposition of the sulfide during heating is an important process during flash smelting of sulfides. The evolved sulfur reacts in the gas boundary layer surrounding the particle. The resulting oxidation reaction is highly exothermic and proceeds at extremely fast reaction rates, heating the particle to its ignition temperature. Since the dissociation of sulfur is an endothermic process, external heat is required to reach the decomposition temperature of the sulfide. The sudden introduction of cold sulfide particles into a high-temperature environment is essential for intensive flash reactor design (Kim, 1987).

Since flash smelting was initially designed to process copper and its related sulfide minerals it follows that majority of the work published has been on the ignition behaviour of chalcopyrite. The ignition of chalcopyrite during flash smelting has been suggested to proceed in three stages (Jorgersen, 1983; Kim, 1987):

(i) Thermal decomposition of the chalcopyrite to its high-temperature stable phases and the dissociation of labile sulfur

$$5\ CuFeS_{2\,(s)} \rightarrow Cu_5FeS_{4\,(s)} + 4FeS_{\,(s)} + S_{2\,(g)}$$

(ii) Gas-phase oxidation of sulfur in the gas boundary layer

$$S_{2\,(g)} + O_{2\,(g)} \rightarrow 2\ SO_{2\,(g)}$$

(iii) Oxidation of the resulting decomposed sulfides by gas-solid and/or gas-liquid reactions

Gas-solid reactions

$$FeS_{(s)} \rightarrow Fe_{1-x}S_{(s)} + xFe_{(s)}$$

$$3\ Fe_{(s)} + O_{2(g)} \rightarrow Fe_3O_{4(s)}$$

$$3\ Fe_{1-x}S_{(s)} + (5-2x)\ O_{2(g)} \rightarrow (1-x)\ Fe_3O_{4(s)} + 3SO_{2(g)}$$

$$Cu_5FeS_{4(s)} + zO_{2(g)} \rightarrow \frac{5}{(2-y)}\ Cu_{2-y}S_{(s)} + \frac{1}{(1-x)}\ Fe_{1-x}S_{(s)} + zSO_{2\,(g)}$$

Gas-liquid reaction

$$Cu_xFe_yS_zO_{w\,(l)} + aO_{2\,(g)} \rightarrow Cu_xFe_yO_{2a+w-2z\,(l)} + zSO_{2\,(g)}$$

When the sulfide particles are initially introduced into a preheated furnace the particles experience an induction stage during which they are heated by convection and radiation from the furnace. The amount of sulfur removal in this stage is minor and the rate of oxidation is chemically controlled. The particles continue to increase in temperature until they display a sudden rapid increase in temperature. This is defined as the ignition temperature. At the ignition temperature the sulfide decomposes and the loss of sulfur rapidly increases. The rate of decomposition and oxidation of the evolved sulfur inhibits the direct oxidation of the sulfide. The gaseous sulfur burns within the boundary layer surrounding the particle, consuming the oxygen and limits the

diffusion of oxygen to the sulfide particle surface. Desulfurisation of particles smaller than 25 μm had reached completion (Kim and Themelis, 1986; Kim, 1987).

The rate of sulfur loss follows a parabolic rate and despite the significant increase in the temperature of the particles the rate of sulfur removal decreases. The decrease in the loss of sulfur from the surface of the particle allows oxygen to diffuse through the gas boundary layer. Therefore, simultaneous decomposition and oxidation at the particle surface occur during this stage.

Due to the difference in the melting point temperature between oxides and sulfides the unreacted core melts first and the reaction mechanism changes from a gas-solid to a gas-liquid reaction. The molten sulfide is extremely unstable due to vigorous dissociation and oxidation reactions occurring. The oxidation of the molten sulfide core is controlled by the mass transport of oxygen through the oxide liquid film. The particle temperature continues to increase and the entrained gas in the molten sulfide expands. At moderate heating rates the sulfide melt is contained within the oxide crust where it is oxidised by incoming oxygen to form a solid oxide phase or a viscous oxide melt. Pore blocking of the oxide crust may cause a build up in the internal pressure and result in fragmentation. The outer oxide layers are spherical in shape suggesting that the oxide is near its melting point.

Under more rapid heating rates the molten sulfide is ejected through the oxide crust, fracturing the oxide layer and reducing the internal vapour pressure. Larger particles are more likely to fragment due to a larger volume of molten sulfide and entrained labile sulfur (Munroe, 1987). The final stage involves the oxidation of the molten sulfide fragments.

Some researchers have reported that the molten sulfide particles may undergo agglomeration rather than fragmentation during the final stages of the ignition process

(Kemori, Ojima and Kondo, 1988; Kimura *et al.*, 1986). Agglomeration has been suggested to occur when the flow in the shaft is highly turbulent and the density of the particle suspension is sufficient to allow frequent collisions between the molten fragments (Themelis, Wu and Jiao, 1988).

Ignition studies on nickel sulfide concentrates containing violarite have shown they ignite at significantly lower temperatures than concentrates containing pentlandite (Jorgensen, 1978; Dunn, Davies and Mackey, 1989; Dunn and Mackey, 1991; Dunn *et al.*, 1991; Stromberg *et al.*, 1995). Desulfurisation of violarite and pentlandite concentrates using a laminar flow furnace showed the violarite concentrate had almost completely desulfurised in the temperature range of 500-700°C, while the pentlandite concentrate did not exhibit any significant desulfurisation prior to 700°C (Stromberg *et al.*, 1995).

Thermoanalytical studies on the ignition behaviour of violarite showed that the reaction was initiated by the decomposition of the violarite at 460°C resulting in the liberation of sulfur (Mackey, 1991; Dunn and Mackey, 1991; Dunn and Mackey, 1993). Analysis of the decomposition product showed the sulfide had lost approximately 19% of the total available sulfur during decomposition. The particle morphology of the violarite particles heated above the decomposition temperature in an inert atmosphere resembled those quenched during ignition. The violarite particles exhibited a porous structure, attributed to the rapid loss of sulfur during the decomposition. The porous structure is suggested to allow the ingress of oxygen into the particle where the iron sulfide is preferentially oxidised forming a porous hematite product. The nickel sulfide is not oxidised until temperatures well in excess of the ignition temperature are obtained.

Metal-rich sulfides such as pentlandite do not seem to have the potential to evolve sulfur during the decomposition of the sulfide and appear to ignite by an alternative

mechanism (Mackey, 1991; Dunn and Mackey, 1993). Thermoanalytical studies of the pyrolytic decomposition of pentlandite showed no tendency for sulfur to be evolved at the ignition temperature. The morphology of the ignition products were consistent with oxygen attack at the surface with the reaction proceeding by the shrinking core mechanism. The mechanism was suggested to be initiated by the decomposition of pentlandite at 610°C forming an iron sulfide and nickel sulfide species. The iron sulfide component was preferentially oxidised accounting for the exothermic activity observed by the sample under ignition conditions (Mackey, 1991).

1.5.3 Ignition of Associated Iron Sulfides.

Pyrite and pyrrhotite are common iron sulfides found in association with both copper and nickel sulfide concentrates. The ignition behaviour of pyrite has been extensively studied compared to pyrrhotite. Mineralogical examination of chalcopyrite concentrates containing pyrite revealed that both gas-liquid and gas-solid oxidation may occur within the reaction shaft of the flash furnace (Hagni and Vierrether, 1988; Hagni, Vierrether and Sohn, 1988). Products isolated from the reaction shaft showed that the pyrite initially decomposes to form pyrrhotite resulting in the loss of sulfur from the particles. The pyrrhotite product had a porous grain structure radiating outwards from the pyrite core. The reaction products ranged from pyrite particles composed entirely of pyrrhotite to pyrite grains which exhibited partial alteration with a thin rim of pyrrhotite surrounding an unaltered pyrite core. Oxidation of the radial fibrous pyrrhotite may occur with the formation of magnetite and hematite. The hematite particles are very fine grained and have a porous structure resembling the pyrrhotite. Complete oxidation of the pyrrhotite to hematite is commonly found in the reaction shaft products.

Alternatively the pyrite may decompose to pyrrhotite and melt. The pyrrhotite does not commence melting until the pyrite has completely decomposed to pyrrhotite. The

products collected from the reaction shaft ranged from thin magnetite rims surrounding pyrrhotite particles to completely oxidised spheres containing mainly magnetite. Cenospheres are thought to occur as a result of expansion of entrained gas (Jorgensen, 1980a).

The ignition mechanism of pyrite has been investigated under simulated flash smelting conditions (Jorgensen, 1981; Mackey, 1991). The ignition reaction was speculated to proceed in four stages:

(i) Heating of the pyrite particles to their ignition temperature, 550-600°C. A minor amount of direct oxidation of the pyrite may occur prior to the ignition temperature according to the following reaction:

$$2FeS_{2\,(s)} + 7O_{2(g)} \rightarrow 2\,Fe_2O_{3\,(s)} + 4SO_{2\,(g)}$$

(ii) Decomposition of pyrite to pyrrhotite at 700°C resulting in the formation of a porous pyrrhotite structure and the burning of the evolved sulfur at the particle-gas interface.

$$2FeS_{2\,(s)} \rightarrow 2FeS_{\,(s)} + S_{2\,(g)}$$

$$S_{2\,(g)} + 2O_{2\,(g)} \rightarrow 2SO_{2\,(g)}$$

(iii) Oxidation of the pyrrhotite particles producing an oxide-sulfide intergrowth surrounded by a more oxidised zone composed mainly of hematite.

$$4FeS_{(s)} + 7O_{2\,(g)} \rightarrow 2Fe_2O_{3\,(s)} + 4SO_{2\,(g)}$$

(iv) Sulfide-oxide particles fuse together to form an Fe-S-O melt and rapid escalation of the particle temperature.

Ignition of the pyrite is thought to be initiated by the decomposition of the pyrite to pyrrhotite producing a 20.1% reduction in the volume of the sulfide. This is accommodated by the pyrrhotite assuming a porous structure. The evolved sulfur rapidly oxidises near the particle surface. As the oxidation of the sulfur decreases, and the protective sulfur dioxide sheath diminishes, oxygen can diffuse into the particle resulting in a further reduction in volume as the sulfide is converted to an oxide. A total reduction of 37.5% was calculated after complete oxidation.

Thermoanalytical studies on the ignition behaviour of pyrite and pyrrhotite have shown that the temperature required to initiate an ignition reaction is substantially higher for pyrrhotite than for pyrite, with respective ignition temperatures of 450°C and 540°C for 75-45 μm particle size fraction (Mackey, 1991). Pyrrhotites ($Fe_{1-x}S$) are normally sulfur rich compared with stoichiometric iron sulfide, troilite (FeS). Unlike pyrite, which loses one atom of sulfur during the decomposition of pyrite to pyrrhotite, pyrrhotite slowly evolves sulfur over a 250°C temperature range as the pyrrhotite tends towards the stoichiometric endmember troilite according to the following equation (Dunn and Chamberlain, 1991; Mackey, 1991):

$$Fe_{1-x}S_{(s)} + \text{heat} \rightarrow (1-x)FeS_{(s)} + xS_{(g)}$$

This gradual loss of sulfur produces a gas phase reaction between sulfur and oxygen, causing the particle temperature to increase resulting in a further loss of sulfur. The particle temperature may increase sufficiently to trigger an ignition reaction. This was supported by a study on synthetic pyrrhotite samples with varying iron:sulfur ratios (Dunn and Chamberlain, 1991). It was found that as the pyrrhotite composition became increasingly more sulfur rich the ignition temperature decreased. There was a correlation between the ignition temperature and the temperature at which the sulfur was evolved.

1.5.4 Ignition of Other Sulfides.

Two other sulfides, galena (PbS) and sphalerite (ZnS), have been investigated under simulated flash smelting conditions. The combustion of these sulfides provide supporting evidence for a sulfur vaporisation mechanism. The reaction rate was found to rapidly increase when the sulfide melting point was exceeded (Jorgensen, 1980b), which was attributed to an increase in sulfur vapour pressure above the melt. Below their melting points, galena formed a basic lead sulfate layer, lanarkite ($PbO.PbSO_4$), while sphalerite formed a zinc oxide layer, zincite (ZnO) (Jorgensen, 1980b). The oxidation was found to be limited by the diffusion of oxygen through the oxide layers and no appreciable reaction was observed prior to their melting points.

The oxidation of sphalerite during cyclone smelting has been extensively studied (Barin and Sauert, 1980; Barin, Modigell and Sauert, 1983). In the upper zone of the cyclone the particles experience high turbulence due to high velocities in the solid-gas flow. As a result the mass and heat transfer rates are extremely high. For example, particles with a diameter of 250 μm reach temperatures in excess of 1600°C within 30 ms. Under these conditions the sphalerite vaporises and dissociates to form sulfur triggering an ignition reaction according to the following sequence of reactions:

$$2ZnS_{(s)} \rightarrow 2Zn_{(g)} + S_{2(g)}$$

$$2Zn_{(g)} + S_{2(g)} + O_{2(g)} \rightarrow 2Zn_{(g)} + 2SO_{2(g)}$$

$$2Zn_{(g)} + S_{2(g)} + 3O_{2(g)} \rightarrow ZnO_{(g)} + 2SO_{2(g)}$$

Residence times in the cyclone have been estimated to be of the order of 80ms. Mathematical modelling of oxidation of the sphalerite by diffusion of oxygen through an oxide product layer, i.e. shrinking core model, required a residence time of 29 s at a temperature of 1630°C for the reaction to reach completion. As the residence time of the particles is less than 80 ms, the ignition reaction by a solid-gas reaction proceeds

too slowly for the observed reaction rates. Hence, the reaction seems to be initiated by a gas phase reaction mechanism.

There is mounting evidence that ignition of sulfides is triggered by the loss of sulfur resulting in a gas phase reaction. This reaction is dependent on the whether the sulfide has the ability to lose sulfur. Metal-rich sulfides such as pentlandite appear not to evolve sulfur at the solid-gas interface and oxidise according to a shrinking core model. This may explain why the relative reactivity of pentlandite is lower than sulfides such as pyrite and violarite which are sulfur rich.

1.6 Variables Affecting Ignition in the Flash Smelter

The parameters affecting the ignition of sulfide minerals in the flash smelter include the temperature of the preheated process gas, level of oxygen enrichment, particle size distribution of the concentrate and mineralogical composition. These variables have been extensively studied to determine their effect on the flash smelting process.

1.6.1 Preheat Temperature of the Process Gas

The predominant mechanism of heat transfer to small particles (<100 μm) prior to ignition in a flash smelter is by conduction from the surrounding air rather than radiation from the furnace walls (Jorgensen, 1979). Hence in order to achieve ignition it is essential that the process gas introduced into the flash smelter is at a temperature high enough to provide the necessary heating effect in the particles. Increasing the temperature beyond the minimum temperature to initiate an ignition reaction has a minor effect on the rate of reaction (Themelis, Makinen and Munroe, 1985).

1.6.2 Oxygen Concentration in the Process Gas

Increasing the oxygen concentration increases the rate of oxidation in an ignition reaction. This effect has been well established in both laboratory and pilot scale studies on nickel sulfide concentrates. Using a laminar flow furnace at 700°C, a change in the oxygen concentration by converting the atmosphere from air to 32% oxygen to pure oxygen produced an increase in the extent of oxidation of the nickel concentrate from 60 to 70 to 85% (Jorgensen, 1978). In a separate study using a thermobalance at 500°C, a change from air to pure oxygen resulted in an increase in the extent of oxidation from 55 to 80% (Dunn, 1983). Mathematical modelling studies of the flash smelting process have shown similar findings (Hahn and Sohn, 1990; Chaubal, 1986; Kim, 1987; Themelis, Makinen and Munroe, 1985).

1.6.3 Particle Size Distribution

A decrease in the particle size of a solid is expected to increase the rate of reaction due to an increase in the surface area available for contact with the gaseous oxidant. The effect of particle size on the ignition temperature has been found to vary with mineral type (Dunn and Smith, 1984; Mackey, 1991). The preheated furnace temperature required to ignite pentlandite in a thermal analyser varied from 635-640°C for the 45-20 μm particle size fraction, up to 765-770°C for the 125-90 μm fraction. This represents an increase in the ignition temperature of 130°C due to particle size. The corresponding temperatures for the same size fractions of pyrrhotite were 470-475°C and 575-580°C, representing an increase of 105°C. The relative order of reactivity of these two minerals changes with increasing particle size. Violarite showed a 80°C, and pyrite a 60°C, difference in their ignition temperature between the coarsest and finest fractions (Mackey, 1991). Hence, the ignition temperature of sulfur rich sulfides such as violarite and pyrite tend to be less dependent on particle size than stoichiometric metal rich sulfides such as pyrrhotite and pentlandite.

Hence larger particles of the sulfides require higher temperatures to cause ignition than do smaller particles.

1.6.4 Mineralogical Composition

There are four main sulfide minerals present in the feed material to the Kalgoorlie Nickel Smelter, namely pentlandite ($(Fe,Ni)_8S_9$), violarite ($(Fe,Ni)_3S_4$), pyrite (FeS_2) and pyrrhotite ($Fe_{1-x}S$). Laboratory studies using the isothermal TG technique have established that violarite and pyrite are far more reactive than pentlandite and pyrrhotite (Dunn and Smith, 1984; Mackey, 1991). The results of an independent study using a laboratory laminar flow furnace were in agreement with the above stated order of reactivity (Jorgensen, 1978). According to their relative reactivities, violarite was more reactive than pyrite followed by pyrrhotite. Pentlandite was reported as the least reactive mineral (Mackey, 1991). This order was determined using 75-45 μm nickel concentrate samples at different temperatures.

Since individual mineral phases have different reactivities towards oxidation, it follows that concentrates which differ in their mineralogical composition will also differ in their reactivity. Concentrates which contain violarite and/or pyrite will tend to ignite more readily than those which contain pentlandite and/or pyrrhotite. Since ignition temperatures are dependent upon particle size, care is required in comparing values. However, even taking the effect of particle size into account violarite ignites at a lower temperature relative to the other major sulfides.

1.7 Proposed Research

Recent studies have demonstrated that changes in the stoichiometry of an individual mineral can affect the reactivity. For example, a clear relationship has been shown to exist between the stoichiometry of pyrrhotite ($Fe_{1-x}S$) and the ignition temperature. A decrease in the Fe:S ratio from $Fe_{1.00}S$ to $Fe_{0.83}S$ caused a 210°C decrease in the ignition temperature for 125-90 μm sized particles (Dunn and Chamberlain, 1991). Natural assemblages of violarite and pentlandite show a wide range of iron:nickel ratios. Violarite, which has a general formula of $(Fe,Ni)_3S_4$, may vary in composition from Ni_3S_4 to Fe_3S_4, with synthetic samples restricted between the range from $FeNi_2S_4$ to Ni_3S_4 (Misra and Fleet, 1974; Craig, 1971). Natural violarites are often slightly sulfur deficient relative to the ideal metal:sulfur ratio of 3:4 (Desborough and Czamanske, 1973). Similarly for natural assemblages of pentlandite, $(Fe,Ni)_9S_8$, the composition ranges from $Fe_{5.91}Ni_{3.09}S_8$ to $Fe_{3.19}Ni_{5.80}S_8$ (Misra and Fleet, 1973). Synthetic pentlandites show a slightly larger range in composition from $Fe_{6.09}Ni_{3.08}S_8$ to $Fe_{2.57}Ni_{6.43}S_8$ (Vaughan and Craig, 1978; Misra and Fleet, 1973). The variations in the metal:sulfur ratios of pentlandite are quite small compared to variations in the iron:nickel ratio. The field expands symmetrically on either side of the ideal stoichiometry with the range considered to be $(Fe,Ni)_{8.5}S_8$ to $(Fe,Ni)_{9.5}S_8$ (Misra and Fleet, 1973; Harris and Nickel, 1972).

The literature to date has reported the ignition behaviour of specific naturally occurring mineral sulfides. However, there are no publications on the systematic study of the effect of stoichiometry on the oxidation behaviour of iron-nickel sulfides. Based on the results obtained from pyrrhotites, it is likely that changes in the stoichiometry of violarite and pentlandite will result in changes in their ignition behaviour and hence flash smelting.

A major difficulty in measuring the properties of iron-nickel sulfides is obtaining these sulfide minerals free from other reactive sulfides. Hence, a range of violarites and pentlandites with varying iron:nickel ratios were synthesized and characterised.

During ignition sulfides normally decompose or undergo a phase transition to form a more stable high-temperature species which may result in the loss of sulfur. Therefore, the pyrolytic decomposition mechanism for violarite and pentlandite was established using TG-DTA. Decomposition products were isolated at various temperatures and mineralogically examined.

The oxidation behaviour of violarite and pentlandite under mild and vigorous conditions was examined using TG-DTA, and the oxidation products isolated at various temperatures. Mineralogical examination of the products was performed with a view to establishing the reaction mechanism.

The ignition behaviour of the iron-nickel sulfides was established using isothermal thermogravimetric analysis. The ignition temperature and extent of oxidation at increasing furnace temperatures were determined for each sample. These measurements enabled the effect of stoichiometry on the reactivity to be established. The sulfides were fractionated in order to examine the effects of particle size on the ignition temperature and extent of oxidation.

The results of these experiments will be discussed in subsequent sections of the thesis.

CHAPTER 2

EXPERIMENTAL

2.0 EXPERIMENTAL

2.1 Synthesis of Iron-Nickel Sulfides

A two-stage synthesis was employed to form homogeneous violarite with a general composition of $(Fe,Ni)_3S_4$. The procedure was based on methods previously described by Kullerud and Yund (1962) and Vaughan and Craig (1978). Iron, nickel and sulfur of greater than 99.99% purity were obtained from Aldrich Chemical Company (Inc.). All experiments were performed using Vycor® glass tubing obtained from Corning (Inc.) with an internal diameter of 9 mm and length of approximately 100 mm. Each reaction tube was sealed at one end and labelled by a diamond-tipped pencil. A maximum of 4 g was synthesized at once due to heat dissipation problems during quenching.

A typical experiment required firstly the synthesis of mss containing iron and nickel to give the desired stoichiometry. For example, the synthesis of ideal violarite, $FeNi_2S_4$, required 0.7409 g of iron, 1.5577 g of nickel and 1.5080 g of sulfur. Constituents were weighed accurately to ±5 mg into a glass weighing cup. The iron, nickel and sulfur were mixed thoroughly and the sample transferred via a long stemmed glass funnel into a Vycor® tube. The tube was then evacuated to 0.01013 kPa using a two stage vacuum pump with an adjustable leak. A constriction was made near the end of the tube to prevent the sample from being expelled from the tube during evacuation. A swivel connector attached to the end of the Vycor® tube allowed the tube to be rotated while being sealed in a natural gas-oxygen flame.

After the tube was sealed the contents were spread evenly along the length of the tube so the diameter was never constricted. The reaction tube was heated in a nichrome-wound furnace attached to an automatic temperature controller accurate to ±2°C. The sealed tube was placed in a stainless steel tube, crimped at one end. An initial

quenched after 48 and 96 hours and the sulfide ground. The pentlandite samples were finally quenched after 15 days and stored in an evacuated desiccator.

2.2 Characterisation of Synthetic Iron-Nickel Sulfides

2.2.1 Chemical Analysis

The percentage iron, nickel and sulfur in each sample was determined using classical wet chemical techniques. Each analysis was carried out in duplicate as follows:

(i) Nickel analysis

A 0.2 g sample in duplicate was accurately weighed and decomposed with bromine. A 3:1 mixture of concentrated nitric and hydrochloric acid was added and heated to dryness on a steam bath. After heating, the residue was dissolved in hydrochloric acid and diluted with deionised water. Iron was precipitated out with dilute NH_4OH and filtered. The filtrate was collected and the nickel determined gravimetrically as NiDMG.

(ii) Iron analysis

The iron content was determined titrimetrically with potassium dichromate. Samples were digested as for nickel analysis in duplicate. Iron hydroxide was precipitated from solution, filtered using a Whatman 541 filter paper, and redissolved prior to the dichromate titration.

(iii) Sulfur analysis

The percentage sulfur in each sample was determined by gravimetric analysis. A 0.2 g sample was accurately weighed and decomposed in bromine. The residue was dissolved in acid and diluted with deionised water. The resulting solution was percolated through a cation exchange column to remove the iron and nickel. Barium sulfate was precipitated by the addition of barium chloride. The solution was filtered through a clean, dried, sintered crucible, dried at 120°C, and the precipitate weighed. The percentage sulfur was calculated.

2.2.2 Particle Sizing

Each sample was dry sieved through a stack of Brass Endecott Laboratory Test Sieves to isolate four fractions, 125-90, 90-63, 63-45 and <45 μm. Sieving was carried out for 15 minutes on a Rotaps Sieve Shaker. The base pan was emptied and the stack of sieves shaken for another 10 minutes. This procedure was repeated until a negligible amount of material appeared in the <45 μm fraction.

A 45-20 μm fraction was then obtained by wet sieving the <45 μm fraction through a Lab Technics stainless steel 20 μm sieve with petroleum spirit. The <45 μm fraction was initially placed in a beaker with a small quantity of petroleum spirit and ultrasonicated for 5 minutes to remove any ultra-fines adhered to the particles. The suspended fines were decanted through the 20 μm test sieve. Additional petroleum spirit was added to the beaker and decanted off. This was repeated until the solution was clear of any fines. The sample was then sieved to obtain a 45-20 μm fraction.

2.2.3 Surface Area Measurement

The BET surface area of each synthetic sample was measured using an automatic gas-adsorption analyser (Quantachrome Autosorb-1) at the Particle Analysis Facility, Curtin University of Technology.

2.2.4 XRD Analysis

Approximately 100 mg of sample was weighed with 10% α-quartz as an internal standard. The sample was then ground carefully in an agate mortar and pestle to produce an optimum particle size of <10 μm. The sample was mounted onto an amorphous glass sample holder using pressure sensitive double-sided Scotch tape and pressed with a glass slide to give a flat surface.

XRD patterns were acquired using a Siemens D500 Diffractometer fitted with a copper X-ray tube, rotating specimen stage and sodium iodide scintillation detector. The X-ray tube was operated at 40 kV and 30 mA. Patterns were recorded with Cu Kα (λ=1.5418Å) radiation with graphite monochromator. A two-theta angle range of 10-110° was scanned using a goniometer speed of 0.04°/step with a 1 second step. X-ray spectra were analysed on Socabim data analysis software in conjunction with JCPDS - X-ray spectra search and match analysis.

2.2.5 Optical Microscopy

Approximately 5-10 mg samples were mounted in a 25 mm epoxy resin button. The required amount of sample holes were drilled with a suitable diameter to a depth of approximately 2 mm into the surface of the button. The sample was placed in the hole and a small amount of resin placed over the sample. The button was placed under vacuum for a short period of time to remove any air present in the sample. After the

resin had cured the button was placed on a kerosene diamond lap and ground until the surface of the button was smooth and a cross section of the sample obtained. Final polishing of the sections was achieved on 3-6 μm, followed by 1-0.5 μm, diamond-impregnated polishing wheels.

Optical examination of the polished sections was performed under reflected light using a Nikon Labophot-2 optical microscope. Optical micrographs were taken on Kodak Ektar ASA 100 35 mm photographic film using a Nikon FX-35W camera.

2.2.6 SEM Examination

SEM was performed using a JEOL JSM-6400 scanning electron microscope fitted with a LINK X-ray Energy Dispersive Spectrometer (EDS) detector. Polished sections were carbon coated prior to examination to render them electrically conductive. Secondary electron (SE) and back-scattered electron (BSE) micrographs were collected using an accelerating voltage of 20 kV. Micrographs were taken using Ilford 35mm black and white roll film. EDS spectra were processed using SPEED spectral analysis software (Ware, 1981) and RECALC2 (Griffin *et al.*, 1991). Pure samples of millerite and iron were used as secondary standards.

2.2.7 EPMA

EPMA was performed on carbon-coated polished sections of synthetic violarite and pentlandite using a Cameca SX-50 Electron Probe at the CSIRO Division of Exploration Geoscience. Results were collected using the ANU/CSIRO WANU-SX Software V7.03 and processed by CITZAF Microprobe Data Correction Software Version 3.04 (Armstrong, 1988) and Cameca PAP. A tungsten filament provided a source of primary electrons accelerated to 20 kV and the beam current was set to

20.0 nA. Pyrite and nickel metal standards were used. A count time of 40.0 seconds was used to measure the X-rays for iron, nickel and sulfur. A minimum of 30 particles were analysed in each sample. Traverse scans were also performed across individual grains to determine the homogeneity. Approximately 10 particles were analysed with a 5 point step across each grain.

2.3 Thermal Methods of Analysis

2.3.1 Simultaneous Thermogravimetric and Differential Thermal Analysis (TG-DTA)

TG-DTA measurements were performed using a Stanton-Redcroft Thermal Analyser STA-781 interfaced to an IBM compatible computer using TAPP700 software. A mixed standard containing quartz and zinc was used to check the temperature calibration on a regular basis. All experiments were carried out in alumina crucibles measuring 4 mm in diameter and 5 mm depth. 5 mg samples were weighed accurately on a Perkin Elmer AD-2 Microbalance, the sample spread evenly across the bottom of the crucible to form a monolayer, and placed in the TG-DTA apparatus. A gas flow of 40 ml min^{-1} was established prior to each experiment. Oxidation studies were carried out using heating rates of 10°C min^{-1} in an air atmosphere, and 40°C min^{-1} in an oxygen atmosphere. The decomposition of each sample was examined in a nitrogen atmosphere at 10° and 40°C min^{-1}.

In order to identify the intermediate products present at various stages of reaction, multiple runs were performed using 5 mg of fresh sample. Each was heated to a preselected temperature, at which the heating program was terminated. The samples were cooled in a nitrogen atmosphere and collected for characterisation by a range of instrumental techniques including FTIR, XRD, SEM, and EPMA.

2.3.2 Evolved Gas Analysis (EGA)

EGA was performed using a Netzsch STA-409 TG-DTA instrument interfaced with a Bruker IFS 55 FTIR spectrometer fitted with a MCT (Hg-Cd-Te) detector. The infrared spectra were collected using OPUS software version 2.0. Approximately 5 mg of sample was placed in an alumina crucible. The TG-DTA instrument was evacuated with a roughing pump and purged with a dry air gas stream. After a steady gas stream had been established the sample was heated to 1000°C at a rate of 10°C min^{-1}. The evolved gases were transferred from the furnace to the FTIR spectrometer via a heated transfer line maintained at 200°C. The gases then passed through a heated light pipe arrangement fitted with outer (KBr) and inner (ZnSe) windows. The light pipe was heated to avoid condensation on the windows. The infrared beam passed through the light pipe and the infrared spectrum was acquired. Twenty scans were averaged to produce an infrared spectrum between 4000-650 cm^{-1} every 5 seconds. The Gram Schmidt chromatogram showed the infrared activity between 4000-650 cm^{-1} as a function of time. The infrared spectrum may be extracted at any point within the chromatogram.

2.3.3 Isothermal Thermogravimetry.

Ignition temperature measurements were performed using a Stanton-Redcroft TG-750 Thermobalance. The sample temperature was measured using a platinum - 13% rhodium thermocouple located at a constant distance below the sample crucible. A series of melting point standards were used to determine the sample temperature as a function of the thermocouple temperature. Approximately 5 mg samples were weighed into a platinum sample crucible, measuring 5 mm in diameter and 2 mm in depth. The sample was spread evenly across the bottom of the crucible to form a monolayer. An oxygen atmosphere of greater than 99.9% purity was established in the furnace at a flowrate of 25 ml min^{-1}. The furnace was situated directly below the

sample crucible. An asbestos plate was positioned over the furnace while a sample was being weighed into the sample crucible. The plate prevented heat dissipating to the surrounding environment. The furnace was preheated to a set temperature between 400°C and 900°C. The insulating plate was removed and the furnace raised on a cam shaft around the sample. The sample can experience heating rates in excess of 5000°C min^{-1}.

The ignition temperature of each synthetic sample was measured by increasing the temperature of the furnace at 5°C increments until the sample underwent ignition and a rapid mass loss was observed.

The extent of reaction was also determined at the ignition temperature. By obtaining the maximum weight loss at 900°C the percentage extent of reaction is directly proportional to the observed mass loss at any particular furnace temperature.

$$\text{Percentage extent of reaction} = \frac{\text{Mass loss T°C}}{\text{Mass loss at 900°C}} \times 100\%$$

2.4 Identification of Thermal Analysis Products

Various instrumental methods were used to determine the composition of partially oxidised and decomposed intermediate products collected from the TG-DTA equipment. Ignition products collected from isothermal gravimetric studies prior to ignition and after ignition were also examined.

2.4.1 XRD of Partially Oxidised and Decomposition Products

Approximately 5 mg of sample was taken in a small agate mortar and pestle and ground in petroleum spirit to produce an optimum particle size <10 μm. The fine powder was then suspended in the solvent using an ultrasonic bath and filtered onto a

Millipore Type GV filter (pore size 0.80 μm, diameter 25 mm). The Millipore filter was then mounted on an amorphous glass slide with double-sided Scotch tape. Prior to running the samples a background X-ray diffraction pattern of the Millipore filter and glass slide was collected using a Siemens D500 diffractometer, equipped with a copper X-ray tube operated at 40 kV and 30 mA, over a two theta angular range of 10-110° at 0.04° per second.

2.4.2 FTIR Spectroscopy

FTIR spectra were obtained on a Perkin Elmer 1720 spectrometer equipped with a triglycine sulfate (TGS) detector and IBM compatible computer running Perkin Elmer IRDM version 2 software. One hundred scans were collected for each sample at a mirror velocity of 0.2 cm s^{-1} and a resolution of 4 cm^{-1} in the wavelength range of 4000-400 cm^{-1}. A sample shuttle was used to take the interferograms of the sample and background alternately to ratio the CO_2 and water vapour in the atmosphere.

Transmission spectra of solid samples were obtained by a potassium bromide pressed-pellet technique. Approximately 2 mg of sample was finely ground in an agate mortar and pestle and mixed with 100 mg KBr. The KBr and sample were pressed in a cylindrical stainless steel 13 mm die for 1 minute under a load of 8 tonne in an evacuated system. The resulting pellet was 13 mm in diameter and approximately 0.2 mm thick. A blank KBr pellet was used to collect the background spectrum.

2.4.3 SEM Examination

SEM analysis was performed using a JEOL JSM-6400 scanning electron microscope. Polished sections were prepared and analysed as previously outlined in section 2.2.6. SE images of isothermal products were obtained by mounting the sample on a SEM stub using double-sided adhesive tape. The sample was gold coated to render it

electrically conductive. Micrographs were taken using Ilford 35 mm black and white film.

2.4.4 EPMA

EPMA of quenched products from the thermal analysis equipment was performed as outlined in section 2.2.7. BSE images were used to identify different phases within each particle. On average 5-10 particles were analysed for each collection temperature.

CHAPTER 3

CHARACTERISATION OF SYNTHETIC VIOLARITE AND PENTLANDITE

3.1 CHARACTERISATION OF SYNTHETIC VIOLARITE

3.1.1 Wet Chemical Analysis

The bulk composition for each synthetic violarite was determined by wet chemical analysis. Duplicate samples were analysed for iron and nickel. Only a single sulfur analysis was performed on each synthetic violarite sample due to limited sample available. Results of the analysis are presented in Table 3.1. The stoichiometry for each violarite sample was determined from the iron and nickel analysis with the sulfur calculated by difference. The calculated stoichiometry of the bulk sample is given in the last column of Table 3.1. The total experimental error was approximately ±2%. The error in the final stoichiometry for each synthetic violarite is given in Table 3.1. For example, for the violarite close to the ideal stoichiometry of $FeNi_2S_4$, the stoichiometry may range from $Fe_{0.98}Ni_{1.98}S_{4.03}$ to $Fe_{0.96}Ni_{1.94}S_{3.97}$.

Sample	Composition (wt. %)				Stoichiometry
	Fe	Ni	S	Total	
1	18.24	38.66	43.34	100.24	$Fe_{0.97\pm0.01}Ni_{1.96\pm0.02}S_{4\pm0.03}$
2	13.54	43.98	44.19	101.71	$Fe_{0.73\pm0.01}Ni_{2.26\pm0.02}S_{4\pm0.03}$
3	8.59	48.69	43.98	101.26	$Fe_{0.46\pm0.01}Ni_{2.49\pm0.02}S_{4\pm0.03}$
4	3.74	53.32	43.39	100.45	$Fe_{0.20\pm0.01}Ni_{2.72\pm0.02}S_{4\pm0.03}$

Table 3.1 Results of wet chemical analysis for synthetic violarites.

3.1.2 EPMA of Synthetic Violarite

Approximately 60 particles were examined for each violarite sample to determine the homogeneity of each sample. Figure 3.1 shows the distribution of iron, nickel and sulfur in each particle analysed for each sample. The average weight percent were calculated for each violarite sample and normalised to 100% (Table 3.2). The average stoichiometry and standard deviation for each violarite sample is given in Table 3.2.

A comparison of the EPMA results with those obtained by wet chemical analysis revealed a systematic error. The iron values determined by EPMA were approximate 2-3 wt. % higher than the values obtained by chemical analysis, while the nickel and sulfur values were 1-2 wt. % lower. There are several explanations for these differences. One explanation is that the high nickel content in the violarite samples caused the fluorescence of the iron and sulfur by the absorption of the nickel x-rays. Iron is more susceptible to fluorescence than sulfur due to the higher K-shell fluorescences yield (ω_K) factor. For iron the fluorescence yield factor is 0.340, while for sulfur the yield factor is approximately 4.3 times lower with a factor of 0.078 (Scott, Love and Reed, 1995). The fluorescence correction performed by the

Sample	Composition (wt. %)				Stoichiometry
	Fe	Ni	S	Total	
1	20.50	37.63	41.87	100.00	$Fe_{1.12\pm0.05}Ni_{1.96\pm0.05}S_{4\pm0.05}$
2	15.70	42.79	41.51	100.00	$Fe_{0.87\pm0.05}Ni_{2.25\pm0.05}S_{4\pm0.03}$
3	10.76	47.54	41.70	100.00	$Fe_{0.59\pm0.05}Ni_{2.49\pm0.06}S_{4\pm0.04}$
4	5.98	52.20	41.82	100.00	$Fe_{0.33\pm0.04}Ni_{2.73\pm0.06}S_{4\pm0.06}$

Table 3.2 Summary of EPMA results obtained for each synthetic violarite sample. Results were processed using Cameca PAP and normalised to 100%. Standard deviations were calculated to within a 99% confidence level.

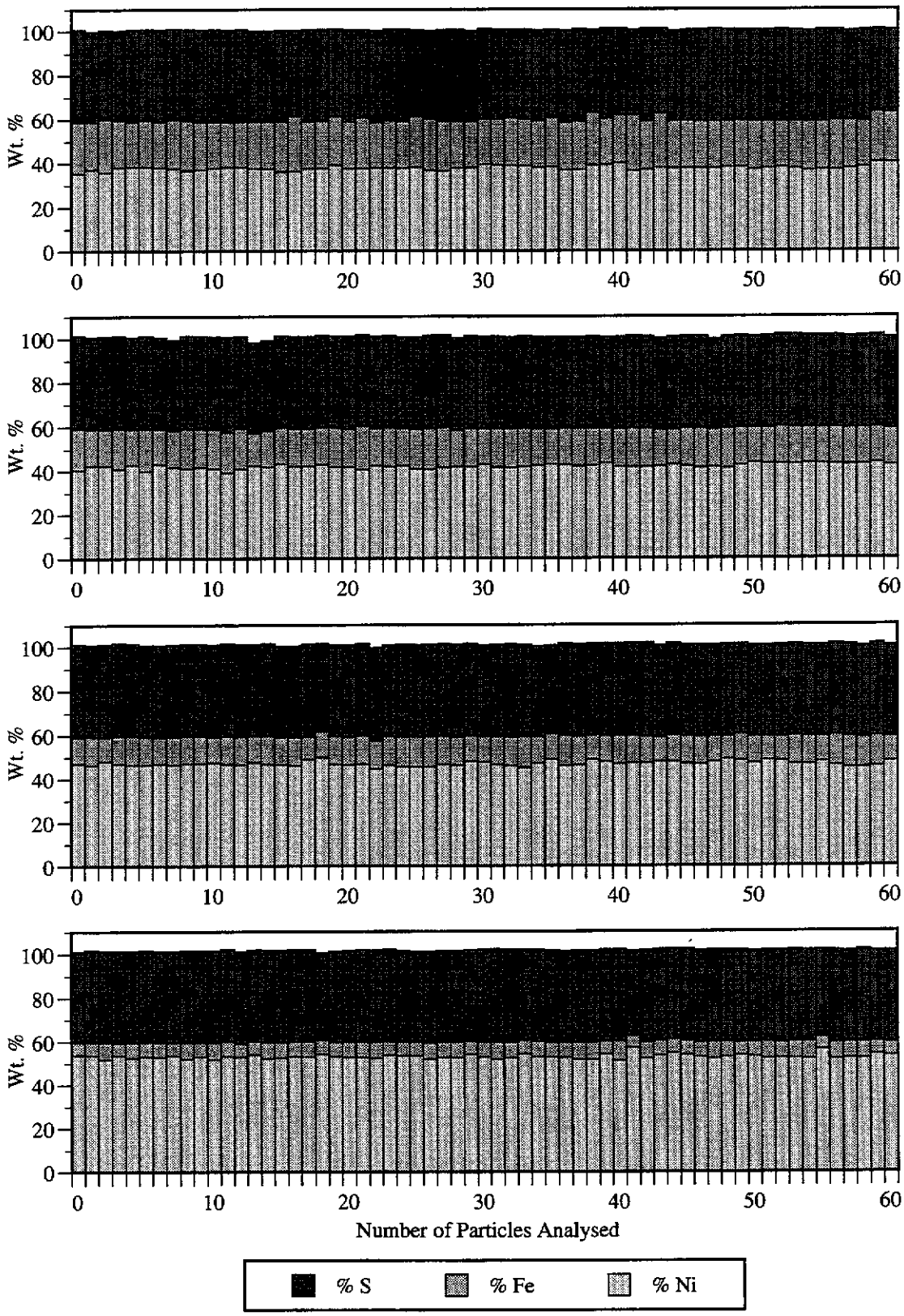

Figure 3.1 Distribution of iron, nickel and sulfur in a number of individual particles (single-point analysis at the centre of each particle) for the entire range of synthetic violarite samples. Starting from the top $Fe_{0.97}Ni_{1.96}S_4$, $Fe_{0.73}Ni_{2.26}S_4$, $Fe_{0.46}Ni_{2.49}S_4$, and $Fe_{0.20}Ni_{2.72}S_4$.

correctional software appears to be inappropriate for violarite resulting in a systematic error in the EPMA results (Essene, 1996; Henderson, 1996).

Another cause for the discrepancy in the EPMA results may have been due to the selection of pyrite and nickel metal as standards used for the analysis. Metal standards may cause large Z (atomic number) and potentially significant A (x-ray absorption) and F (fluorescence) corrections. This can be minimised by selecting sulfide standards near in composition to the phase being analysed (Essene, 1996). However, appropriate EPMA sulfide standards are difficult to obtain in pure forms due to most of them forming solid solutions with other chalcophile elements.

Finally, high iron and low nickel and sulfur values may have been caused by an oxide film on the polished section. The analysis totals were generally low, between 98-99%, and were normalised to 100%. Considerable care was taken when preparing the polished section to minimise their exposure to the atmosphere. The samples were carbon coated within half an hour after being polished, and analysed. Violarites are very reactive and exposure of the fresh sulfide surfaces to the atmosphere may cause a thin oxide film to form in a short period of time (Harrowfield, 1996).

Although there were differences between the EPMA and chemical analysis, the EPMA results still indicated that the synthetic violarite samples were homogeneous with only a minor variation in the composition of the particles from the mean stoichiometry (see Figure 3.1). The variation in the composition of the particles analysed was minor compared to the difference in the stoichiometry between the violarite samples.

Traverse scans were also performed across individual particles to determine the homogeneity within individual particles (Figure 3.2). The composition was determined at five points across the diameter of the particle. The average stoichiometry for the 10 particles analysed and the standard deviation is given in Table 3.3.

The composition was found to vary slightly within individual particles as a result of compositional zoning, which may occur in synthetic minerals when the reaction has not reached equilibrium (Vaughan and Craig, 1978). After the initial reaction between the mss and additional sulfur, the reaction continues as a solid-state reaction. Solid state reactions are normally slow to proceed and equilibrium is not reached until after an extended period of time. The reaction kinetics can be increased by repeated grinding stages during the synthesis. However, these grinding stages have the effect of decreasing the particle size of the final product. Therefore, a compromise must be achieved between the number of grinding stages, particle size and the homogeneity of the final product.

Although each sample showed a minor variation in the stoichiometry from particle to particle and within individual particles, indicating the reaction had not reached equilibrium, this variation was minor compared to the difference in stoichiometry between each of the violarite samples.

Sample	Composition (wt. %)				Stoichiometry
	Fe	Ni	S	Total	
1	20.62	37.77	41.61	100.00	$Fe_{1.14\pm0.05}Ni_{1.98\pm0.06}S_{4\pm0.08}$
2	15.39	43.23	41.38	100.00	$Fe_{0.85\pm0.04}Ni_{2.28\pm0.04}S_{4\pm0.05}$
3	11.03	47.21	41.76	100.00	$Fe_{0.61\pm0.05}Ni_{2.47\pm0.05}S_{4\pm0.03}$
4	5.66	52.18	42.16	100.00	$Fe_{0.31\pm0.06}Ni_{2.70\pm0.05}S_{4\pm0.06}$

Table 3.3 Summary of EPMA results obtained from traverse scans across 10 particles for each synthetic violarite sample. Results were processed using Cameca PAP and normalised. Standard deviations are within a 99% confidence level.

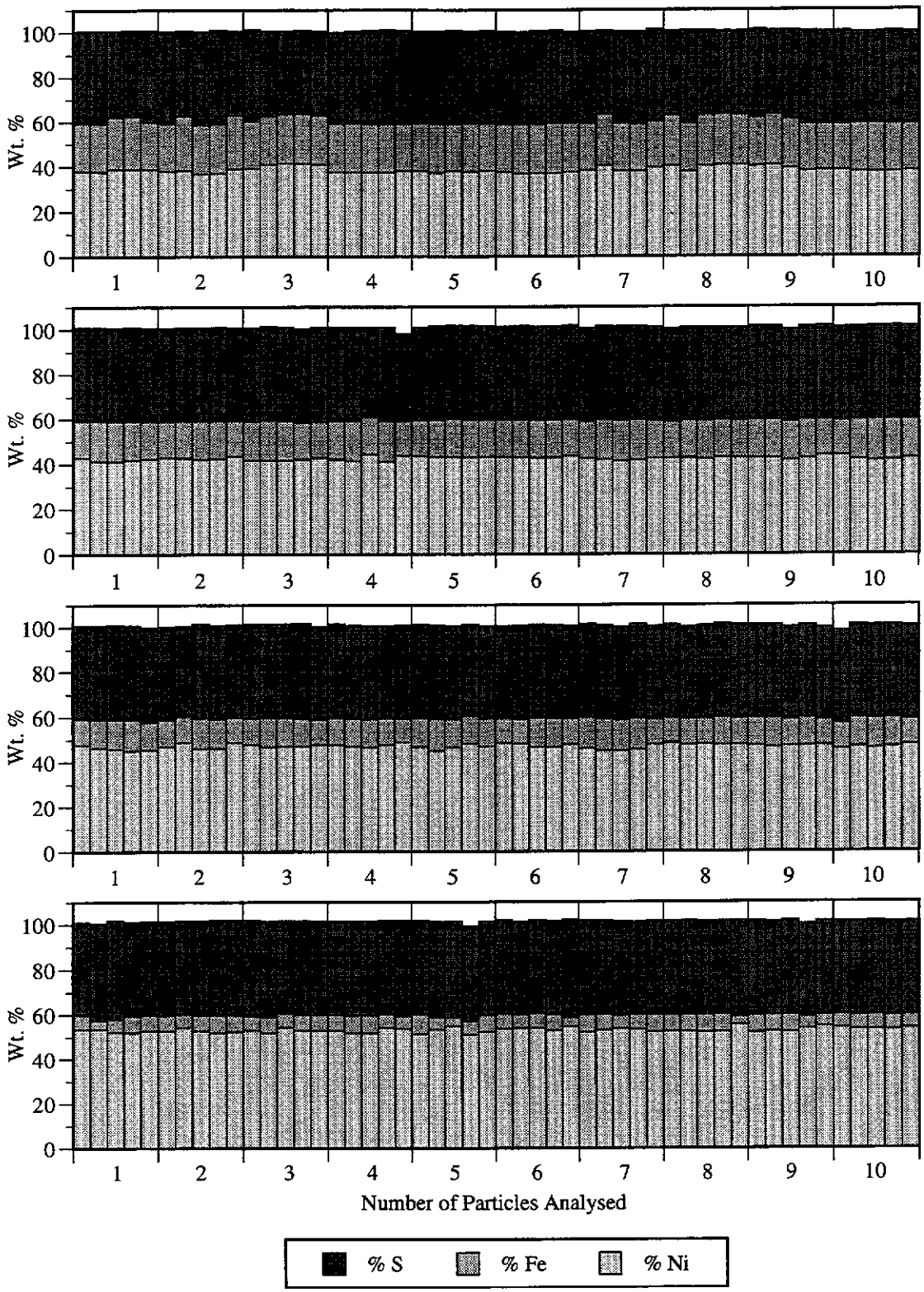

Figure 3.2 Distribution of iron, nickel and sulfur within 10 particles for each synthetic violarite sample. Each particle was analysed at 5 points across the diameter. Starting from the top $Fe_{0.97}Ni_{1.96}S_4$, $Fe_{0.73}Ni_{2.26}S_4$, $Fe_{0.46}Ni_{2.49}S_4$, and $Fe_{0.20}Ni_{2.72}S_4$.

3.1.3 SEM Examination of Synthetic Violarite

BSE micrographs for the two endmembers of the violarite series, $Fe_{0.97}Ni_{1.96}S_4$ and $Fe_{0.20}Ni_{2.72}S_4$, with a particle size distribution of <125 μm, are shown in Figures 3.3a and 3.3b. The particles were irregular in shape with some particles exhibiting small gaseous inclusions appearing as small pits in the surface. These inclusions were probably formed during the initial reaction between the iron, nickel and sulfur.

The violarite samples appeared to be relatively pure with only a minor amount of vaesite detected. The lower metal:sulfur ratio exhibited by the vaesite phase enables it to be easily identified due to its dark appearance compared to violarite in the BSE micrographs. The vaesite was present as either individual grains or inclusions in the violarite phase. Violarite was prepared using a two-stage synthesis. During the first stage iron, nickel and sulfur are heated in an evacuated quartz reaction tube to form mss with the desired iron:nickel ratio. The second stage involved the addition of sulfur, increasing the sulfur:metal ratio, to form violarite. The presence of vaesite suggested there was a slight excess of sulfur present during the second stage of the synthesis. Examination of all four violarite samples showed no evidence of mss remaining.

BSE micrographs of $Fe_{0.97}Ni_{1.96}S_4$ and $Fe_{0.20}Ni_{2.72}S_4$ showed typical examples of compositional zoning (Figures 3.3a and 3.3b). The texture of the zones appeared brighter than the bulk of the violarite phase. EPMA of the bright zones showed there was a slight decrease in the iron:nickel ratio, due to an increase in nickel content, resulting in an increase in the metal:sulfur ratio. This was apparent in the EPMA results obtained from the traverse scans across individual violarite particles, with a small amount of grains exhibiting higher metal:sulfur ratio within regions of the particles (Figure 3.2).

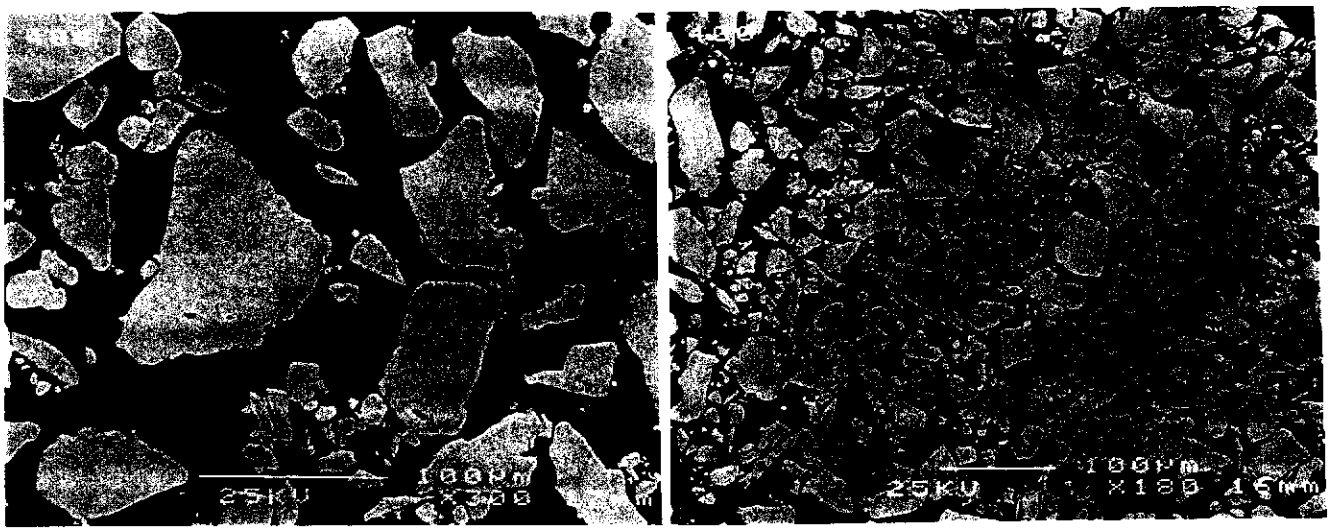

Figure 3.3a BSE micrographs of $Fe_{0.97}Ni_{1.96}S_4$.

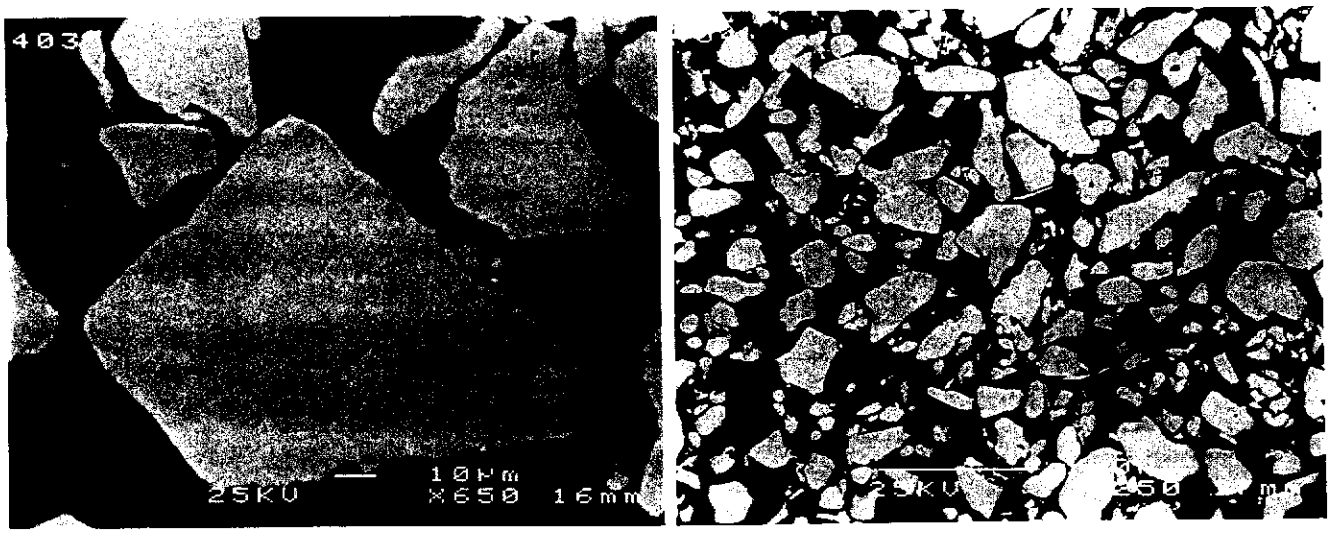

Figure 3.3b BSE micrographs of $Fe_{0.20}Ni_{2.72}S_4$.

3.1.4 XRD Analysis of Synthetic Violarite

All four violarite samples were analysed by XRD to determine their purity. A quartz internal standard was added to each synthetic violarite sample. Violarite and quartz accounted for all the lines in the diffraction pattern with no other phases evident.

The unit cell dimension of each violarite sample was calculated from the observed two-theta angles using PCPIRUM (Werner, 1969). Craig (1971) showed that the unit cell dimension of violarite was dependent on the iron:nickel ratio. The calculated unit cell dimension '*a*' is given in Table 3.4 for each synthetic violarite. The unit cell size of synthetic violarite was found to increase non-linearly as the iron:nickel ratio decreased. For example, as the stoichiometry approached the ideal endmember of the violarite solid-solution, $FeNi_2S_4$, the unit cell size became less dependent on the amount of iron substitution in the violarite lattice. The unit cell dimensions reported by Craig (1971) were approximately 0.1% higher than the values calculated for the current study. However, the relationship between the unit cell size and composition was identical to that found by the current study.

Sample	Iron:Nickel Ratio	Unit Cell Dimension (Å)
$Fe_{0.97}Ni_{1.96}S_4$	0.49	9.4532±0.0006
$Fe_{0.73}Ni_{2.26}S_4$	0.32	9.4555±0.0007
$Fe_{0.46}Ni_{2.49}S_4$	0.18	9.4620±0.0007
$Fe_{0.20}Ni_{2.72}S_4$	0.07	9.4667±0.0007

Table 3.4 Calculated unit cell dimension for the entire range of synthetic violarites.

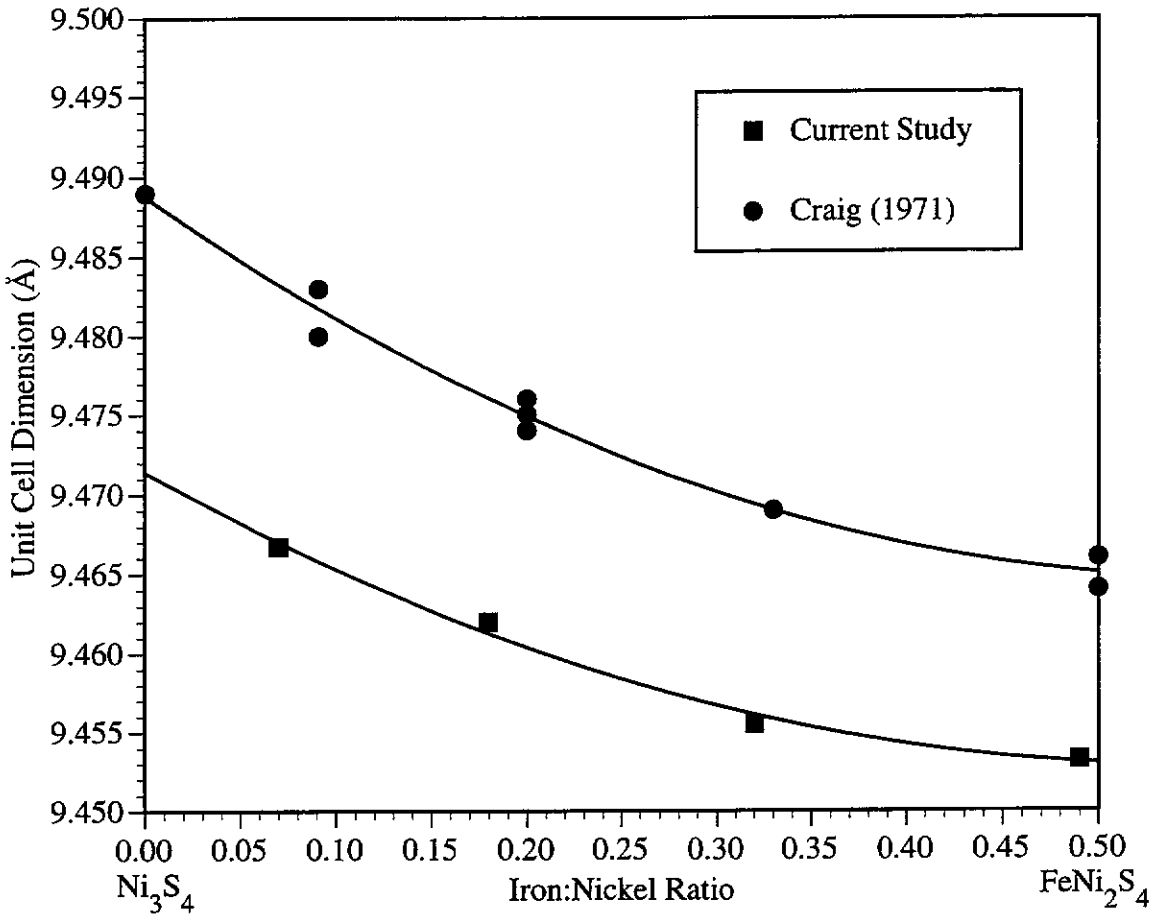

Figure 3.4 Variation in unit cell dimension '*a*' with composition between $Fe_{0.97}Ni_{1.96}S_4$ and $Fe_{0.20}Ni_{2.72}S_4$. Previous cell parameters reported by Craig (1971) have been included.

A decrease in the unit cell dimension, as the iron substitution increased in the violarite lattice, can be attributed to a decrease in the number of electrons occupying the antibonding orbitals of the σ^* band. The antibonding orbitals of the σ^* band are in close proximity to the sulfur ligands, therefore, the electron-electron repulsion will decrease as the number of electrons in the antibonding orbitals decreases and as a result the unit cell size will decrease (Craig, 1971).

3.1.5 BET Surface Area Analysis

Surface area measurements were determined by a 10 point BET method on the 63-45 μm particle size fraction for the entire range of synthetic violarite samples. Results from the BET analysis are presented in Table 3.5. The results indicated that all four synthetic violarites are extremely non-porous with the surface area measurements ranging from approximately 0.03-0.12 m^2g^{-1}. Figure 3.5 shows the surface area plotted against the iron:nickel ratio. There is a clear relationship between the stoichiometry of synthetic violarite and surface area, with the surface area decreasing as the iron:nickel ratio increases. For example, the surface area decreases from 0.12 to 0.03 m^2g^{-1} as the iron:nickel ratio increases from 0.07 ($Fe_{0.20}Ni_{2.72}S_4$) to 0.49 ($Fe_{0.97}Ni_{1.96}S_4$). The surface areas are considerable lower than compared to natural violarite samples. During the supergene alteration of pentlandite or pyrrhotite the number of sulfur atoms in the lattice is maintained while the iron and nickel are leached from the sulfide lattice (Nickel, Ross and Thornber, 1974). The loss of iron and nickel was calculated to cause a reduction in volume by 15% and 8% during the formation of violarite from pentlandite and pyrrhotite respectively. This reduction in volume is accommodated by an increase in porosity of the violarite. Therefore, the surface areas for the range of synthetic violarite samples would be more typical of hypogene or primary violarites.

Sample	Iron:Nickel Ratio	BET-Surface Area (m^2g^{-1})
$Fe_{0.97}Ni_{1.96}S_4$	0.49	0.03
$Fe_{0.73}Ni_{2.26}S_4$	0.32	0.05
$Fe_{0.46}Ni_{2.49}S_4$	0.18	0.09
$Fe_{0.20}Ni_{2.72}S_4$	0.07	0.12

Table 3.5 Surface area analysis of synthetic violarite using a 10 point BET method.

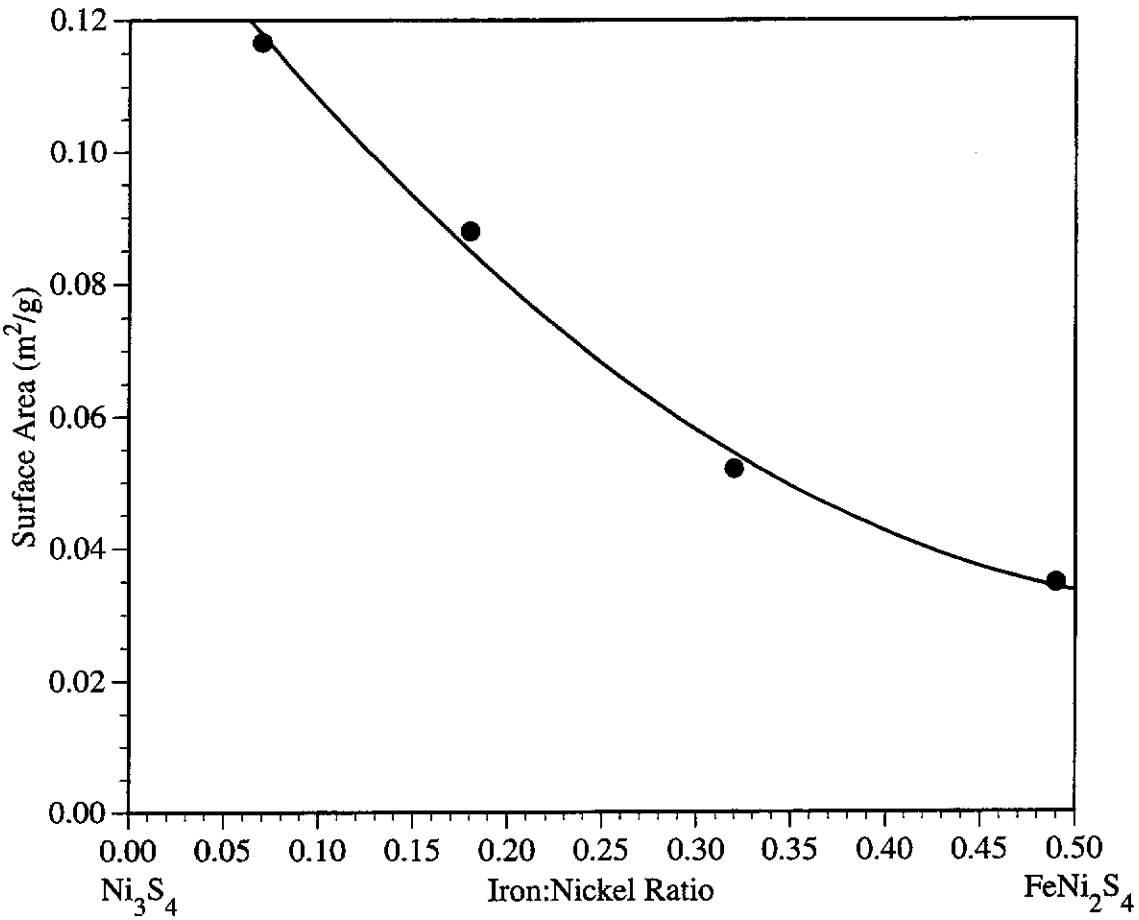

Figure 3.5 Effect of stoichiometry on the surface area of synthetic violarite.

3.1.6 Summary

The bulk composition of each of the synthetic violarite samples was determined by wet chemical analysis with the stoichiometry ranging from $Fe_{0.97}Ni_{1.96}S_4$ to $Fe_{0.20}Ni_{2.72}S_4$. All four violarite samples were of greater than 99% purity with a cubic thiospinel crystal structure. The unit cell dimension varied from 9.453 to 9.467Å. BET analysis revealed the samples to be extremely non-porous, with a slight increase in the surface area as the stoichiometry tended toward the nickel-rich endmember of the violarite series. Vaesite was the only impurity detected under SEM examination. Compositional zoning was evident within the violarite particles, however the variation in composition was minor when compared with the bulk composition of the sample.

3.2 CHARACTERISATION OF SYNTHETIC PENTLANDITE

3.2.1 Wet Chemical Analysis

The bulk composition of each pentlandite sample was determined by wet chemical analysis. As with the violarite samples, iron and nickel were determined in duplicate while only a single sulfur analysis was performed on each sample due to a limited amount of sample available for characterisation. Table 3.6 summarises the results obtained from the wet chemical analysis for iron, nickel and sulfur. The iron:nickel ratio ranged from 1.84 to 0.61 with respective stoichiometries of $Fe_{5.80}Ni_{3.15}S_8$ to $Fe_{3.40}Ni_{5.55}S_8$ for the two endmembers of the pentlandite series. The last two samples are sulfur-rich pentlandites with similar compositions of $Fe_{4.20}Ni_{4.16}S_8$ and $Fe_{4.22}Ni_{4.15}S_8$.

Sample	Composition (wt. %)				Stoichiometry
	Fe	Ni	S	Total	
1	42.32	24.16	34.54	101.02	$Fe_{5.80\pm0.10}Ni_{3.15\pm0.03}S_{8\pm0.06}$
2	40.57	26.09	34.62	101.28	$Fe_{5.59\pm0.10}Ni_{3.42\pm0.03}S_{8\pm0.06}$
3	38.46	28.59	34.82	101.87	$Fe_{5.36\pm0.10}Ni_{3.79\pm0.04}S_{8\pm0.06}$
4	36.44	30.62	34.05	101.11	$Fe_{5.08\pm0.10}Ni_{4.06\pm0.04}S_{8\pm0.06}$
5	33.17	33.62	34.16	100.98	$Fe_{4.59\pm0.08}Ni_{4.43\pm0.04}S_{8\pm0.06}$
6	29.18	37.40	34.39	100.97	$Fe_{4.01\pm0.07}Ni_{4.89\pm0.05}S_{8\pm0.06}$
7	24.59	42.20	34.47	101.26	$Fe_{3.40\pm0.06}Ni_{5.55\pm0.06}S_{8\pm0.06}$
8	31.90	33.22	35.60	100.72	$Fe_{4.20\pm0.07}Ni_{4.16\pm0.04}S_{8\pm0.06}$
9	32.03	33.11	35.10	100.24	$Fe_{4.22\pm0.07}Ni_{4.15\pm0.04}S_{8\pm0.06}$

Table 3.6 Results of wet chemical analysis for synthetic pentlandites.

3.2.2 EPMA of Synthetic Pentlandite

EPMA was performed on 35 particles from each pentlandite sample to determine the homogeneity between individual particles. The distribution of iron, nickel and sulfur in each particle is shown in Figure 3.6. The average weight percent for the major elements and the calculated stoichiometry are given in Table 3.7. All results were processed using Cameca PAP and CITZAF microprobe correctional software (Armstrong, 1988). The EPMA results correlated with the wet chemical results. For example, if the iron-rich and nickel-rich endmembers of the pentlandite series are considered, the stoichiometry calculated from the bulk analysis were $Fe_{5.80}Ni_{3.15}S_8$ and $Fe_{3.40}Ni_{5.55}S_8$ while for the EPMA results the calculated stoichiometries were $Fe_{5.83}Ni_{3.25}S_8$ and $Fe_{3.53}Ni_{5.51}S_8$ for the respective endmembers. The variation in composition between the individual particles was very minor. This is illustrated in Figure 3.6 showing each

Sample	Composition (wt. %)				Stoichiometry
	Fe	Ni	S	Total	
1	42.12	24.69	33.19	100.00	$Fe_{5.83\pm0.08}Ni_{3.25\pm0.07}S_{8\pm0.10}$
2	40.88	26.05	33.07	100.00	$Fe_{5.68\pm0.07}Ni_{3.44\pm0.05}S_{8\pm0.10}$
3	38.45	28.42	33.13	100.00	$Fe_{5.33\pm0.03}Ni_{3.75\pm0.03}S_{8\pm0.04}$
4	36.42	30.46	33.12	100.00	$Fe_{5.05\pm0.03}Ni_{4.02\pm0.03}S_{8\pm0.04}$
5	33.31	33.63	33.06	100.00	$Fe_{4.63\pm0.02}Ni_{4.44\pm0.02}S_{8\pm0.04}$
6	29.86	37.12	33.02	100.00	$Fe_{4.15\pm0.02}Ni_{4.91\pm0.02}S_{8\pm0.04}$
7	25.35	41.05	33.00	100.00	$Fe_{3.53\pm0.02}Ni_{5.51\pm0.02}S_{8\pm0.05}$
8	31.95	33.34	34.71	100.00	$Fe_{4.23\pm0.07}Ni_{4.20\pm0.04}S_{8\pm0.06}$
9	32.00	33.38	34.62	100.00	$Fe_{4.24\pm0.07}Ni_{4.21\pm0.04}S_{8\pm0.06}$

Table 3.7 Summary of EPMA results for each synthetic pentlandite sample. Results have been processed using Cameca PAP and normalised. Standard deviations in the stoichiometry are calculated to within a 99% confidence level.

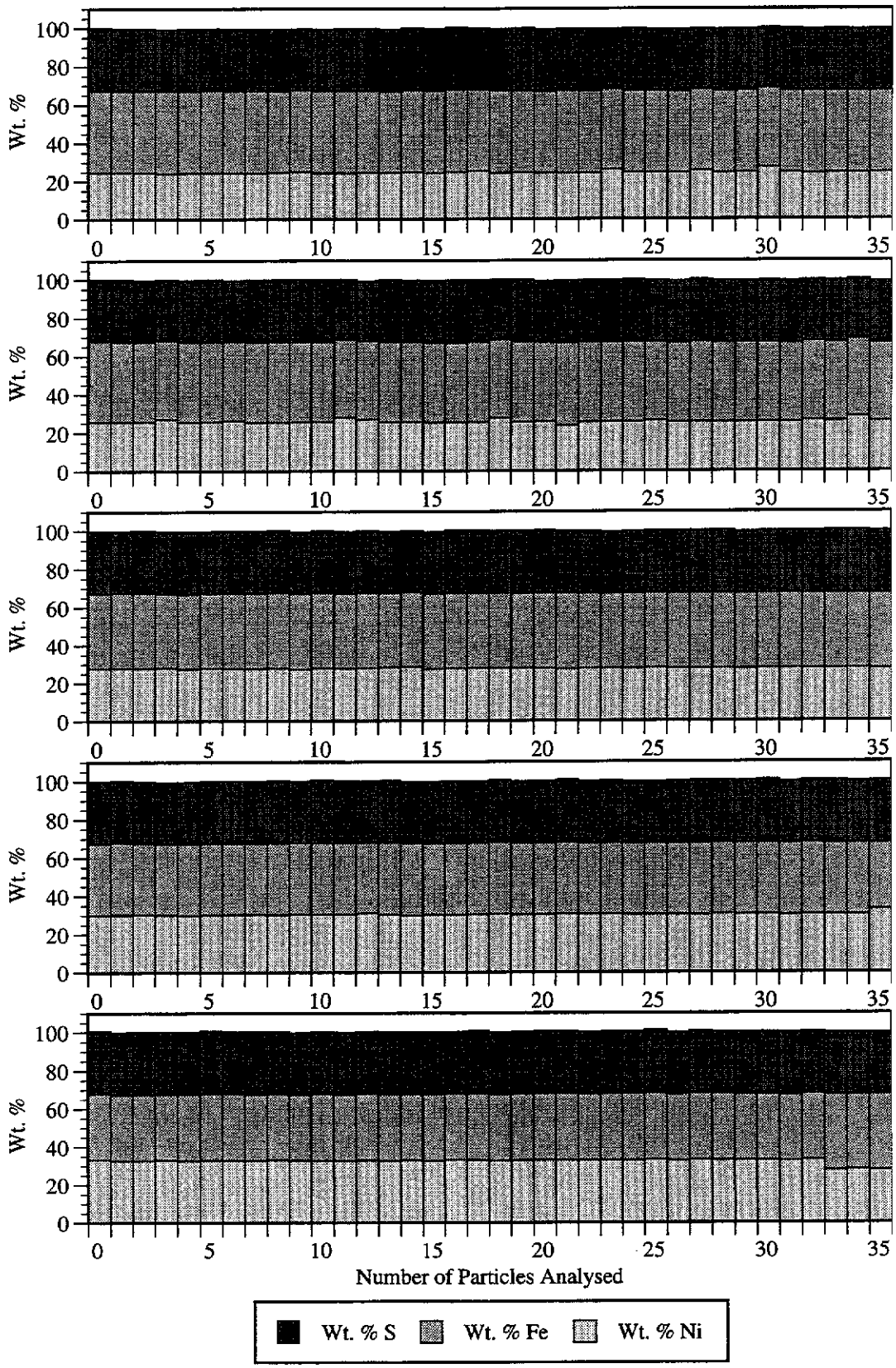

Figure 3.6 Distribution of iron, nickel and sulfur in a number of individual particles (single-point analysis at the centre of each particle) for the entire range of synthetic pentlandite samples. Starting from the top $Fe_{5.80}Ni_{3.15}S_8$, $Fe_{5.59}Ni_{3.42}S_8$, $Fe_{5.36}Ni_{3.79}S_8$, $Fe_{5.08}Ni_{4.06}S_8$, and $Fe_{4.59}Ni_{4.43}S_8$.

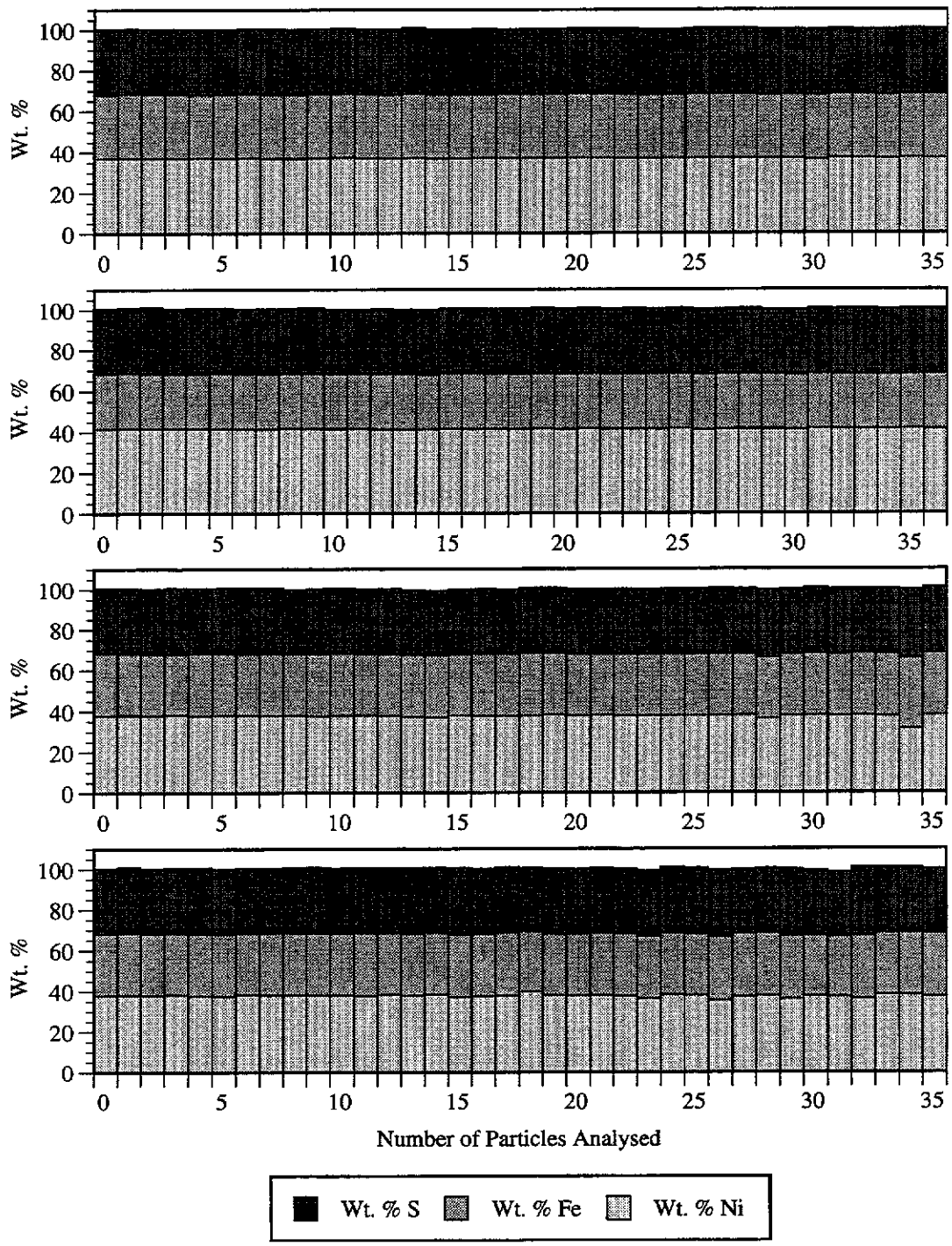

Figure 3.6 (con't) Distribution of iron, nickel and sulfur in a number of individual particles (single-point analysis at the centre of each particle) for the entire range of synthetic pentlandite samples. Starting from the top $Fe_{4.01}Ni_{4.89}S_8$, $Fe_{3.40}Ni_{5.55}S_8$, $Fe_{4.20}Ni_{4.16}S_8$, and $Fe_{4.22}Ni_{4.15}S_8$.

sample is relatively homogeneous with only minor variations in the distribution of iron, nickel and sulfur. The iron-rich pentlandite sample exhibited the largest deviation from the mean stoichiometry with the composition ranging from $Fe_{5.91}Ni_{3.32}S_{8.1}$ to $Fe_{5.75}Ni_{3.18}S_{7.9}$.

The homogeneity within individual particles was examined by performing traverse scans on a number of particles for the two endmembers of the pentlandite series, $Fe_{5.80}Ni_{3.15}S_8$ and $Fe_{3.40}Ni_{5.55}S_8$, and for the pentlandite corresponding closely to an ideal 1:1 iron:nickel ratio, $Fe_{4.5}Ni_{4.5}S_8$, with a stoichiometry of $Fe_{4.59}Ni_{4.43}S_8$. Figure 3.7 shows the iron, nickel and sulfur distribution at 5 points across 10 particles analysed for each sample. The stoichiometry and standard deviation for each sample analysed were calculated from the average weight percents shown in Table 3.8. The results show there was only a very minor variation in the composition within the particles. For example, the first particle for the iron-rich pentlandite sample varied in stoichiometry from $Fe_{5.78}Ni_{3.26}S_8$ to $Fe_{5.81}Ni_{3.27}S_8$ across the diameter of the particle. Similarly for the nickel-rich pentlandite sample the stoichiometry for the first particle varied from $Fe_{3.49}Ni_{5.48}S_8$ to $Fe_{3.52}Ni_{5.52}S_8$. Therefore, the synthetic particles appear to be homogeneous, with virtually no variation in composition across individual particles or from particle to particle.

Sample	Composition (wt. %)				Stoichiometry
	Fe	Ni	S	Total	
1	42.03	24.69	33.28	100.00	$Fe_{5.80\pm0.02}Ni_{3.24\pm0.02}S_{8\pm0.03}$
5	33.32	33.52	33.16	100.00	$Fe_{0.81\pm0.04}Ni_{2.19\pm0.04}S_{4\pm0.05}$
7	25.29	41.63	33.08	100.00	$Fe_{3.51\pm0.02}Ni_{5.50\pm0.02}S_{8\pm0.04}$

Table 3.8 Summary of EPMA results obtained from traverse scans across 10 particles for a range of synthetic pentlandite samples. Results were processed using Cameca PAP and normalised. Standard deviations in the stoichiometry are calculated to within a 99% confidence level.

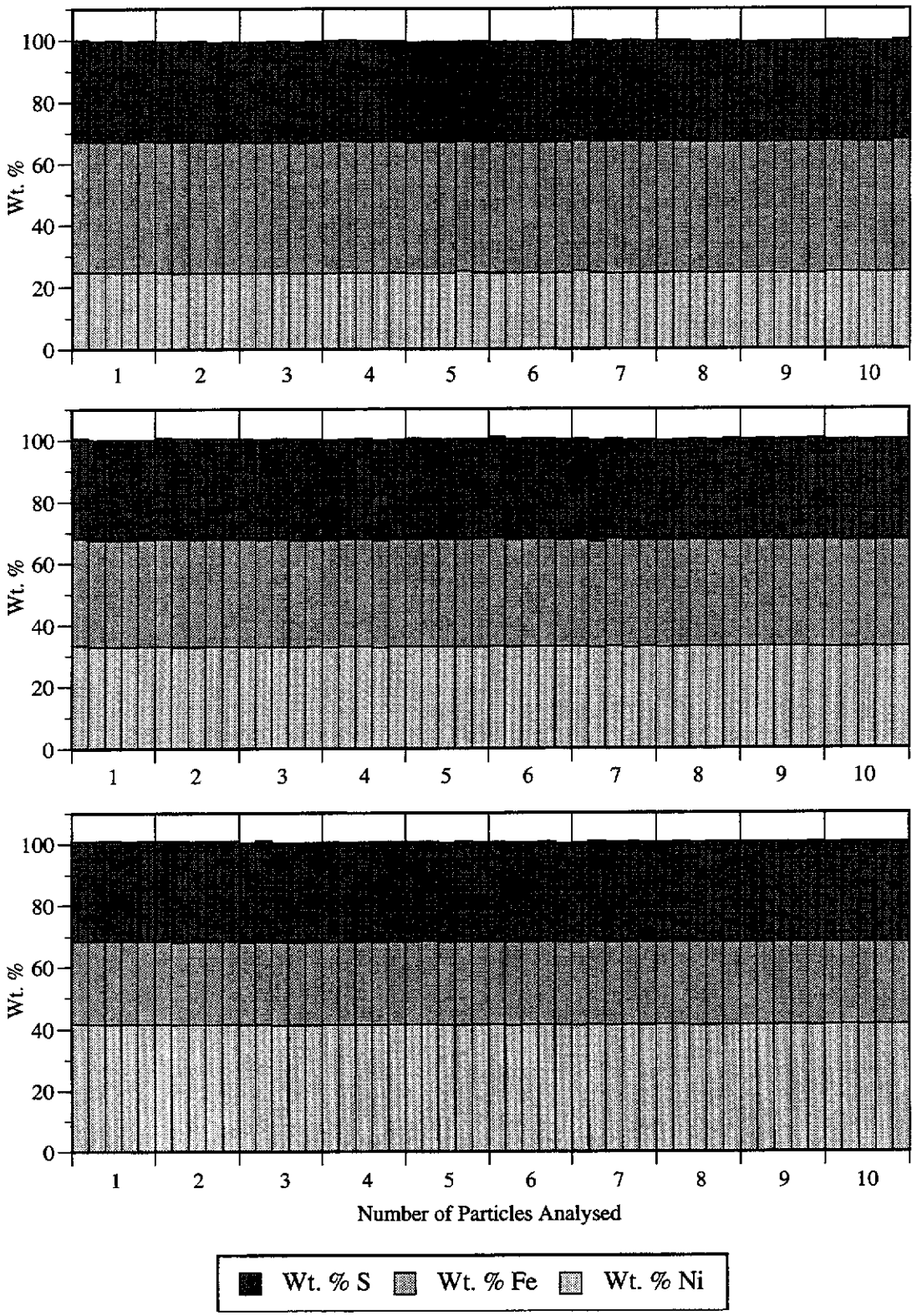

Figure 3.7 Typical distribution of iron, nickel and sulfur within 10 particles for $Fe_{5.80}Ni_{3.15}S_8$ (top), $Fe_{4.59}Ni_{4.43}S_8$ (middle), and $Fe_{3.40}Ni_{5.55}S_8$ (bottom). Each particle was analysed at 5 points across its diameter.

3.2.3 SEM Examination of Synthetic Pentlandite

Each of the synthetic pentlandite samples were examined under the electron microscope to determine whether there were any minor impurities formed during the synthesis of the pentlandites. Typical BSE micrographs of $Fe_{5.80}Ni_{3.15}S_8$, $Fe_{4.59}Ni_{4.43}S_8$, $Fe_{3.40}Ni_{5.55}S_8$ and $Fe_{4.20}Ni_{4.16}S_8$, with a particle size distribution of <125 μm, are shown in Figures 3.8a-3.8d. Pentlandite was the only phase evident with no impurities detected. The particles appeared to be angular in shape with some particles exhibiting small gaseous inclusions probably formed during the initial reaction between sulfur vapour and the iron and nickel metal.

The pentlandite were homogeneous with no compositional zoning evident in the particles. This is supported by the EPMA results obtained for the range of pentlandite samples. The absence of compositional zoning in the pentlandites samples compared to the violarite samples is possibly due to the higher temperature at which the pentlandites were synthesized. The higher temperatures enabled the sulfide to equilibrate in a shorter time period compared to synthetic violarite which was synthesized at more moderate temperatures. The increased temperature causes higher partial pressures of sulfur within the reaction tube and an increase in the solid diffusion of both iron and nickel, driving the reaction to completion.

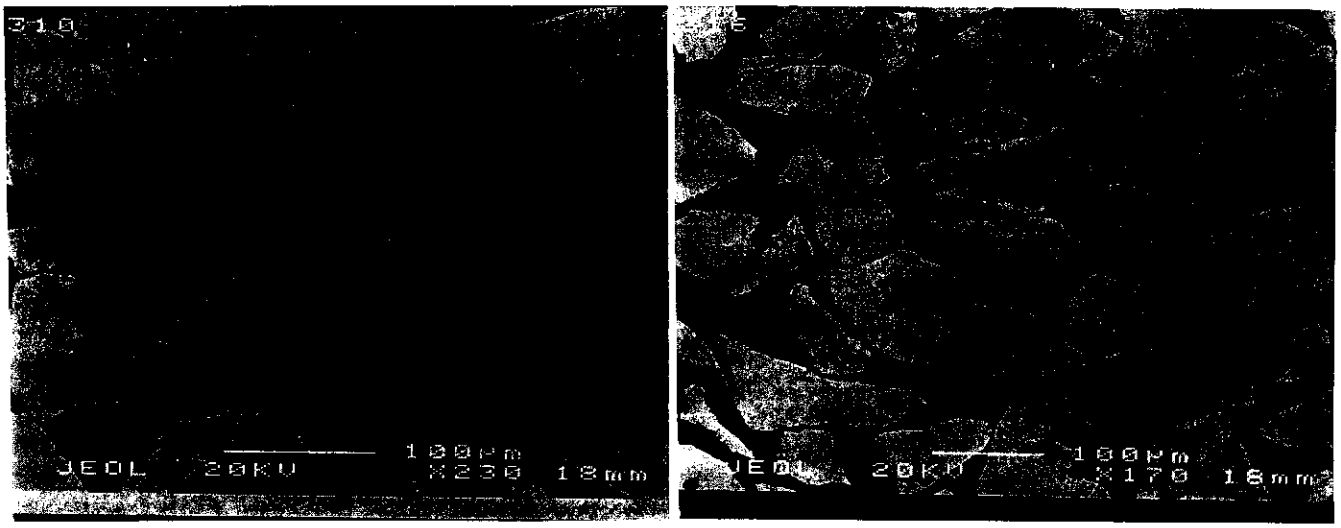

Figure 3.8a BSE micrograph of a iron-rich pentlandite, $Fe_{5.80}Ni_{3.15}S_8$ (left), and ideal pentlandite, $Fe_{4.59}Ni_{4.43}S_8$ (right).

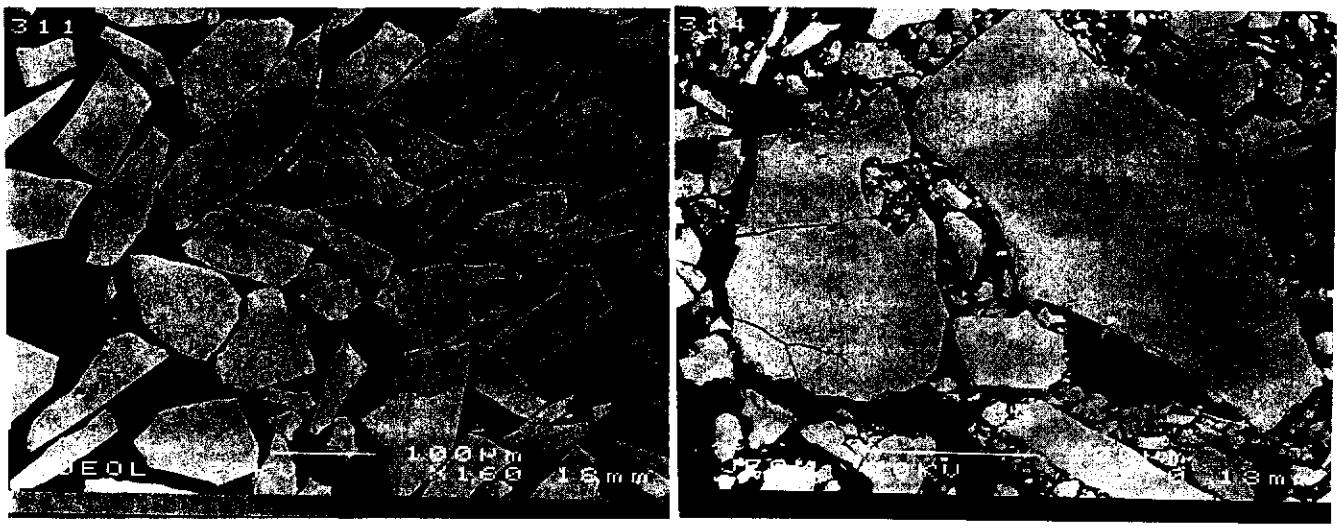

Figure 3.8b BSE micrograph of nickel-rich pentlandite, $Fe_{3.40}Ni_{5.55}S_8$ (left), and sulfur-rich pentlandite, $Fe_{4.20}Ni_{4.16}S_8$ (right).

3.2.4 XRD Analysis of Synthetic Pentlandite

XRD analysis was performed on each synthetic pentlandite sample using a quartz internal standard. Pentlandite and quartz accounted for all the lines in the diffraction. The unit cell dimension of each pentlandite sample was calculated from the observed two-theta angles in the XRD pattern using PCPIRUM (Werner, 1969). The unit cell parameters for the range of synthetic pentlandites (Table 3.9) are in agreement with those calculated by Knop, Ibrahim and Sutarno (1965) shown in Figure 3.9. The variation in the unit cell parameter '*a*' rapidly decreases as the iron:nickel ratio decreases with the unit cell dimension becoming less dependent on the iron:nickel ratio as it decreases towards the nickel-rich end of the solid-solution. This variation has been attributed to the metal addition in the solid solution for iron-rich compositions and metal omission for nickel-rich compositions to maintain a uniform number of *d* electrons in the unit cell.

This relationship can be explained by examining the pentlandite crystal structure. Pentlandite has a cubic crystal structure with the unit cell consisting of 36 metal atoms and 32 sulfur atoms. The metal atoms occupy four of the octahedral sites and 32 of the tetrahedral sites, while sulfur atoms are arranged in a cubic close-packed sublattice. The metal-rich sulfide structure appears to be stabilised by the formation of three metal-metal bonds formed extending from each of the tetrahedral cations resulting in the formation of a metallic cube cluster (Rajamani and Prewitt, 1973). In order for the pentlandite structure to be stabilized the number of *3d* electrons in the unit cell must remain constant despite large variations in the iron:nickel ratio (Rajamani and Prewitt, 1973). Ideal pentlandite with a stoichiometry of $Fe_{4.5}Ni_{4.5}S_8$ exhibits the most stable composition in the solid-solution with the structure stabilised by seven *d* electrons per cation.

The general formula for Fe-Ni pentlandite has been assigned as

$[Fe_uNi_v]^{IV}(Fe_xNi_yT_z)_8{}^{VI}S_8$ where (Rajamani and Prewitt, 1973),

u and v = mole fraction of Fe and Ni in the octahedral sites

x and y = mole fraction of Fe and Ni in the tetrahedral sites,

Tz = tetrahedral vacancy for Ni-rich compositions or excess cations for Fe-rich compositions.

Therefore, the increase in the unit cell parameter as the iron:nickel ratio increases is due to the addition of larger iron atoms within the pentlandite unit cell, while the unit cell becomes less dependent on the iron:nickel ratio as it decreases due to ommision of iron from the pentlandite lattice.

Sample	Iron:Nickel Ratio	Unit Cell Dimension (Å)
$Fe_{5.80}Ni_{3.15}S_8$	1.84	10.1750±0.0006
$Fe_{5.59}Ni_{3.42}S_8$	1.63	10.1622±0.0006
$Fe_{5.36}Ni_{3.79}S_8$	1.41	10.1436±0.0006
$Fe_{5.08}Ni_{4.06}S_8$	1.25	10.1228±0.0006
$Fe_{4.59}Ni_{4.43}S_8$	1.04	10.1148±0.0007
$Fe_{4.01}Ni_{4.89}S_8$	0.82	10.0987±0.0007
$Fe_{3.40}Ni_{5.55}S_8$	0.62	10.0987±0.0007

Table 3.9 Calculated unit cell dimension '*a*' for a range of synthetic pentlandites with varying iron:nickel ratios.

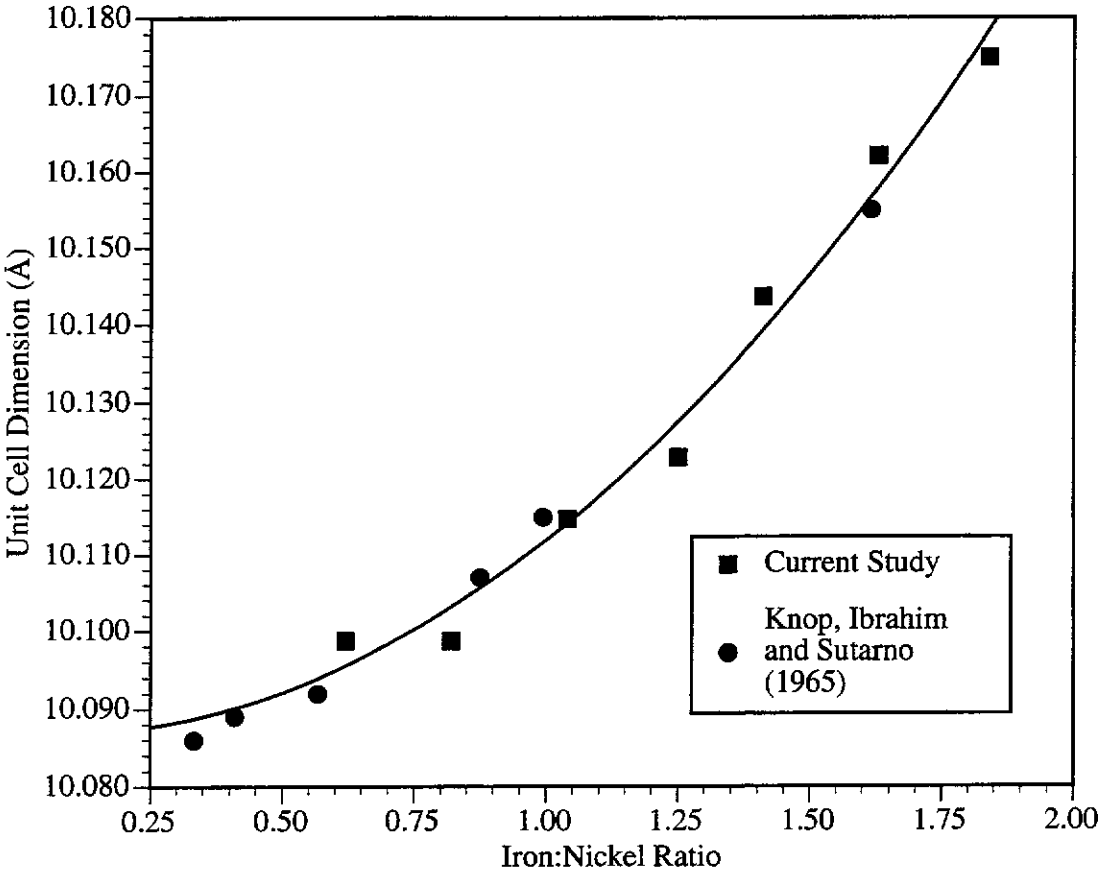

Figure 3.9 Variation in the unit cell parameter '*a*' with composition of synthetic pentlandite. Calculated cell parameters for a range of natural pentlandites by Knop, Ibrahim and Sutarno (1965) are shown.

There is appreciable variation in the d_{115} spacing of pentlandite as the composition varies (Figure 3.10). Shewman and Clark (1970) established the relationship by the following expression:

$$d_{115} = 1.9407 - 0.0023x + 0.0077x^2$$

where x represents the iron:nickel weight ratio. The d_{115} for the range of synthetic pentlandites follow this relationship and are in good agreement with the finding from Shewman and Clark (1970).

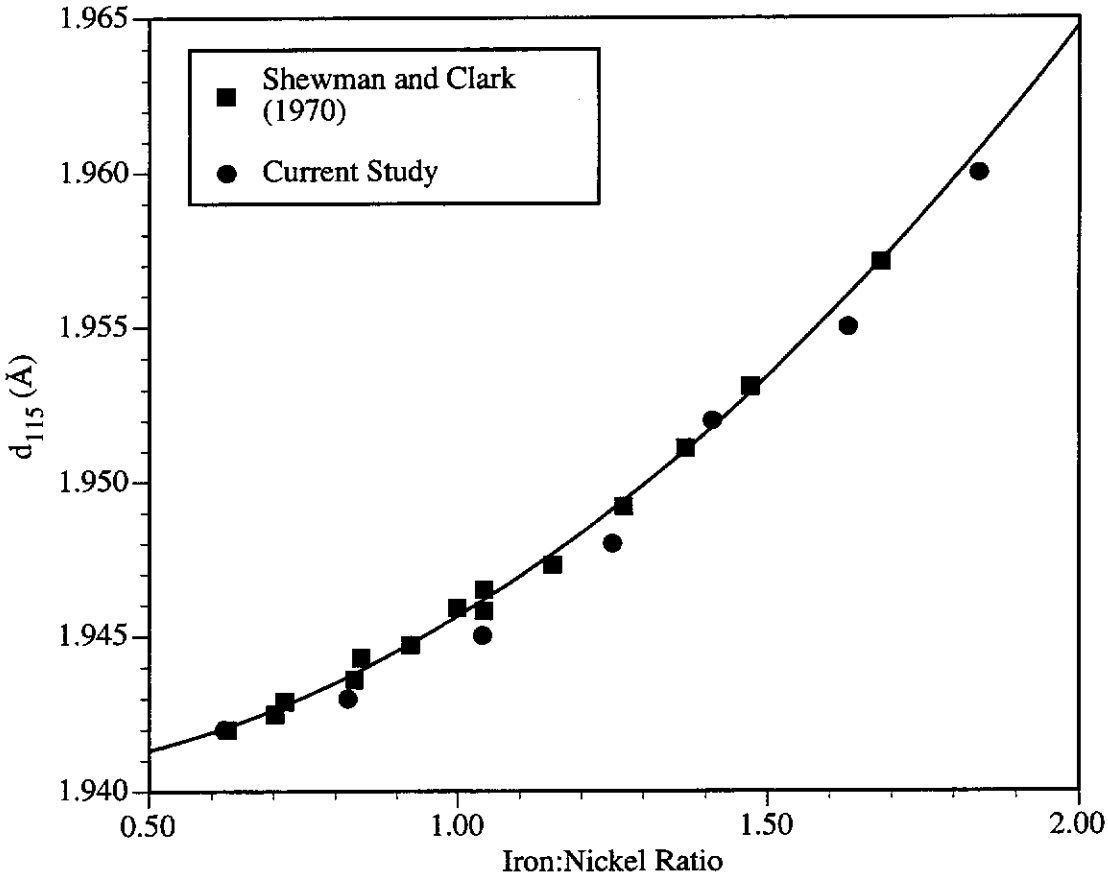

Figure 3.10 The effect of the iron:nickel mole ratio of synthetic pentlandite on the d_{115} spacing.

3.2.5 BET Surface Area Analysis

The surface area for each synthetic pentlandite with a particle size range of 63-45 μm is presented in Table 3.10. Figure 3.11 shows the relationship between the surface area and the iron:nickel ratio and metal:sulfur ratio of synthetic pentlandite. There appeared to be no correlation between the iron:nickel ratio or the metal:sulfur ratio on the surface area of synthetic pentlandite. The surface areas were very low ranging from 0.25 to 0.38 m^2g^{-1} over the entire pentlandite series. Natural pentlandites predominantly occur as primary iron-nickel sulfides and will tend to have a relatively low surface areas, while secondary sulfides are more porous due to weathering and will generally have surface areas much higher than those of primary sulfide minerals.

Sample	Iron:Nickel Ratio	Metal:Sulfur Ratio	BET-Surface Area (m^2g^{-1})
$Fe_{5.80}Ni_{3.15}S_8$	1.84	1.119	0.36
$Fe_{5.59}Ni_{3.42}S_8$	1.63	1.126	0.26
$Fe_{5.36}Ni_{3.79}S_8$	1.41	1.144	0.25
$Fe_{5.08}Ni_{4.06}S_8$	1.25	1.142	0.38
$Fe_{4.59}Ni_{4.43}S_8$	1.04	1.128	0.31
$Fe_{4.01}Ni_{4.89}S_8$	0.82	1.112	0.34
$Fe_{3.40}Ni_{5.55}S_8$	0.62	1.119	0.34
$Fe_{4.20}Ni_{4.16}S_8$	1.01	1.045	0.25
$Fe_{4.22}Ni_{4.15}S_8$	1.01	1.046	0.29

Table 3.10 Surface area analysis of synthetic pentlandite using a 10 point BET method.

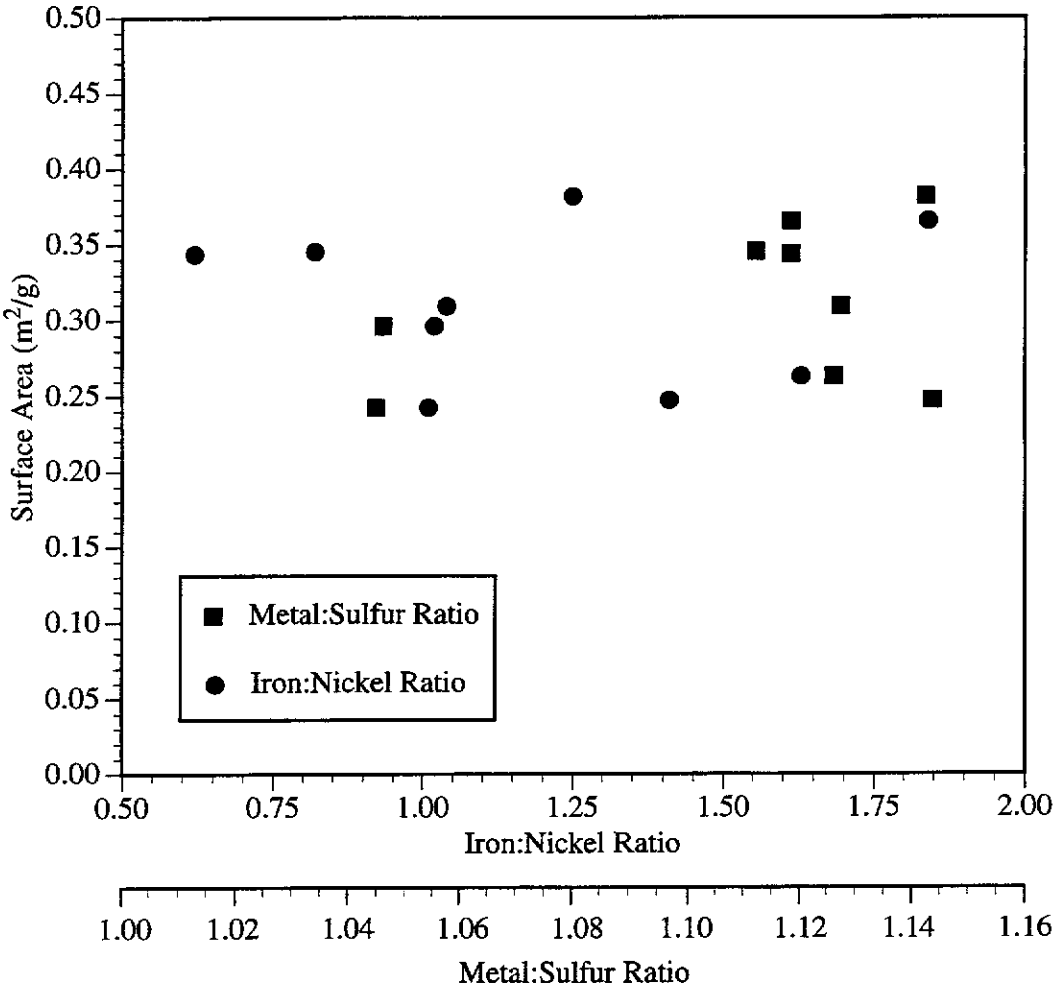

Figure 3.11 The effect of stoichiometry on the surface area of synthetic pentlandite.

3.2.6 Summary

The bulk composition for each synthetic pentlandite sample was determined by wet chemical analysis with the stoichiometry ranging from $Fe_{5.80}Ni_{3.15}S_8$ to $Fe_{3.40}Ni_{5.55}S_8$ for the series. Each sample was of greater than 99% with no other phases detected. EPMA analysis of the pentlandite particles showed they were homogeneous with no significant variation in the composition from particle to particle or within the individual particles. The synthetic pentlandites had a cubic crystal structure with the unit cell dimensions increasing non-uniformly from 10.0987 to 10.1750Å as the iron:nickel ratio increased from 0.61 to 1.84. BET surface area analysis indicated the samples were non-porous with the surface area remaining relatively constant as the iron:nickel ratio and metal:sulfur varied.

CHAPTER 4

THE PYROLYTIC DECOMPOSITION AND OXIDATION OF SYNTHETIC VIOLARITE

4.0 INTRODUCTION

In this Chapter the results of TG-DTA studies on the thermal decomposition in nitrogen, and the oxidation in air and oxygen, of synthetic violarite are reported. Violarites of various stoichiometries were prepared, and the two endmembers, $Fe_{0.97}Ni_{1.96}S_4$ and $Fe_{0.20}Ni_{2.72}S_4$, were examined in detail at slow heating rates in nitrogen and air to determine the effect of changes in the iron:nickel ratio on their reaction sequences. $Fe_{0.97}Ni_{1.96}S_4$ is close to the ideal stoichiometry of $FeNi_2S_4$, while $Fe_{0.20}Ni_{2.72}S_4$ is a nickel-rich violarite. The two endmembers will be referred to as "ideal violarite" and "nickel-rich violarite". The ignition behaviour of the entire range of stoichiometries was examined by isothermal TG to determine the effect of changes in the iron:nickel ratio on ignition temperature, and hence the relative order of reactivity.

In the discussion of the thermal analytical results, the temperature ranges stated will normally refer to the extrapolated onset and offset of the TG-DTA event. The onset and offset temperatures of the TG-DTA events were reproducible to within ±5°C. Any small mass gains observed prior to 300°C were due to buoyancy effects of the gas stream. The mass varied by ±0.05% between each replicate TG-DTA trace. Samples were collected at predetermined temperatures for analysis by various instrumental techniques such as XRD, SEM, FTIR and EPMA.

4.1 Pyrolytic Decomposition of Synthetic Violarite

Previous studies on the thermal decomposition of synthetic violarite were performed using evacuated silica tube experiments (Craig, 1971; Misra and Fleet, 1974). A maximum thermal stability of 461±3°C was found for violarite with a composition of $Fe_{0.92}Ni_{2.08}S_4$, in equilibrium with sulfur vapour (Craig, 1971, p.1306). The stability of the violarite solid solution is illustrated in the Fe-Ni-S ternary phase diagram shown in Figure 4.1. The upper stability temperature of polydymite, Ni_3S_4, is 356±3°C. Below this temperature the violarite field extends from ideal violarite to polydymite. The solubility of iron in the violarite solid solution is restricted to the ideal violarite composition, $FeNi_2S_4$. The compositional range of the violarite solid solution remains constant down to 200°C, the lowest temperature investigated, with no evidence of the iron-rich end of the solid solution increasing beyond the ideal violarite endmember (Kullerud, 1963; Craig, 1971).

In this study the mechanism for the pyrolytic decomposition of the two endmembers from the violarite solid solution was examined. Ideal violarite will be discussed in detail. Synthetic violarite samples were heated at 10°C min^{-1} in a nitrogen atmosphere using simultaneous TG-DTA. Samples were collected at various temperatures for characterisation and examination of the particle morphology. The effect on the particle morphology and mechanism of pyrolytic decomposition was also studied at an increased heating rate of 40°C min^{-1} in a nitrogen gas flow.

In a dynamic system, such as the TG-DTA apparatus used in this study, the gaseous products evolved from the iron-nickel sulfide are continually purged from the furnace, hence the sample is in continuous contact with a fresh inert gas stream. The partial pressure of sulfur above the sample is decreased by the purging action, thus equilibrium between the vapour phase and the sample will not be achieved and the reaction will tend to proceed to completion. Therefore, caution must be taken when

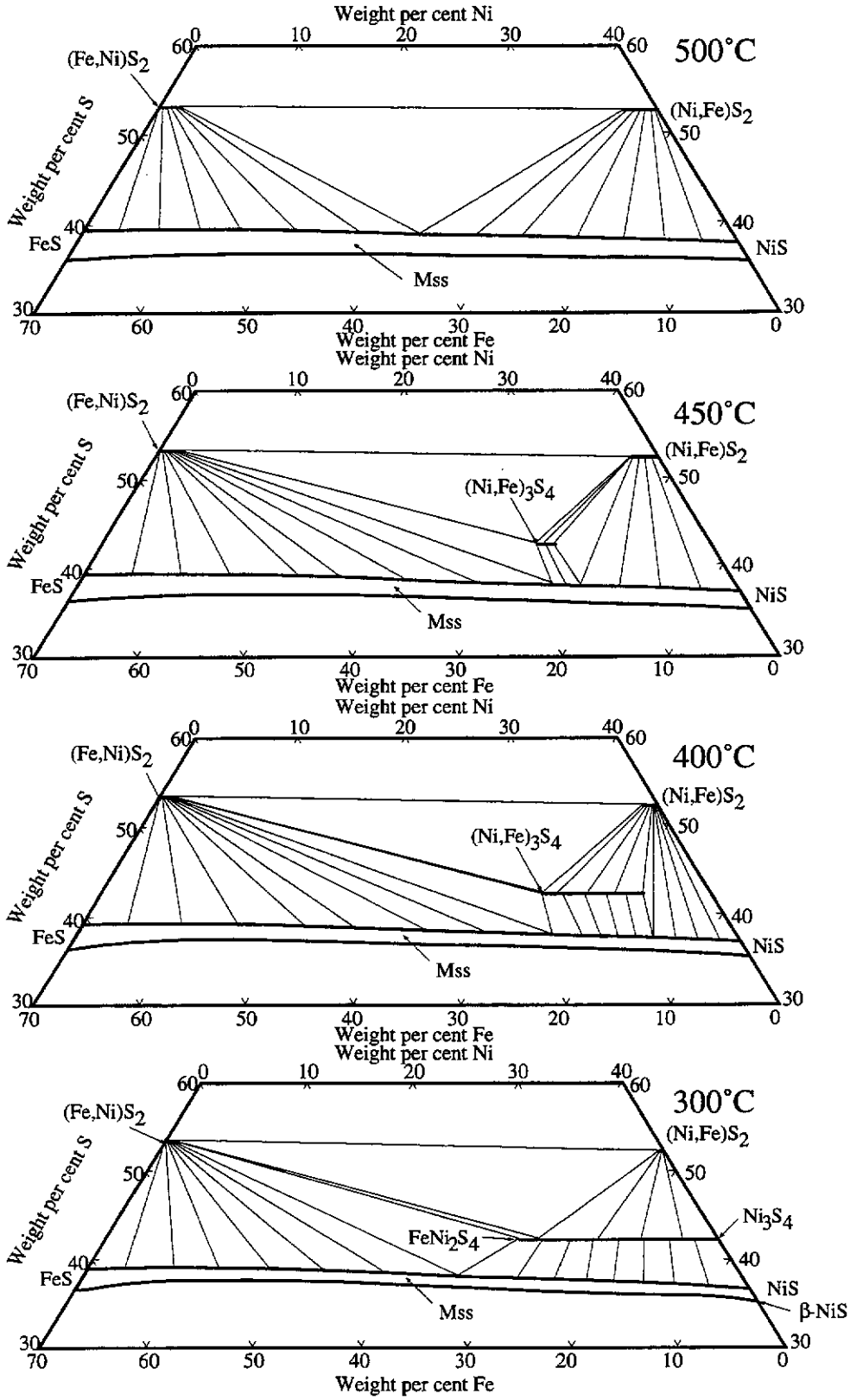

Figure 4.1 Fe-Ni-S ternary phase diagram illustrating the thermal stability of the violarite-polydymite solid solution at: 500°C, 450°C, 400°C, 300°C (Redrawn from data obtained from Craig, 1971).

comparing TG-DTA results with those from previous studies carried out under equilibrium conditions.

4.1.1 Pyrolytic Decomposition of Ideal Violarite

Figure 4.2 shows a typical TG-DTA curve for $Fe_{0.97}Ni_{1.96}S_4$ (ideal violarite), with a particle size range of 63-45μm heated at 10°C min^{-1} in nitrogen. There was no TG-DTA activity observed prior to 420°C. Micrographs taken of polished samples collected between 385-420°C showed no evidence of pyrolytic decomposition. EPMA results were consistent with those obtained for the initial violarite sample.

Above 420°C the commencement of pyrolytic decomposition for ideal violarite was evident with a small mass loss of 2.25% observed between 420-525°C. Analysis by XRD of samples collected at 425°C revealed violarite as the major phase with a minor trace of mss present (see Figure 4.3). BSE micrographs taken of a sample collected at 425°C showed small ragged regions of mss within the violarite host (Figure 4.4a). When analysed by EPMA, violarite and mss had an average composition of $Fe_{1.14}Ni_{1.86}S_{3.86}$ and $Fe_{0.36}Ni_{0.56}S_{1.00}$ respectively. The EPMA results showed an increase in the iron:nickel ratio for both violarite and mss compared to the initial violarite starting material. SEM examination of the quenched products revealed a small amount of vaesite, $(Ni,Fe)S_2$, present. This would account for the decrease in the nickel concentration in the violarite and mss.

By 490°C, mss and violarite were identified as the major phases in the XRD pattern along with a minor amount of vaesite. SEM examination of the violarite sample still showed a significant portion of violarite remaining with an increase in the amount of mss as the next major phase (Figure 4.4b). A minor amount of vaesite was also detected. There was no evidence of vaesite found in association with violarite. In all cases the vaesite was exsolved within the mss phase. A small porous outer rim

approximately 2 μm thick was evident around the majority of the particles, probably caused by the evolution of sulfur vapour from the surface of the particle. EPMA results of the violarite and mss at 490°C showed a large decrease in the sulfur concentration. Approximately 20 particles were analysed for each phase present. The sulfur concentration was significantly lower for the mss phase compared with the composition found at 425°C, with the composition approaching a 1:1 metal:sulfur ratio. The mean composition of the violarite host was $Fe_{1.15}Ni_{1.85}S_{3.87}$, whereas the mss had a mean stoichiometry of $Fe_{0.38}Ni_{0.54}S_{1.00}$. The violarite still exhibited a cubic thiospinel crystal structure despite having lost a small amount of sulfur from its lattice.

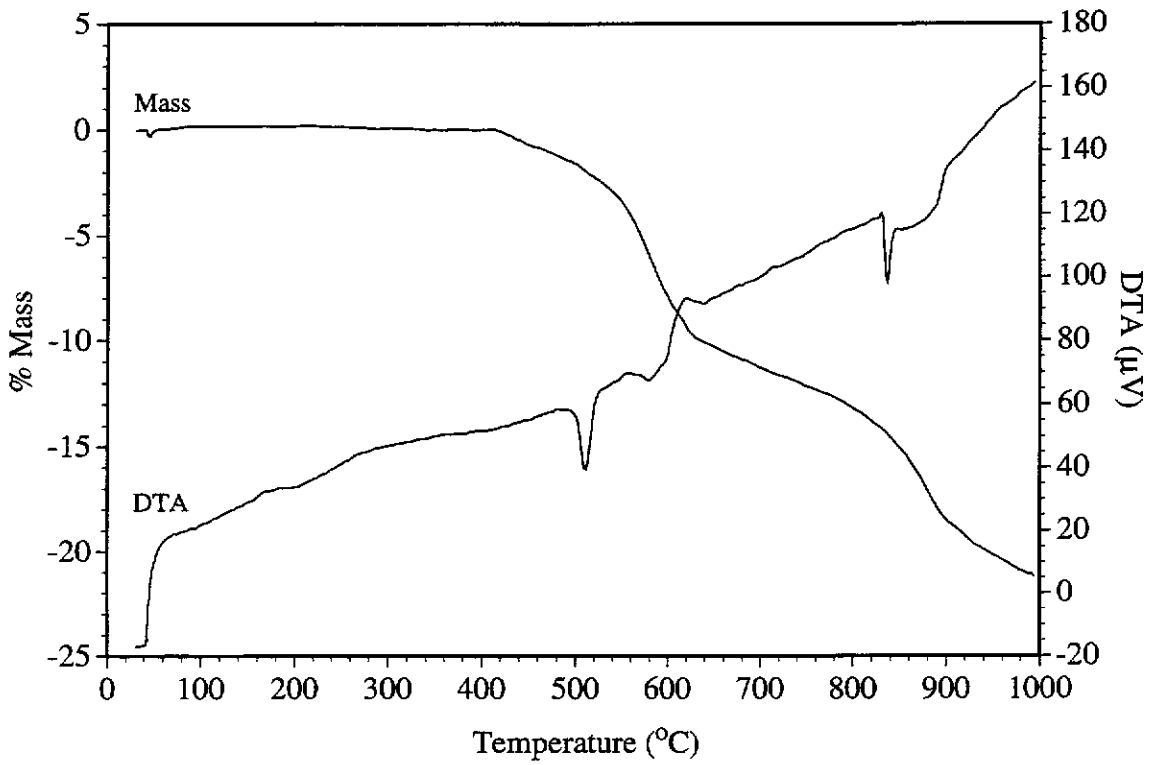

Figure 4.2 Typical TG-DTA trace of ideal violarite ($Fe_{0.97}Ni_{1.96}S_4$), 5.01 mg sample, heating rate 10°C min^{-1} in a nitrogen atmosphere, 63-45 μm particle size fraction.

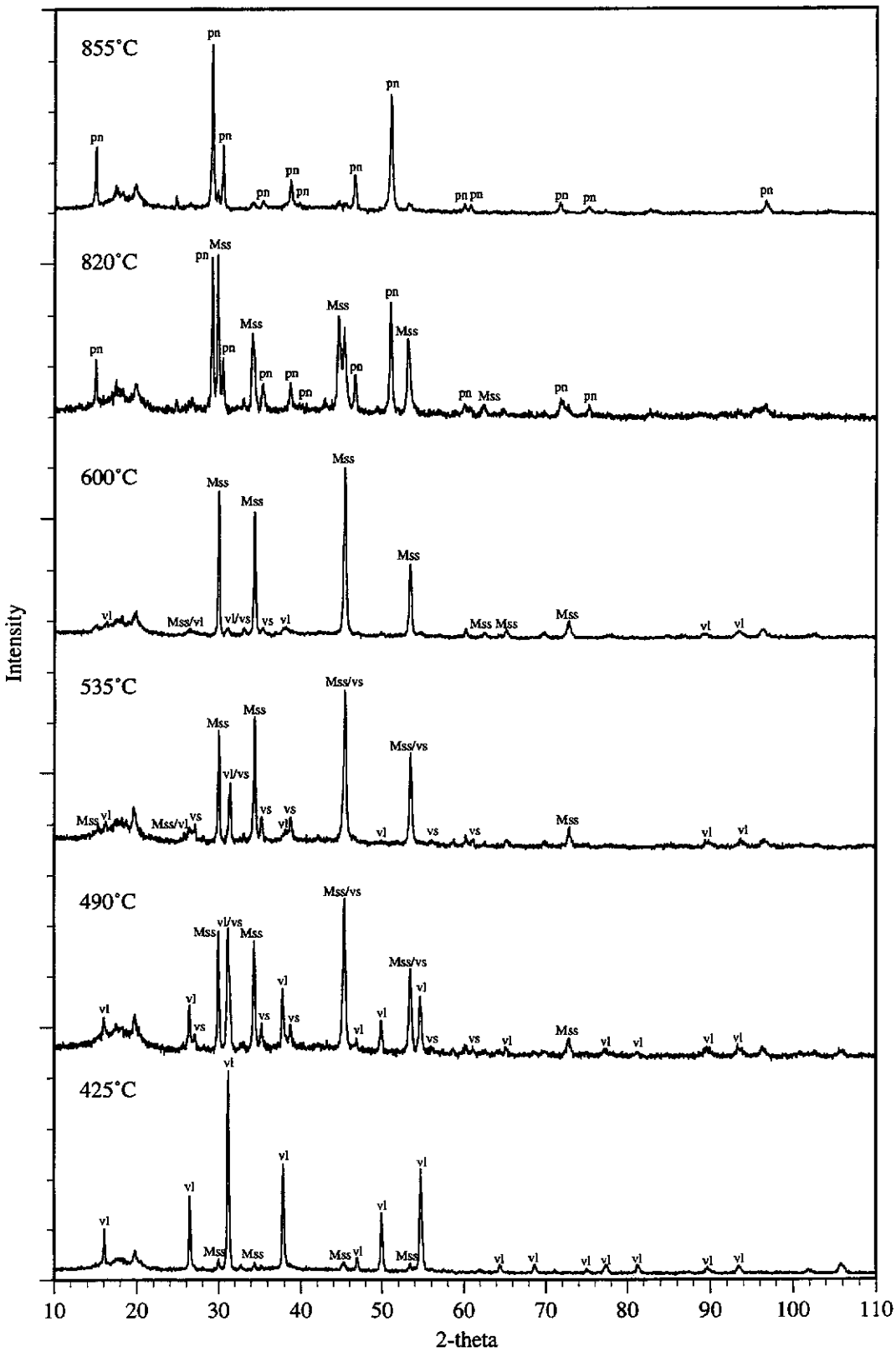

Figure 4.3 XRD pattern for ideal violarite ($Fe_{0.97}Ni_{1.96}S_4$) heated at 10°C min^{-1} in a nitrogen atmosphere and collected at pre-selected temperatures. The temperature and phases identified are indicated on each pattern. (vl - violarite, mss - monosulfide solid solution, vs - vaesite, pn - pentlandite).

Hence, the evolution of sulfur gas from the violarite lattice resulting in the formation of mss would account for the small mass loss between 420-525°C observed in the TG curve for ideal violarite. The evolution of sulfur from the violarite can be represented by the following reaction:

$$(2\text{-}2x)\ (Fe,Ni)_3S_4 \rightarrow 6\ (Fe,Ni)_{1-x}S + (1\text{-}4x)\ S_{2\,(g)}$$

At 495°C a sharp endothermic peak was observed in the DTA trace with an onset and offset temperature of 495°C and 525°C respectively. This was unlikely to be associated with the gradual mass loss observed in the TG trace, due to the intensity of the peak and the small temperature range over which the peak occurred compared with the temperature range of the mass loss. A sample of ideal violarite was heated 10°C past the offset temperature of the endothermic peak and allowed to cool at 10°C min^{-1}. During cooling an exothermic peak of similar intensity was observed between 495-465°C. This is characteristic of a reversible phase transition. Above a cooling rate of 10°C min^{-1} the phase transition seemed to be non-reversible. Analysis by XRD of the pyrolysis product collected at 535°C showed that violarite had completely decomposed with mss and vaesite as the major products. SEM examination of the pyrolysed products showed mss as the major phase with thin dark regions of vaesite within the mss grains (Figure 4.4c). The mean composition of the vaesite phase was $Ni_{0.83}Fe_{0.17}S_{1.85}$, similar to the ideal stoichiometry of $(Ni,Fe)S_2$. The metal:sulfur ratio for the mss had increased slightly with an average composition of $Fe_{0.38}Ni_{0.55}S_{1.00}$.

Synthetic sulfides with the general formula AB_2S_4 have been shown to form either a spinel or a cation-deficient NiAs crystal structure (Tressler, Hummel and Stubican, 1968). The latter crystal structure consists of two different types, namely monoclinic or hexagonal structure. Spinels have one-third of the ions, A^{2+}, occupying tetrahedral sites and the remaining two-thirds, B^{3+}, are octahedrally coordinated, while in the

defect-NiAs crystal structure all the cations are octahedrally coordinated. Therefore, the latter should have a higher density due to higher coordination of the cations. The defect NiAs structures have a higher density indicating that under high pressure and temperature a spinel may undergo a phase transition to a defect NiAs phase. Albers and Rooymans (1965) reported daubreelite, $FeCr_2S_4$, underwent a first-order phase transition at high temperature and pressure to a hexagonal nickel-arsenide type crystal structure. The transition was later confirmed by Bouchard (1967). Both studies found there was an increase in the density of approximately 8% compared with daubreelite. By analogy Kullerud (1968) suggested that other sulfides such as polydymite and violarite may also undergo such a transformation to defect NiAs structures at elevated pressures and temperatures forming a mixture of monosulfide and disulfide. During an earlier investigation on the Ni-S system Kullerud and Yund (1962) reported that the decomposition of polydymite occurred at 356°C. The decomposition was described by the following reaction:

$$(1\text{-}2x)\ Ni_3S_4\ (\text{cubic}) \Leftrightarrow 2\ Ni_{1-x}S\ (\text{hexagonal}) + (1\text{-}4x)\ NiS_2\ (\text{cubic})$$

The volumes of the products were smaller than that of the initial cubic Ni_3S_4. Similar results were found for linnaeite, Co_3S_4, which, when heated above 664°C, decomposed to hexagonal $Co_{1-x}S$ and cubic CoS_2.

Since polydymite is the endmember of the violarite solid solution, one would expect that violarite with varying iron:nickel ratios would behave similarly. Therefore, the phase transition shown in the DTA curve occurring between 495-525°C can be attributed to the pyrolytic decomposition of ideal violarite to mss and vaesite according to the following reaction:

$$(1\text{-}2x)\ (Fe,Ni)_3S_4\ (\text{cubic}) \Leftrightarrow 2\ (Fe,Ni)_{1-x}S\ (\text{hexagonal}) + (1\text{-}4x)\ (Ni,Fe)S_2\ (\text{cubic})$$

The proposed mechanism for the pyrolytic decomposition of violarite between 420°C and 525°C is supported by the series of Fe-Ni-S isothermal sections shown in Figure 4.1. Between 300°C and 400°C the Fe-Ni-S phase diagram shows a decrease in the violarite stability field with univariant regions formed between violarite, mss and ferroan vaesite $(Ni,Fe)S_2$ or violarite, mss and nickeloan pyrite $(Fe,Ni)S_2$. The nickel-rich end of the stability field decreases more rapidly than the ideal stoichiometric end of the violarite solid solution. As sulfur is evolved from the violarite sample between 420-525°C the composition falls below the ideal metal:sulfur ratio of 3:4. This shift in the composition of the sulfide below the violarite stability field results in the exsolution of mss within the violarite host. Analysis of the violarite and mss showed there was a shift in the iron:nickel ratio towards the iron boundary of the Fe-Ni-S ternary phase diagram. The decrease in nickel from the violarite and mss can be accounted for by the formation of vaesite. Therefore, the bulk composition of the violarite sample must lie within the expanding univariant region formed between violarite, mss and vaesite. Between 450°C and 500°C the ternary phase diagram shows violarite decomposes to form a divariant region between mss and vaesite. The decomposition of the ideal violarite commenced at 495°C. This was approximately 35°C higher than the maximum thermal stability temperature previously reported by Craig (1971) for synthetic violarite using evacuated silica tube experiments. The difference in the decomposition temperature of violarite can be attributed to the different experimental conditions used. By 525°C the violarite has completely decomposed to mss and vaesite.

Between 525°C and 615°C the rate of mass loss increased, with a loss of 7.65% observed. The mass loss coincided with a broad endotherm occurring in the temperature range of 560-625°C. The XRD pattern showed mss as the major phase with only a very minor trace of violarite remaining after 600°C. No vaesite was evident in the XRD pattern. The minor trace of violarite was likely formed during the cooling stage of the pyrolysis product due to the reversible reaction between mss and

the remaining vaesite. Micrographs of samples collected at 600°C showed the outer rim of the sulfide particle to be quite irregular in shape with a porous structure (Figure 4.4d). Large macropores were evident in a number of particles. The formation of the pores was probably due to the rapid evolution of sulfur caused by high internal pressures from within the sulfide particle as the vaesite decomposed to mss according to the following general reaction:

$$(2\text{-}2x)\ (Ni,Fe)S_2 \rightarrow 2\ (Fe,Ni)_{1-x}S + (1\text{-}2x)\ S_{2\,(g)}$$

An increase in the surface area of the sulfide particles can be clearly seen from the micrographs after the decomposition of violarite. However, surface area analysis by BET was not possible due to the large sample sizes required by this technique. Analysis of a number of mss particles by EPMA showed that they were homogeneous with a mean composition of $Fe_{0.36}Ni_{0.59}S_{1.00}$. The composition of the mss was in close agreement with the theoretical composition of $Fe_{0.31}Ni_{0.64}S_{1.00}$, calculated from the mass loss from the TG curve observed between 420°C and 625°C.

Between 615°C and 845°C a gradual mass loss of 4.10% was observed. This mass loss was associated with a slight endothermic drift in the DTA baseline commencing at 620°C. Pyrolysis products collected at 725°C and examined by SEM revealed a homogeneous mss phase. By 795°C the mss phase exhibited partial melting (see Figure 4.4e). The surfaces of the particles were relatively smooth compared to those particles collected at 600°C (Figure 4.4d). A number of the macropores had collapsed leaving small gaseous inclusions in the sulfide particles. EPMA analysis of the mss phase collected at 725°C and 795°C showed a loss of sulfur with average compositions of $Fe_{0.36}Ni_{0.66}S_{1.00}$ and $Fe_{0.37}Ni_{0.74}S_{1.00}$ at the respective temperatures. A minor trace of pentlandite was also detected within some mss particles collected at 795°C appearing as a brighter phase when compared with the mss phase.

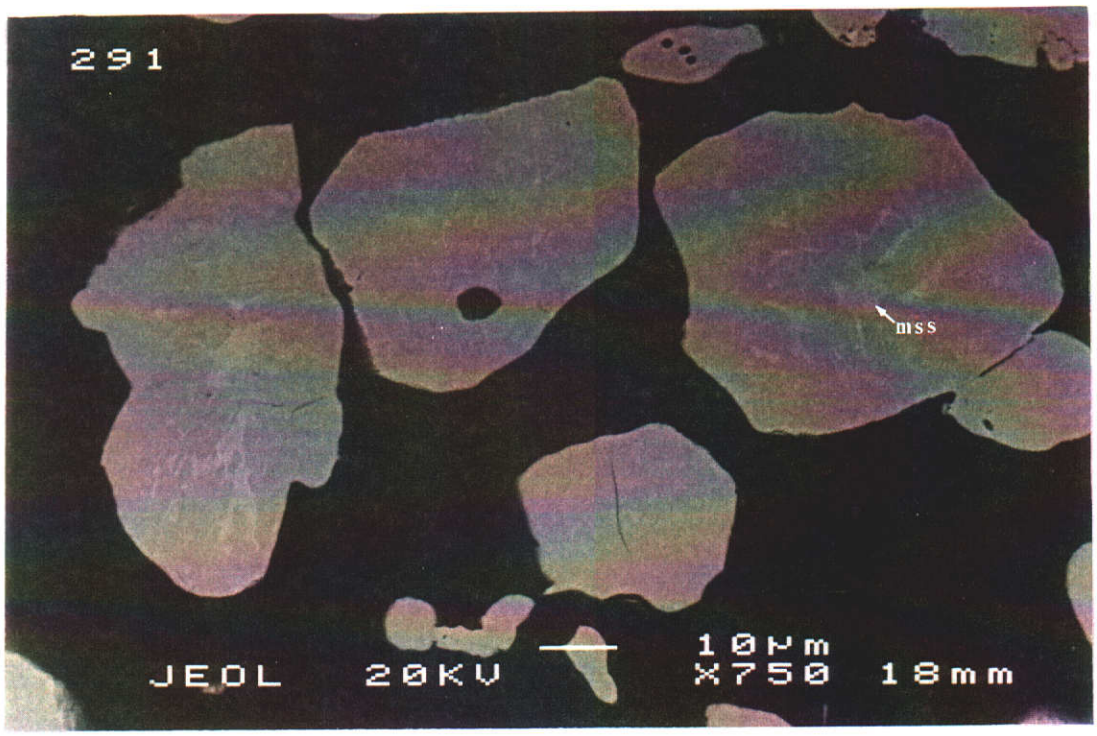

Figure 4.4a BSE micrograph of ideal violarite collected at 425°C, (heating rate 10°C min^{-1}, 63-45 µm particle size fraction). Note mss phase (light grey) in the unreacted violarite (dark grey) host.

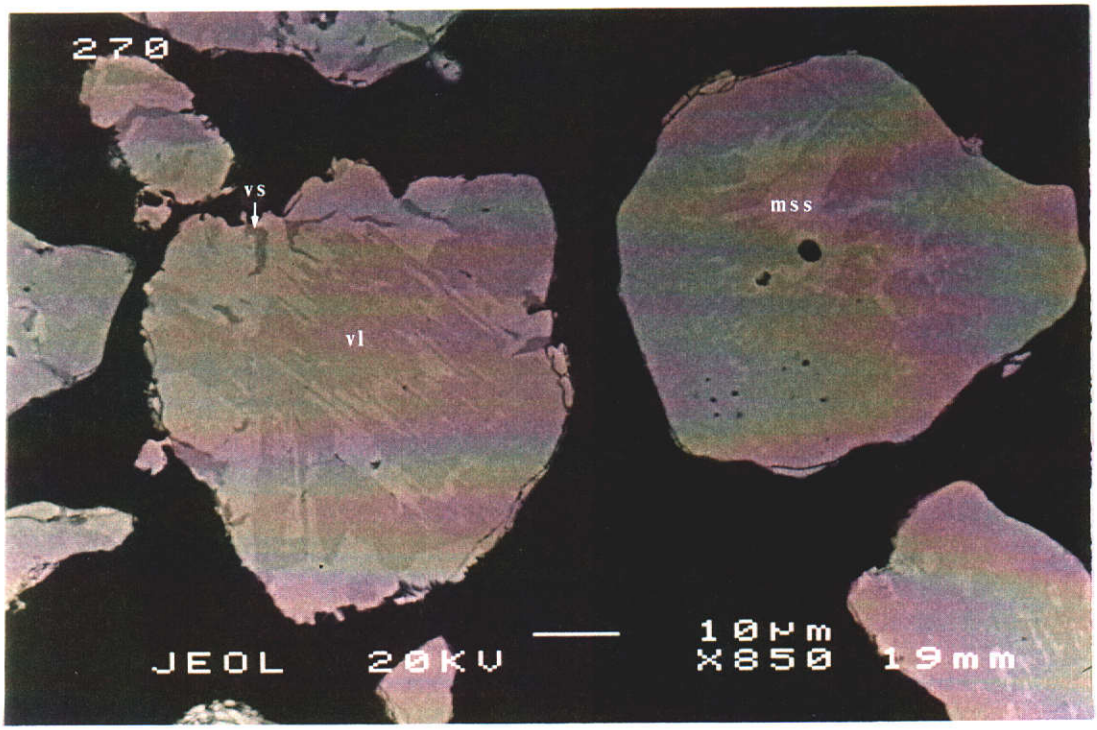

Figure 4.4b Micrograph of ideal violarite sample collected at 490°C. Violarite is still the major phase with mss exsolved within the violarite host. A small amount of vaesite was detected which can be seen in the particle on the left as the small dark grey phase in the mss.

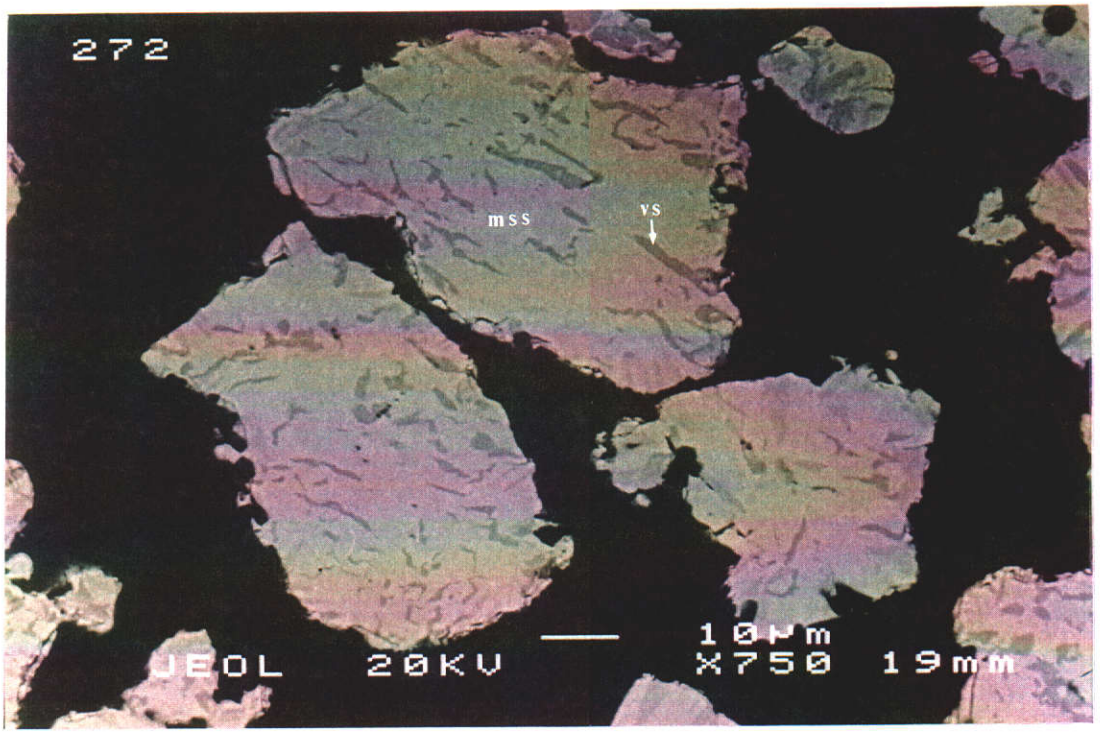

Figure 4.4c Typical BSE micrograph of ideal violarite collected at 535°C. The violarite has undergone complete pyrolytic decomposition to form mss (defect NiAs structure) and vaesite (cubic disulfide phase).

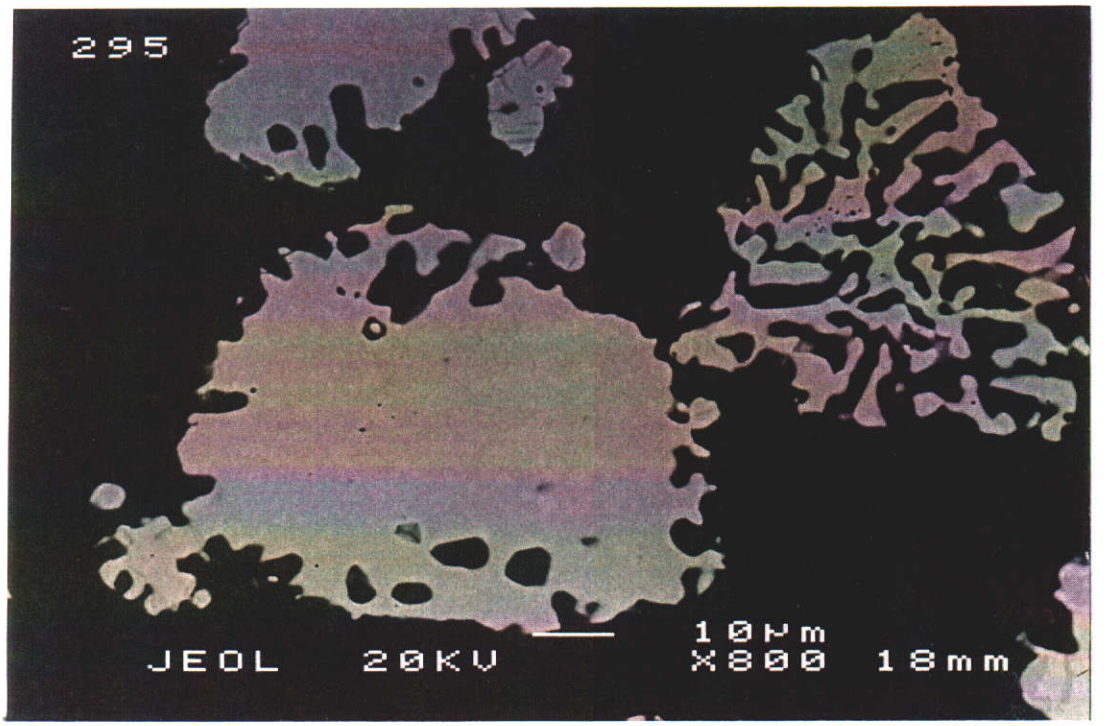

Figure 4.4d BSE micrograph of ideal violarite collected at 600°C. Mss is the major phase evident with the decomposition of vaesite. Large macropores are evident in a number of the particles.

Hence, the gradual mass loss between 615°C and 795°C can be associated with the continual loss of sulfur from the mss phase.

$$(Fe,Ni)_{1\pm x}S \rightarrow (Fe,Ni)_{1+x}S + S_{2\,(g)}$$

The reaction sequence between 615°C and 795°C can be explained by a series of Fe-Ni-S ternary phase diagrams. Figure 4.5 shows an isothermal section at 650°C from the Fe-Ni-S ternary phase system. At 650°C, mss and $(Fe,Ni)_{3\pm x}S_2$ may coexist in equilibrium with each other. A central sulfide liquid region appears at 635°C and forms a divariant region with $(Fe,Ni)_{3\pm x}S_2$. By 860°C the central sulfide liquid region expands considerably with a univariant region formed between mss and $(Fe,Ni)_{3\pm x}S_2$, and a divariant region with $(Fe,Ni)_{3\pm x}S_2$ (see Figure 4.6). Between 615°C and 795°C the mss stability field expands vertically allowing the metal:sulfur ratio to increase resulting in the loss of sulfur. Analysis of the mss between 725°C and 795°C showed the metal:sulfur ratio increased from 1.02 to 1.11. According to the ternary phase diagram shown in Figure 4.6, the composition of the mss falls below the mss stability field in this temperature range resulting in the formation a high temperature $(Fe,Ni)_{3\pm x}S_2$ phase coexisting in equilibrium with mss.

The presence of the high temperature $(Fe,Ni)_{3\pm x}S_2$ was confirmed by a sharp endotherm with an onset temperature of 835°C observed in the DTA trace. This corresponded to the incongruent melting point of $(Fe,Ni)_{3\pm x}S_2$ to mss and the central sulfide liquid phase (Kullerud, 1962). Kullerud and Yund (1962) reported the melting point of a ternary phase with a metal:sulfur composition of nearly 3:2, $Ni_{3\pm x}S_2$, similar to heazlewoodite, to be 806°C.

$$(Fe,Ni)_{3\pm x}S_{2\,(s)} \Leftrightarrow (Fe,Ni)_{3\pm x}S_{2\,(l)}$$

$$(Fe,Ni)_{3\pm x}S_{2\,(l)} \rightarrow (Fe,Ni)_{1\pm x}S_{(s)} + (Fe,Ni)_{1+x}S_{(l)}$$

XRD results obtained from a sample collected at 820°C, coinciding with the melting point transition, detected mss and pentlandite present. The high temperature $(Fe,Ni)_{3\pm x}S_2$ phase is a non-quenchable phase. On cooling the central sulfide liquid will react with mss to form $(Fe,Ni)_{3\pm x}S_2$ at 862°C (Kullerud, 1963). Between 862°C and 610°C the mss and $(Fe,Ni)_{3\pm x}S_2$ assemblage remains stable. Below 610°C pentlandite is formed by the reaction between mss and $(Fe,Ni)_{3\pm x}S_2$ (Kullerud, 1963; Ewers, 1973). Therefore, any central sulfide liquid or $(Fe,Ni)_{3\pm x}S_2$ present during the cooling of the pyrolysis product will completely react to form pentlandite with excess mss remaining. By 855°C there was only slight evidence of mss present with pentlandite as the major phase.

A broad endotherm followed the melting point transition with onset and offset temperatures of 845°C and 900°C. A mass loss of 4.85% coincided with the endotherm. This was associated with the continual loss of sulfur from the mss phase to form additional central sulfide liquid phase.

$$(Fe,Ni)_{1\pm x}S_{(s)} \rightarrow (Fe,Ni)_{1+x}S_{(l)} + S_{2(g)}$$

By 890°C the sulfide was completely molten forming spherical metal sulfide prills during quenching of the sample. BSE micrographs taken of the molten product quenched at 870°C (Figure 4.4f) showed preferred orientation of pentlandite along the mss during recrystallisation. The exsolved pentlandite formed thin coherent needles with either the (111) pentlandite plane parallel to the (0001) mss plane or (110) pentlandite plane parallel to the (1010) mss plane (Francis *et al.*, 1976). Rapidly quenched samples of $(Fe,Ni)_{1-x}S$ solid solutions showed the pentlandite recrystallised in randomly oriented blebs due to the planes of exsolved pentlandite not aligning with the mss.

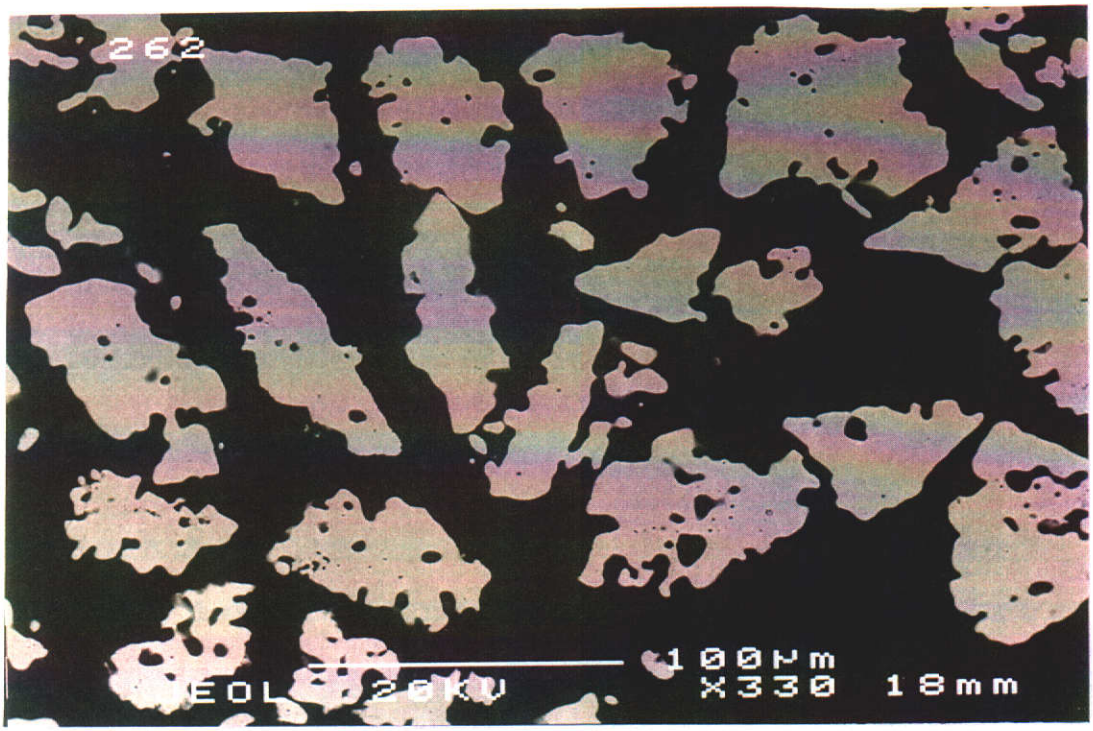

Figure 4.4e BSE micrograph of ideal violarite collected at 795°C. Partial melting of the mss can be observed with a number of the macropores collapsed forming holes within the mss particle.

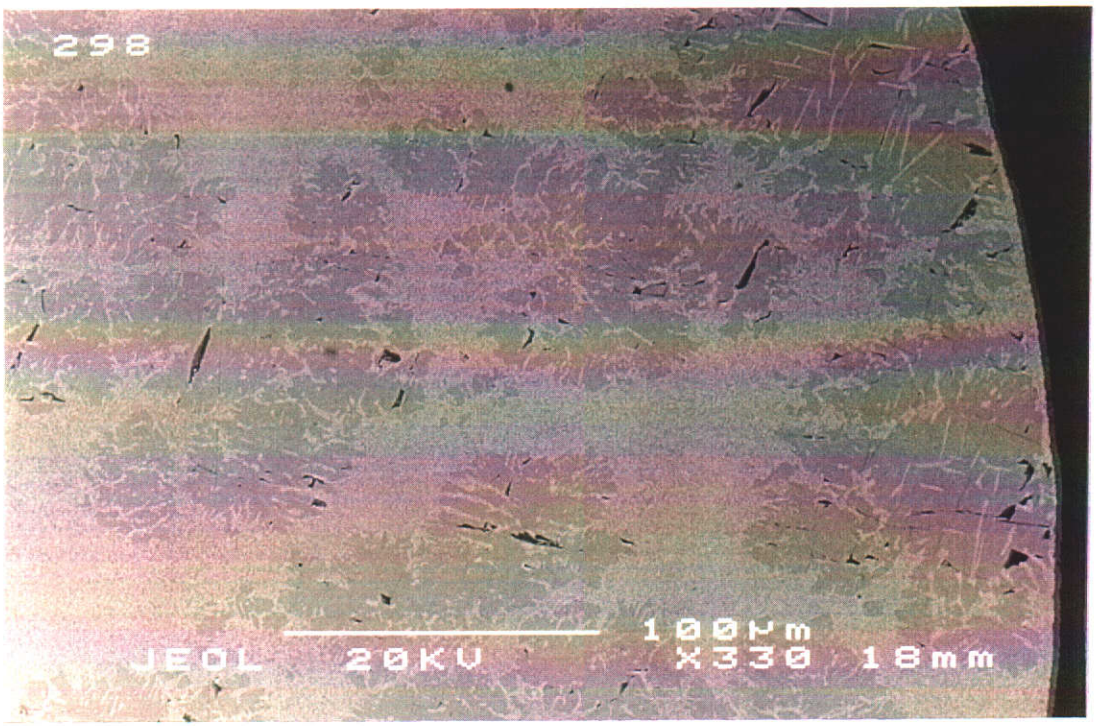

Figure 4.4f BSE micrograph of ideal violarite quenched at 870°C. The molten product has two phases present, pentlandite and mss. The thin crystals of pentlandite have recrystallised along the (0001) plane of the mss.

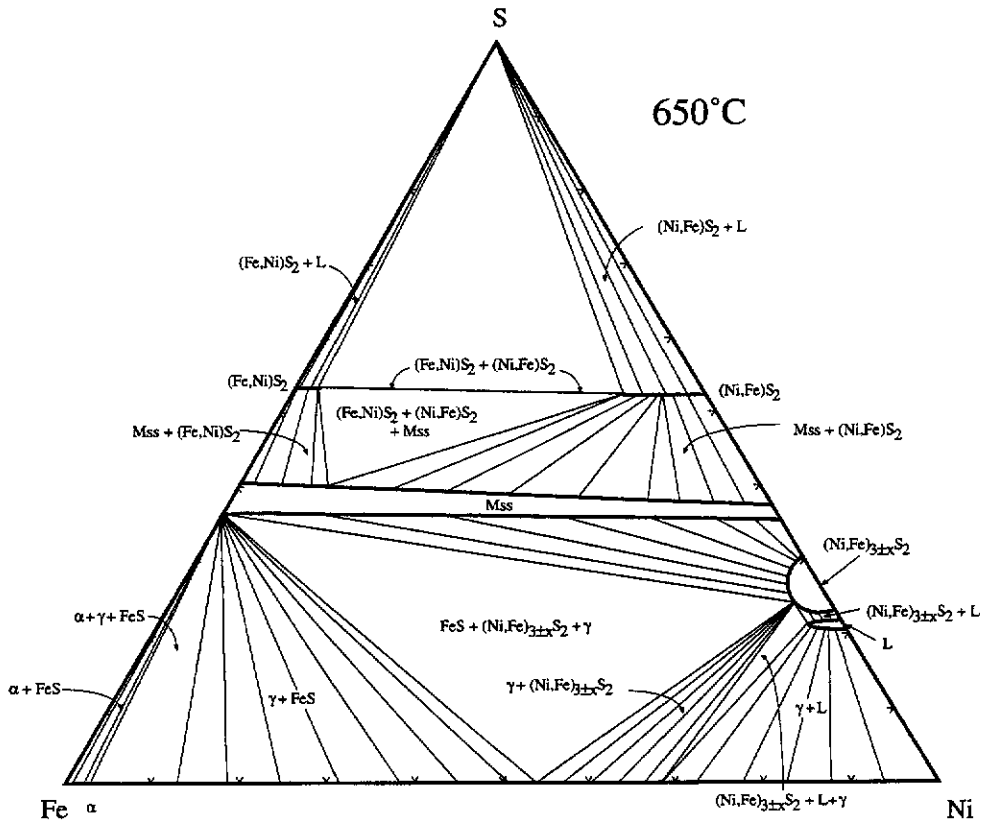

Figure 4.5 Fe-Ni-S phase diagram at 650°C (redrawn from Kullerud 1963). All phases and assemblages coexist with sulfur vapour.

The average composition of the pentlandite phase collected at 890°C was $Fe_{3.11}Ni_{6.00}S_8$. The composition is in agreement with the general formula of pentlandite, $(Fe,Ni)_9S_8$, with the Fe:Ni ratio corresponding to the initial violarite composition. The TG curve showed a continued loss of mass up to 1000°C with no DTA activity. A total loss of 21.45% was observed from ambient temperature to 1000°C. The calculated composition from the observed mass loss falls within the central sulfide phase stability field of the Fe-Ni-S ternary phase diagram at 1000°C.

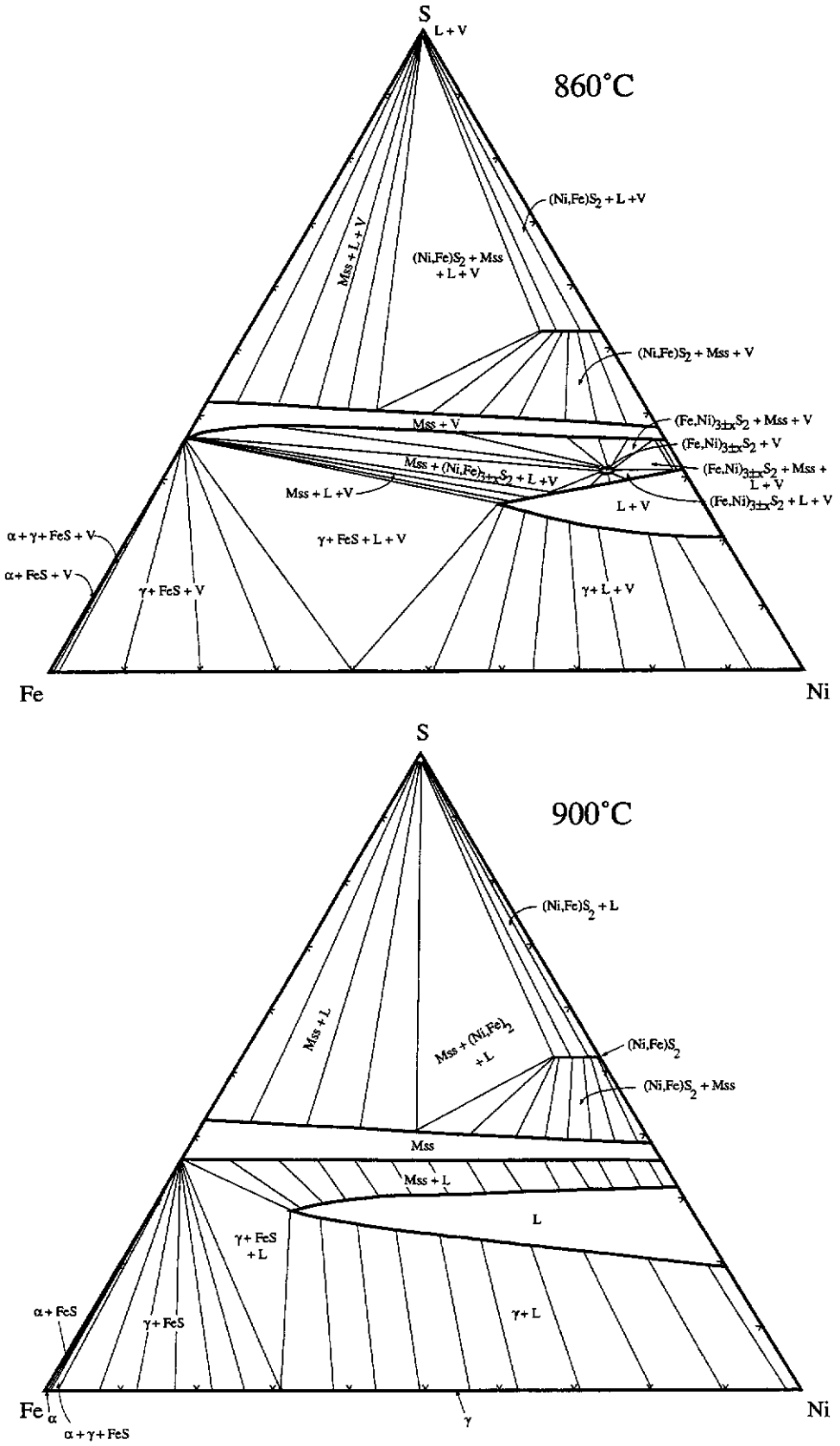

Figure 4.6 Fe-Ni-S phase diagram at 860°C and 900°C (redrawn from Kullerud 1963). All phases and assemblages coexist with sulfur vapour.

4.1.2 Summary

The pyrolytic decomposition of synthetic violarite demonstrated it evolves sulfur at relatively low temperatures. An initial loss of sulfur occurred between 420°C and 525°C associated with the gradual conversion of violarite to mss. Between 495°C and 525°C the violarite stability field no longer remained stable resulting in the phase transition of violarite to mss and vaesite. The vaesite decomposed to mss between the temperature range of 525-615°C resulting in a rapid loss of sulfur. The evolution of sulfur and reduction in volume due to the formation of mss produced a porous particle structure. Sulfur continued to be evolved between 615°C and 845°C as metal:sulfur ratio of the mss increased resulting in formation of $(Fe,Ni)_{3\pm x}S_2$. A second rapid loss of sulfur occurred between 845°C and 900°C commencing at the incongruent melting point transition of $(Fe,Ni)_{3\pm x}S_2$ to mss and a sulfide liquid phase. The loss of sulfur was associated with the conversion of mss to a sulfide liquid phase. Sulfur continued to be evolved from the sample beyond 1000°C.

4.1.3 Effect of Stoichiometry on the Pyrolytic Decomposition of Synthetic Violarite

Thermal analysis was performed on the entire range of synthetic violarites to determine the effect of stoichiometry on the mechanism of pyrolytic decomposition. The TG-DTA traces for each synthetic violarite are presented in Figure 4.7. The extrapolated onset and offset temperatures for each endothermic event are tabulated in Table 4.1. The reaction mechanism for the decomposition of synthetic violarite was not affected by a change in the iron:nickel ratio. However, there were significant shifts in the onset and offset temperatures for the TG-DTA events as the iron:nickel ratio tended towards the nickel-rich endmember of the violarite series. The intensity and range of the endothermic peaks also showed minor variations with the stoichiometry of the violarite.

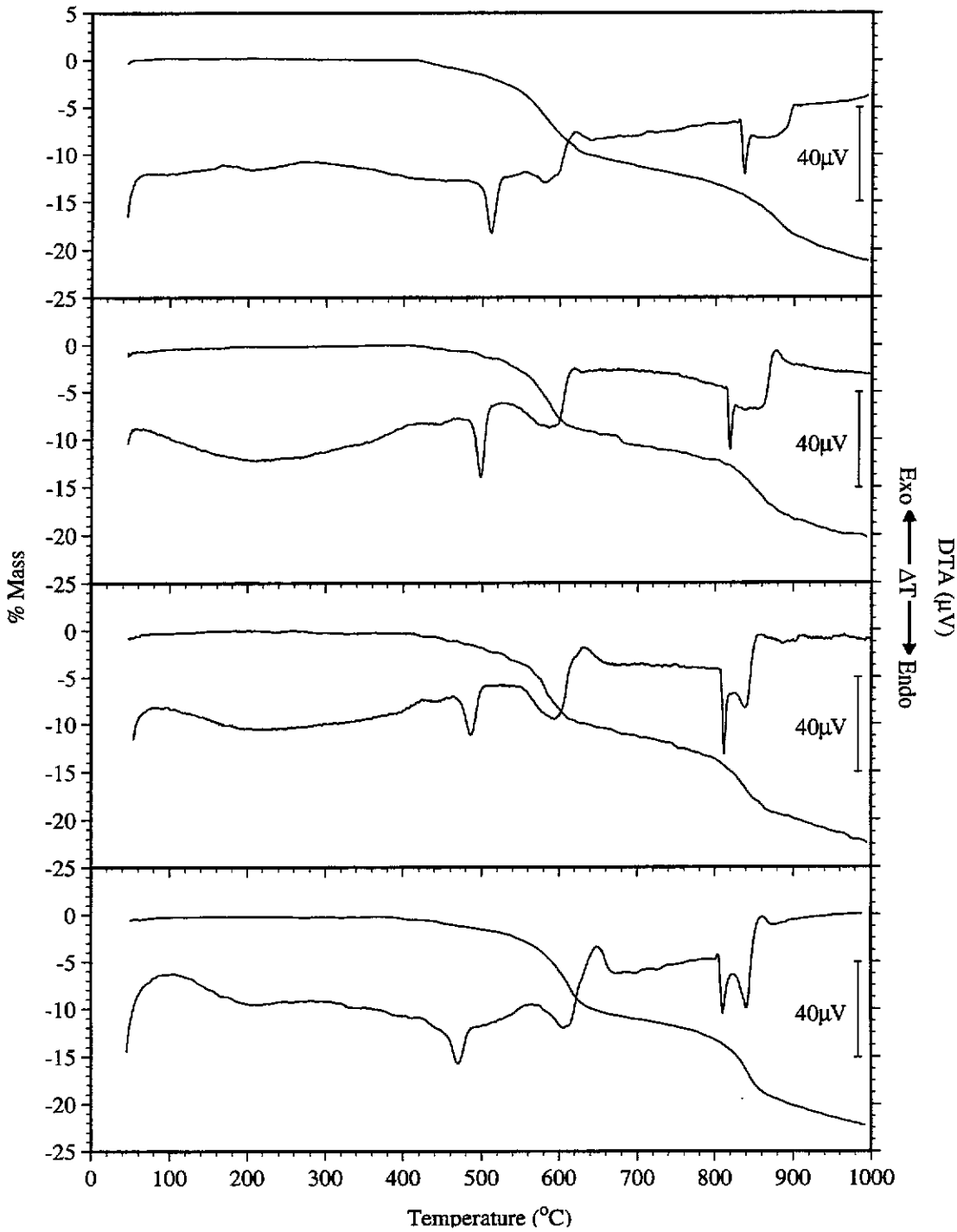

Figure 4.7 Typical TG-DTA traces for the entire range of synthetic violarites, heated at 10°C min^{-1} in a nitrogen atmosphere. Approximately 5 mg of the 63-45 μm particle size fraction was used. Starting from the top $Fe_{0.97}Ni_{1.96}S$ (ideal violarite), $Fe_{0.63}Ni_{2.26}S_4$, $Fe_{0.44}Ni_{2.57}S_4$, and $Fe_{0.20}Ni_{2.72}S_4$ (nickel-rich violarite).

Sulfide	Temperature of Endothermic Events (°C)			
	Phase transition from thiospinel → Mss (defect NiAs structure) + vaesite	Decomposition of vaesite to Mss	Incongruent melting point transition of high temperature $(Fe,Ni)_{3\pm x}S_2$	Evolution of sulfur from central liquid phase
$Fe_{0.97}Ni_{1.96}S_4$ (Ideal violarite)	495-525	560-625	835-845	845-900
$Fe_{0.73}Ni_{2.26}S_4$	485-510	545-615	815-825	825-870
$Fe_{0.46}Ni_{2.49}S_4$	470-500	550-620	810-820	825-850
$Fe_{0.20}Ni_{2.72}S_4$ (Nickel-Rich Violarite)	450-485	575-650	805-825	825-855

Table 4.1 Comparison of the extrapolated onset and offset temperatures for the major endothermic activity for a range of synthetic violarites under pyrolytic decomposition conditions of 10°C min^{-1} in a nitrogen atmosphere using TG-DTA.

The onset temperature for the initial endotherm associated with the incongruent phase transition of violarite to mss and vaesite showed a significant decrease as the iron:nickel ratio decreased. The pyrolytic decomposition temperature of synthetic violarite was characterised earlier in section 4.1.1 by the onset temperature of the phase transition of violarite to mss and vaesite. Figure 4.8 shows the effect of stoichiometry of synthetic violarite on the pyrolytic decomposition temperature, which decreases linearly as the iron:nickel ratio decreases from ideal to nickel-rich violarite. For example, the onset temperature decreased from 495°C (ideal violarite) to 450°C (nickel-rich violarite), representing a 45°C decrease in the pyrolytic decomposition temperature as the iron:nickel ratio decreased from 0.49 (ideal violarite) to 0.07 (nickel-rich violarite). The pyrolytic decomposition temperature of synthetic violarite heated at 10°C min^{-1} in nitrogen can be described by the equation derived from line of least-squares of Temp(°C) = 107.7(Fe:Ni ratio) + 445.9 with a correlation coefficient of 0.99.

A comparison of BSE micrographs taken of ideal and nickel-rich violarite collected prior to the pyrolytic decomposition temperature both exhibited mss present within the violarite host (see Figure 4.9a). A minor amount of vaesite was evident in both sulfide samples with the mss and vaesite being more abundant in the nickel-rich violarite. The particle morphology was identical for the two endmembers of the violarite series. At the offset temperature of the pyrolytic decomposition of synthetic violarite, mss and vaesite were identified as the final products for both violarite samples. The particle morphology was very similar for the two endmembers of the violarite solid solution (Figure 4.9b).

The onset temperature of the broad endothermic peak associated with the decomposition of vaesite remained constant for all four violarite samples. Figure 4.9c shows a comparison of the mss product collected at 600°C (ideal violarite) and 665°C

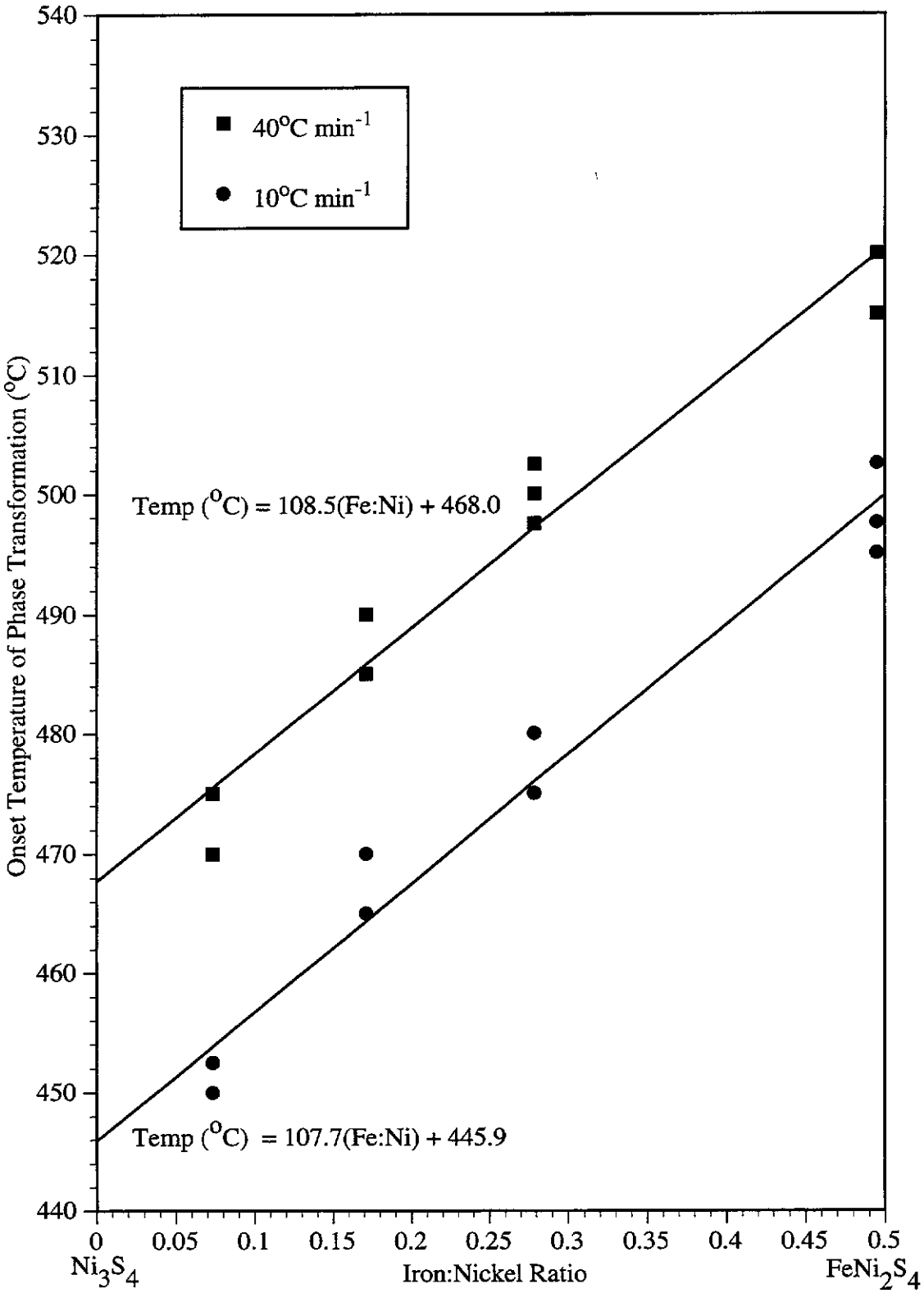

Figure 4.8 The effect of composition on the pyrolytic decomposition of synthetic violarite characterised by the phase transformation of spinel crystal structure → defect NiAs structure and disulfide. Each sulfide was analysed in triplicate (some points may overlap).

(nickel-rich violarite). Both samples had a similar particle morphology with large macropores evident in the mss phase. The average composition of the mss phase for ideal and nickel-rich violarite was $Fe_{0.36}Ni_{0.59}S_{1.00}$ (Fe:Ni=0.61; M:S=0.95) and $Fe_{0.10}Ni_{0.91}S_{1.00}$ (Fe:Ni=0.11; M:S=1.01) respectively. The iron:nickel ratio of the mss product was dependent on the initial composition of the synthetic violarite. The stoichiometry of the mss product correlated well with the theoretical compositions of $Fe_{0.31}Ni_{0.64}S_{1.00}$ (25-615°C) and $Fe_{0.06}Ni_{0.91}S_{1.00}$ (25-635°C), calculated from the observed mass loss assuming the iron:nickel ratios have remained constant.

The incongruent melting point of $(Fe,Ni)_{3\pm x}S_2$ showed a decrease from 830°C to 805°C as the iron:nickel ratio decreased. DTA experiments performed by Kullerud in sealed silica tubes reported a 56°C increase in the melting point from 806°C to 862°C, between $Ni_{3\pm x}S_2$ and an iron-saturated $(Fe,Ni)_{3\pm x}S_2$ phase (Kullerud, 1962, p.362). Comparison of micrographs taken of quenched samples collected prior to the incongruent melting point, at 795°C for both ideal and nickel-rich violarite, showed the partial melting of the mss phase. Small holes were evident in both samples where the macropores had collapsed within the particles (Figure 4.9d).

The incongruent melting point transition was immediately followed by another broader endotherm. The temperature range in which the endothermic peak was observed decreased as the iron:nickel ratio decreased. The mass loss coinciding with the endotherm increased as the iron:nickel ratio decreased, with losses of 4.85% (845-900°C) and 6.10% (815-865°C) observed for the ideal violarite and nickel-rich violarite respectively. Total mass losses of 21.50% and 22.55% respectively were observed for ideal and nickel-rich violarite between 25-1000°C.

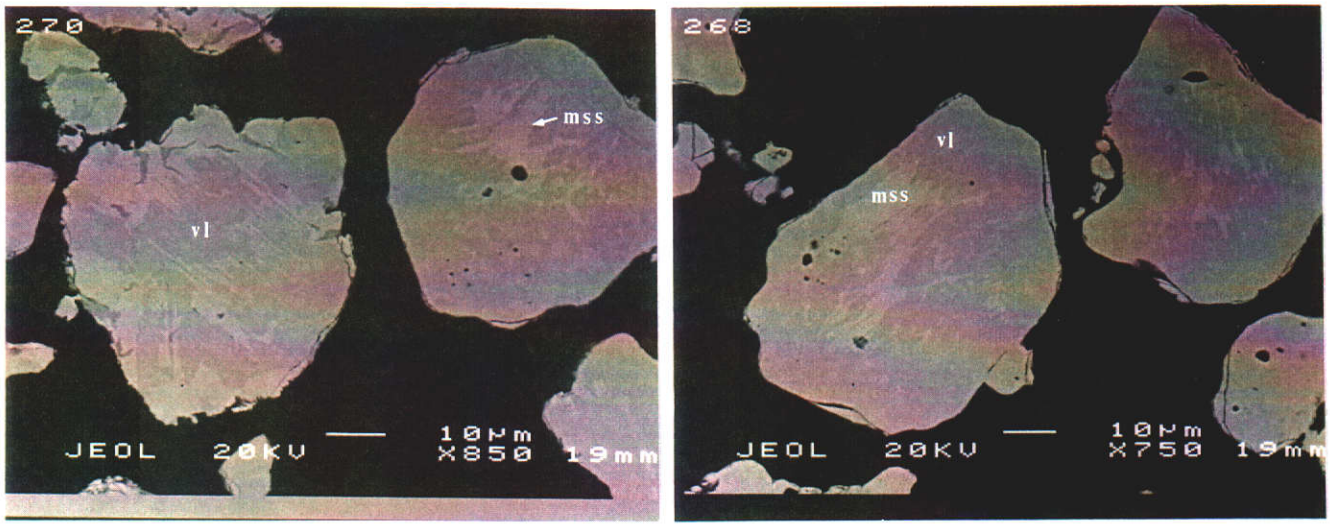

Figure 4.9a Comparison of BSE micrographs taken of ideal (left) and nickel-rich (right) violarite collected at 495°C and 425°C respectively. Violarite was identified as the major phase with mss appearing as the brighter phase in the micrographs. A small amount of vaesite is present in the nickel-rich sample appearing as dark regions in the mss phase.

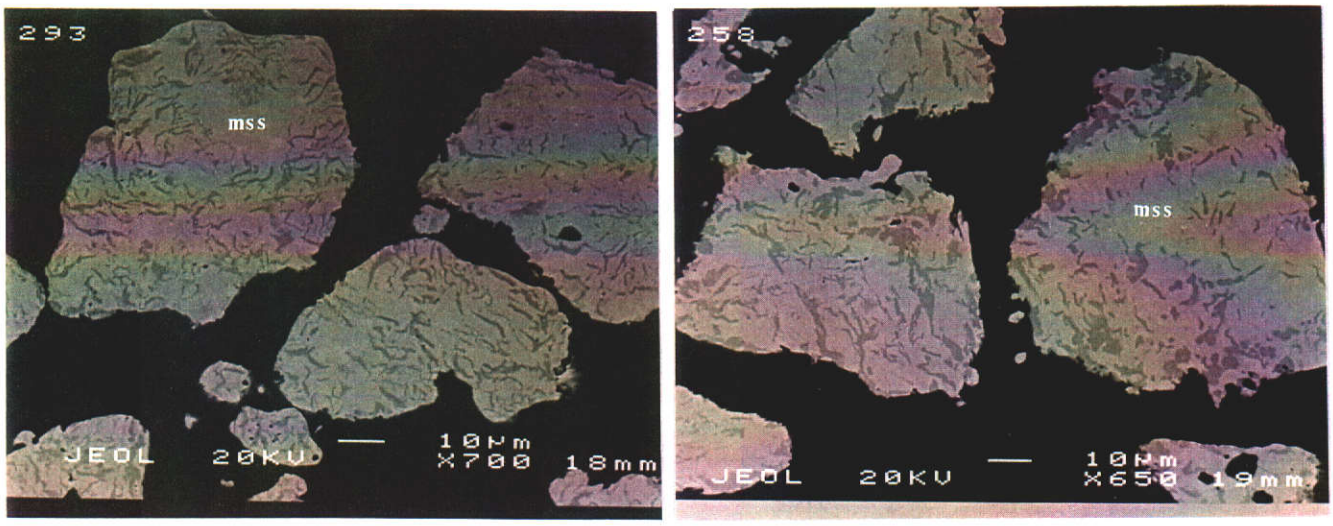

Figure 4.9b BSE micrographs of ideal (left) and nickel-rich (right) violarite quenched at 535°C and 490°C respectively. Both samples show the complete pyrolytic decomposition of violarite to mss and vaesite.

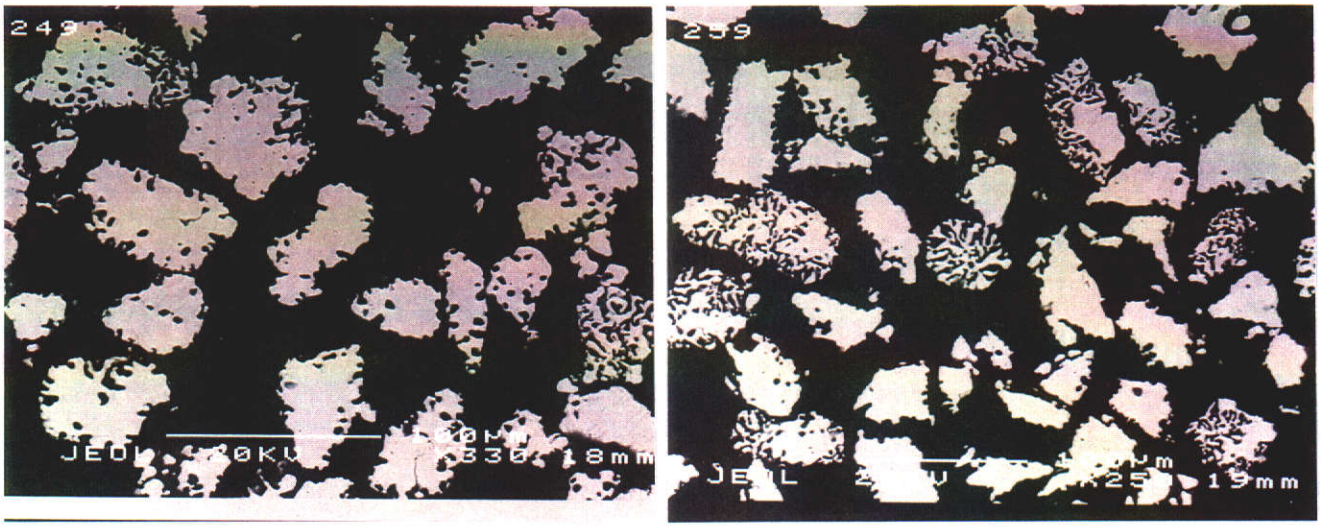

Figure 4.9c BSE micrographs showing a comparison between ideal (left) and nickel-rich (right) violarite collected at 600°C and 665°C respectively. Large macropores are evident in both samples indicating the rapid loss of sulfur from the sulfide particle.

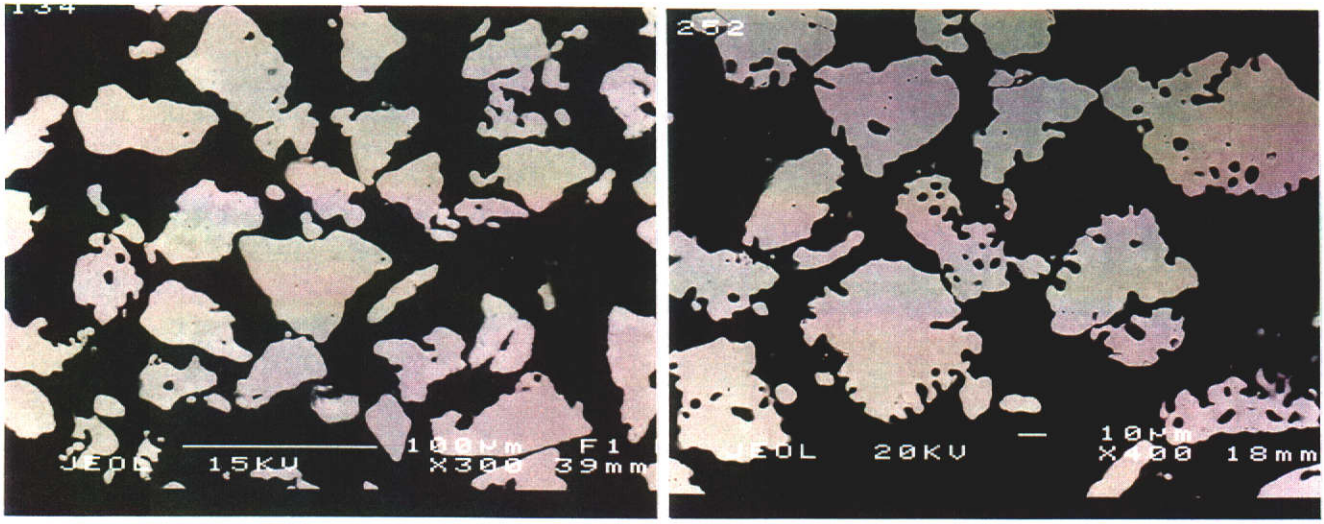

Figure 4.9d BSE micrographs of ideal (left) and nickel-rich (right) violarite quenched at 795°C. Both samples show partial melting has occurred with the disappearance of the macropores.

4.1.4 Effect of Heating Rate on the Pyrolytic Decomposition

The TG-DTA profiles for the 63-45 μm particle size fraction for each synthetic violarite heated at 40°C min^{-1} in a nitrogen atmosphere are presented in Figure 4.10. The extrapolated onset and offset temperatures for each endothermic event are tabulated in Table 4.2. The pyrolytic decomposition proceeded via the same reaction mechanism as previously described under heating conditions of 10°C min^{-1} in a nitrogen atmosphere.

A fourfold increase in the heating rate resulted in a shift in the observed onset temperature of the TG-DTA events by 15-50°C. This effect was mainly due to the finite heat capacity of the sample resulting in a temperature lag between the sample temperature and the temperature recorded by the thermocouple (Wendlandt, 1986, p.41). The temperature lag will increase with heating rate, and the onset temperatures of the TG-DTA events will apparently be higher. The effect of stoichiometry on the onset temperature for the pyrolytic decomposition of synthetic violarite heated at 40°C min^{-1} is shown in Figure 4.8.

The intensity of the endothermic peaks also increased as the heating rate was increased. This was mainly due to an instrumental effect where the response of the instrument increases as the heating rate increased (Wendlandt, 1986, pp.228-232). The incongruent phase transition of violarite to mss and vaesite was followed by the thermal decomposition of vaesite to mss. The rate of mass loss associated with the thermal decomposition of vaesite was similar to that previously observed under slower heating conditions. Hence, the rate of sulfur evolution from the violarite sample was relatively unaffected by a fourfold increase in the heating rate.

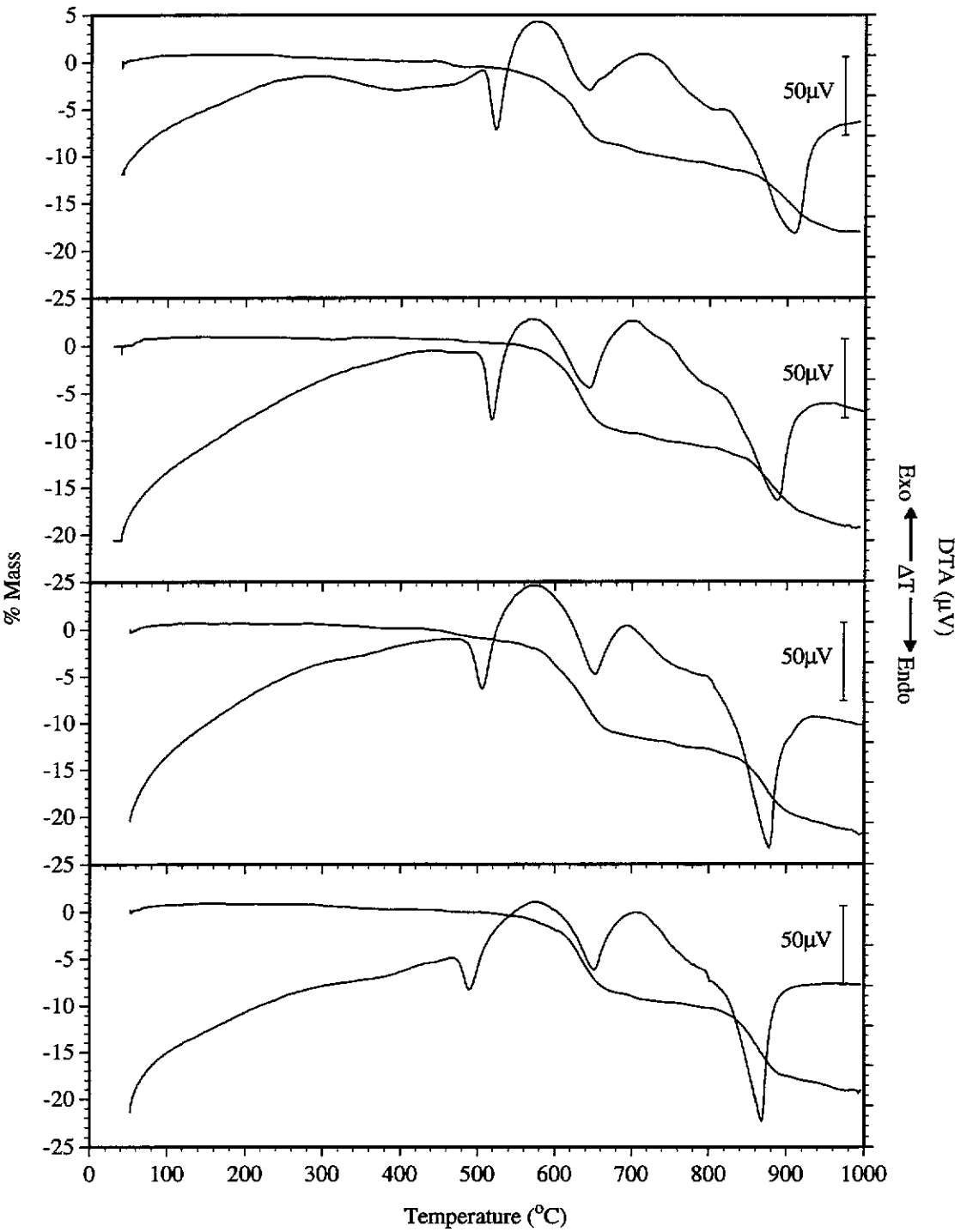

Figure 4.10 Typical TG-DTA profiles for each synthetic violarite, heated at 40°C min^{-1} in a nitrogen atmosphere. Approximately 5 mg of the 63-45 µm particle size fraction was used. Starting from the top $Fe_{0.97}Ni_{1.96}S$ (ideal violarite), $Fe_{0.63}Ni_{2.26}S_4$, $Fe_{0.44}Ni_{2.57}S_4$, and $Fe_{0.20}Ni_{2.72}S_4$ (nickel-rich violarite).

Sulfide	Temperature of Endothermic Events (°C)			
	Phase transition from thiospinel → Mss (defect NiAs structure) + vaesite	Decomposition of vaesite to Mss	Continual loss of sulfur from Mss	Evolution of sulfur from central liquid phase
$Fe_{0.97}Ni_{1.96}S_4$ (Ideal violarite)	510-545	595-700	730-820	820-930
$Fe_{0.73}Ni_{2.26}S_4$	505-540	585-680	715-805	825-910
$Fe_{0.46}Ni_{2.49}S_4$	485-535	600-680	695-800	820-890
$Fe_{0.20}Ni_{2.72}S_4$ (Nickel-Rich Violarite)	475-525	605-680	715-800	820-880

Table 4.2 Comparison of the extrapolated onset and offset temperatures for the major endothermic activity for a range of synthetic violarites under pyrolytic decomposition conditions of 40°C min^{-1} in a nitrogen atmosphere using TG-DTA.

A gradual mass loss was observed by all four violarite samples over a temperature range of 650-850°C due to the gradual loss of sulfur from mss. This was followed by the second major mass loss commencing at the incongruent melting point transition of $(Fe,Ni)_{3\pm x}S_2$. The sharp endotherm associated with the incongruent melting point transition was not evident in the DTA curve since it coincided with onset temperature of the decomposition of mss to the central sulfide liquid phase.

Therefore, the TG-DTA results showed that there was only a minor increase in the rate of sulfur evolution from the series of violarite samples by increasing the heating rate from 10°C min^{-1} to 40°C min^{-1}.

4.2 Oxidation of Synthetic Violarite

There has been a limited amount of work published on the oxidation of violarite. Previous studies on the oxidation of violarite have used natural samples (Mackey, 1991; Dunn and Mackey, 1993). Natural violarite is normally associated with other secondary minerals such as pyrite and marcasite due to supergene alteration of the primary ore body. It is very difficult to separate and obtain clean uncontaminated samples of these supergene minerals. Therefore, artefacts observed during the oxidation of natural violarite may be attributed to these other minerals rather than the violarite. The use of synthetic samples enables very pure samples to be obtained and the oxidation mechanism of the mineral can be accurately ascertained.

The oxidation mechanism of synthetic violarite was examined under a heating rate of 10°C min^{-1} in an air atmosphere. Samples were quenched at preselected temperatures in the TG-DTA profile and examined using the usual range of instrumental techniques including XRD, FTIR, EPMA and SEM. The thermal analytical results for the ideal violarite sample will be discussed in detail and the effect of the iron:nickel ratio on the reaction mechanism will be established.

4.2.1 Oxidation of Ideal Violarite

The oxidation of synthetic violarite proceeded in several stages. A typical TG-DTA trace and FTIR Gramm Schmidt chromatogram for $Fe_{0.97}Ni_{1.96}S_4$ (ideal violarite) heated at 10°C min^{-1} in an air atmosphere is shown in Figure 4.11. Sulfur dioxide gas accounted for all the peaks observed in the Gramm Schmidt chromatogram.

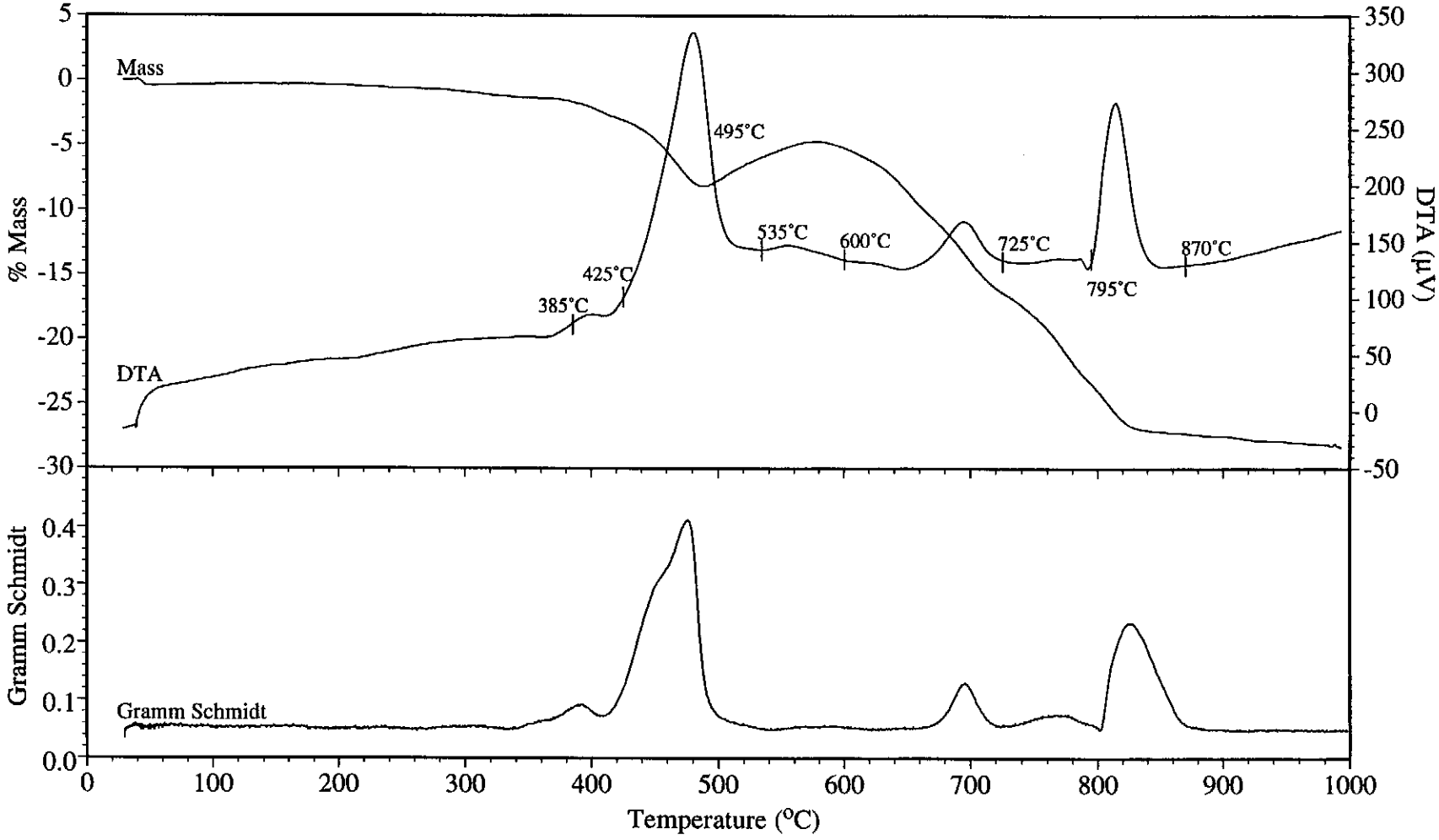

Figure 4.11 Typical TG-DTA profile for ideal violarite ($Fe_{0.97}Ni_{1.96}S_4$), 5.07 mg of sample heated at 10°C min^{-1} in an air atmosphere for the 45-63 µm particle size fraction. Oxidation products were collected at the indicated temperatures on the DTA profile. The Gramm Schmidt chromatogram is shown below.

A small degree of exothermic activity was first evident in the TG-DTA trace with an exothermic drift in the DTA baseline commencing at 210°C. This was accompanied by a 1.20% mass loss between the temperature range of 210-385°C. As the temperature increased, the rate of mass loss increased with a loss of 1.80% observed between 385-420°C. A small exothermic peak coincided with the mass loss with onset and offset temperatures of 370°C and 420°C respectively. The evolved gas chromatogram showed a small amount of SO_2 gas evolved from the violarite sample over the temperature range corresponding with the mass loss.

Analysis of the oxidation product quenched at 385°C by XRD indicated violarite as the major phase with a minor trace of mss detected in the diffraction pattern (Figure 4.14). Examination of the oxidation product by SEM showed some minor evidence of oxidation occurring at the solid-gas interface of the sulfide particles, with the majority of the particles showing no evidence of oxidation (Figure 4.15a). The mss phase was more evident in the BSE micrograph appearing as bright blebs in the violarite particles. EPMA results showed the average composition of the mss was $Fe_{0.34}Ni_{0.52}S_{1.00}$. The violarite also exhibited a small loss of sulfur with an average composition of $Fe_{1.06}Ni_{1.94}S_{3.84}$. The violarite composition was consistent with the theoretical composition of $Fe_{0.99}Ni_{2.01}S_{3.87}$, calculated from the observed mass loss from ambient temperature to 385°C, assuming the iron:nickel ratio remained constant.

By 425°C there was evidence of oxidation in the violarite particles (see Figure 4.15b). However, there were still some violarite particles present with no evidence of oxidation. The composition of the mss within the centres of the violarite particles was consistent with the composition determined at 385°C with an average composition of $Fe_{0.34}Ni_{0.51}S_{1.00}$. There was a slight increase in the iron:nickel and metal:sulfur ratios of the violarite phase, with a composition of $Fe_{1.16}Ni_{1.84}S_{3.81}$.

The BSE micrograph showed a dark oxidation product, approximately 2-5 μm wide, around sections of the outer rim (Figure 4.15b). The oxidation seemed to commence along a preferred axis of the violarite lattice. Analysis of the oxidation product by EPMA was difficult due to its porosity resulting in low weight percent totals. However, the results suggested that $FeSO_4$ was the main oxidation product, with a minor trace of $NiSO_4$ and Fe_2O_3 evident. The XRD pattern showed no evidence of sulfate. Dunn, De and O'Connor (1989a) had previously reported the low crystallinity of sulfates formed during the oxidation of pyrite. Due to their amorphous structure, both $FeSO_4$ and $Fe_2(SO_4)_3$ may be undetected by XRD when present in amounts in excess of 20% in oxidised pyrite samples.

Infrared spectroscopy has been recognised as a useful instrumental technique for the identification of amorphous phases, such as sulfates, in the oxidation products of sulfides (Banerjee, 1976; Dunn, Gong and Shi, 1992; Dunn and Howes, 1994). Figure 4.12 shows a series of reference infrared spectra of various sulfates and oxides which have been identified in the oxidation products. The infrared spectrum for each oxidation product quenched during the TG-DTA trace is shown in Figure 4.13. The presence of SO_4^{2-} was confirmed by FTIR spectroscopy with the spectrum showing vibrational peaks at 1109, 982, and 618 cm^{-1}. The infrared peaks observed at 1109 and 618 cm^{-1} can be assigned to free SO_4^{2-} ion. Tetrahedral SO_4^{2-} exhibits four modes of vibration when its full (T_d) symmetry is retained. Only two of these modes are infrared active with the stretch and bending modes, υ_3 and υ_4, observed at 1105 and 611 cm^{-1} respectively. When SO_4^{2-} bonds to a metal cation such as Fe^{2+} or Ni^{2+} the full (T_d) symmetry of the sulfate ion is no longer maintained. Both $FeSO_4$ and $NiSO_4$ have an assigned site symmetry of $C_{2\upsilon}$ (Farmer, 1974). Reference spectra of $FeSO_4$ and $NiSO_4$ species are shown in Figure 4.12. Both sulfates show all four vibration modes, υ_1 (symmetric stretching), υ_2 (symmetric bending), υ_3 (asymmetric stretching), and υ_4 (asymmetric bending). The υ_3 and υ_4 vibrational modes split

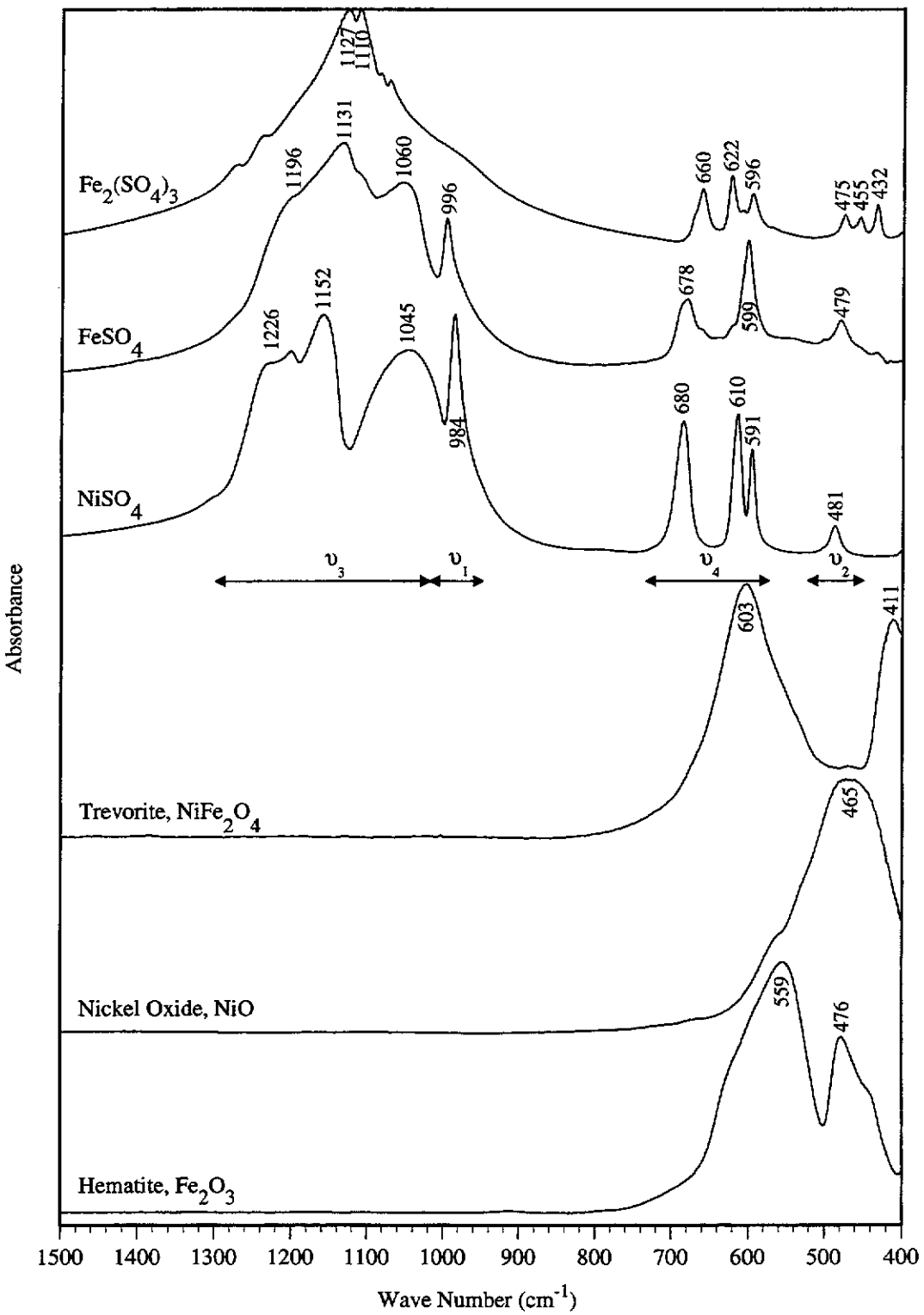

Figure 4.12 Reference infrared spectra of typical anhydrous oxidation products identified during oxidation of synthetic violarite.

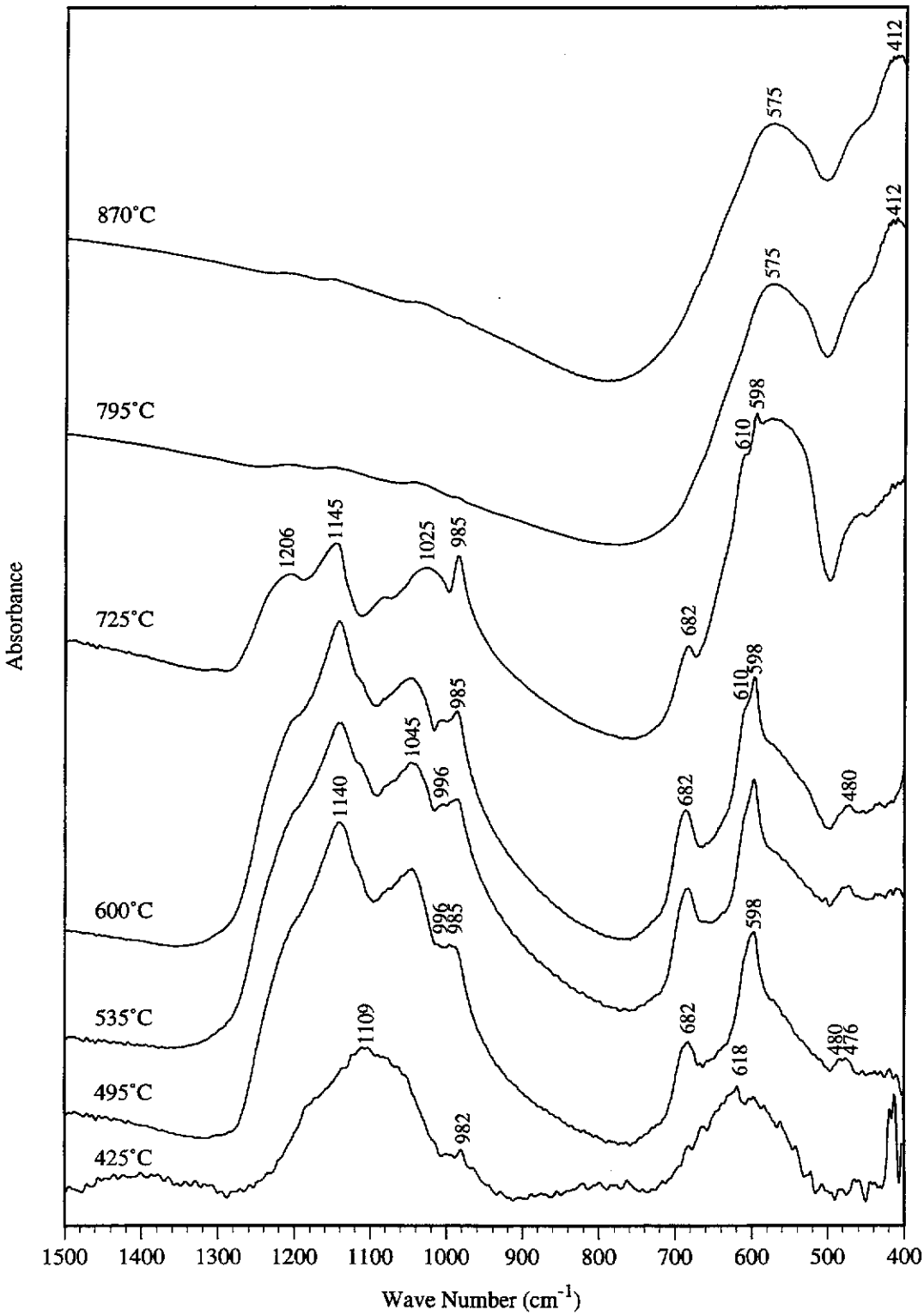

Figure 4.13 FTIR spectra of oxidation products quenched at preselected temperatures in the TG-DTA trace for ideal violarite, heated at 10°C min^{-1} in an air atmosphere.

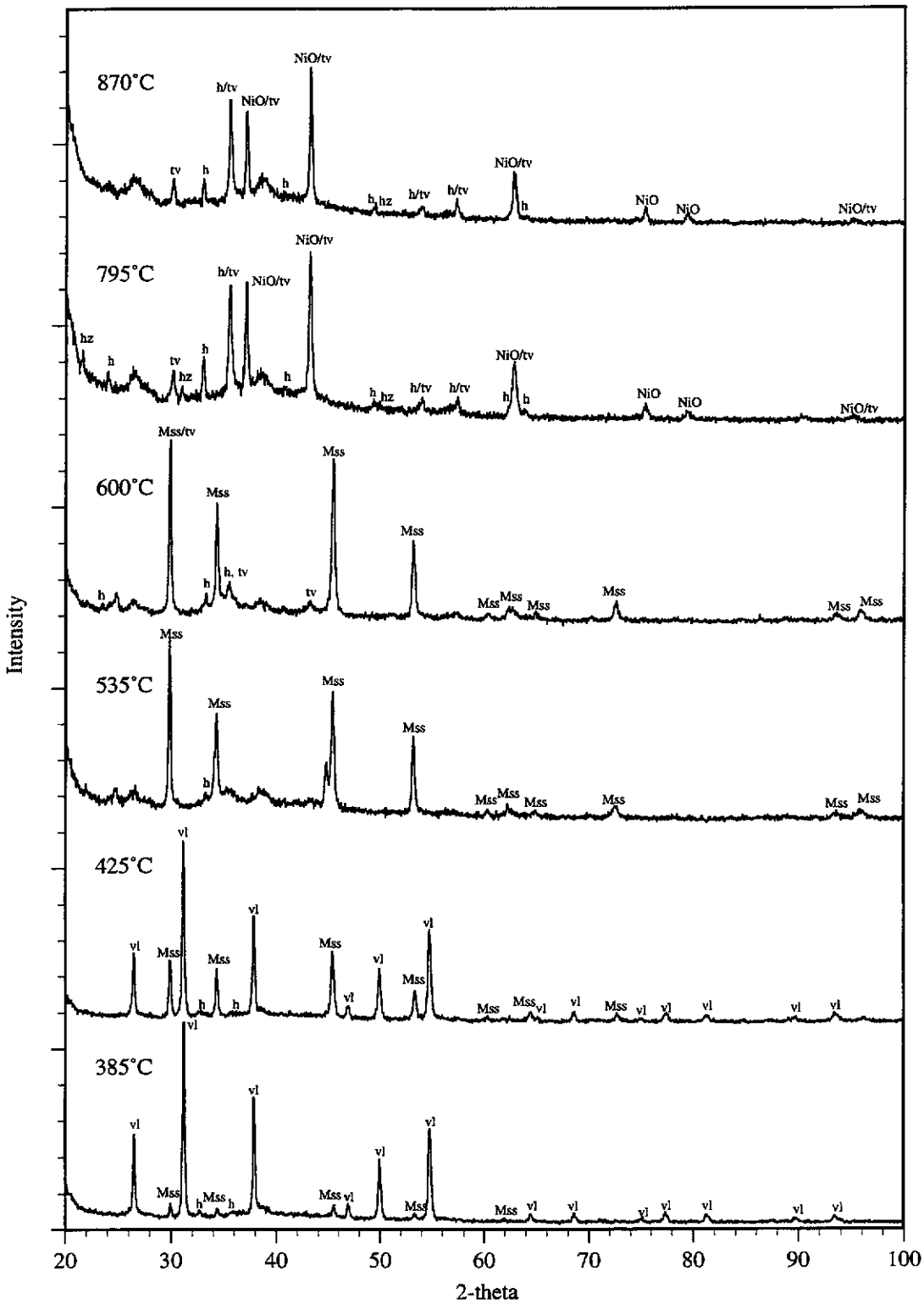

Figure 4.14 XRD patterns of oxidation products quenched at preselected temperatures in the TG-DTA trace for ideal violarite, heated at 10°C min^{-1} in air. (vl - violarite, mss - monosulfide solid solution, h - hematite, tv - trevorite, NiO - nickel oxide, hz - heazlewoodite)

forming three vibration peaks for $NiSO_4$, while for $FeSO_4$ the υ_3 mode splits to form three vibrational peaks and the υ_4 vibrational mode two peaks (Nakamoto, 1987; Farmer, 1974). Therefore, the FTIR spectrum at 425°C indicated that a minor trace of SO_4^{2-} was present in the oxidation product. This was weakly associated with a metal cation as indicated by the peak observed at 982 cm^{-1}. The metal sulfate species was probably $FeSO_4$, but this could not be confirmed as there were insufficient spectral peaks present.

Between 385°C and 425°C there was a significant increase in the amount of mss in the oxidation product, according to the relative peak intensities in the XRD pattern (425°C) of violarite and mss. This was evident in the BSE micrograph (Figure 4.15b), with the formation of mss adjacent to the oxidation product located around the edge of the particle. Approximately 10 particles were analysed by EPMA. The composition of the mss phase adjacent to the mss-sulfate interface varied significantly with the iron:nickel ratio decreasing and metal:sulfur ratio increasing as the electron probe traversed across the violarite-mss interface to the mss-sulfate interface. The average composition of the mss phase was $Fe_{0.26}Ni_{0.70}S_{1.00}$. Therefore, iron and sulfur had preferentially migrated to the mss-sulfate interface where they were oxidised resulting in nickel enrichment in the unreacted mss phase. There was some minor evidence of Fe_2O_3 present in the XRD pattern.

The phenomenon of preferential migration and oxidation of iron was initially reported by Thornhill and Pidgeon (1957) during roasting experiments performed on chalcopyrite, $CuFeS_2$, and pentlandite, $(Fe,Ni)_9S_8$. The oxidation of chalcopyrite proceeded by the preferential oxidation of iron and sulfur at the particle interface with the formation of digenite, $Cu_{1.8}S$. The formation of digenite permitted the rapid diffusion of iron from the chalcopyrite core to the sulfide-oxide interface with the copper diffusing inwards towards the core. The reaction continued until all chalcopyrite had completely converted to digenite leaving a multilayered oxide product

around the remaining copper sulfide core. Similarly for pentlandite, the iron was preferentially oxidised leaving a nickel sulfide core.

Tsukada *et al.* (1981) and Asaki *et al.* (1984) studied the isothermal oxidation mechanism of a synthetic copper-iron sulfide composed of a mixture of bornite, Cu_5FeS_4, and troilite, FeS. During the initial stage, preferential oxidation of iron occurred by diffusion of iron from the inner sulfide core to the sulfide-oxide interface where it was oxidised to form a dense magnetite layer. This initial formation of magnetite coincided with a mass gain and no evidence of SO_2 evolution. As the magnetite was further oxidised, a porous layer of hematite formed over the inner magnetite layer. As the temperature was increased, the rate-controlling mechanism of the initial oxidation changed from iron diffusion (<850°C) to mass transfer of oxygen through the magnetite boundary layer (>850°C) (Asaki *et al.*, 1983, p.111; Asaki *et al.*, 1984, p.491). This was due to the increased mobility of iron in the sulfide lattice as the temperature increased. $FeSO_4$ was not formed as the experimental temperature exceeded the decomposition temperature of $FeSO_4$.

In the oxidation of ideal violarite, as the temperature increased the rate of reaction increased with a sharp mass loss of 5.35% observed between 420-485°C. This was accompanied by a major exotherm in the DTA trace in the temperature range 420-505°C. The exothermic peak coincided with a large SO_2 gas emission which was observed in the evolved gas chromatogram (Figure 4.11). XRD analysis of samples collected at 495°C showed mss as the major phase with a minor trace of hematite. There was no evidence of violarite in the XRD pattern. The BSE micrograph showed a homogeneous mss core surrounded by a dark porous sulfate-oxide product, ranging from 2-10 μm in thickness (see Figure 4.15c). EPMA traverses were performed across the mss core. Table 4.3 shows the average composition of the core, middle and edge of the mss particles quenched at 495, 535 and 600°C.

Section Across the Mss Core	Temperature (°C)		
	495°C	535°C	600°C
Centre	$Fe_{0.35}Ni_{0.62}S_{1.00}$	$Fe_{0.25}Ni_{0.76}S_{1.00}$	$Fe_{0.17}Ni_{0.85}S_{1.00}$
Middle	$Fe_{0.27}Ni_{0.71}S_{1.00}$	$Fe_{0.21}Ni_{0.80}S_{1.00}$	$Fe_{0.16}Ni_{0.86}S_{1.00}$
Edge	$Fe_{0.19}Ni_{0.81}S_{1.00}$	$Fe_{0.18}Ni_{0.83}S_{1.00}$	$Fe_{0.10}Ni_{0.93}S_{1.00}$

Table 4.3 The average composition of the mss core quenched at various temperatures in the TG-DTA trace, analysed by EPMA.

The results indicated that as the iron is preferentially oxidised the iron concentration across the mss core decreases. This can be attributed to the limited rate of iron diffusion from the centre of the mss core to the oxidation interface. This is clearly shown in Table 4.3, where the iron:nickel ratio of the mss phase decreases from 0.56 to 0.23 between the centre and the edge of the unreacted mss sulfide core at 495°C. The metal:sulfur ratio also showed an increased from 0.97 to 1.00 from the centre to the edge of the unreacted mss core.

Analysis of the oxidation product collected at 495°C by FTIR spectroscopy showed $FeSO_4$ as the major phase. A minor trace of $Fe_2(SO_4)_3$ was also detected in the infrared spectrum with peaks observed at 432, 455, 472, 599, 620, and 660 cm^{-1}. There was only one characteristic peak assigned to $NiSO_4$ at 685 cm^{-1}. A minor trace of hematite was also evident in the FTIR spectrum with a shoulder observed on the $FeSO_4$ peak at 560 cm^{-1} and a peak at 472 cm^{-1}. Hematite normally shows two spectral peaks located at 559 and 476 cm^{-1} (see Figure 4.12).

Therefore, the major exotherm and the accompanying mass loss over the temperature range 385-485°C can be attributed to the pyrolytic decomposition of violarite to mss with sulfur gas evolved at the mss-sulfate interface. The gaseous reaction between the evolved sulfur and oxygen is highly exothermic and would account for the large

exotherm. The large emission of SO_2 gas observed in the evolved gas chromatogram confirms the gaseous reaction. The sulfate product was relatively porous and the diffusion of sulfur through the sulfate product layer to the solid-gas interface did not seem to restrict the gaseous oxidation of the evolved sulfur.

$$(2\text{-}2x)\ (Fe,Ni)_3S_4 \rightarrow 6\ (Fe,Ni)_{1-x}S + (1\text{-}4x)\ S_{2\,(g)}$$

$$(1\text{-}4x)\ S_{2\,(g)} + (2\text{-}8x)\ O_{2\,(g)} \rightarrow (2\text{-}8x)\ SO_{2\,(g)}$$

The formation of mss phase seemed to be critical for the diffusion of iron and sulfur to the mss-sulfate interface. Mss forms an extensive solid solution with a wide range of iron:nickel and metal:sulfur ratios between $Ni_{1-x}S$ and $Fe_{1-x}S$. The deficiency of iron and nickel in the mss phase, i.e. $(Fe,Ni)_{1-x}S$, is attributed to vacancies in the iron and nickel sites rather than the presence of excess sulfur atoms (Vaughan and Craig, 1978, p.46). The vacant sites may enable the migration of cations through the mss lattice.

The rapid oxidation of the sulfur evolved from the pyrolytic decomposition of violarite to mss would cause the temperature at the solid-gas interface to escalate resulting in an increase in the mobility of the iron and nickel. The preferential sulfation of the iron in the mss phase at the interface can be described by the following reaction:

$$2(Fe_{1-x}Ni_{1-y})S + (16\text{-}8x\text{-}8y)O_{2\,(g)} \rightarrow (2\text{-}2x)FeSO_4 + (2\text{-}2y)NiSO_4 + (1\text{-}x\text{-}y)S_{2\,(g)}$$

$$(1\text{-}x\text{-}y)\ S_{2\,(g)} + (2\text{-}2x\text{-}2y)\ O_{2\,(g)} \rightarrow (2\text{-}2x\text{-}2y)\ SO_{2\,(g)}$$

After the initial sharp mass loss, a gain of 3.50% was observed for the ideal violarite sample over the temperature range 490-575°C as the iron in the mss continues to form $FeSO_4$. This was accompanied by a small exothermic peak observed between 540-600°C. A minor amount of SO_2 gas was evolved over the temperature range coinciding with the exothermic peak.

FTIR spectroscopy performed on the oxidation product collected at 535°C, prior to the onset temperature of the exotherm for the violarite sample, detected $FeSO_4$ as the major phase with a trace amount of $NiSO_4$ indicated by peaks at 984, 680, 610, and 481 cm^{-1}. The particle morphology was similar to the micrograph shown in Figure 4.15c, with a slight increase in the thickness of the sulfate rim (Figure 4.15d).

The XRD pattern showed mss as the major phase, with traces of hematite and trevorite, $Fe_{3-x}Ni_xO_4$. Trevorite has a spinel crystal structure, with a general formula of AB_2O_4, identical to that of magnetite, $Fe^{2+}Fe^{3+}{}_2O_4$. The Fe^{2+} occupying the divalent tetrahedral A site in magnetite may be substituted for Ni^{2+} forming trevorite. Trevorite has an ideal stoichiometry of $NiFe_2O_4$, however, the stoichiometry can range from Fe_3O_4 to $NiFe_2O_4$. All iron-nickel spinels which fall within this range will be referred to as "trevorite" except for the endmember magnetite. The presence of trevorite in the sample collected at 535°C indicated that direct oxidation of the mss phase had occurred.

EPMA of the oxidation product collected at 535°C showed the continuation of nickel enrichment of the unreacted sulfide core, with the iron:nickel ratio decreasing from 0.32 to 0.21 from the centre to the edge of the mss core. The metal:sulfur ratio was constant across the entire mss core with a calculated ratio of 1.01.

The TG curved showed the mass loss occurred in several stages beyond 575°C. Between 575-635°C a mass loss of 2.25% was observed with a slight endothermic drift in the DTA baseline. The BSE micrograph of the oxidation product collected at 600°C showed virtually no change in particle morphology from that collected at 535°C (Figure 4.15e). There was some evidence of the core shrinking at its interface between the sulfate rim and mss. XRD results indicated an increase in the amount of hematite and trevorite compared with the sample collected at 535°C. A minor amount

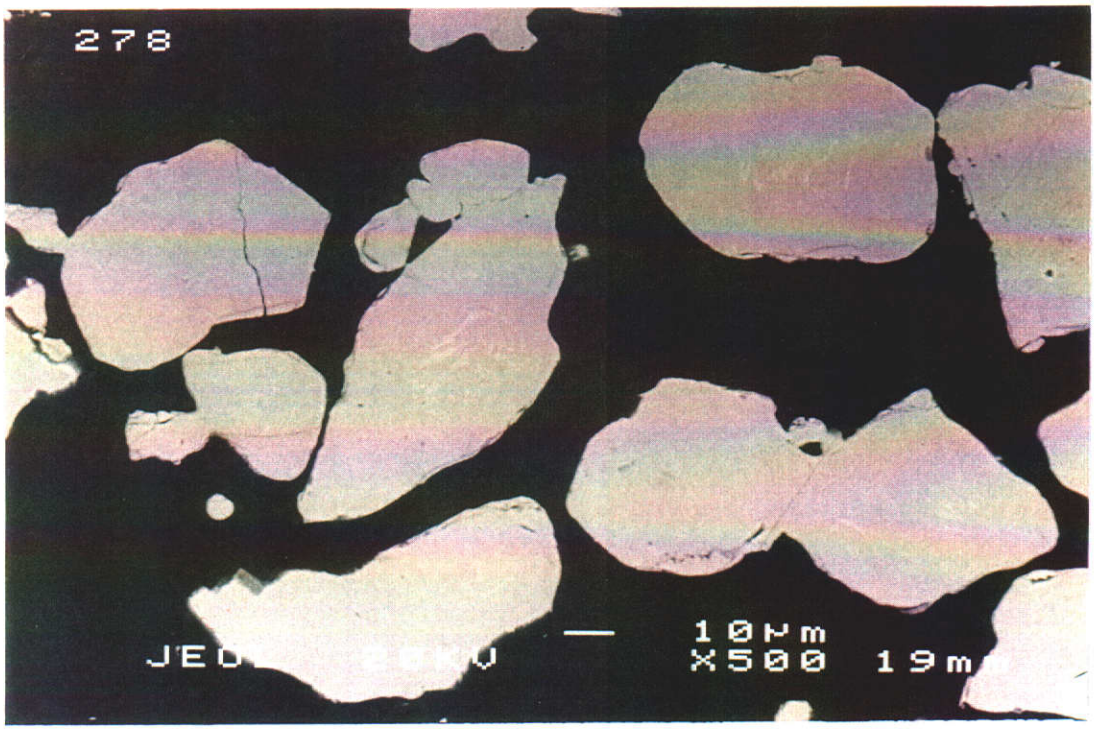

Figure 4.15a BSE micrograph of ideal violarite heated at 10°C min^{-1} in air and quenched at 385°C. Small blebs of mss are present in the violarite core. There is no significant evidence of oxidation of the violarite sample.

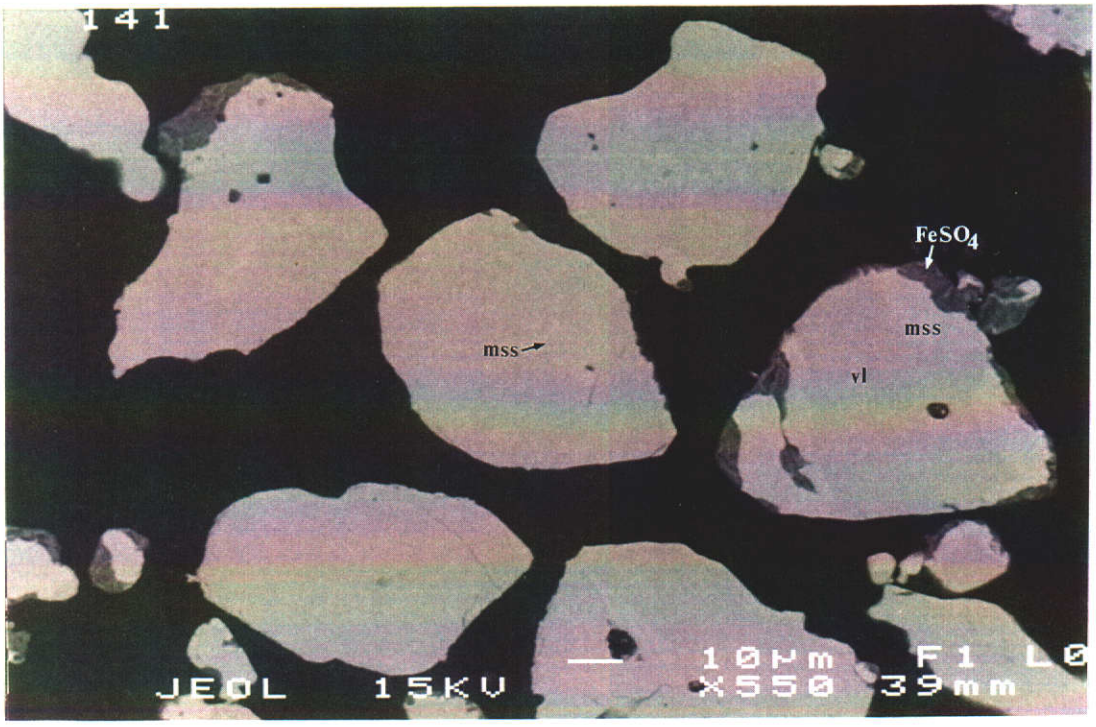

Figure 4.15b Oxidation product of ideal violarite quenched at 425°C. Mss (light grey phase) and $FeSO_4$ (dark grey phase) are both evident in the violarite particles.

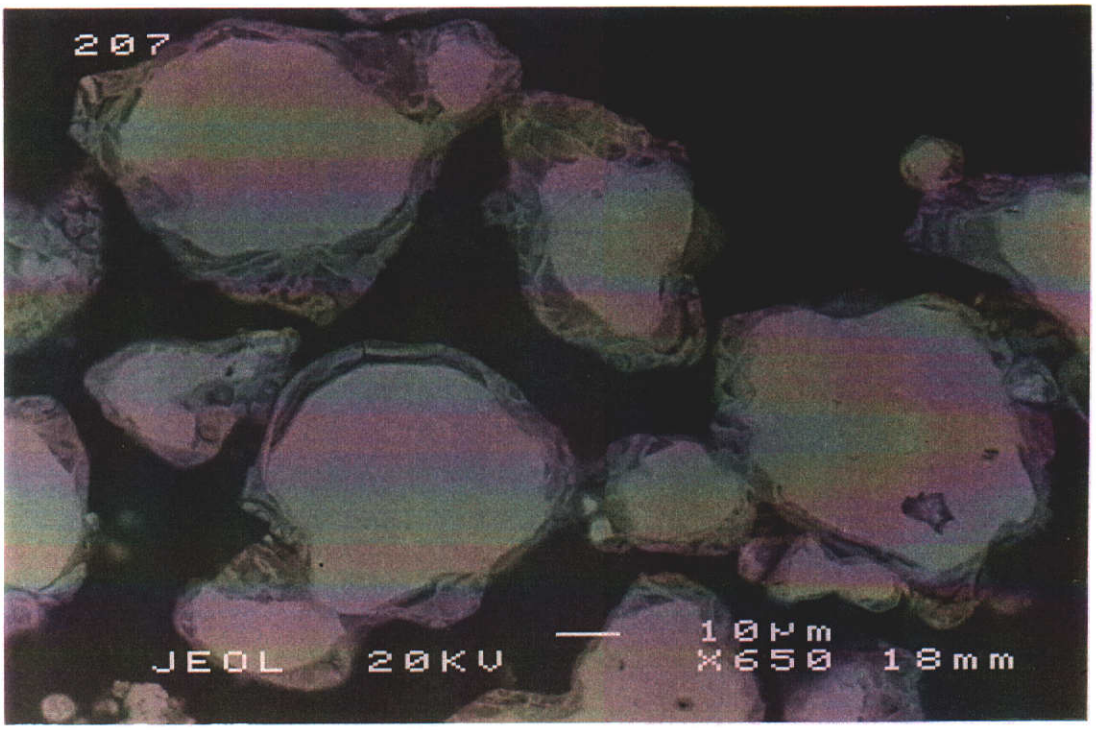

Figure 4.15c BSE micrograph of the oxidation product quenched at 495°C showing a mss sulfide core and a $FeSO_4$ rim.

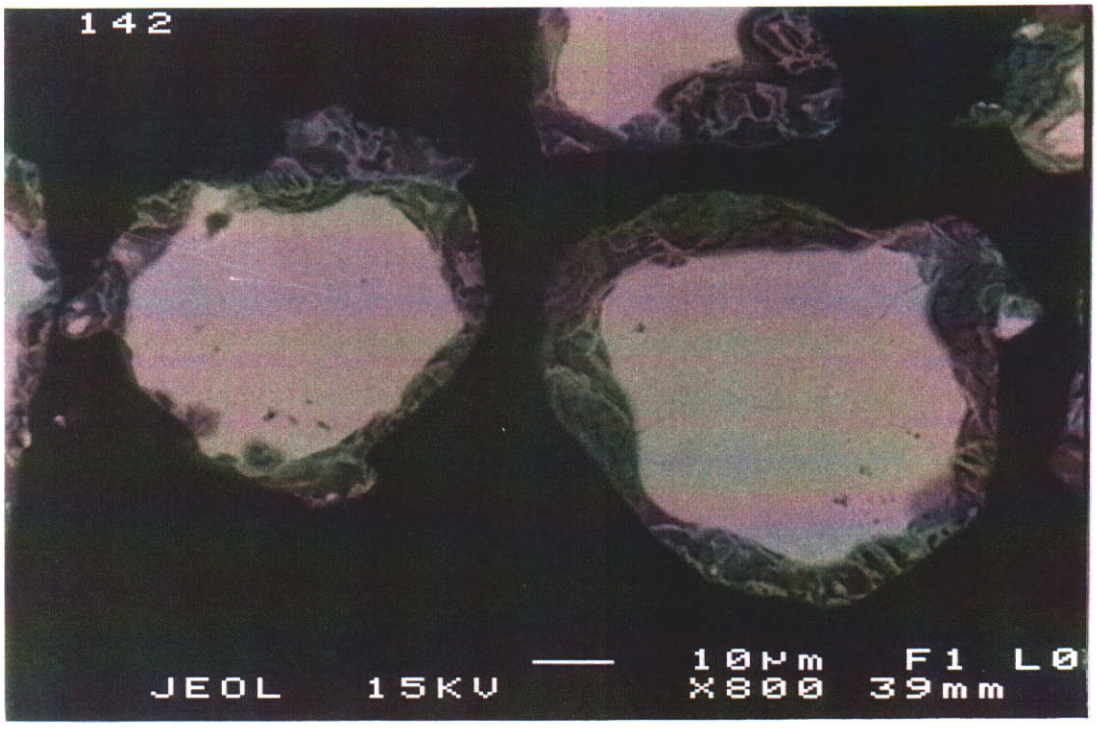

Figure 4.15d BSE micrograph of the oxidation product quenched at 535°C. A slight increase in the thickness of the sulfate rim can be observed compared with the product collected at 495°C.

of heazlewoodite, $(Fe,Ni)_{3\pm x}S_2$, was also detected in the XRD pattern. $FeSO_4$ and $NiSO_4$ were both identified in the FTIR spectrum at 600°C. TG-DTA experiments performed on $FeSO_4$ at identical heating conditions of 10°C min^{-1} in an air atmosphere showed $FeSO_4$ commenced decomposition at 575°C. The decomposition temperature of $FeSO_4$ corresponded with the maximum mass gain observed at 575°C for the ideal violarite before commencement of the mass loss coinciding with an endothermic drift in the DTA baseline.

Therefore, the preferential migration and sulfation of iron to the outer rim of the violarite particle reached a maximum at 575°C. The oxidation of excess sulfur associated with the metal-deficient mss phase would account for the small exotherm observed between 540°C and 600°C. The mass loss and endothermic drift in the DTA baseline were attributed to the decomposition of $FeSO_4$, which can be described by the following reaction:

$$2\ FeSO_4 \rightarrow Fe_2O_3 + 2\ SO_{2\,(g)} + 0.5\ O_{2\,(g)}$$

Direct oxidation of the mss core to trevorite, $Fe_{3-x}Ni_xO_4$, was evident above 575°C. As $FeSO_4$ is thermodynamically unstable above 575°C the remaining iron was oxidised in a stepwise mechanism similar to that previously described by Tsukada *et al.* (1981) and Asaki *et al.* (1984). The remaining iron continued to migrate to the mss-oxide interface where it formed an iron-rich mss phase. The mss phase was oxidised to trevorite forming a dense oxide layer between the mss and the porous hematite layer as described by the following reaction:

$$3\ (Fe,Ni)_{1-x}S + (5-2x)\ O_{2\,(g)} \rightarrow (1-x)\ (Fe,Ni)_3O_4 + 3\ SO_{2\,(g)}$$

The trevorite layer can be clearly seen in the BSE micrograph, between the dark porous hematite layer and the mss core, shown in Figure 4.15e. Oxygen may diffuse

through the porous hematite layer to the trevorite, where the trevorite is further oxidised to hematite and nickel oxide.

The rate of mass loss increased with a 7.45% loss observed between 635°C and 715°C. An exothermic peak was associated with the mass loss with onset and offset temperatures of 665°C and 715°C. An SO_2 peak coincided with the exothermic peak. The rate of mass loss then decreased between 715-745°C with a loss of 2.10%.

Figure 4.15f shows the BSE micrograph of the oxidation product quenched at 725°C. Two sulfide phases were evident in the sulfide core. Large holes were present between the sulfide core and the oxide rim. XRD analysis identified the two sulfide phases as mss and heazlewoodite. EPMA of the sulfide core determined the average composition of the mss and heazlewoodite to be $Fe_{0.04}Ni_{1.19}S_{1.00}$ and $Ni_{3.02}Fe_{0.14}S_{2.00}$ respectively. The high temperature form of heazlewoodite is normally a non-quenchable phase. However, the high temperature form may revert to the low temperature form if the iron:nickel ratio is sufficiently low to lie within the stability field of the low temperature heazlewoodite solid solution.

The large holes observed between the oxide rim and the remaining sulfide core can be attributed to an increase in density between mss and $(Fe,Ni)_{3\pm x}S_2$. Table 4.4 shows the change in the volume for a range of oxidation reactions. The density of mss may range from 4.5-4.8 g cm^{-3} depending on the amount of nickel substitution (Roberts, 1990). Heazlewoodite, Ni_3S_2, has a density of 5.87 g cm^{-3}. The actual density may be slightly higher due to substitution of iron for the larger nickel cation. The conversion of mss to heazlewoodite with the loss of sulfur would result in a 30% decrease in the volume of the sulfide core. Therefore, the decrease in volume of the sulfide is large enough to account for the holes observed in the oxidation product.

Reaction	Δ Mass %	Δ Volume %
$Fe_{0.97}Ni_{1.97}S_{4.00\,(s)} \rightarrow 2.93\ (Fe_{0.33}Ni_{0.67}S_{1.00})_{(s)} + 1.07\ SO_{2\,(g)}$ (ideal violarite) (mss)	-11.5	-9.6
$Fe_{0.33}Ni_{0.67}S_{1.00\,(s)} \rightarrow 0.33\ FeSO_{4\,(s)} + 0.67\ NiS_{(s)}$ (mss) (iron(II) sulfate) (nickel-rich mss)	23.6	37.8
$Fe_{0.33}Ni_{0.67}S_{1.00\,(s)} \rightarrow 0.16\ Fe_2O_{3\,(s)} + 0.67\ NiS_{(s)} + 0.33\ SO_{2\,(g)}$ (mss) (hematite) (nickel-rich mss)	-3.0	-6.4
$Fe_{0.33}Ni_{0.67}S_{1.00\,(s)} \rightarrow 0.22\ Ni_3S_{2\,(s)} + 0.16\ Fe_2O_{3\,(s)} + 0.56\ SO_{2\,(g)}$ (mss) (heazlewoodite) (hematite)	-10.9	-25.2
$Fe_{0.33}Ni_{0.67}S_{1.00\,(s)} \rightarrow 0.67\ NiO_{(s)} + 0.16\ Fe_2O_{3\,(s)} + SO_{2\,(g)}$ (mss) (nickel oxide) (hematite)	-14.9	-36.0
Overall Reaction		
$Fe_{0.97}Ni_{1.97}S_{4.00\,(s)} \rightarrow 1.97\ NiO_{(s)} + 0.485\ Fe_2O_{3\,(s)} + 4\ SO_{2\,(g)}$ (ideal violarite) (nickel oxide) (hematite)	-24.7	-42.2

Table 4.4 Theoretical changes in mass and molecular volume for range of oxidation reactions. Change in molecular volume was calculated from the measured and calculated densities for the individual mineral phase obtained from Roberts (1990).

FTIR spectroscopy performed on the oxidation product collected at 725°C revealed $NiSO_4$ as the major phase. There was no evidence of $FeSO_4$. The FTIR spectrum also showed evidence of NiO, Fe_2O_3, and $Fe_{3-x}Ni_xO_4$. XRD analysis of the oxidation product confirmed the presence of NiO, Fe_2O_3, and $Fe_{3-x}Ni_xO_4$.

The iron:nickel ratio of the mss phase decreased from 0.20 to 0.03 between 600°C and 725°C. The average metal:sulfur ratio of the mss showed a large increase from 1.02 to 1.23. During the pyrolytic decomposition of ideal violarite, discussed in section 4.1.1, the mss phase continued to lose sulfur over the temperature range 615-835°C as the mss stability field expanded. The loss of sulfur caused the mss composition to fall below the mss stability field observed in the Fe-Ni-S ternary phase diagram. As a result, the high temperature heazlewoodite phase was exsolved from the mss phase. During the oxidation of ideal violarite the metal:sulfur ratio of the mss decreased sufficiently resulting in exsolution of the high temperature heazlewoodite phase. The mss and high temperature heazlewoodite are both present in equilibrium with sulfur vapour.

$$3\ (Fe,Ni)_{1\pm x}S \Leftrightarrow (Fe,Ni)_{3\pm x}S_2 + 0.5\ S_{2\,(g)}$$

Approximately one third of a mole of sulfur is released during the exsolution of $(Fe,Ni)_{3\pm x}S_2$ from mss. As the evolved sulfur vapour is oxidised to sulfur dioxide the equilibrium between the mss and high temperature heazlewoodite phases would no longer be maintained and the reaction would be forced to the right, resulting in further formation of $(Fe,Ni)_{3\pm x}S_2$. The oxidation of the sulfur vapour would account for the exothermic peak and SO_2 gas evolved between 665-715°C.

A final mass loss of 9.40% occurred in two stages. The first stage, with a mass loss of 6.05%, occurred over the temperature range 745-795°C and was associated with no

DTA activity. A broad SO_2 peak was observed in the evolved gas chromatogram between 735°C and 795°C.

TG-DTA experiments performed on anhydrous $NiSO_4$ at 10°C min^{-1} in air showed the commencement of thermal decomposition at 710°C. FTIR spectroscopy of quenched oxidation products collected at 795°C confirmed the complete decomposition of $NiSO_4$ over the temperature range 725-795°C. The thermal decomposition of $NiSO_4$ to NiO is an endothermic reaction (Kellogg, 1964). For violarite, the DTA curve showed no activity in this temperature region. Therefore, an exothermic reaction must be occurring over the same temperature range with the net effect resulting in negligible DTA activity. The exothermic reaction may be the preferential oxidation of the remaining iron and sulfur in the mss phase with the continual formation of the high temperature heazlewoodite phase. The thermal decomposition of $NiSO_4$ between 710-795°C can be shown by the following reaction:

$$NiSO_4 \rightarrow NiO + SO_{2\,(g)} + 0.5\,O_{2\,(g)}$$

A final rapid weight loss of 3.35% occurred over the temperature range of 745-820°C. A sharp endothermic peak in the DTA curve was observed at 795°C. This was immediately followed by a large exotherm which coincided with the final weight loss at 790-840°C. The evolved gas chromatogram showed a sharp decrease in the SO_2 evolved before a large SO_2 emission was observed coinciding with the exothermic peak. The decrease in the evolved gas corresponded with the melting point transition of the high temperature heazlewoodite phase. As discussed in section 4.1.1, the endothermic peak can be attributed to the incongruent melting of the high temperature $(Fe,Ni)_{3\pm x}S_2$ phase to give $(Fe,Ni)_{1-x}S$ and central liquid phase. The rapid oxidation of the resulting liquid sulfide gave rise to the large exotherm and the SO_2 peak in the evolved gas chromatogram.

Micrographs of samples quenched at 795°C showed the sulfide cores have almost completely oxidised to NiO, Fe_2O_3 and $Fe_{3-x}Ni_xO_4$ (Figure 4.15g). The particles appear spherical, almost forming cenospheres. A number of $(Fe,Ni)_{3\pm x}S_2$ cores were evident with no oxide rim present. This may have been due to the rapid evolution of sulfur, as the sulfide particle approached the incongruent melting point, which blew off the dense oxide rim. XRD analysis showed heazlewoodite as the only remaining sulfide phase. There were also strong diffraction lines for hematite, nickel oxide and trevorite. EPMA of the remaining $(Fe,Ni)_{3\pm x}S_2$ phase showed a minor amount of iron present in solid solution with nickel, with an average composition of $(Ni_{3.09}Fe_{0.08})S_2$. The process taking place between 745-820°C may be described by the following reactions:

$$(Fe,Ni)_{3\pm x}S_{2\,(s)} \Leftrightarrow (Fe,Ni)_{3\pm x}S_{2\,(l)}$$

$$(Fe,Ni)_{3\pm x}S_{2\,(l)} \Leftrightarrow (Fe,Ni)_{1\pm x}S_{\,(s)} + (Fe,Ni)_{1+x}S_{\,(l)}$$

$$(Fe,Ni)_{1+x}S_{\,(l)} \xrightarrow{O_2} Fe_2O_3 + NiO + (Fe,Ni)_3O_4$$

The TG trace showed a continued mass loss between 825-1000°C with no associated DTA activity. Samples collected at 870°C showed complete oxidation of sulfide with cenosphere formation, and NiO, Fe_2O_3 and $Fe_{3-x}Ni_xO_4$ as the final oxidation products (Figure 4.15h).

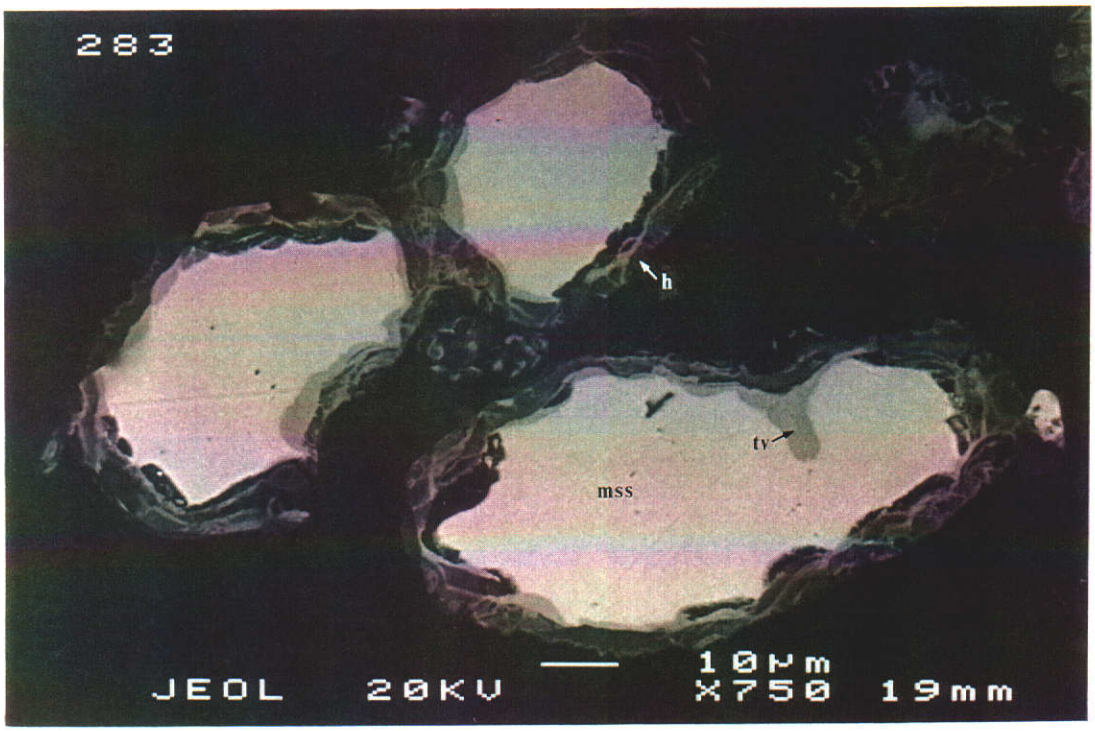

Figure 4.15e BSE micrograph of a partially oxidised sample collected at 600°C. The mss core has decreased in volume. The formation of trevorite (dark phase) between the outer sulfate-oxide rim and the mss is evident.

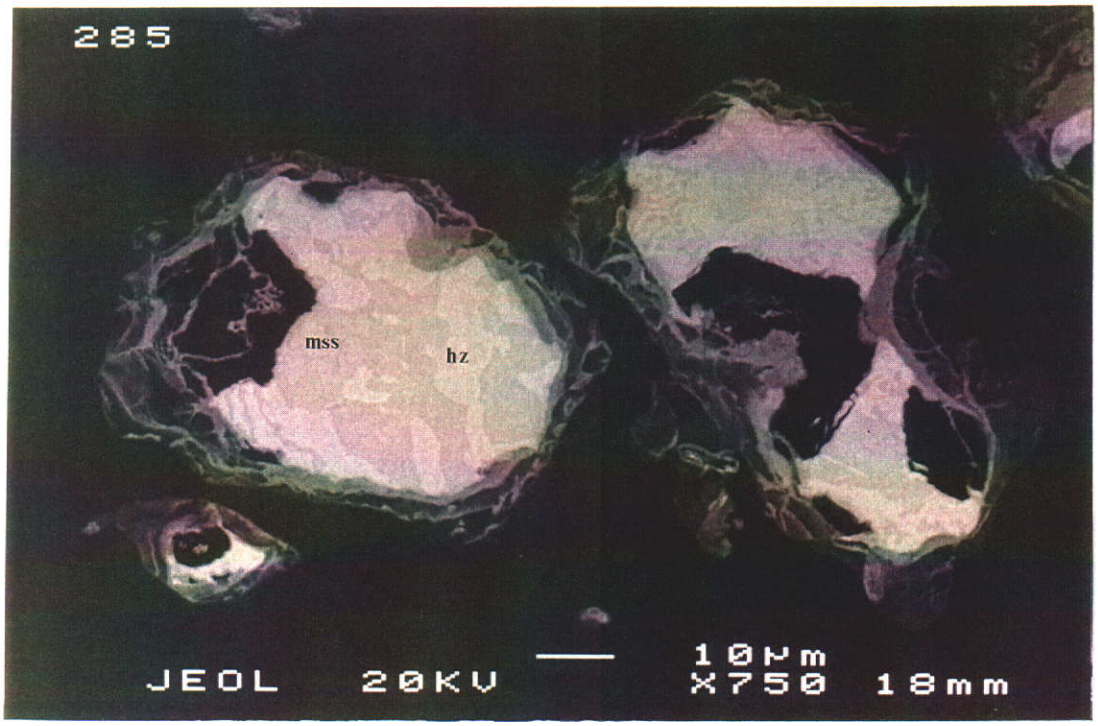

Figure 4.15f Two sulfide phases were evident in the sulfide core in samples collected at 725°C. These are: mss (dark phase) and $(Fe,Ni)_{3\pm x}S_2$. Large holes are evident in the sulfide core. Virtually no sulfur is present in the outer rim following the decomposition of $FeSO_4$.

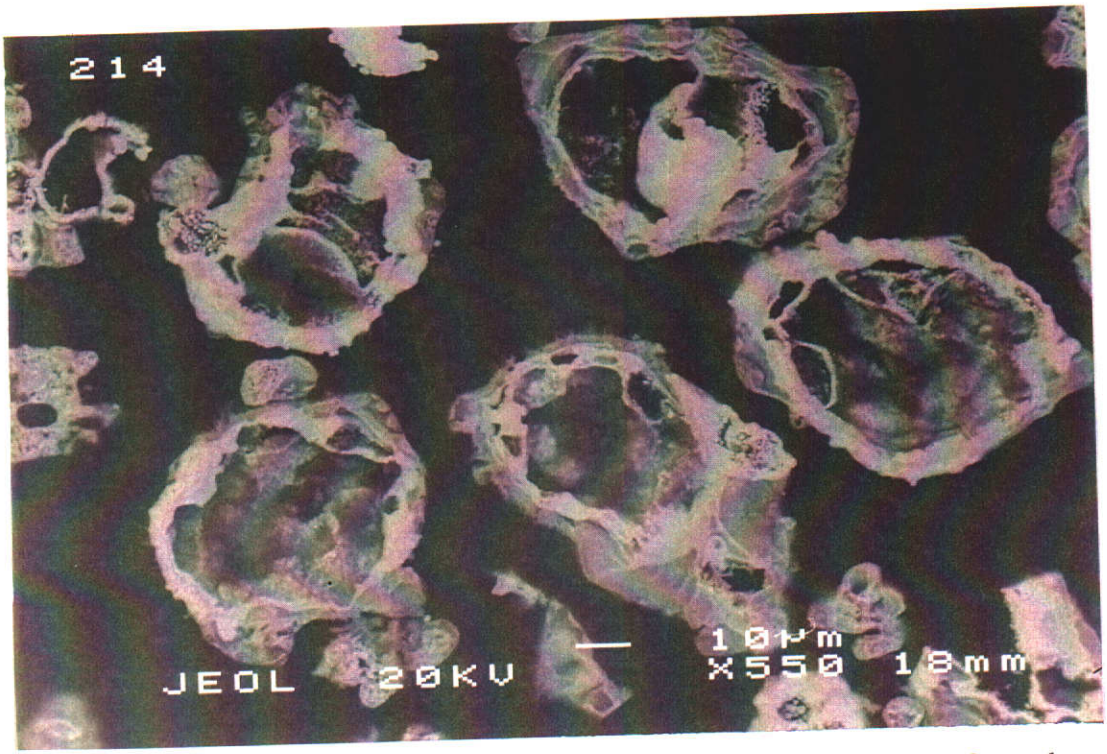

Figure 4.15g Oxidised particles collected at 795°C. Particles have almost formed cenospheres as the $(Fe,Ni)_{3\pm x}S_2$ approaches its incongruent melting point.

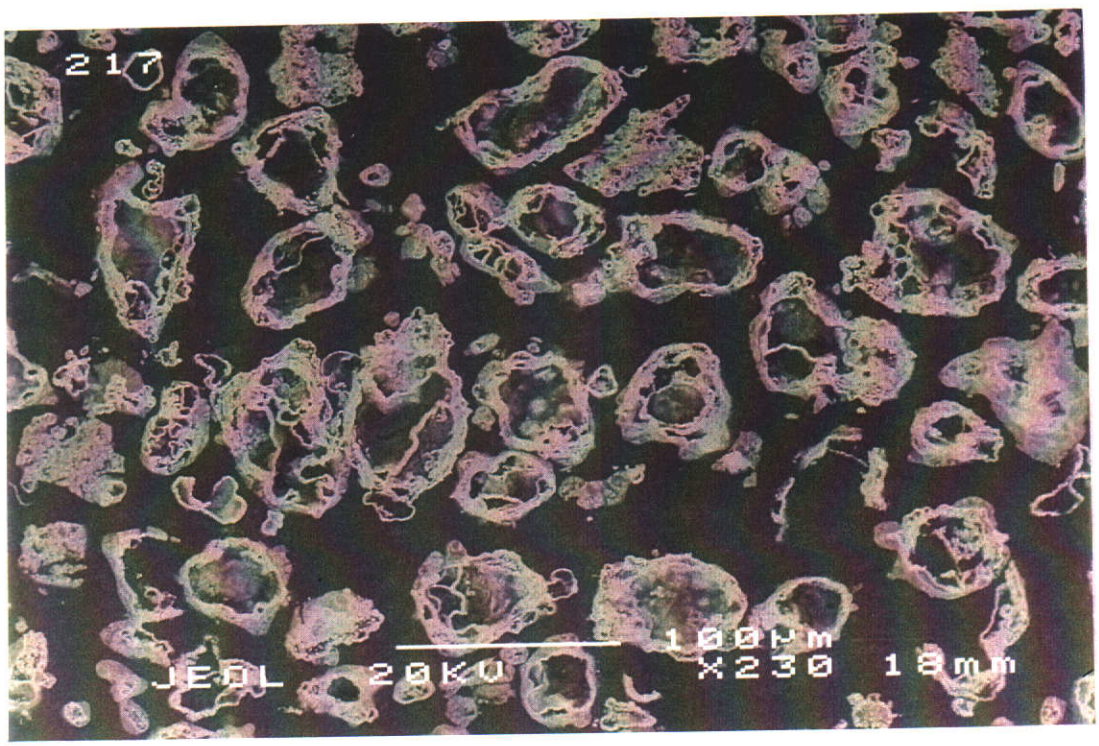

Figure 4.15h Oxidised violarite particles collected at 870°C.

4.2.2 Summary

Table 4.5 summarises the phases detected by XRD and FTIR during the oxidation of ideal violarite in the temperature range 25-1000°C. The oxidation proceeded in three main stages:

(i) Decomposition of synthetic violarite to mss

Under oxidising conditions, violarite decomposed directly to mss between 425°C and 495°C. The rapid oxidation of the evolved sulfur caused the particle temperature to escalate resulting in further loss of sulfur from the violarite lattice. The reaction continued until the violarite had completely decomposed to mss. Therefore, under oxidising conditions, the phase transition of violarite to mss and vaesite was not observed.

(ii) Preferential sulfation and oxidation of iron with nickel enrichment

The preferential sulfation and oxidation of iron in the mss phase was identified as the second major stage in the oxidation of synthetic violarite. The preferential migration of iron from the mss phase to the outer rim of the sulfide particle resulted in sulfation to $FeSO_4$ at temperatures as low as 425°C. The mss core showed a 48.3% decrease in iron content between 425-600°C. The preferential migration and sulfation of the iron continued until the decomposition temperature of $FeSO_4$ was reached at 575°C. After the decomposition temperature was exceeded, the $FeSO_4$ was oxidised to hematite. The remaining iron in the mss phase was oxidised to trevorite between 575-795°C.

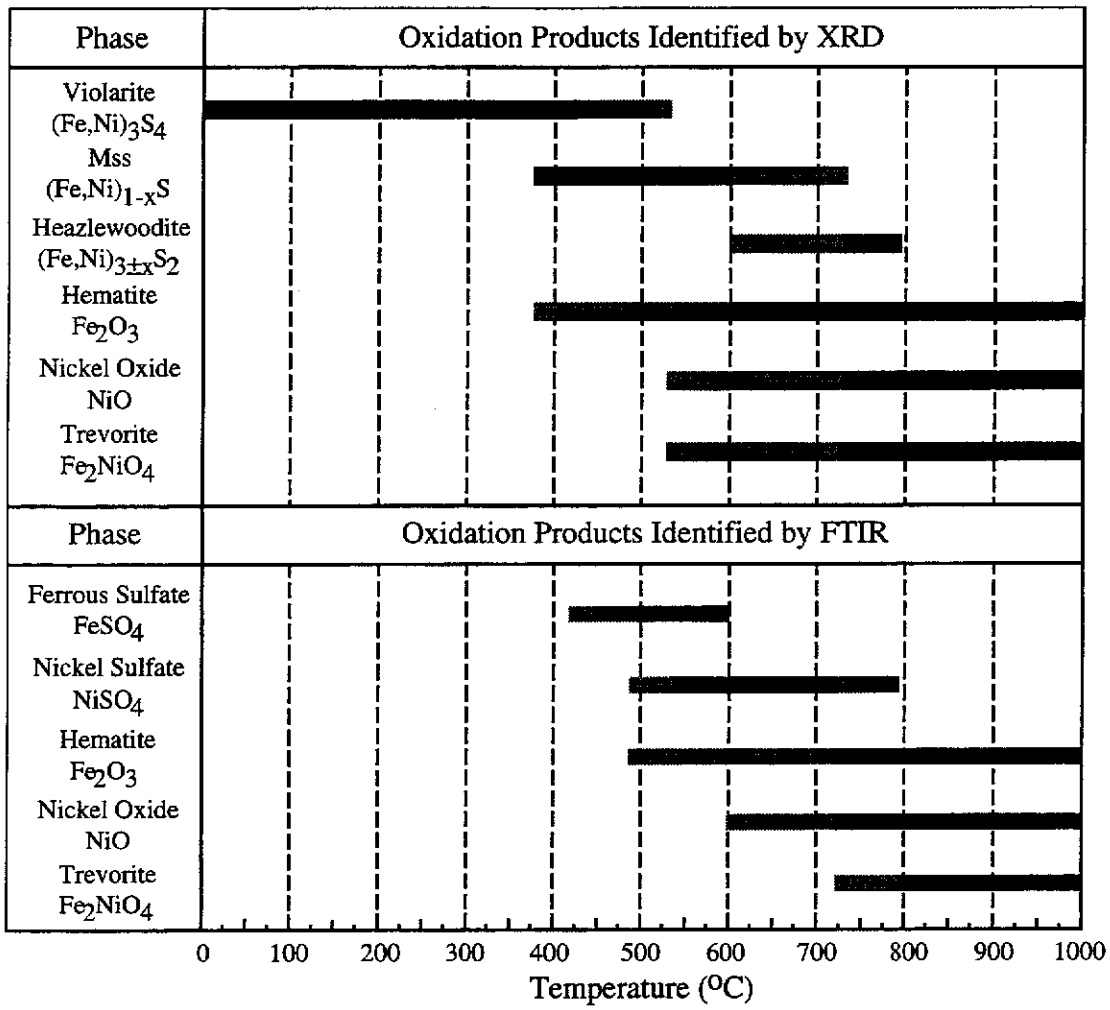

Table 4.5 Summary of the oxidation products identified by XRD and FTIR from 25-1000°C. Minor phases are indicated by the shaded line. Major phases are represented by the dark line.

(iii) Oxidation of nickel sulfide core

Nickel enrichment of the unreacted sulfide core occurred between 425-795°C. A minor trace of nickel sulfate was evident between 495-575°C. However, the rate of formation of $FeSO_4$ far exceeded the rate of $NiSO_4$ formation in this temperature range. After the decomposition of $FeSO_4$, the sulfation of nickel in the mss was the predominant sulfation reaction reaching a maximum at 710°C before $NiSO_4$ decomposed to NiO. Nickel enrichment of the mss continued between 425-615°C until sufficient iron and sulfur had been removed to form a high temperature $(Fe,Ni)_{3\pm x}S_2$ phase. The rate of oxidation of the nickel sulfide core rapidly increased

at the incongruent melting point of $(Fe,Ni)_{3\pm x}S_2$. The final oxidation product included Fe_2O_3, NiO and $Fe_{3-x}Ni_xO_4$.

4.2.3 Effect of Stoichiometry on the Oxidation of Synthetic Violarite.

A typical TG-DTA trace for each synthetic violarite sample heated at 10°C min^{-1} in air is presented in Figure 4.16. The reaction mechanism remained unchanged as the iron:nickel ratio decreased. All four violarite samples showed an initial sharp mass loss associated with a large exotherm. The extent of mass loss and intensity of the exothermic peak were similar for all four samples. However, the onset temperature of the main exothermic peak decreased as the violarite tended towards the nickel-rich end of the series. For example, the onset temperature of the main exothermic peak decreased from 420°C to 370°C between ideal and nickel-rich violarite respectively for the 63-45 μm particle size fraction. This is consistent with the decrease in temperature observed for the initial loss of sulfur associated with exsolution of mss from the violarite lattice as the iron:nickel ratio decreased as shown in Figure 4.7.

The ideal violarite sample has approximately five times more iron than the nickel-rich violarite sample. As a result, the extent of mass gain associated with the sulfation of iron decreased significantly as the iron:nickel ratio decreased. A mass gain of 3.50% was observed for ideal violarite compared with only 2.25% for the nickel-rich violarite over the temperature range 485-575°C. This was clearly observed when BSE micrographs of samples collected from the two endmembers of the violarite series at 495°C were compared (Figure 4.17a). Ideal violarite exhibited a continuous sulfate rim around the entire particle, while the nickel-rich violarite had considerably less sulfate present around the outer rim. FTIR spectroscopy of the nickel-rich violarite sample collected at 450°C showed $FeSO_4$ as the major phase with a trace of $NiSO_4$. Above 450°C, $NiSO_4$ was the major phase for the nickel-rich violarite sample, with $FeSO_4$ also identified in the spectrum.

All four violarite samples commenced mass loss at 575°C associated with the decomposition of $FeSO_4$. The extent of mass loss observed between 575-680°C was proportional to the extent of sulfation. An endothermic drift in the DTA baseline was observed in all four samples. This peaked at 660°C with the rate of mass loss decreasing between 660°C and 680°C. EPMA results from the sulfide cores of the two endmembers of the violarite solid solution showed migration of iron towards the outer rims of the particles, where it was preferentially oxidised. For example, the iron:nickel ratio of the sulfide cores decreased from 0.56-0.20 between 495-600°C and from 0.086-0.009 between 495°C-665°C for ideal and nickel-rich violarite respectively. Similarly, an increase in the metal:sulfur ratio from 0.97-1.02 and from 1.01-1.07 was observed over the same temperature ranges for ideal and nickel-rich violarite respectively.

A sharp mass loss was observed for each violarite sample between 680-715°C. This was attributed to the oxidation of sulfur liberated as $(Fe,Ni)_{1-x}S$ was converted to $(Fe,Ni)_{3\pm x}S_2$. Figure 4.17b shows a comparison between ideal and nickel-rich violarites collected at 725°C. Large holes were evident in the sulfide cores for both samples. The XRD pattern for the nickel-rich violarite sample corresponded to the pattern recorded for the ideal violarite sample, with heazlewoodite and a nickel-rich mss identified as the two sulfide phases present in the core. EPMA of the heazlewoodite and mss phases present in the sulfide cores showed that both phases had similar compositions for the two endmembers of the violarite series . Table 4.6 shows the compositions of the two sulfide phases for ideal and nickel-rich violarites. Both the mss and heazlewoodite phase are slightly more sulfur deficient in the ideal violarite than the nickel-rich violarite.

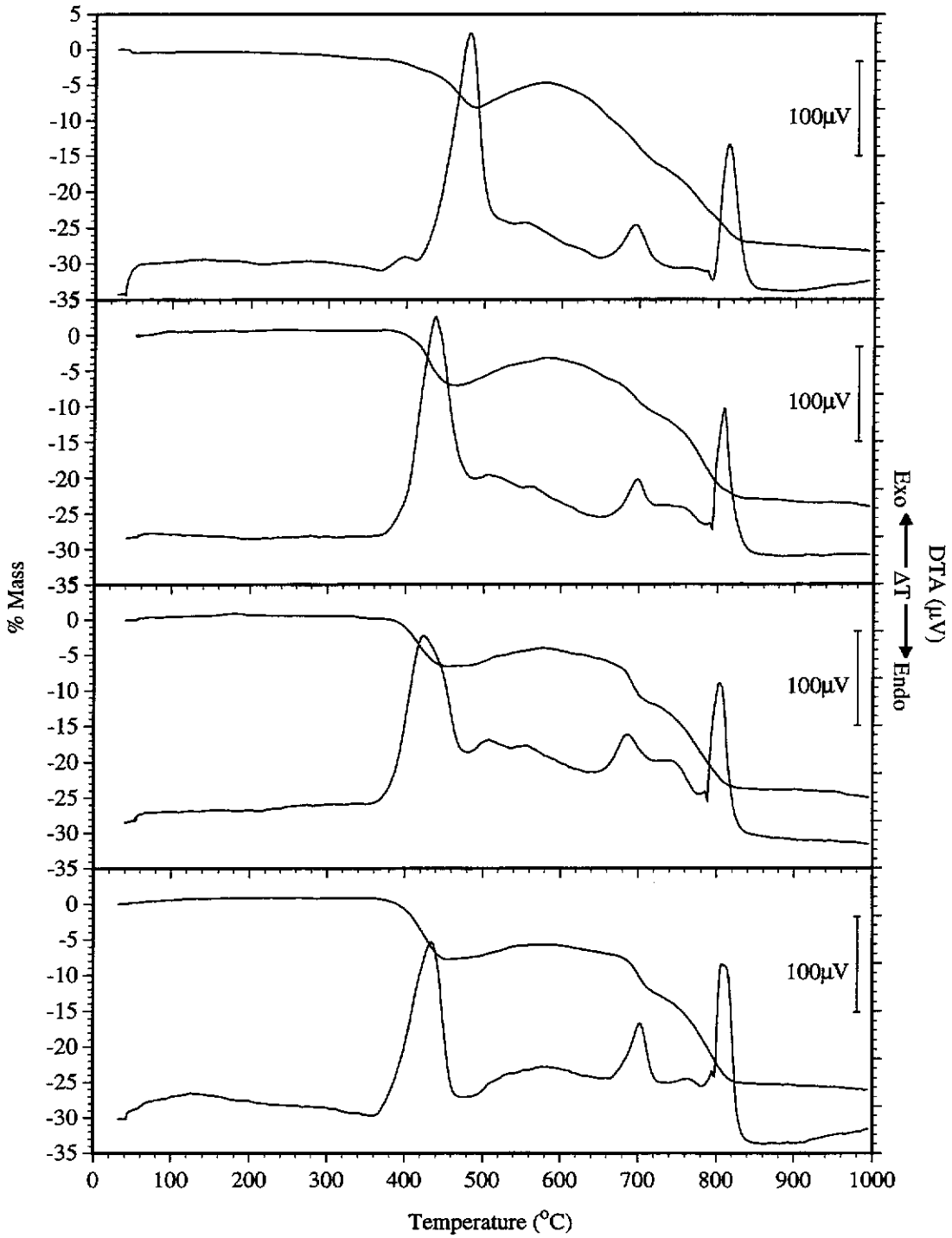

Figure 4.16 Typical TG-DTA traces for the entire range of synthetic violarites, heated at 10°C min^{-1} in an air atmosphere. Approximately 5 mg of the 63-45 μm particle size fraction was used. Starting from the top $Fe_{0.97}Ni_{1.96}S_4$ (ideal violarite), $Fe_{0.73}Ni_{2.26}S_4$, $Fe_{0.46}Ni_{2.49}S_4$, and $Fe_{0.20}Ni_{2.72}S_4$ (nickel-rich violarite).

Temperature	Ideal Violarite		Nickel-Rich Violarite	
(°C)	$(Fe,Ni)_{1-x}S$	$(Ni,Fe)_{3\pm x}S_2$	$(Fe,Ni)_{1-x}S$	$(Ni,Fe)_{3\pm x}S_2$
725	$(Fe_{0.04}Ni_{1.19})S$	$(Ni_{3.02}Fe_{0.14})S_2$	$(Fe_{0.02}Ni_{1.20})S$	$(Ni_{2.98}Fe_{0.07})S_2$
785-795	$(Fe_{0.04}Ni_{1.21})S$	$(Ni_{3.09}Fe_{0.08})S_2$	$(Fe_{0.01}Ni_{1.20})S$	$(Ni_{3.06}Fe_{0.02})S_2$

Table 4.6 Composition of mss and heazlewoodite phases in the sulfide cores of ideal and nickel-rich violarite samples collected at various temperatures in the TG-DTA trace.

Above 710°C, $NiSO_4$ decomposed to NiO and all four violarite samples exhibited a gradual mass loss between 710-750°C.

An endothermic drift in the DTA baseline commenced at approximately 750°C. The drift in the DTA baseline was more prominent for the more nickel-rich violarites. This was associated with the partial melting of the high temperature heazlewoodite phase. The incongruent melting of the high temperature $(Fe,Ni)_{3\pm x}S_2$, characterised by a sharp endothermic peak, occurred at 795°C for both ideal and nickel-rich violarite. This contrasts with the behaviour observed when the endmembers were heated in an inert atmosphere, and a considerable range, from 835°C to 805°C, was observed in the incongruent melting point temperature. The decrease in the temperature range for the onset temperature of the endothermic peak can be attributed to the preferential oxidation of iron resulting in the stoichiometry of the sulfide core approaching the ideal heazlewoodite composition of Ni_3S_2 for all four violarite samples.

Each violarite exhibited a rapid mass loss commencing at the onset temperature of the endothermic drift in the DTA baseline, with the mass loss becoming more rapid at the melting point transition. The extent of mass loss increased slightly as the violarite tended towards the nickel-rich endmember. For example, ideal violarite had a mass loss of 9.40% (745-840°C) while nickel-rich violarite recorded a loss of 11.15% (760-

835°C), an increase of 1.75% in mass loss observed between the endmember samples. This can be attributed to the amount of nickel sulfide remaining in the sulfide core. The nickel-rich samples will have a greater amount of heazlewoodite present prior to the oxidation of the sulfide core due to the lower iron:nickel ratio in the initial violarite.

A large exothermic peak was observed for all four violarite samples coinciding with the incongruent melting point transition. The relative intensities of the DTA peak were constant for all four violarite samples. The particle morphology of the final products was similar for all four violarite samples and comprised of a hollow core surrounded by an outer oxide layer. NiO, Fe_2O_3 and $Fe_{3-x}Ni_xO_4$ were identified as the final oxidation products for all four violarite samples.

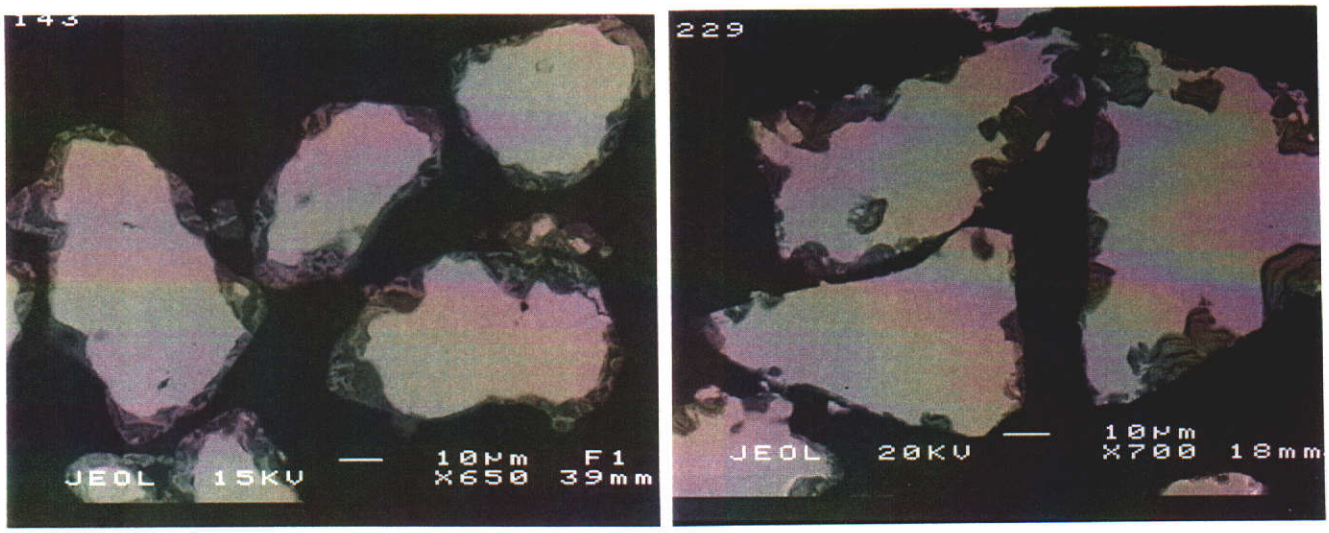

Figure 4.17a Oxidation products of ideal (left) and nickel-rich (right) violarite collected at 495°C. Note the different extent of sulfation products on the outer rims.

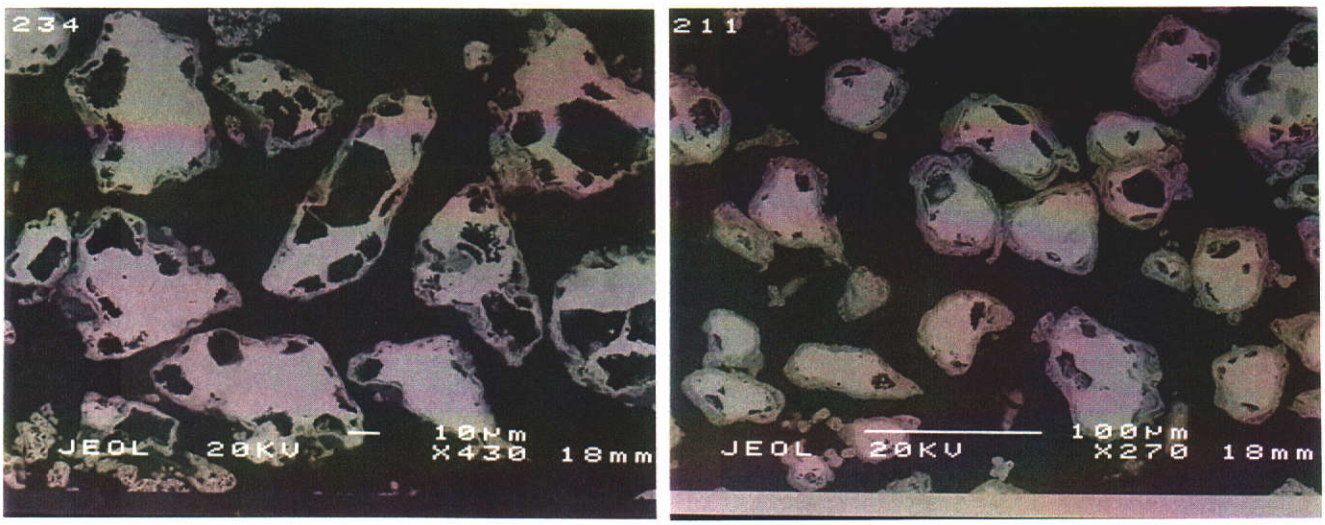

Figure 4.17b BSE micrograph of ideal (left) and nickel-rich (right) violarite collected at 725°C.

4.3 Oxidation of Synthetic Violarite Under Ignition Conditions.

At relatively slow heating rates and low partial pressures of oxygen, the oxidation of sulfides occurs in a stepwise mechanism. The exothermic energy evolved from the oxidation of each sulfide phase is able to dissipate into the surrounding environment before the newly formed or remaining sulfide phases are oxidised. It has been shown that by increasing the heating rate and partial pressure of oxygen ignition conditions may prevail and the sulfide sample may ignite (Dunn, Jayaweera and Davies, 1985; Dunn, De and O'Connor, 1989a). An ignition reaction is characterised using TG-DTA by a single highly exothermic peak occurring over a relatively short period of time (Dunn, Jayaweera and Davies, 1985). The sharp exothermic peak is accompanied by a rapid mass loss and a temperature excursion that rapidly increases well in excess of the programmed furnace temperature.

In this section the ignition behaviour of each violarite will be examined using TG-DTA. An increase in the intensity of the reaction conditions was achieved by increasing the heating rate from 10°C min^{-1} to 40°C min^{-1} and converting the atmosphere from air to oxygen.

4.3.1 Oxidation of Ideal Violarite Under Ignition Conditions

The TG-DTA profile of ideal violarite, with a particle size range of 63-45 μm, heated at 40°C min^{-1} in oxygen is presented in Figure 4.18. An initial mass loss of 10.65% was observed between 410-500°C associated with the decomposition of violarite to mss resulting in the evolution of sulfur vapour at the solid-gas interface. The oxidation of the evolved sulfur produced a large exothermic peak coinciding with the rapid mass loss with an onset and offset temperature of 420°C and 515°C. The onset temperature of the exothermic peak had increased by approximately 50°C under ignition conditions. This was mainly attributed to an instrumental effect caused by an

increase in the heating rate from 10°C to 40°C min^{-1} (Wendlandt, 1986, pp.41-43). The temperature range of the exothermic peak also showed a decrease from 135°C to 95°C as the heating rate was increased, representing a decrease of 40°C in the peak range of the DTA event. Therefore, the DTA event occurred over a shorter time period when heated at a rate of 40°C min^{-1} compared to the DTA trace obtained at 10°C min^{-1}. This is characteristic of an ignition reaction. In addition the intensity of the DTA peaks was also expected to increase as the heating rate increases due to an increase in the response of the instrument (Wendlandt, 1986, pp.228-232). However, the intensity of the exothermic peak was significantly larger than expected due to an increase in the heating rate. A five-fold increase in the peak intensity of the exotherm was observed indicating the oxidation reaction was highly exothermic. At the peak of the exothermic activity the temperature of the ideal violarite sample was 510°C, this was approximately 20°C higher than the programmed furnace value. Hence, once the oxidation reaction began, sufficient energy was produced to generate a sustainable reaction and trigger an ignition reaction resulting in the sample overheating.

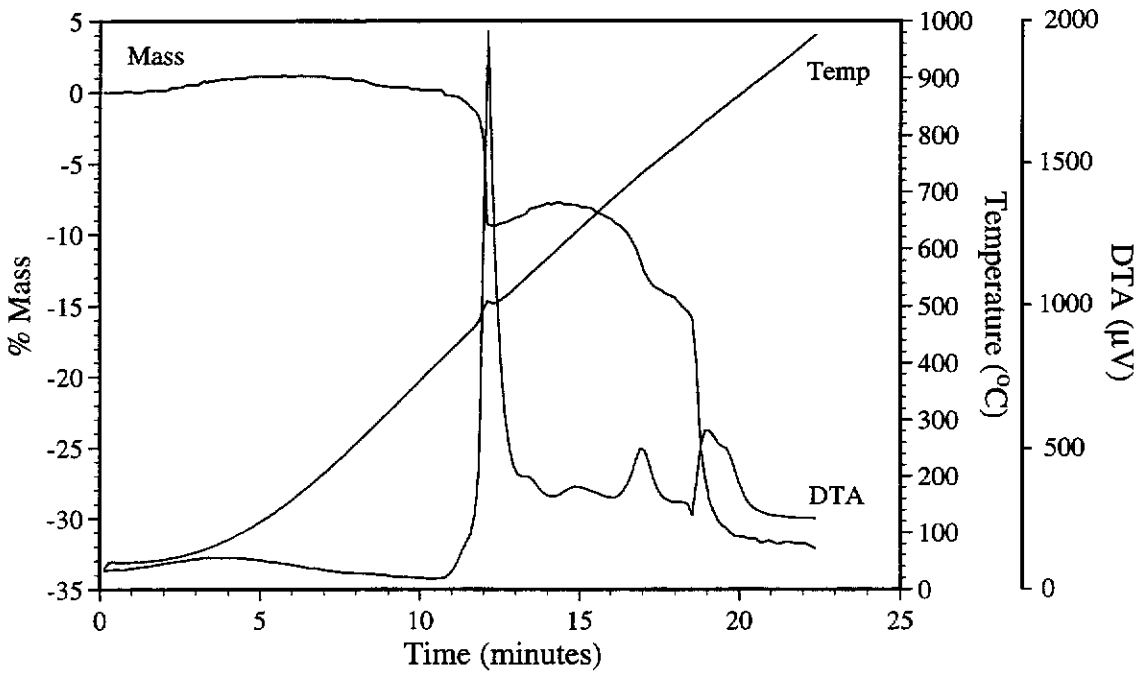

Figure 4.18 TG-DTA trace of ideal violarite ($Fe_{0.97}Ni_{1.96}S_4$), heated at 40°C min^{-1} in an oxygen atmosphere, 63-45 µm particle size fraction.

Analysis of the violarite sample prior to the exothermic activity showed violarite as the major phase with only a minor amount of mss present. Mineralogical examination of the violarite sample quenched at the onset temperature of exotherm showed that the violarite had completely decomposed to mss. A minor amount of hematite was also detected in the oxidation product. Although the temperature program was stopped at the onset temperature, the DTA activity and sample temperature continued to increased. Therefore, the reaction appears to be autogenous and proceeds to completion with the violarite decomposing to mss resulting in the loss of sulfur.

Oxidation products collected at the offset temperature showed there was a significant increase in the amount of hematite present according to the relative peak intensities between mss and hematite. FTIR analysis of the oxidation products collected at 535°C showed $NiSO_4$ as the predominant sulfate species with only a minor amount of $FeSO_4$ remaining. EPMA of the mss core revealed that the majority of the iron had been preferentially oxidised with an average composition of $Fe_{0.10}Ni_{0.91}S_{1.00}$. The particle morphology was similar to the oxidised product collected after the major exotherm under oxidising conditions of 10°C min^{-1} in air, with a homogeneous mss core surrounded by a sulfate-oxide layer.

Therefore, analysis of the oxidation products indicates that the ignition reaction was triggered by the commencement of decomposition of violarite to mss resulting in the loss of sulfur vapour. The oxidation of the sulfur vapour with the gaseous oxidant produced a highly exothermic reaction at the solid-gas interface. The heat generated by the reaction caused the temperature of the particle to increase rather than the temperature of its surroundings resulting in the sample temperature rising significantly above the programmed furnace temperature. The increase in particle temperature resulted in further sulfur loss and the reaction proceeded until the violarite had completely decomposed to mss. The overheating experienced during the major exotherm appeared to be sufficient to decompose the $FeSO_4$ formed prior to the major

exothermic activity. Hence, the particle temperature must have exceeded temperatures in excess of 610°C, the decomposition temperature $FeSO_4$. However, the particle temperature was not high enough to decompose the $NiSO_4$ present with a decomposition temperature of 745°C. During the decomposition of the violarite to mss the sulfur pressure appeared to be sufficiently high to prevent the diffusion of oxygen to the sulfide interface. XRD and EPMA results suggested that iron sulfide component of the mss was oxidised during the later stages of the exothermic activity resulting in the formation of hematite.

As the temperature increased a mass gain of 1.50% occurred between 515-610°C, followed by a similar mass loss between 610-710°C. This was associated with sulfation of the remaining iron sulfide and subsequent decomposition of $FeSO_4$. A small exothermic peak in the DTA curve coincided with the mass gain between 585-690°C. This can be attributed to the oxidation of excess sulfur from the mss phase during the sulfation of iron and nickel. The mass gain observed under ignition conditions was significantly less than that observed under less vigorous oxidising conditions.

Above 710°C the nickel sulfide component then proceeded to oxidise in several stages. Between 710-745°C a mass loss of 3.85% was observed. This was accompanied by a small exothermic peak between 705-760°C. XRD analysis of the oxidation product collected at 710°C showed the mss core had almost completely converted to $(Fe,Ni)_{3\pm x}S_2$, with hematite and trevorite as the major oxide phases present. Nickel sulfate was also evident in the diffraction pattern. This was confirmed by FTIR spectroscopy with vibrational peaks located at 1152, 1045, 984, 680, 610 and 599 cm^{-1}. Therefore, the exotherm was associated with the oxidation of sulfur evolved from the conversion of mss to $(Fe,Ni)_{3\pm x}S_2$.

The rate of mass loss decreased with a loss of 2.70% between 745-805°C, associated with the decomposition of $NiSO_4$. Then the rate increased with a rapid mass loss of 15.50% commencing at 805°C coinciding with the incongruent melting point transition of $(Fe,Ni)_{3\pm x}S_2$. A broad exothermic peak was observed during the rapid mass loss between 805-885°C associated with the oxidation of the remaining nickel sulfide.

Synthetic violarite displayed typical characteristics of an ignition reaction with a major exothermic peak coinciding with a rapid mass loss and a 20°C temperature excursion from the programmed furnace temperature with the sample temperature reaching a maximum of 510°C. However, the ignition behaviour of the violarite sample was not entirely typical of an ignition reaction. Only 10.65% of the total mass loss of 30.85% coincided with the major exothermic activity. While the heat generated by the ignition of the sulfur was sufficient to oxidise the iron sulfide component the remaining nickel sulfide did not ignite but rather oxidised over an extended temperature range analogous to that observed under conditions of 10°C min^{-1} in air (Figure 4.11).

Similar ignition behaviour has been reported by Dunn and Mackey (1993) on a natural violarite-pyrite sulfide concentrate heated under similar conditions. A major exotherm was observed between 460-510°C. The sample temperature exceeded the programmed furnace temperature by 45°C, reaching a maximum of 520°C. Only 16.6% of the total mass loss of 28.3% occurred in association with the major exotherm. The remaining 11.7% mass loss occurred in several stages between the temperature range of 610°C to 820°C associated with only a minor amount of exothermic activity.

The onset temperature of the major exotherm was approximately 40°C higher than the observed onset temperature for synthetic violarite. This was probably due to the violarite concentrate containing a significant quantity of pyrite. The pyrite is less reactive than the violarite and therefore, higher temperatures will be required to ignite the violarite sample (Mackey, 1991). The ignition of the violarite appears to trigger the

ignition of the pyrite resulting in an higher observed mass loss during the major exothermic activity.

4.3.2 Summary

It appears that the decomposition of violarite to mss is instrumental in the ignition. The sulfur evolved from the decomposition rapidly oxidises, causing overheating of the sulfide particles. The diffusion of iron in the mss increases significantly as the temperature of the sulfide particles increases. The iron sulfide component is then preferential oxidised during the later stages of the exothermic activity.

The heat evolved from the major exothermic activity of the ideal violarite sample was insufficient to melt the remaining nickel sulfide, which is essential for its oxidation. Hence, while the decomposition of the violarite and oxidation of the iron sulfide component showed behaviour indicative of an ignition reaction, the remaining nickel sulfide behaved in a manner analogous to that observed under less aggressive oxidising condition. Therefore, conditions of 40°C min^{-1} in oxygen did not achieve complete ignition of the violarite sample.

4.3.3 Effect of Stoichiometry on the Ignition Behaviour of Synthetic Violarite

The TG-DTA profiles for each synthetic violarite sample for each particle size fraction heated at 40°C min^{-1} in an oxygen atmosphere are shown in Figures 4.19 and 4.20. If the 63-45 μm particle size is considered for each violarite sample then as the iron:nickel ratio decreased, the intensity of the major exotherm decreased. There was also a decrease in the observed mass loss associated with the major exotherm as the iron:nickel ratio decreased. Ideal and nickel-rich violarite exhibited losses of 10.65% and 7.20% respectively. XRD showed that both endmembers of the violarite solid solution had completely decomposed to mss by the offset temperature of the main

exothermic peak. Pyrolysis experiments showed that the loss of sulfur decreased as the iron:nickel ratio decreased during the decomposition of violarite to mss. Mass losses of 9.25% (510-650°C) and 8.90% (475-650°C) were observed for ideal and nickel-rich violarite respectively, when heated at 40°C min^{-1} in nitrogen. The decrease in the amount of sulfur evolved during the pyrolytic decomposition, as the iron:nickel ratio decreased, would contribute to the decrease in intensity of the major exotherm under ignition conditions.

XRD analysis of the oxidation products for the two endmembers of the violarite series collected at the offset temperature of the major exotherm showed there was a decrease in amount of hematite present as the iron:nickel ratio decreased, with only a minor trace of hematite evident in the nickel-rich violarite. Hence, the major exotherm is not entirely attributed to the gaseous oxidation of sulfur vapour liberated by the decomposition of violarite to mss, since the intensity of the major exotherm decreases towards the nickel-rich end of the violarite series. The preferential oxidation of the iron present in the mss phase seems to also contribute to the energy evolved from the violarite sample during the major exotherm.

FTIR spectroscopy of the oxidation products collected after the major exotherm showed $NiSO_4$ present in both ideal and nickel-rich violarites, with a greater amount of nickel sulfate present in the nickel-rich sample. Sulfate formation continued with all four violarites exhibiting a mass gain after the major exotherm. The mass gain increased from 1.50% (500-610°C) to 3.30% (470-620°C) between ideal and nickel-rich violarite. The increase in mass gain as the violarite tends towards the nickel-rich endmember can be attributed to the formation of $NiSO_4$. The iron-rich violarite samples may still have some iron present in the mss core which may also be sulfated during this temperature range.

A small exotherm was observed for all four violarite samples between approximately 705-770°C. The intensity and associated mass loss of the small exothermic peak was relatively constant for all four violarite samples. This was attributed to the conversion of mss to $(Fe,Ni)_{3\pm x}S_2$ resulting in the loss of sulfur.

The second major exotherm for the ideal violarite sample, associated with the incongruent melting point and oxidation of $(Fe,Ni)_{3\pm x}S_2$, showed a reverse trend to that found for the major exotherm. The nickel-rich endmember exhibited a sharp mass loss with an extremely sharp exothermic peak occurring over a very narrow temperature range. This is very typical of an ignition reaction. A small temperature excursion of 15°C from the programmed rate was also observed during the exotherm.

4.3.4 Effect of Particle Size on the Ignition Behaviour of Synthetic Violarite

Particle size had a minor influence on the TG-DTA traces. A comparison of all four particle size fractions for ideal violarite showed no change in the reaction mechanism. The extrapolated onset temperatures of the major exothermic peak decreased from 480°C to 460°C for the 125-90 μm and 45-20 μm particle size fractions respectively. The peak temperature range for the major exotherm remained constant for all four violarite samples.

The mass loss associated with the major exotherm increased slightly as the particle size decreased. For example, the 125-90 μm particle size fraction exhibited a loss of 9.25% while for the 45-20 μm fraction there was a loss of 10.85%.

After the major exothermic activity associated with the oxidation of the evolved sulfur and preferential oxidation of the iron sulfide component of the mss phase, the remaining nickel sulfide was not oxidised until the incongruent melting point transition was reached. The most significant effect due to particle size was the mass loss

associated with the oxidation of the nickel sulfide component. A loss of 26.05% was observed for the 125-90 μm fraction between 795-880°C compared with a loss of 8.95% for the 45-20 μm fraction over the temperature range 785-850°C for the ideal violarite sample. When the experiment for the 125-90 μm fraction was repeated, with a lid placed on top of the crucible, a loss of 13.80% was observed between 795-870°C. Hence, this suggests there were particles being ejected from the crucible during the oxidation of the nickel sulfide. This effect decreased as the particle size decreased. The finer particle size fraction had sintered together after reaching the maximum furnace temperature.

The effect of particle size was consistent for all four violarite samples, apart from the finest particle size fraction for the nickel-rich violarite. The nickel sulfide component for the nickel-rich violarite oxidised prior to the incongruent melting of $(Fe,Ni)_{3\pm x}S_2$ with a sharp exothermic peak observed between 710-725°C. The exotherm coincided with the conversion of mss to $(Fe,Ni)_{3\pm x}S_2$ with the loss of sulfur. The energy evolved from the oxidation of sulfur gas was sufficient to oxidise the remaining nickel sulfide. Hence, the subsequent incongruent melting of $(Fe,Ni)_{3\pm x}S_2$ and oxidation was not observed for the 45-20 μm particle size fraction for the nickel-rich violarite sample.

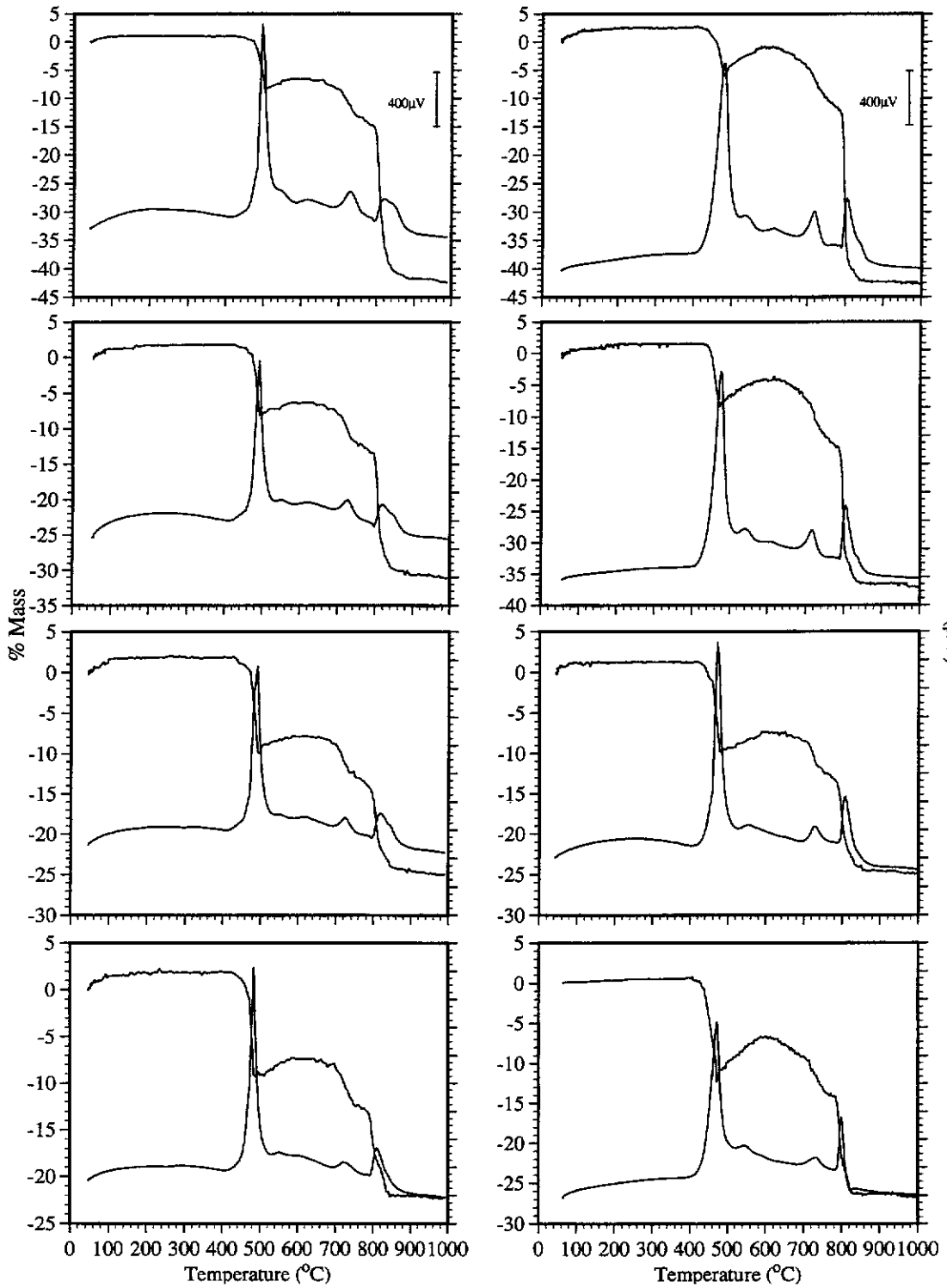

Figure 4.19 Typical TG-DTA for $Fe_{0.97}Ni_{1.96}S_4$ (left) and $Fe_{0.73}Ni_{2.26}S_4$ (right) showing the effect of particle size when heated at 40°C min^{-1} in oxygen. In descending order 125-90, 90-63, 63-45 and 45-20 µm.

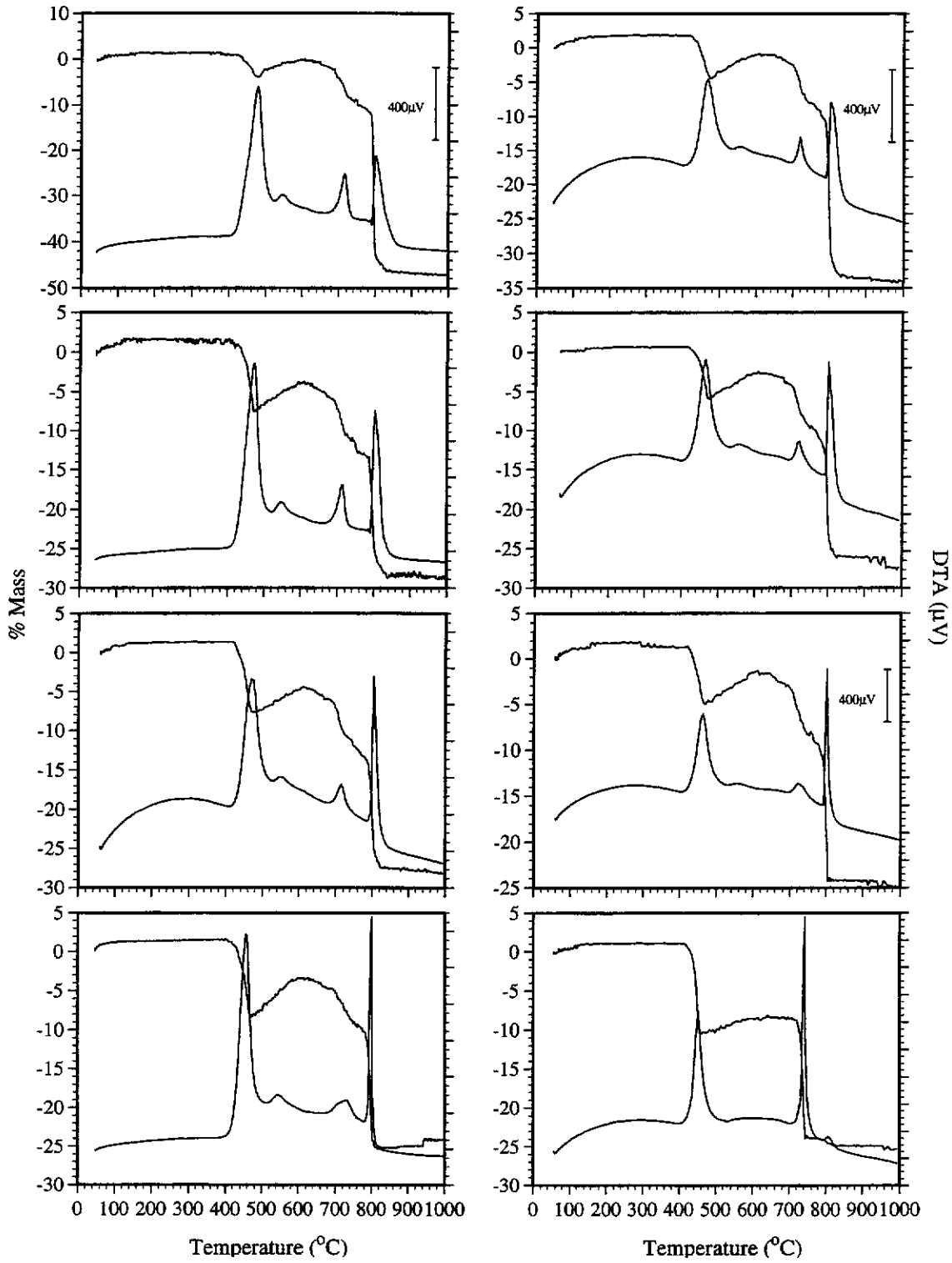

Figure 4.20 Typical TG-DTA for $Fe_{0.46}Ni_{2.49}S_4$ (left) and $Fe_{0.20}Ni_{2.72}S_4$ (right) showing the effect of particle size when heated at 40°C min^{-1} in oxygen. In descending order 125-90, 90-63, 63-45 and 45-20 µm.

4.4 Determination of the Ignition Temperature of Synthetic Violarite by Isothermal TG

The ignition temperature was determined for each synthetic violarite using isothermal gravimetric analysis (Dunn, Jayaweera and Davies, 1985). Isothermal gravimetric analysis provides a controlled environment for the systematic study of the ignition behaviour of sulfide minerals while simulating the very rapid heating rates experienced in a flash smelter process. The heating rate will vary according to the furnace temperature and sample mass, with larger masses requiring longer induction times to reach the furnace temperature and hence experiencing lower heating rates (Dunn, Jayaweera and Davies, 1985).

4.4.1 Ignition of Synthetic Violarite.

A typical isothermal TG trace for $Fe_{0.97}Ni_{1.96}S_4$ (ideal violarite), 63-45 μm particle size fraction, is illustrated in Figure 4.21. The ignition reaction was sensitive to small changes in temperature. A 5°C increase in the furnace temperature was sufficient for ignition conditions to prevail. Ignition temperatures were reproducible to within ±5°C.

Below the ignition temperature at a preheated furnace temperature of 420°C, a small induction period was observed which was shown by the sharp decrease in the temperature profile as the sample reached the furnace temperature. This was followed by a small temperature excursion typical of a non-ignition reaction. A slight mass loss of 0.5% was recorded over a 5 minute period as the violarite slowly oxidised.

As the furnace temperature was increased to the ignition temperature (425°C) a sharp mass loss of approximately 25% was observed (see Figure 4.21). This coincided with a large temperature excursion from the pre-set furnace temperature. The average time lapsed between the introduction of the sample into the pre-heated furnace and the

commencement of the ignition reaction was approximately 15 seconds. This equated to a heating rate of approximately 1700°C min^{-1}. The reaction was completed after approximately 30 seconds. Therefore, the ignition temperature was characterised by a sharp mass loss coinciding with a deviation in the temperature profile above the programmed furnace temperature.

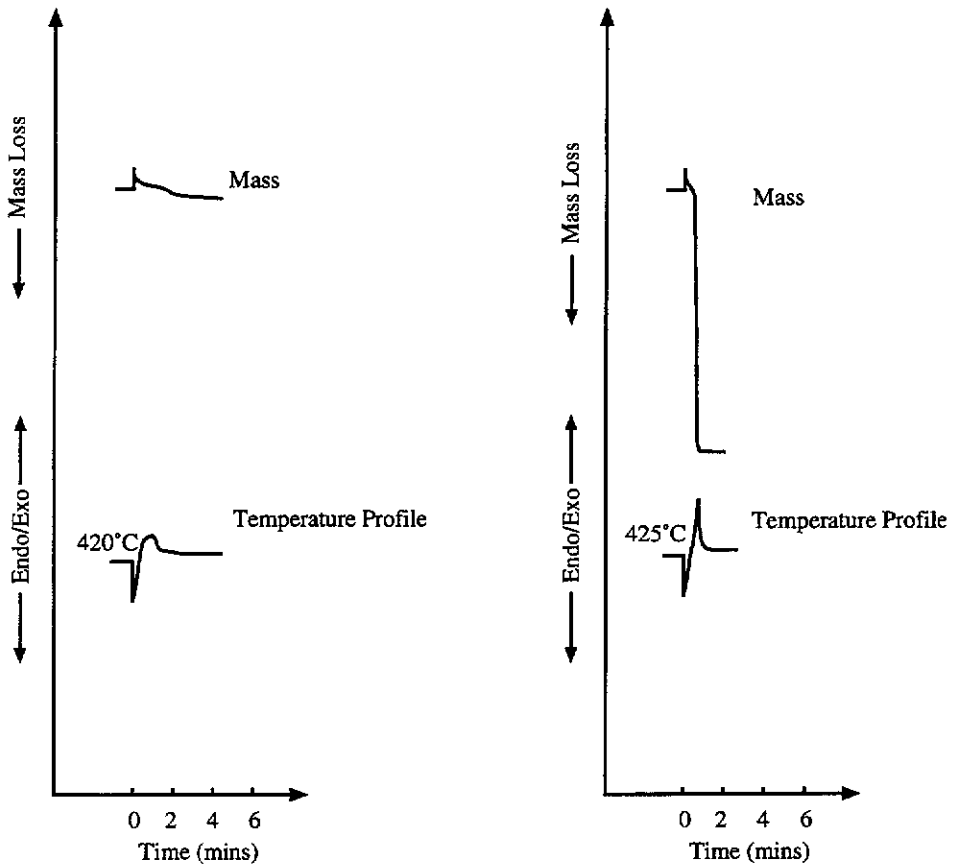

Figure 4.21 Schematic diagram of an isothermal TG trace for $Fe_{0.97}Ni_{1.96}S_4$ (63-45 μm fraction) prior to the ignition temperature (left) and at the ignition temperature (right). Heating rate approximately 1700°C min^{-1}, 5 mg sample in an oxygen atmosphere (25 ml min^{-1}).

4.4.2 Effect of Stoichiometry on the Ignition Temperature of Synthetic Violarite.

Previous studies have shown that mineralogical composition has an effect on the relative reactivity of sulfide concentrates. The relative order of reactivity of the main nickel-bearing sulfides and their associated iron sulfides was initially established by Dunn and Smith (1984). Pyrite and violarite were found to be far more reactive than pentlandite and pyrrhotite. Mackey (1991) established that the relative reactivity increased in the following order:

violarite > pyrite > pyrrhotite > pentlandite

It has been demonstrated that the stoichiometry of the mineral also has an effect on the ignition temperature (Dunn and Chamberlain, 1991). The ignition temperature of synthetic pyrrhotite of particle size 125-90 μm decreased by 210°C as the stoichiometry ranged from FeS to $Fe_{0.83}S$. Violarite forms an extensive solid solution with the iron:nickel ratio varying from $FeNi_2S_4$ to Ni_3S_4. Therefore, it may be expected that the relative reactivity of the sulfide would vary with changes in the stoichiometry.

The ignition temperatures for all four synthetic violarite samples are presented in Table 4.7. The effect of stoichiometry on the ignition temperature of synthetic violarite is illustrated in Figure 4.22.

There is a clear relationship between the iron:nickel ratio of synthetic violarite and the ignition temperature (see Figure 4.22). For example, there was an increase in the ignition temperature from 415°C to 435°C for the endmembers of the violarite solid solution, $Fe_{0.97}Ni_{1.96}S_4$ and $Fe_{0.20}Ni_{2.72}S_4$, for the 63-45 μm particle size fraction. This is a 20°C increase in the ignition temperature as the iron:nickel ratio decreases

from 0.49 to 0.07. However, the effect of stoichiometry on the ignition temperature was not linearly dependent. The ignition temperature showed an increase of 10°C from 415°C to 425°C between $Fe_{0.97}Ni_{1.96}S_4$ and $Fe_{0.46}Ni_{2.49}S_4$, while a similar increase from 425°C to 435°C was observed between $Fe_{0.46}Ni_{2.49}S_4$ and $Fe_{0.20}Ni_{2.72}S_4$. Hence a decrease of 0.31 in the iron:nickel ratio from 0.49 to 0.18 resulted in a 10°C increase in the ignition temperature whereas a similar increase in the ignition temperature was found after only a further decrease of 0.11 in the iron:nickel ratio from 0.18 to 0.07. Therefore, synthetic violarite became increasingly more difficult to ignite as the stoichiometry approached the nickel-rich endmember of the violarite solid solution.

Therefore, the relative order of reactivity using isothermal TG of the synthetic violarite series was established as the following:

$$Fe_{0.97}Ni_{1.96}S_4 > Fe_{0.73}Ni_{2.26}S_4 > Fe_{0.46}Ni_{2.49}S_4 > Fe_{0.20}Ni_{2.72}S_4$$

Increase in reactivity as iron:nickel ratio increases

Sample	Fe:Ni Ratio	Particle Size Fraction (μm)			
		125-90	90-63	63-45	45-20
$Fe_{0.96}Ni_{1.97}S_4$	0.49	440	430	415	400
$Fe_{0.73}Ni_{2.26}S_4$	0.32	445	435	420	405
$Fe_{0.46}Ni_{2.49}S_4$	0.18	455	445	425	410
$Fe_{0.20}Ni_{2.72}S_4$	0.07	465	455	435	415
Difference (°C)		25	25	20	15

Table 4.7 Ignition temperatures (°C) for each synthetic violarite sample for a range of particle size fractions as measured using isothermal gravimetric analysis.

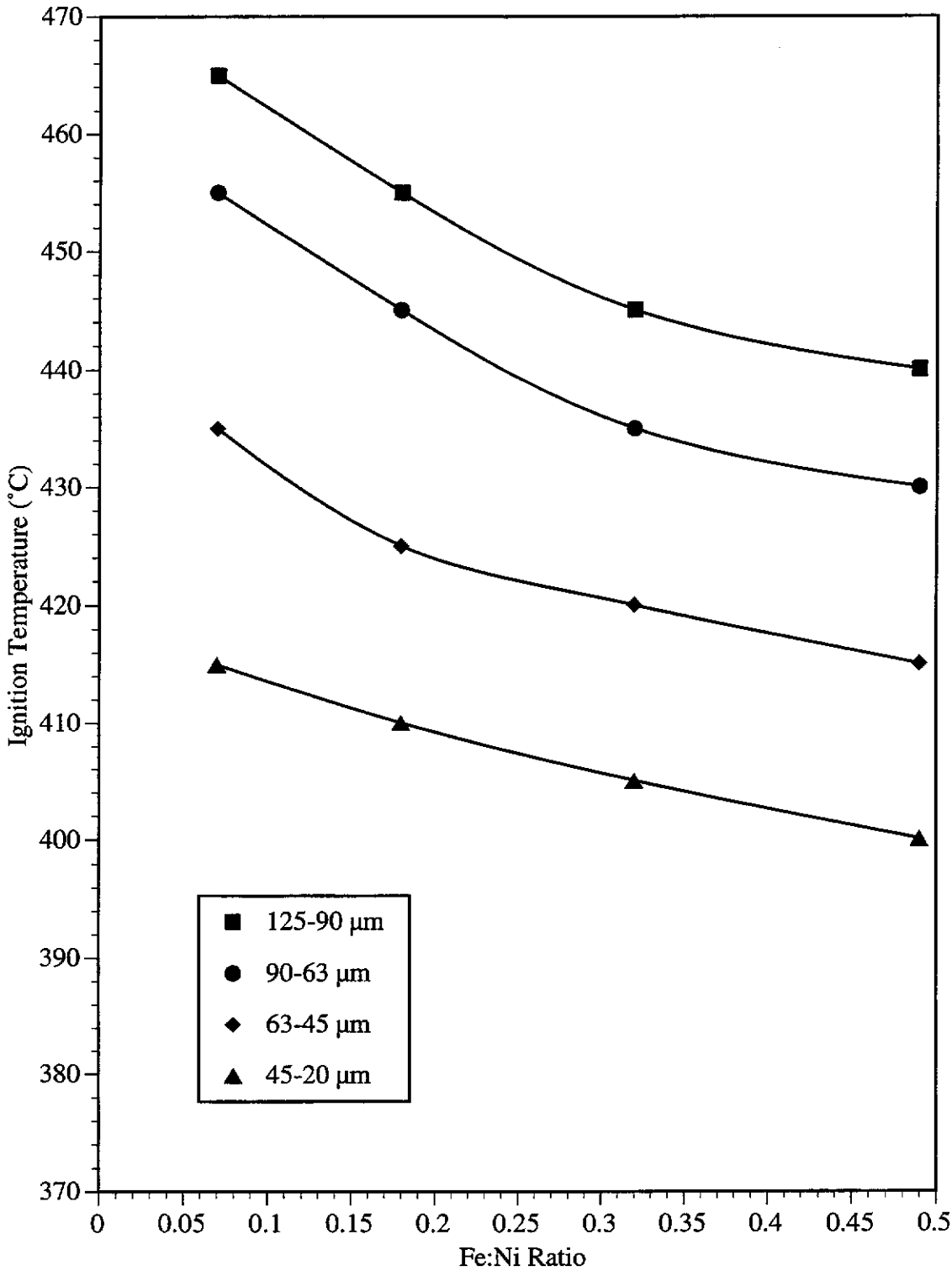

Figure 4.22 The effect of Fe:Ni ratio on the ignition temperature of synthetic violarite for a range of particle sizes.

The ignition behaviour of naturally occurring samples of violarite from the Leinster and Kambalda regions of Western Australia, using isothermal TG, has been reported by Dunn and Smith (1984) and Mackey (1991). An ignition temperature of 395-400°C was reported by Dunn and Smith (1984) for a violarite concentrate with no stated stoichiometry and a particle size range of 75-45 μm. A slightly higher value of 430-435°C was obtained by Mackey (1991) for a violarite-pyrite concentrate, with reported stoichiometries of $Fe_{1.05}Ni_{2.00}S_4$ for violarite and $Fe_{0.99}S_2$ for pyrite, for the same particle size fraction. The ignition temperature of ideal violarite with a particle size range of 63-45 μm, i.e. 415-420°C, falls between the two reported values. As the equipment used in each of the studies was identical, the discrepancies can only be attributed to the mineralogical composition and the physical properties of the samples.

The mineralogical composition of the concentrate was the main cause of the discrepancies in the ignition temperature. The violarite concentrate studied by Dunn and Smith (1984) was approximately 75% pure, with the majority of the remaining sulfide material consisting of pentlandite (12%). The violarite-pyrite concentrate studied by Mackey (1991) comprised of 82-87% sulfide, with equal proportions of violarite and pyrite, and the remainder being made up of silicates and carbonates. Both pentlandite and pyrite would increase the ignition temperature of the violarite, however pentlandite would have a far greater effect than pyrite, according to their relative order of reactivity. Other contaminantes, such as silicates, would tend to decrease the relative reactivity of the violarite concentrate.

Physical properties, such as surface area and the presence of fines adhering to larger particles as a result of inefficient sieving techniques, will influence the relative reactivities. Since wet sieving was not performed by Dunn and Smith (1984), a lower ignition temperature may have been expected due to the presence of fines.

The surface area of the violarite-pyrite concentrate studied by Mackey (1991) was 0.6 m^2g^{-1}. This was significantly higher than the value obtained for synthetic violarite (average 0.1 m^2g^{-1}). Micrographs of the initial starting materials showed the synthetic violarite was less porous than natural violarite which had undergone supergene enrichment. The morphology of synthetic violarite is similar to hypogene forms of violarite. Therefore, ignition temperatures for natural samples may be slightly lower than those of their synthetic equivalents.

4.4.3 Effect of Particle Size on the Ignition Temperature of Synthetic Violarite.

The effect of particle size on the ignition temperature has been well established. As the particle size decreases the ignition temperature decreases. Some minerals are more susceptible to particle size effect than others, with the decreasing order of susceptibility established as (Dunn and Smith, 1984; Dunn, Davies and Mackey, 1989):

pentlandite > pyrrhotite > violarite > pyrite

The effect of particle size on the ignition temperature was investigated using all four violarite samples. Four particle size fractions were examined, 125-90, 90-63, 63-45 and 45-20 μm. The effect of particle size on the ignition temperature of synthetic violarite is presented in Table 4.8. The difference in the ignition temperature between the 125-90 μm and the 45-20 μm particle size fraction for each violarite is shown in the end column of Table 4.8.

Figure 4.23 illustrates the effect of particle size on the ignition temperature. The violarite samples showed a decrease in ignition temperature as the particle size decreased. For example, the ignition temperature of ideal violarite ($Fe_{0.97}Ni_{1.96}S_4$) decreased from 440°C to 400°C between the coarsest and finest particle size fractions.

The iron:nickel ratio also influenced the effect of particle size on the ignition temperature (Figure 4.23). For example, the ignition temperature of $Fe_{0.20}Ni_{2.72}S_4$ (nickel-rich violarite) decreased by 50°C compared with 40°C for $Fe_{0.97}Ni_{1.96}S_4$ (ideal violarite). Therefore, the effect of particle size increased as the stoichiometry of the violarite tended towards the nickel-rich end of the violarite solid solution. This was evident from the plot of ignition temperature against the geometric mean particle size of the synthetic violarite. As the particle size decreases the ignition temperature curves converge.

Hence, the effect of particle size on ignition behaviour of synthetic violarite decreased in the following order:

$$Fe_{0.20}Ni_{2.72}S_4 > Fe_{0.46}Ni_{2.49}S_4 > Fe_{0.73}Ni_{2.26}S_4 = Fe_{0.97}Ni_{1.96}S_4$$

The difference in the ignition temperatures between ideal and nickel-rich violarite is 25°C for the 125-90 μm particle size fraction and 15°C for the 45-20 μm fraction. Hence, the effect of stoichiometry can be minimised by a reduction in particle size.

Sample (μm)	Iron:Nickel Ratio	Geometric Mean Size (μm)				Difference (°C)
		106	75	53	30	
$Fe_{0.97}Ni_{1.96}S_4$	106	440	430	415	400	40
$Fe_{0.73}Ni_{2.26}S_4$	75	445	435	420	405	40
$Fe_{0.46}Ni_{2.49}S_4$	53	455	445	425	410	45
$Fe_{0.20}Ni_{2.72}S_4$	30	465	455	435	415	50

Table 4.8 The effect of particle size on the ignition temperature of synthetic violarite.

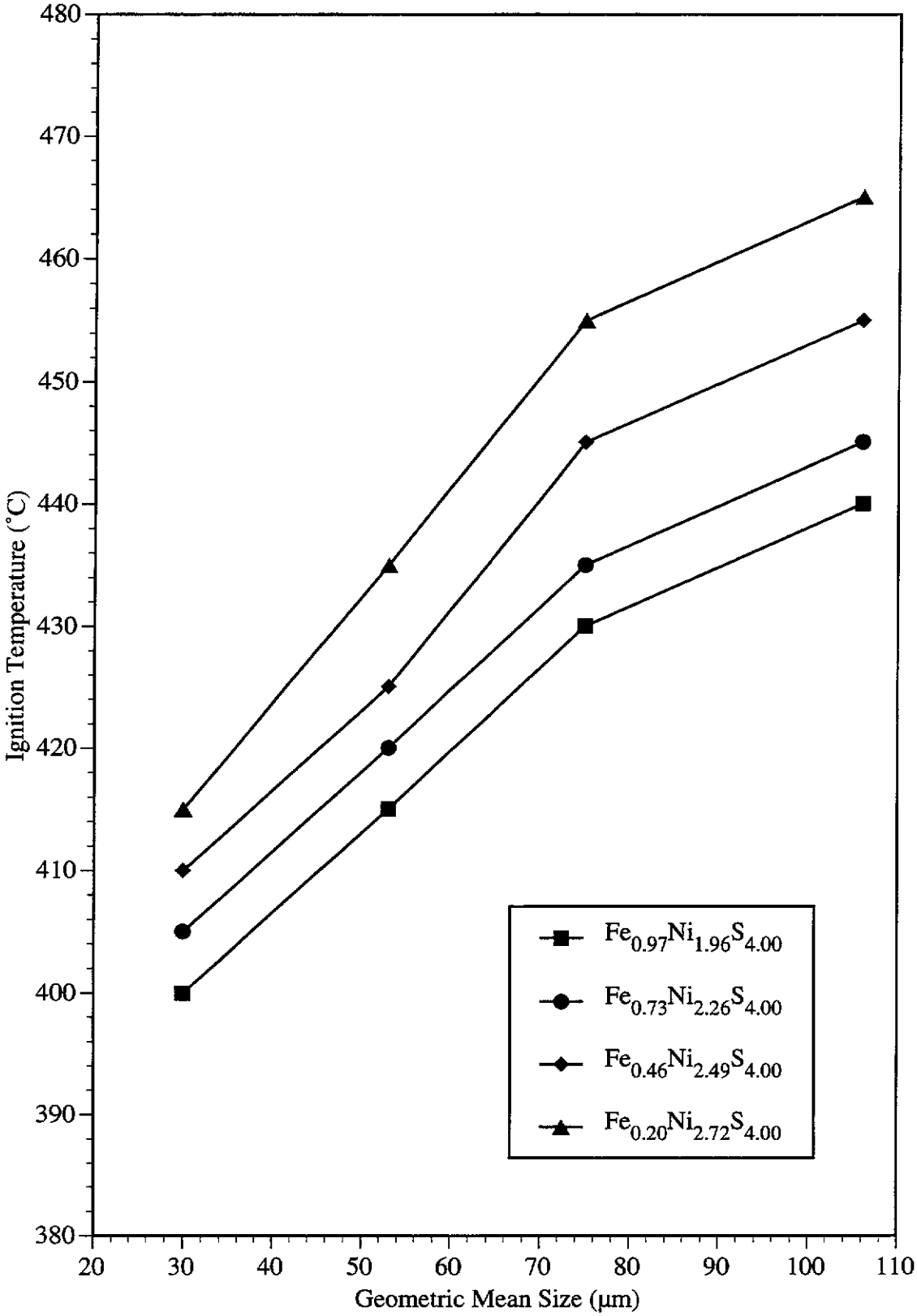

Figure 4.23 Effect of particle size on the ignition temperature for the series of synthetic violarite samples.

Table 4.9 presents the ignition temperatures from previous studies on natural violarite samples and those from the current study for ideal violarite over a range of particle size fractions. The effect of particle size on the ignition temperatures of ideal violarite was comparable with that established by Dunn and Smith (1984) and Mackey (1991).

Dunn and Smith (1984)		Mackey (1991)		Present Study	
Particle Size (μm)	Ignition Temp. (°C)	Particle Size (μm)	Ignition Temp. (°C)	Particle Size (μm)	Ignition Temp. (°C)
125-89	430-435	125-90	490-495	125-90	440-445
89-75	410-415	90-75	480-495	90-63	430-435
75-45	395-400	75-45	430-435	63-45	415-420
-45	380-385	45-20	410-415	45-20	400-405

Table 4.9 Ignition temperatures of violarite concentrates and synthetic violarite ($Fe_{0.97}Ni_{1.96}S_4$) using isothermal TG.

4.5 Determination of the Extent of Oxidation by Isothermal TG.

The extent of oxidation of synthetic violarite was determined by the isothermal TG technique (Dunn, Davies and Mackey, 1989). The temperature of the furnace was increased by 50°C increments, and each sample analysed in triplicate. The maximum mass loss corresponding to complete oxidation was observed at 900°C. Therefore, the extent of oxidation at any particular furnace temperature (T_1) was directly proportional to the mass loss observed at 900°C.

$$\frac{\text{Mass loss at } T_1}{\text{Mass loss at } 900^\circ C} \times 100\% = \text{percentage extent of oxidation}$$

The extent of oxidation will establish the manner in which synthetic violarite behaves with an increase in temperature under shock heating conditions.

The TG profiles for ideal violarite at the ignition temperature, 425°C, and maximum furnace temperature, 900°C, are illustrated in Figure 4.24. As the furnace temperature was increased above the ignition temperature the TG profile remained unchanged, with the extent of oxidation and temperature excursion associated with the rapid mass loss increasing slightly (Figure 4.24). Between 650-750°C the extent of oxidation remained constant with no increase in the mass loss. Above 750°C the mass loss occurred in two discrete stages (Figure 4.24). The first stage was due to the initial ignition reaction corresponding to the decomposition and preferential oxidation of iron sulfide. This was followed by a short period of no mass loss. After this a second gradual mass loss was observed over an extended period of time. This was due to the oxidation of the remaining nickel sulfide.

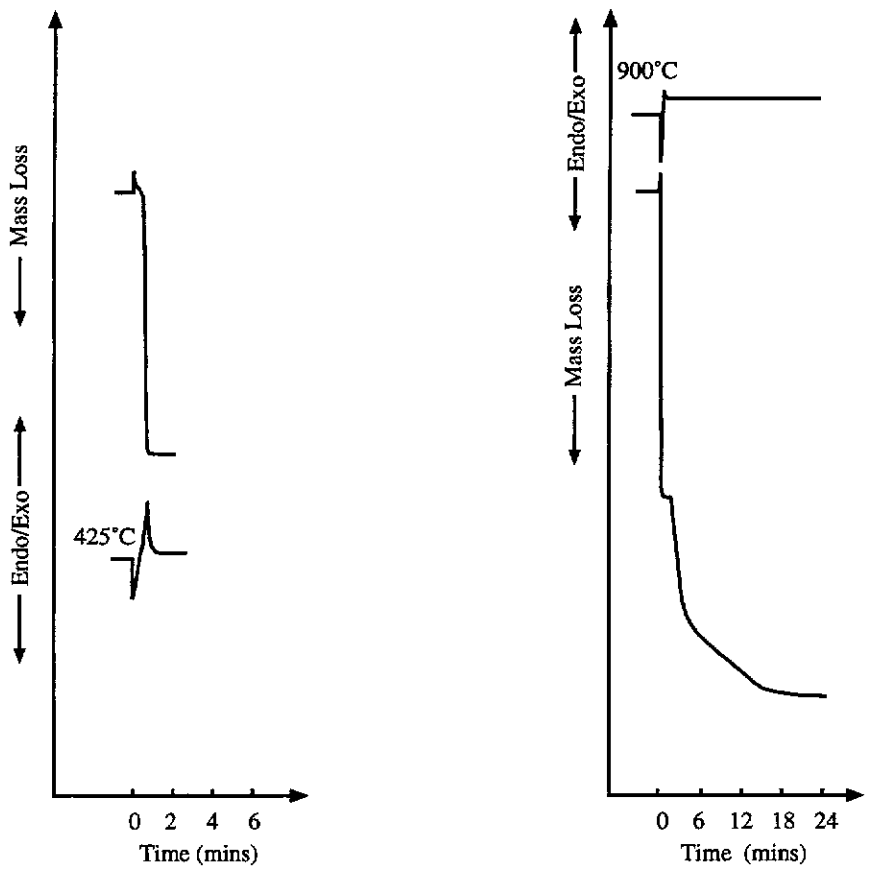

Figure 4.24 Typical isothermal TG trace for $Fe_{0.97}Ni_{1.96}S_4$ (63-45 μm fraction) at 425°C and 900°C. Note the different time scales for each plot. At the ignition temperature (left) the TG profile shows a rapid mass loss typical of an ignition reaction, while at 900°C (right) a two-stage mass loss is observed with the second loss occurring over an extended time period.

Table 4.10 shows the extent of oxidation for all four violarite samples with a particle size of 63-45 μm. Figure 4.25 shows the effect of stoichiometry on the extent of oxidation. The extent of oxidation prior to the ignition temperature was minimal for all four violarite samples. A rapid increase in the extent of oxidation was observed at the ignition temperatures of the respective violarite samples. Ideal violarite ($Fe_{0.97}Ni_{1.96}S_4$) underwent a 7.95% mass loss at its ignition temperature. A total mass loss of 24.8% was observed at 900°C. This mass loss corresponded to 100% extent of oxidation. The observed mass loss agrees with the theoretical mass loss of 24.81% that would be observed if violarite was fully oxidised to hematite (Fe_2O_3) and nickel oxide (NiO). Therefore, ideal violarite had oxidised only 32% at its ignition temperature.

Temperature (°C)	Extent of Oxidation			
	$Fe_{0.97}Ni_{1.96}S_4$	$Fe_{0.73}Ni_{2.26}S_4$	$Fe_{0.46}Ni_{2.49}S_4$	$Fe_{0.20}Ni_{2.72}S_4$
350	0	0	0	0.1
400	1.5	0	0	8.8
450	40.9	46.3	16.9	15.0
500	48.3	51.8	41.5	42.0
550	57.9	63.4	57.2	45.0
600	67.8	73.2	65.9	58.6
650	76.5	75.7	66.2	68.8
700	79.4	73.9	66.5	67.1
750	87.0	77.6	69.5	67.6
800	97.9	99.2	90.4	99.4
900	100.0	100.0	100.0	100.0

Table 4.10 Extent of oxidation for each synthetic violarite with a particle size fraction of 63-45 μm.

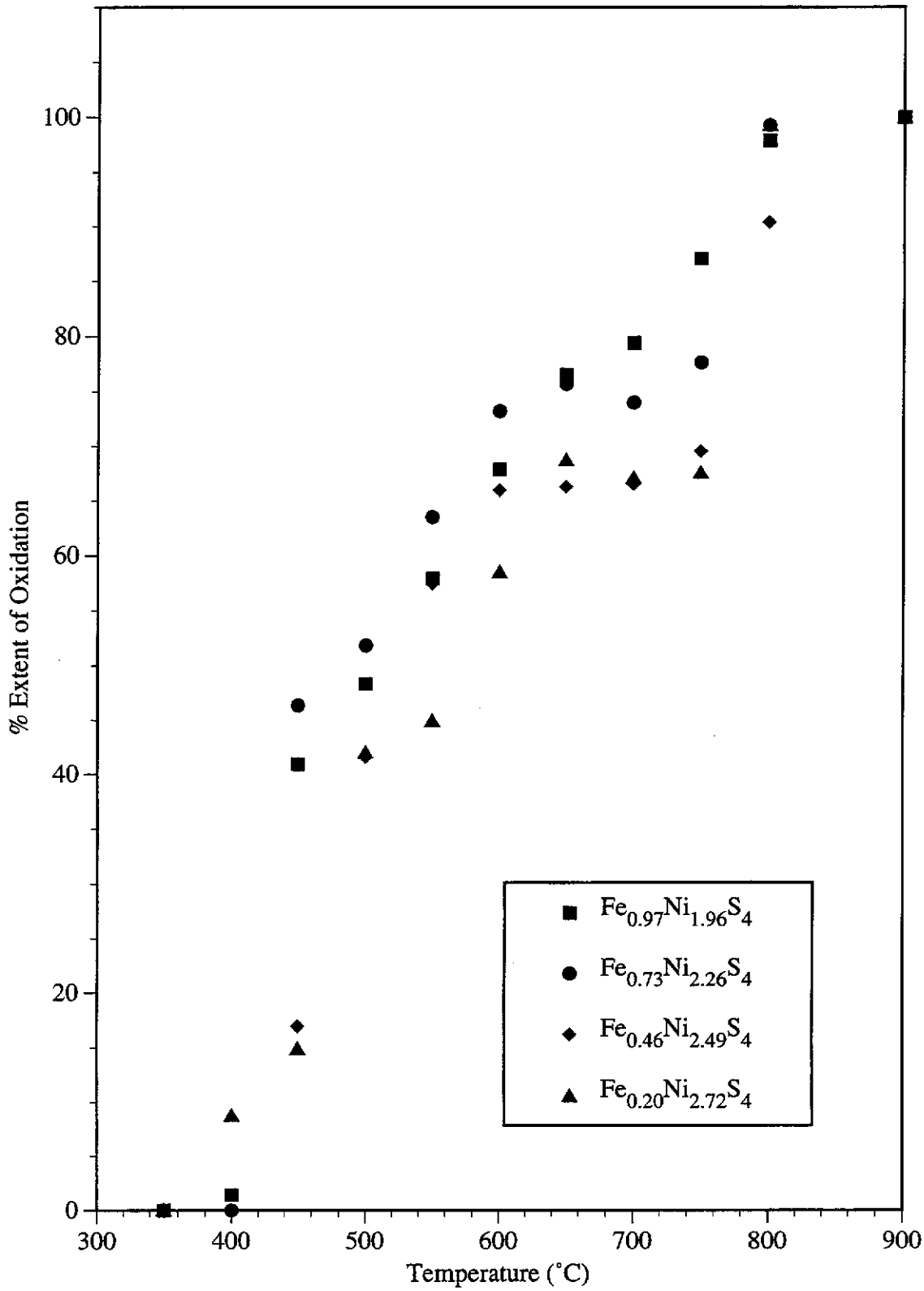

Figure 4.25 The effect of stoichiometry on the extent of oxidation using isothermal TG for the 63-45 μm particle size fraction.

The two iron-rich violarite samples, $Fe_{0.97}Ni_{1.96}S_4$ and $Fe_{0.73}Ni_{2.26}S_4$, had undergone a greater extent of oxidation than the nickel-rich samples between the temperature range 400-650°C. For example, at 500°C $Fe_{0.97}Ni_{1.96}S_4$ (ideal violarite) had oxidised 48% while $Fe_{0.20}Ni_{2.72}S_4$ (nickel-rich violarite) had only oxidised 42%. The extent and rate of oxidation decreased as the iron:nickel ratio decreased between 650°C and 750°C. For example, the ideal violarite sample showed an increase in the extent of oxidation from 76% to 87% over the temperature range 650-750°C, while the extent of oxidation for the nickel-rich endmember remained relatively constant at 68% over the same temperature range. As the temperature of the furnace was increased above 750°C, the extent of oxidation increased with all four violarite samples approaching 100% oxidation by 800°C.

Hence, the stoichiometry of the violarite has an effect on the extent of oxidation in the middle temperature range of 400°C to 750°C, with the extent of oxidation increasing with an increase in the iron:nickel ratio of the sulfide. The effect of stoichiometry became less significant as the temperature was increased above 750°C.

Tables 4.10 and 4.11 give the extent of reaction for the two endmembers of the violarite series for the particle size ranges of 125-90, 90-63, 63-45, and 45-20 μm. The results indicate a greater particle size effect in the lower temperature range. Ideal violarite ($Fe_{0.97}Ni_{1.96}S_4$) had only undergone 8% oxidation at 450°C for the 125-90 μm particle size fraction compared with 40% for the 45-20 μm fraction. By 500°C, the extent of oxidation for the two respective particle size fractions were 53% and 52%. For the nickel-rich violarite sample at 500°C, the 125-90 μm fraction had oxidised by 14% compared with 41% oxidation for the 45-20 μm particle size fraction. By 600°C the extent of oxidation had increased significantly, with the coarser particle size fraction showing an increase from 14% to 64% extent of oxidation representing an increase of 50%, compared with only a 19% increase in the extent of oxidation from 41% to 60% for the 45-20 μm fraction. Hence, a 100°C increase in the furnace

temperature significantly decreased the effect of particle size on the extent of oxidation. The extent of oxidation remained relatively constant between each particle size fraction as the temperature was increased up to 900°C.

Figure 4.26 shows a plot of the results presented in Tables 4.10 and 4.11 for the finest and coarsest particle size fractions. Figure 4.26 clearly shows the effect of stoichiometry on the extent of oxidation. The 125-90 μm particle size fraction for ideal violarite had oxidised 82% by 650°C, while the nickel-rich violarite sample had undergone only 66% oxidation at the same temperature. As the temperature increased above 740°C, the effect of stoichiometry decreased as the extent of oxidation approached 100%.

Therefore, the effect of particle size on the extent of oxidation is significant in the lower temperature range of 350°C to 450°C, while the effect of stoichiometry tends to be more important in the mid temperature range of 400°C to 750°C. Above 750°C, particle size and stoichiometry have a limited effect on the extent of oxidation.

Temperature (°C)	Particle Size Fraction (μm)			
	125-90	90-63	63-45	45-20
350	0	0	0	0
400	0	0	1.4	0
450	7.6	5.8	29.7	39.8
500	53.0	43.6	48.3	52.4
550	68.4	57.0	57.9	64.5
600	75.1	71.0	67.8	74.2
650	81.9	77.5	76.5	78.0
700	78.2	82.7	79.4	78.2
750	86.6	87.7	87.0	80.1
800	100.0	98.7	97.8	98.0
900	100.0	100.0	100.0	100.0

Table 4.11 Extent of oxidation of $Fe_{0.97}Ni_{1.96}S_4$ (ideal violarite) for each particle size fraction.

Temperature (°C)	Particle Size Fraction (μm)			
	125-90	90-63	63-45	45-20
350	0	0	0.1	0
400	10.3	10.8	8.8	5.8
450	13.0	18.7	15.0	21.3
500	13.9	36.3	42.0	40.9
550	31.5	37.1	45.0	48.2
600	64.0	50.9	58.6	59.6
650	65.7	63.7	68.8	65.7
700	62.9	64.5	67.1	63.3
750	68.2	65.6	67.6	66.3
800	97.8	97.6	99.4	96.0
900	100.0	100.0	100.0	100.0

Table 4.12 Extent of oxidation of $Fe_{0.20}Ni_{2.72}S_4$ (nickel-rich violarite) for each particle size fraction.

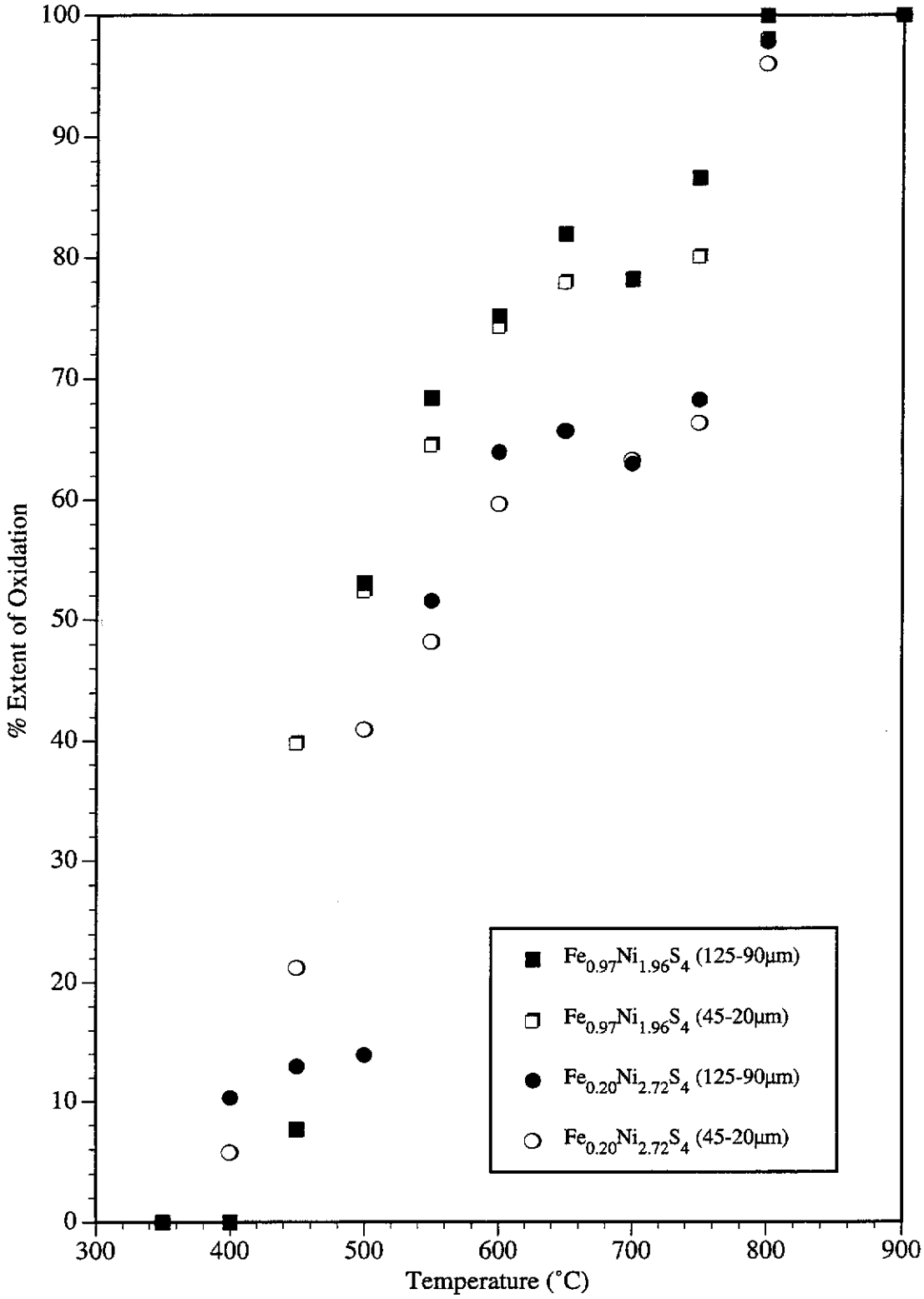

Figure 4.26. Extent of oxidation of $Fe_{0.97}Ni_{1.96}S_4$ and $Fe_{0.20}Ni_{2.72}S_4$, the endmembers of the violarite solid solution. The graph shows a comparison between the two extreme particle size fractions for both violarite samples.

4.6 Ignition Mechanism of Synthetic Violarite

In order to establish the ignition mechanism, partially oxidised and ignited products from isothermal TG experiments were examined. Due to the furnace design, the samples were able to be rapidly quenched from the ignition temperature to room temperature in a matter of seconds. Samples were collected at 5-10°C prior to the ignition temperature and then at 50°C intervals beyond the ignition temperature up to 900°C. Both polished sections and individual grains were mounted for optical and SEM examination. Mineralogical examination of the ignition products was performed using XRD and EPMA.

Examination of both ideal and nickel-rich violarite prior to the ignition temperature showed only a minor amount of oxidation. The particle morphology and composition were similar to those observed for ideal and nickel-rich violarite heated under non-ignition conditions (section 4.2), with a mss and sulfate-oxide layer formed around an unreacted violarite core. Approximately 10 particles from a partially oxidised sample of ideal violarite collected at 420°C were analysed by EPMA. The average composition of the mss and violarite phases was $Fe_{0.35}Ni_{0.58}S_{1.00}$ and $Fe_{1.17}Ni_{1.97}S_{4.00}$ respectively. This was consistent with the composition for ideal violarite quenched at a similar temperature when heated at 10°C min^{-1} in air. SEM micrographs of the ideal violarite sample showed small cracks evident on the surface of the violarite particles. The particle morphology was probably due to thermal shock as the sample was introduced into the furnace.

As the furnace temperature was increased to the ignition temperature, the morphology of the synthetic violarite underwent a dramatic change. Figure 4.27a shows a BSE micrograph of ideal violarite collected at 425°C for the 63-45 μm particle size fraction. The majority of the violarite particles exhibited a porous structure with hematite evident within the particle pores. The degree of porosity varied from particle to particle with

the pores penetrating non-uniformly through the mss core. XRD revealed mss and hematite as the major phases present, with a minor amount of NiO also present in the ignition product. No violarite or vaesite was evident in the XRD pattern. There was a large variation in the composition of the mss phase. EPMA results provided strong evidence of preferential migration and oxidation of iron. Analysis of approximately 10 particles of ideal violarite showed the mss stoichiometry ranged from $Fe_{0.32}Ni_{0.67}S_{1.00}$ to $Fe_{0.16}Ni_{0.83}S_{1.00}$ with the iron:nickel ratio decreasing between the sulfide core and outer edge of the violarite particle.

Figure 4.27a shows a secondary electron micrograph of a number of unsectioned particles collected at the ignition temperature. The surfaces of the particles show a random network of pores likely to have formed as sulfur was evolved from the particle surface as violarite pyrolytically decomposed to mss.

There were also a number of particles which had exceeded the melting point transition of heazlewoodite (795°C). This was caused by localised heating due to the rapid oxidation of sulfur vapour. SE and optical micrographs show partial melting of the violarite particles (Figure 4.27b). The particles are hollow spheres which resemble cenospheres. A number of particles had fused together forming a molten mass. The BSE micrograph of the polished section showed two distinctive phases present. EPMA revealed the bright phase to be heazlewoodite with average composition of $(Fe_{0.31}Ni_{2.79})S_2$. The second darker phase was probably an oxide phase. This appeared darker when compared with the heazlewoodite phase due to a lower average atomic number. No accurate analysis of this phase was obtained due to fine grain size, but EPMA results suggested that it was trevorite.

The porosity of the violarite ignition product resembled that of synthetic violarite which had undergone complete pyrolytic decomposition to mss when heated at 40°C min^{-1} in a nitrogen atmosphere. During the pyrolytic decomposition of ideal violarite to mss, a rapid mass loss was observed in the temperature range 450-650°C and was associated with a broad endotherm between 595°C and 700°C. Large macropores were formed during the rapid loss of sulfur. The porous structure formed during the pyrolytic decomposition of vaesite was not as fine as that observed for the ignition product. However, this was likely due to the loss of sulfur from the sulfide particle being more rapid. Even though the furnace temperature was only 425°C, the formation of heazlewoodite and melting indicated that the particle temperature far exceeded the pre-set furnace temperature. Therefore, the particle morphology suggests that the violarite underwent pyrolytic decomposition to mss and vaesite, followed by decomposition of the vaesite with the rapid evolution of sulfur to form a porous mss particle.

The morphology of the nickel-rich violarite at its ignition temperature was similar to that observed under pyrolytic conditions, with larger macropores distributed throughout the mss core. Hematite was clearly visible within the macropores.

Particles collected above the ignition temperature showed a slight increase in the porosity. As the temperature approached the melting point of heazlewoodite (750-800°C) large molten masses of heazlewoodite were found (Figure 4.27c). Some cenosphere formation was also evident in a number of particles. Once the temperature exceeded the melting point transition of heazlewoodite the remaining nickel sulfide was oxidised to completion.

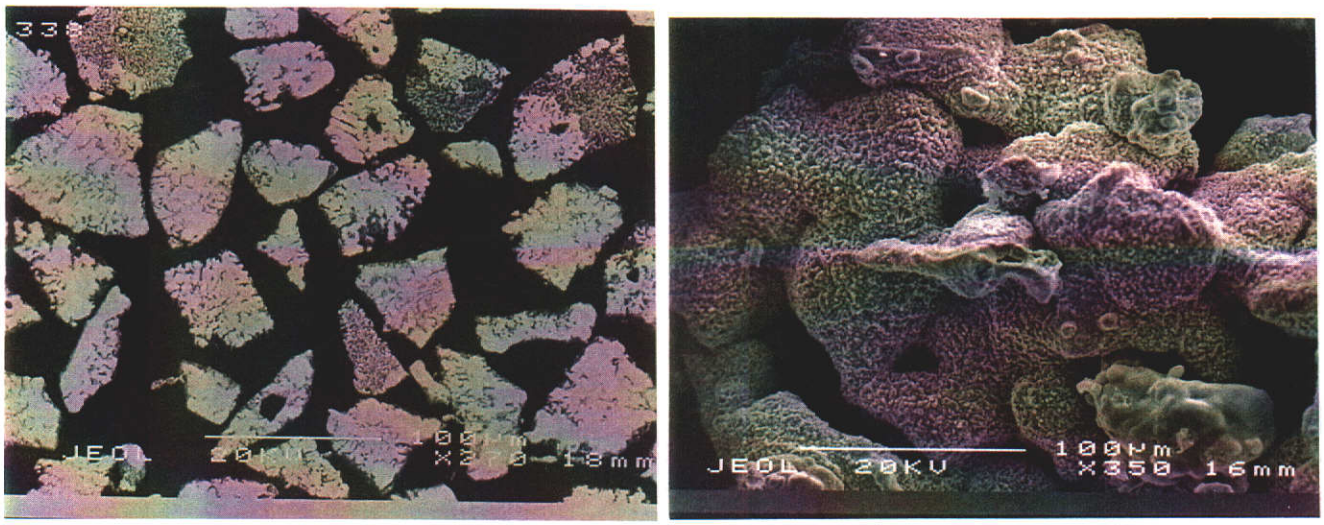

Figure 4.27a BSE (left) and SE (right) micrographs of ideal violarite, 63-45 µm particle size fraction, at the ignition temperature (425°C).

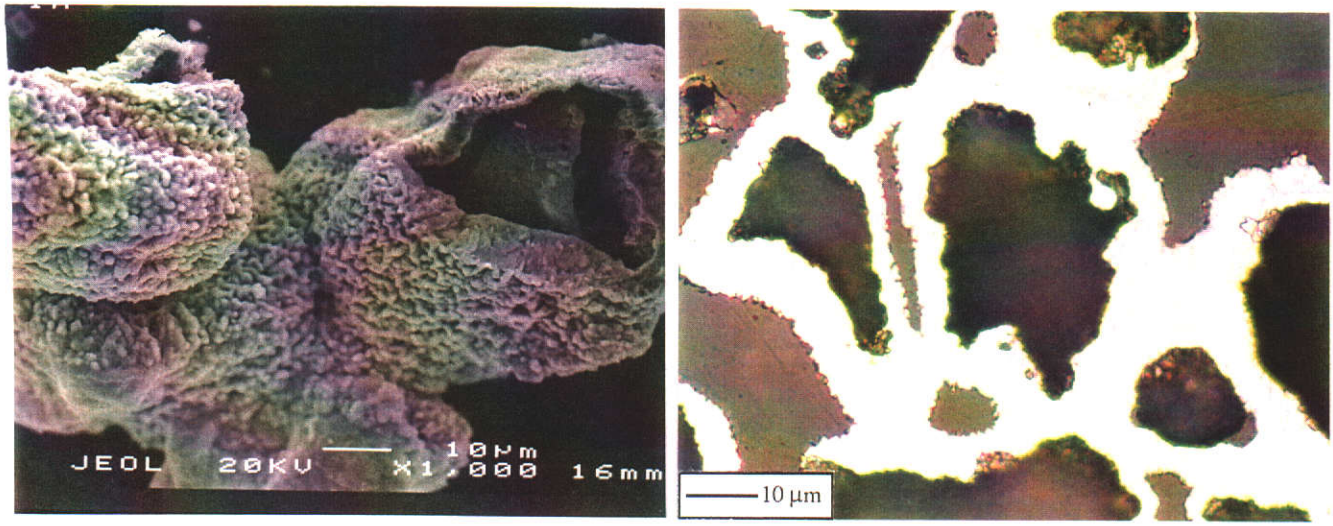

Figure 4.27b SE (left) and optical (right) micrographs showing molten spheres of heazlewoodite collected at 450°C.

A similar particle morphology was reported by Mackey (1991) at the ignition temperature of violarite. Mackey (1991) proposed that the ignition mechanism for violarite proceeded via decomposition of violarite at 460°C with the evolution of sulfur vapour generating a porous product. The increase in porosity allowed ready access of oxygen resulting in the preferential oxidation of iron.

Pyrite also has the ability to liberate sulfur during oxidation forming a porous product (Dunn and Mackey, 1991; Nguyen, 1990; Dunn, De and O'Connor, 1989a & 1989b; Jorgensen and Moyle, 1984; Jorgensen and Moyle, 1982; Thornhill and Pidgeon, 1957). For example, Thornhill and Pidgeon (1957) found that once a certain roasting temperature was reached the sulfur vapour pressure was of sufficient magnitude to cause the particle temperature to exceed the furnace temperature and for the reaction to become self driven. Jorgensen and Moyle (1982) reported that the decomposition of pyrite to pyrrhotite, with the liberation of sulfur vapour, occurred above 550°C when

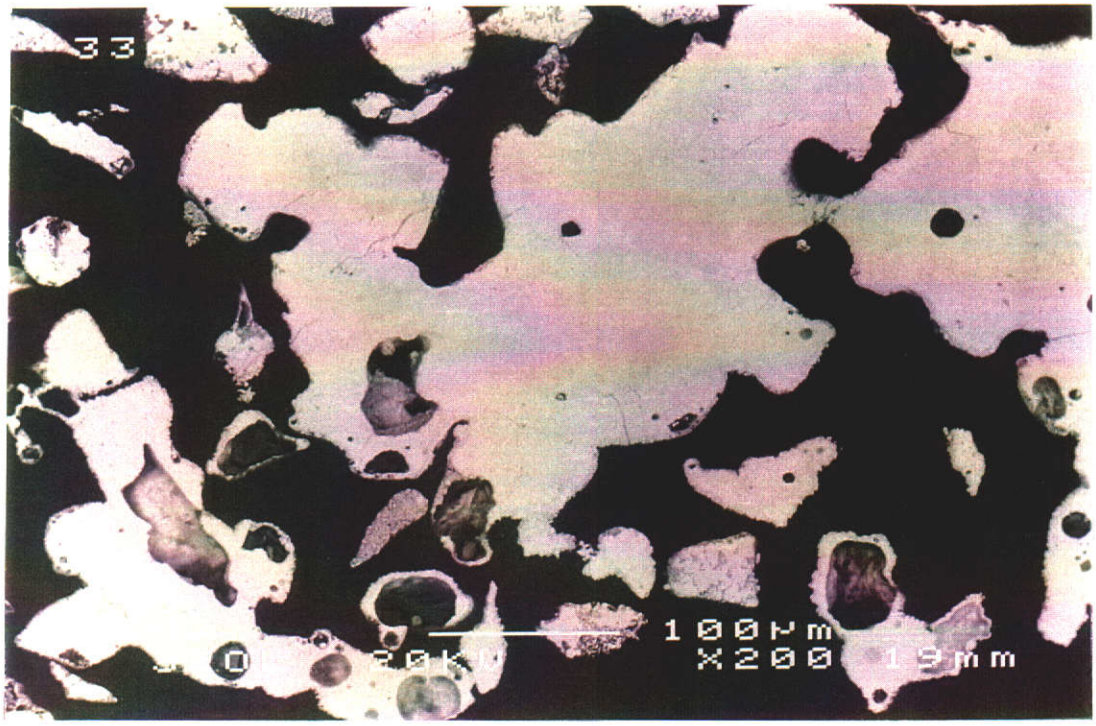

Figure 4.27c BSE micrograph of ideal violarite collected at 750°C.

the sample was heated at 10°C min^{-1} in an air atmosphere. The formation of a porous pyrrhotite structure was attributed to a 20% volume reduction when compared with pyrite. Nguyen (1990) found that when roasting pyrite below 500°C, the pyrite particles consisted of concentric layers of hematite typical of a "Shrinking Core" model. When the roasting temperature was increased from 500°C to 550°C the morphology of the pyrite particles dramatically changed. A porous network described as "radial" developed throughout the oxide particles. Nguyen (1990) concluded that the reaction mechanism involved the complete decomposition of pyrite to pyrrhotite prior to the oxidation of the newly formed porous pyrrhotite. The diffusion of oxygen was prohibited due to the positive pressure of sulfur evolved from the particle.

The following reaction mechanism is proposed for the ignition of synthetic violarite:

(i) Pyrolytic decomposition of violarite to mss.

Above a critical temperature, pyrolytic decomposition of violarite to mss and vaesite occurs. The decomposition of vaesite results in the rapid evolution of sulfur from the violarite particle. The vapour pressure of the evolved sulfur inhibits the diffusion of oxygen through the pores. The sulfur rapidly oxidises at the particle surface causing the temperature of the particle to rapidly escalate. The porous product is partly due to the rapid evolution of sulfur from the particle, however, a volume reduction also occurs as violarite decomposes to mss. With the loss of one mole of sulfur and the iron:nickel ratio remaining constant, a 14% reduction in volume would be anticipated.

(ii) Preferential oxidation of iron sulfide.

During the ignition of violarite, iron migrates to the particle pores and outer rim where it is preferentially oxidised leaving a nickel-rich mss core. The preferential oxidation

appears to occur once the partial pressure of the evolved sulfur gas decreases sufficiently to allow the diffusion of oxygen through the porous structure.

(iii) Oxidation of remaining sulfide core.

The extent of oxidation of the remaining nickel sulfide increases as the temperature increases. The reaction is limited by the gaseous diffusion of oxygen through the surrounding oxide layer. The reaction goes to completion when the particle temperature exceeds the melting point transition of $(Fe,Ni)_{3\pm x}S_2$. Consequently, the nickel sulfide species does not ignite but rather oxidises at an elevated temperature. This accounts for the temperature dependence of the extent of oxidation of violarite once the iron and sulfur has been preferentially oxidised.

The energy emanating from steps (i) and (ii) is insufficient to cause the reaction in step (iii) to go to completion in the TG equipment at the ignition temperature. Therefore steps (i) and (ii) describe the ignition mechanism of synthetic violarite under isothermal conditions and an oxygen atmosphere.

CHAPTER 5

THE PYROLYTIC DECOMPOSITION AND OXIDATION OF SYNTHETIC PENTLANDITE

5.0 INTRODUCTION.

In this Chapter the results of TG-DTA studies of the thermal decomposition in argon, and oxidation in air and oxygen, of synthetic pentlandite are reported. A range of pentlandites with varying iron:nickel ratios were prepared, and the two endmembers, $Fe_{5.80}Ni_{3.15}S_8$ and $Fe_{3.40}Ni_{5.55}S_8$, were examined in detail under argon and air to determine the effect of changes in the iron:nickel ratio on their reaction sequence. $Fe_{5.80}Ni_{3.15}S_8$ and $Fe_{3.40}Ni_{5.55}S_8$ will be referred to as "iron-rich" and "nickel-rich pentlandite" respectively. The effect of the metal:sulfur ratio was also examined. Two sulfur-rich pentlandites were synthesized with stoichiometries of $Fe_{4.20}Ni_{4.16}S_8$ and $Fe_{4.22}Ni_{4.15}S_8$. Both of these samples showed identical behaviour. Therefore, $Fe_{4.20}Ni_{4.16}S_8$ will only be discussed in detail and will be referred to as "sulfur-rich pentlandite".

The ignition behaviour for the entire range of synthetic pentlandites was established using isothermal TG to determine the effect of changes in the iron:nickel ratio and metal:sulfur ratio on the ignition temperature, and hence their relative reactivity.

5.1 Pyrolytic Decomposition of Synthetic Pentlandite.

The thermal stability of pentlandite has been extensively studied, by heating stoichiometric quantities of the elements in evacuated silica tubes until equilibrium has been achieved. The tubes are then quenched, and the products identified (Newhouse, 1927; Kullerud, 1962; Shewman and Clark, 1970; Misra and Fleet, 1973). Newhouse (1927) reported that pentlandite incongruently dissociated to form pyrrhotite and a nickel sulfide similar to heazlewoodite, Ni_3S_2. Kullerud (1962) investigated the thermal stability of pentlandite using a range of techniques including quenching experiments, DTA and high-temperature XRD on synthetic pentlandite sealed in silica reaction tubes. Synthetic pentlandite, with an ideal composition of

$Fe_{4.5}Ni_{4.5}S_8$, was found to thermally decompose at 610±2°C forming mss and $(Fe,Ni)_{3\pm x}S_2$ (Kullerud, 1962). The limits of the pentlandite stability field were extensively studied by Shewman and Clark (1970) and Misra and Fleet (1973). The stability of the pentlandite solid solution is illustrated by a series of Fe-Ni-S ternary phase diagrams shown in Figure 5.1. As the temperature decreases below 610°C the stability field expands either side of $Fe_{4.5}Ni_{4.5}S_8$ with the composition ranging from $Fe_{4.93}Ni_{4.18}S_8$ to $Fe_{3.60}Ni_{5.44}S_8$ at 600°C. The pentlandite solid solution also exhibits a variation in the metal:sulfur ratio with the pentlandite composition ranging from $Fe_{4.5}Ni_{4.5}S_{7.74}$ to $Fe_{4.5}Ni_{4.5}S_{8.54}$. As the temperature decreases the pentlandite solid solution increases further ranging from $Fe_{5.83}Ni_{3.32}S_8$ to $Fe_{2.57}Ni_{6.43}S_8$, while the range in the metal:sulfur ratio decreases with the range extending from $Fe_{4.5}Ni_{4.5}S_{7.88}$ to $Fe_{4.5}Ni_{4.5}S_{8.25}$ at 500°C. Between 500°C and 400°C the iron-rich end of the solid solution continues to expand while the nickel-rich end contracts with the stability field ranging from $Fe_{6.09}Ni_{3.08}S_8$ to $Fe_{3.57}Ni_{5.48}S_8$ at 400°C. The range in the metal:sulfur ratio continues to decrease with the composition ranging from $Fe_{4.5}Ni_{4.5}S_{7.88}$ to $Fe_{4.5}Ni_{4.5}S_{8.10}$. Below 400°C the compositional range remains constant (Shewman and Clark, 1970).

In the next section the pyrolytic decomposition of synthetic pentlandite is examined using simultaneous TG-DTA under heating conditions of 10 and 40°C min^{-1} in an argon atmosphere. Iron-rich pentlandite will be discussed in detail. Samples were quenched at preselected temperatures and examined using a range of techniques.

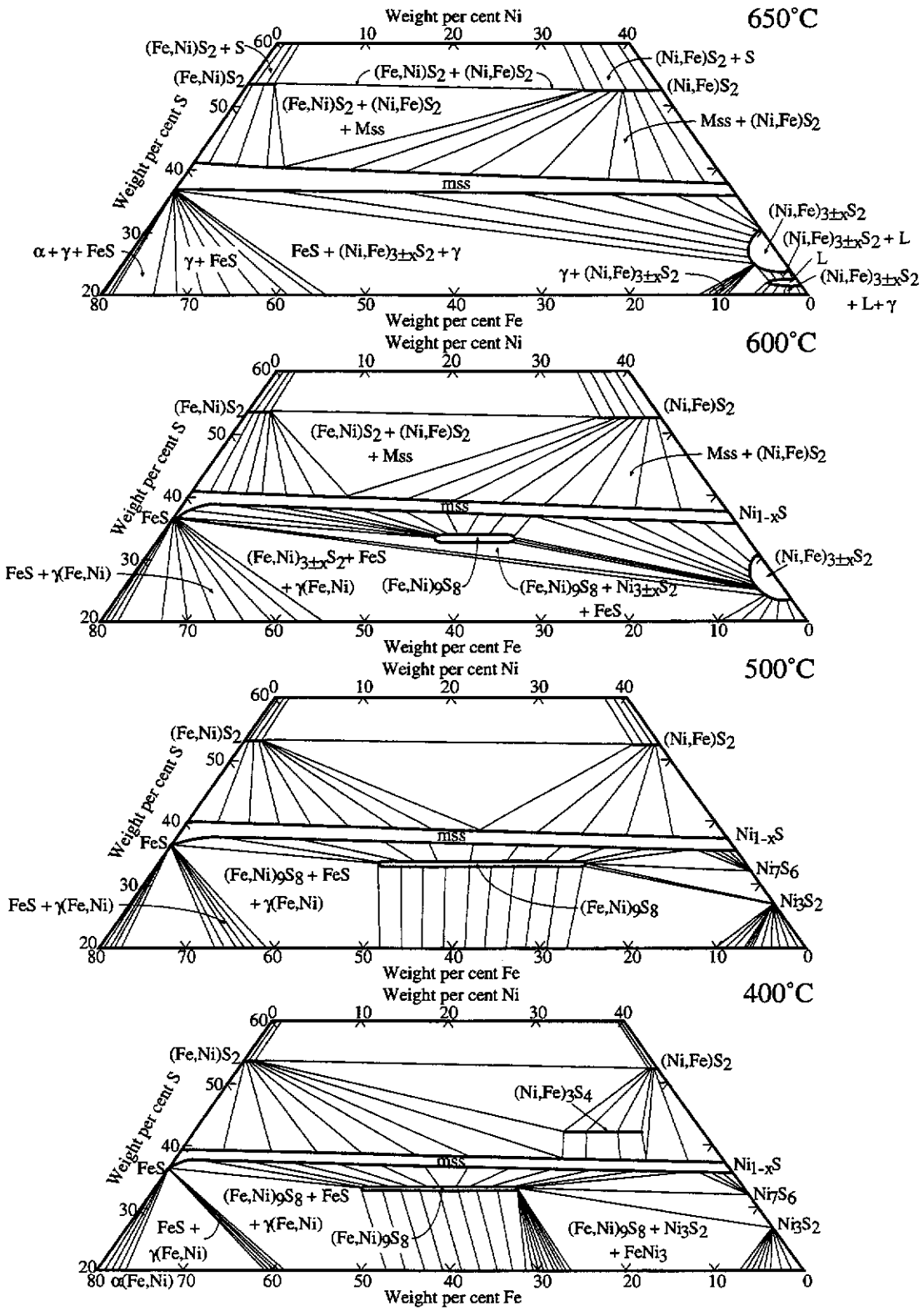

Figure 5.1 Fe-Ni-S ternary phase diagram illustrating the thermal stability of the pentlandite solid solution at: 650°C, 600°C, 500°C and 400°C (Shewman and Clark, 1970; Kullerud, 1963).

5.1.1 Pyrolytic Decomposition of Iron-Rich Pentlandite

A typical TG-DTA trace for iron-rich pentlandite heated at 10°C min^{-1} in an argon atmosphere is shown in Figure 5.2. There was no DTA activity evident between ambient and 500°C. Analysis of the iron-rich pentlandite quenched at 400°C confirmed that there were no pyrolytic decomposition products present.

Between 500°C and 580°C a small endothermic drift was observed in the DTA baseline with no associated mass loss. XRD analysis of samples collected at 500°C and 550°C, prior to the endothermic peak, showed mss associated with pentlandite. The two phases were clearly evident in the pyrolysis product quenched at 550°C with the pentlandite phase appearing brighter than the mss phase due to a higher metal:sulfur ratio (Figure 5.4a). The composition of the pentlandite phase ranged from $Fe_{5.37}Ni_{3.78}S_8$ to $Fe_{4.57}Ni_{4.66}S_8$ with an average composition of $Fe_{4.92}Ni_{4.39}S_8$,

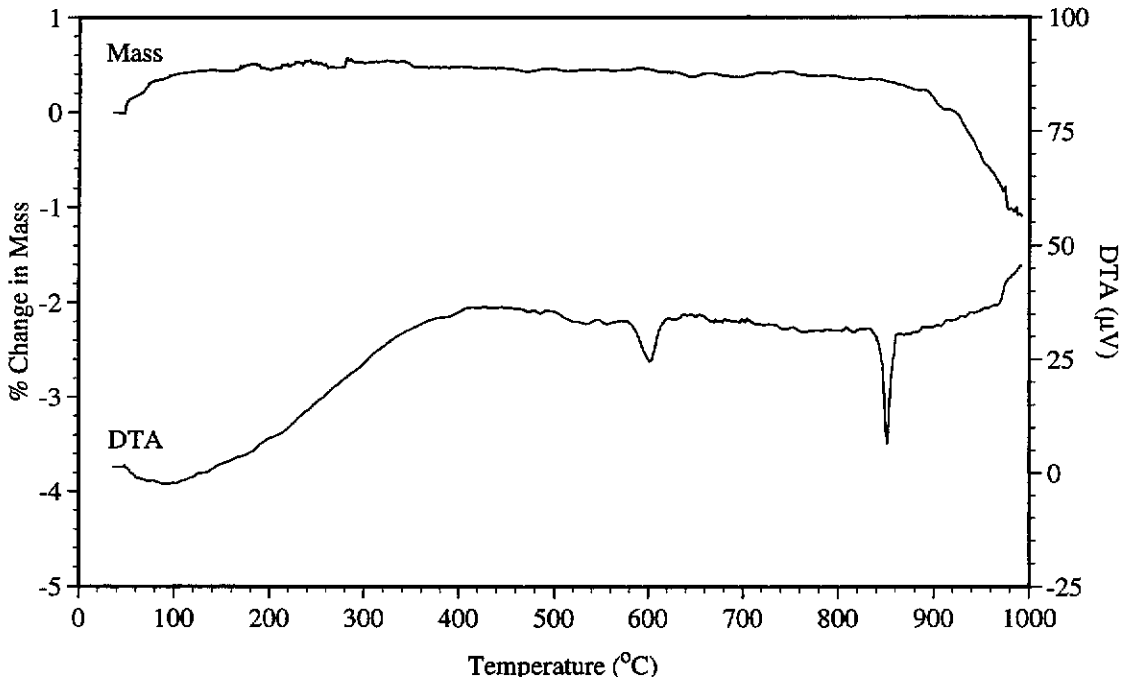

Figure 5.2 Typical TG-DTA trace of iron-rich pentlandite ($Fe_{5.80}Ni_{3.15}S_8$), 5.23 mg sample, heating rate 10°C min^{-1} in an argon atmosphere, 63-45 μm particle size fraction.

while the mss composition ranged from $Fe_{0.80}Ni_{0.17}S_{1.00}$ to $Fe_{0.64}Ni_{0.44}S_{1.00}$ with an average composition of $Fe_{0.60}Ni_{0.36}S_{1.00}$. Therefore, the composition of the pentlandite phase tended towards the ideal composition of pentlandite, $Fe_{4.5}Ni_{4.5}S_8$, whereas the composition of the mss phase tended towards the iron-rich end of the mss stability field approaching the pyrrhotite endmember, $Fe_{1-x}S$. According to the Fe-Ni-S ternary phase diagram at 400°C the iron-rich pentlandite lies within the pentlandite stability field with the composition of the solid solution ranging from $Fe_{5.83}Ni_{3.32}S_8$ to $Fe_{2.57}Ni_{6.43}S_8$ (Figure 5.1). As the temperature increases above 400°C the iron-rich end of the pentlandite stability field decreases. Between 500°C and 550°C the iron-rich pentlandite no longer remains within the pentlandite stability field. Therefore, as the temperature increases above 400°C the bulk composition of the iron-rich pentlandite falls within the divariant region formed between mss and pentlandite illustrated by tie lines joining the iron-rich end of the mss solid solution and the pentlandite solid solution (Figure 5.1). This results in the thermal dissociation of pentlandite to mss and a more stable pentlandite phase.

As the temperature increases further an endothermic peak was observed between 580°C and 615°C with no loss of mass. Mss and pentlandite were identified in the XRD pattern of decomposition products collected after the offset temperature of the endothermic peak at 650°C (Figure 5.3). BSE micrographs taken of the pyrolytic decomposition products showed no apparent change in morphology or relative abundance of mss and pentlandite compared to the BSE micrographs taken of the decomposition products collected prior to the endothermic peak (see Figure 5.4a). There was minor trace of trevorite evident in the XRD pattern due to oxidation of the pentlandite.

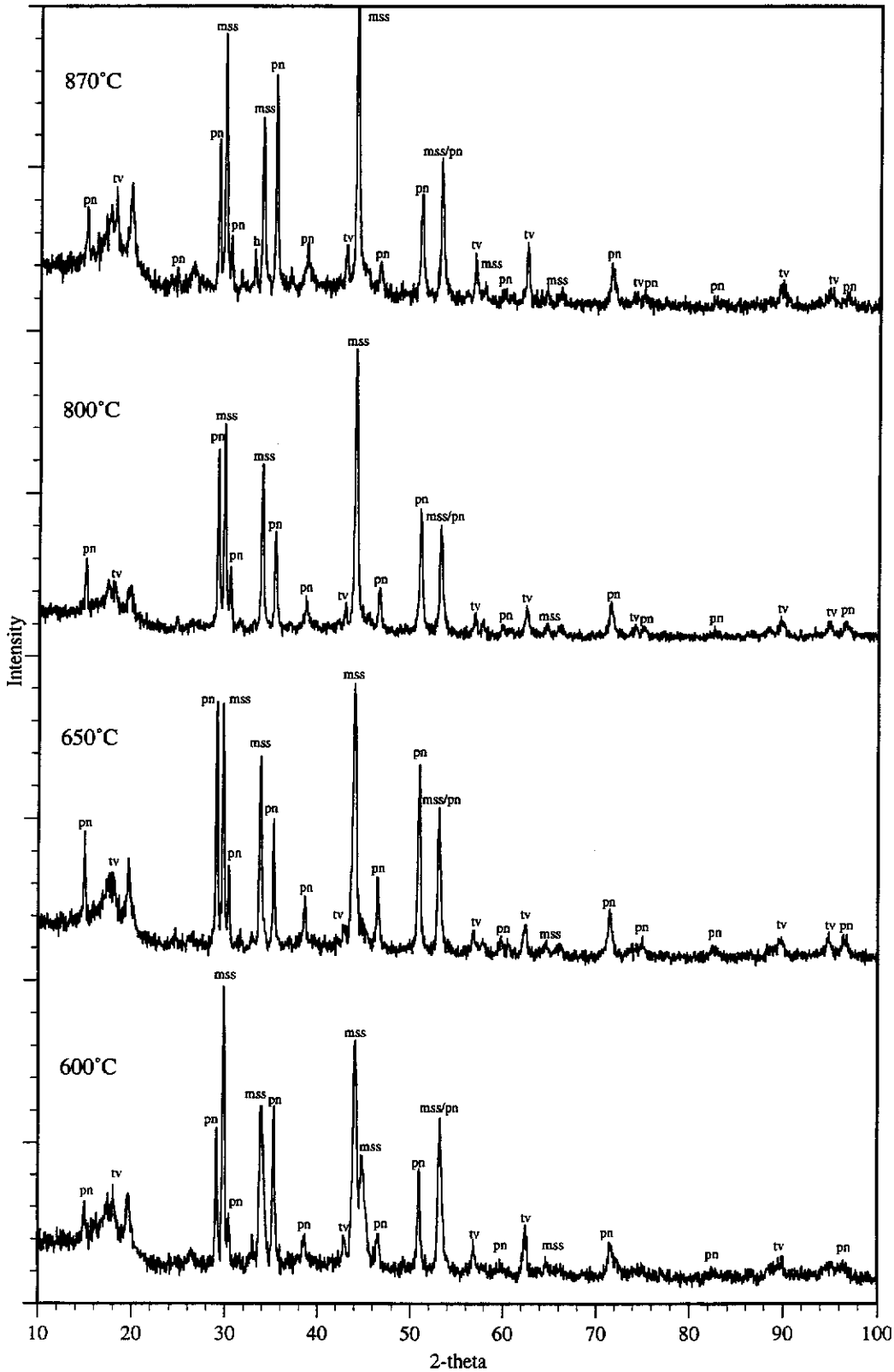

Figure 5.3 XRD patterns for iron-rich pentlandite ($Fe_{5.80}Ni_{3.15}S_8$) heated at 10°C min^{-1} in an argon atmosphere and quenched at pre-selected temperature. The temperature and phases identified are indicated on each pattern. Unassigned peaks are due to the millipore background. (mss - monosulfide solid solution, pn - pentlandite, tv - trevorite).

The endothermic peak can be assigned to the pyrolytic decomposition of the remaining pentlandite resulting in the formation of mss and a non-quenchable high-temperature form of heazlewoodite, $(Fe,Ni)_{3\pm x}S_2$. During quenching of the decomposition products the mss and non-quenchable $(Fe,Ni)_{3\pm x}S_2$ react to reform pentlandite with a composition close to the ideal stoichiometry of $Fe_{4.5}Ni_{4.5}S_8$. In order to establish whether the incongruent phase transition was a reversible reaction a sample of iron-rich pentlandite was heated to 650°C and then cooled at 10°C min^{-1}. During the cooling cycle the sample exhibited a sharp exothermic peak with an onset and offset temperature of 610°C and 590°C. Hence, this confirmed that the phase transition was a reversible reaction. The onset temperature of the exothermic peak had shifted by approximately 30°C compared to the onset temperature on the endothermic transition. This shift in the onset temperature during cooling cycle was probably due to the formation of pentlandite with an iron:nickel ratio close to the ideal composition of 1:1. A synthetic pentlandite sample with a composition of $Fe_{4.59}Ni_{4.43}S_8$ was heated at 10°C min^{-1} and then cooled at the same rate. The onset temperature for both the endothermic and exothermic transition during the heating and cooling cycles associated with the incongruent phase transition occurred at 610°C. The onset temperature of the endotherm and exotherm during the forward and reverse reactions of the phase transition agree with the DTA results previously reported by Kullerud (1962) for pentlandite with a composition of $Fe_{4.5}Ni_{4.5}S_8$.

Therefore, the pyrolytic decomposition of pentlandite is characterised by an endothermic peak with no associated mass loss resulting in the formation of mss and $(Fe,Ni)_{3\pm x}S_2$ expressed by the following incongruent phase transition:

$$(Fe,Ni)_9S_8 \text{ (cubic)} \Leftrightarrow (Fe,Ni)_{1-x}S \text{ (hexagonal)} + (Fe,Ni)_{3\pm x}S_2 \text{ (cubic)}$$

According to the Fe-Ni-S ternary phase diagram at 650°C, shown in Figure 5.1, the mss will be iron-rich while the high temperature heazlewoodite phase will be nickel-

rich with the composition approaching $Ni_{3\pm x}S_2$ due to its limited solid solution formed with iron at 650°C.

As the temperature increases both mss and $(Fe,Ni)_{3\pm x}S_2$ remain stable until the $(Fe,Ni)_{3\pm x}S_2$ incongruently melts to form a central sulfide liquid and mss. A sharp endothermic peak was observed in the DTA trace associated with the incongruent melting point of $(Fe,Ni)_{3\pm x}S_2$ between 845-860°C. The onset temperature of the endothermic peak coincided with the commencement of mass loss. XRD analysis of pyrolysis products collected prior to the endotherm at 800°C showed mss and pentlandite as the major phases (Figure 5.4b). There was no significant change in the particle morphology or texture of the particles compared with the pyrolysis products quenched at 650°C. After the offset temperature of the endothermic peak the BSE micrograph shows partial melting of the sulfide phases with the mss and pentlandite particles fusing together to form a molten mass (Figure 5.4b). Hence, the incongruent melting point transition of the high temperature $(Fe,Ni)_{3\pm x}S_2$ phase can be represented by the following reactions:

$$(Fe,Ni)_{3\pm x}S_{2\,(s)} \Leftrightarrow (Fe,Ni)_{3\pm x}S_{2\,(l)}$$

$$(Fe,Ni)_{3\pm x}S_{2\,(l)} \rightarrow (Fe,Ni)_{1\pm x}S_{(s)} + (Fe,Ni)_{1+x}S_{(l)}$$

A mass loss of 1.50% was observed between 845-1000°C coinciding with a endothermic drift in the DTA baseline between 860-970°C. The loss of sulfur was associated with the formation of the sulfide liquid phase, $(Fe,Ni)_{1+x}S$. Analysis of the pyrolysis product quenched at 870°C showed the pentlandite and mss were relatively homogeneous with an average composition of $Fe_{4.66}Ni_{4.67}S_8$ and $Fe_{0.84}Ni_{0.17}S_{1.00}$. Both the mss and pentlandite phases were metal-rich with metal:sulfur ratios of 1.17 and 1.01 respectively.

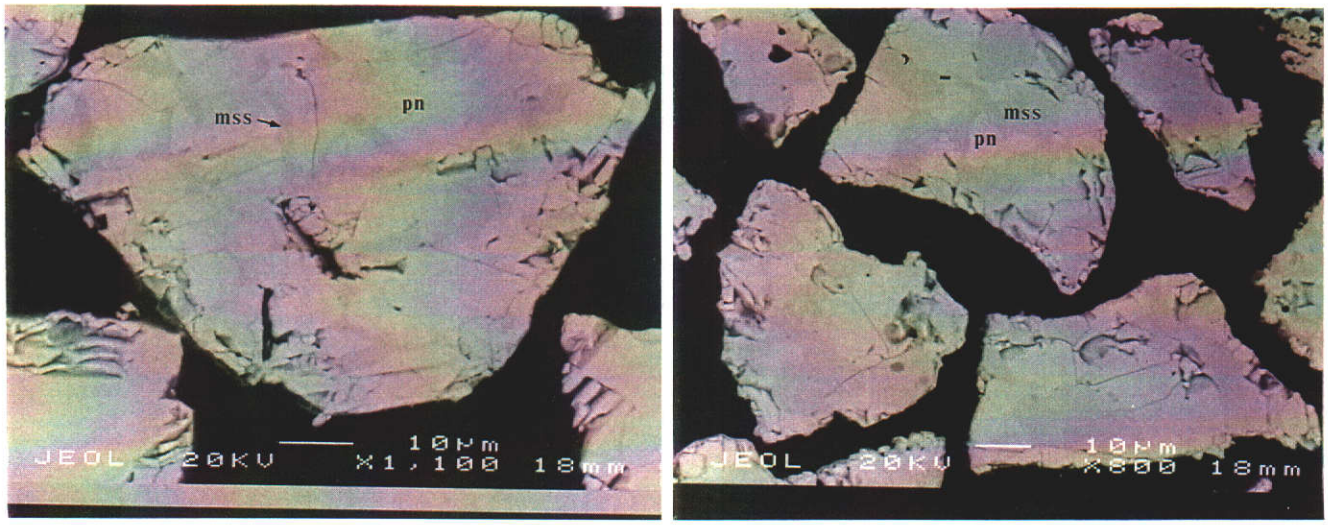

Figure 5.4a BSE micrograph of iron-rich pentlandite collected at 550°C (left) and 650°C (right). Mss and pentlandite phases are both evident in the particles at 650°C.

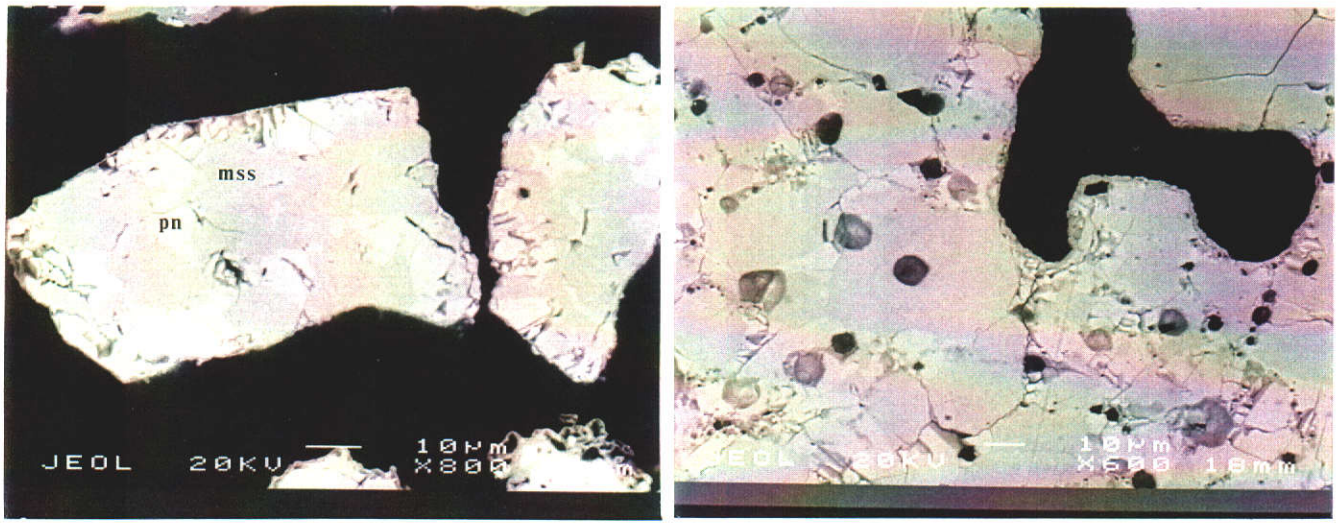

Figure 5.4b Iron-rich pentlandite collected at 800°C (left) and 860°C (right). Partial melting has occurred with mss and pentlandite as the major phases.

5.1.2 Summary

The iron-rich pentlandite decomposed between the temperature range of 580°C to 615°C to mss and $(Fe,Ni)_{3\pm x}S_2$ with no associated loss of sulfur. Sulfur was not evolved until the incongruent melting point of the high temperature heazlewoodite phase was reached. Between the temperature range of 845°C to 1000°C the mss was gradually converted to a sulfide liquid phase, resulting in the evolution of sulfur vapour.

5.1.3 The Effect of Iron:Nickel Ratio on the Pyrolytic Decomposition of Synthetic Pentlandite

Thermal analysis was performed on the entire range of synthetic pentlandite samples to determine the effect of the iron:nickel ratio on the pyrolytic decomposition. Figure 5.5 shows a typical TG-DTA trace for each synthetic pentlandite sample for the 63-45 μm particle size fraction. The extrapolated onset and offset temperatures for the DTA events are tabulated in Table 5.1.

The pyrolytic decomposition mechanism was not affected by the variation in the iron:nickel ratio. However, the onset and offset temperatures of the DTA events varied due to changes in the iron:nickel ratio. The effect of stoichiometry on the pyrolytic decomposition of synthetic pentlandite, characterised by the onset temperature of the incongruent phase transition of pentlandite to mss and high temperature $(Fe,Ni)_{3\pm x}S_2$, is illustrated in Figure 5.6. Both iron-rich and nickel-rich pentlandites exhibited the lowest thermal stability with a decomposition temperature of 580°C, while ideal pentlandite, $Fe_{4.59}Ni_{4.43}S_8$, showed the maximum thermal stability of 610°C. The thermal stability of synthetic pentlandite can be described by the following equation:

$$\text{Temp } (°C) = 70.2.(Fe:Ni)^3 - 331.(Fe:Ni)^2 + 471.(Fe:Ni) + 398$$

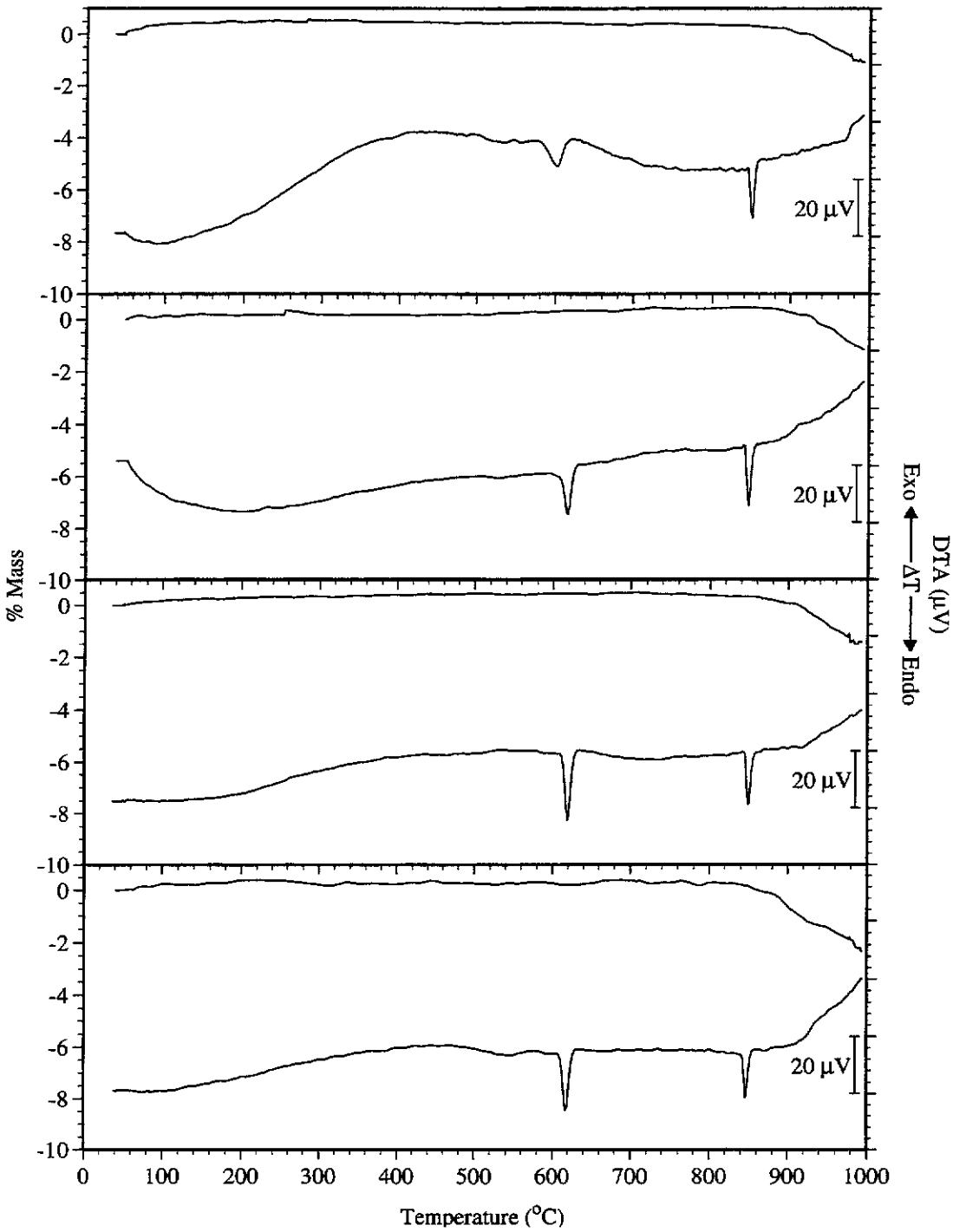

Figure 5.5 Typical TG-DTA traces for the entire range of synthetic pentlandite, heated at 10°C min^{-1} in an argon atmosphere. Approximately 5 mg of 63-45 μm particle size fraction was used. Starting from the top $Fe_{5.80}Ni_{3.15}S_8$ (iron-rich pentlandite), $Fe_{5.59}Ni_{3.42}S_8$, $Fe_{5.36}Ni_{3.79}S_8$, and $Fe_{5.08}Ni_{4.06}S_8$.

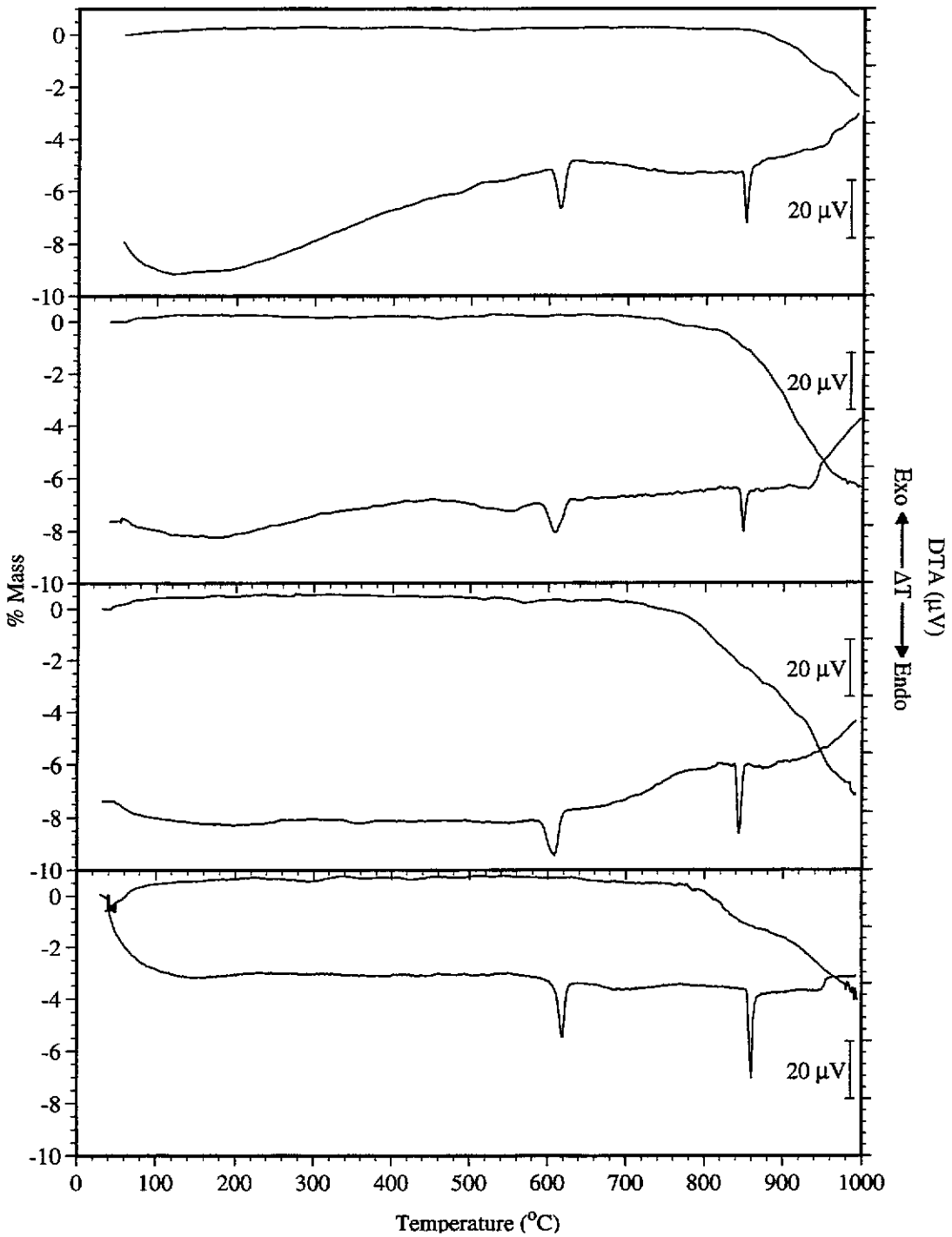

Figure 5.5 (con't) Starting from the top $Fe_{4.59}Ni_{4.43}S_8$ (ideal pentlandite), $Fe_{4.01}Ni_{4.89}S_8$, $Fe_{3.40}Ni_{5.55}S_8$ (nickel-rich pentlandite) and $Fe_{4.20}Ni_{4.16}S_8$ (sulfur-rich pentlandite).

Sulfide	Iron:Nickel Ratio	Temperature of Endothermic Events (°C)	
		Incongruent phase transition of pentlandite→mss and $(Fe,Ni)_{3\pm x}S_2$	Incongruent melting point transition of high temperature $(Fe,Ni)_{3\pm x}S_2$
$Fe_{5.80}Ni_{3.15}S_8$	1.84	580 - 620	845 - 860
$Fe_{5.59}Ni_{3.42}S_8$	1.63	595 - 630	850 - 865
$Fe_{5.36}Ni_{3.79}S_8$	1.41	600 - 630	850 - 865
$Fe_{5.08}Ni_{4.06}S_8$	1.25	605 - 630	845 - 860
$Fe_{4.59}Ni_{4.43}S_8$	1.04	610 - 630	845 - 860
$Fe_{4.01}Ni_{4.89}S_8$	0.82	600 - 630	840 - 860
$Fe_{3.40}Ni_{5.55}S_8$	0.61	580 - 615	840 - 850
$Fe_{4.20}Ni_{4.16}S_8$	1.01	610 - 625	855 - 865
$Fe_{4.22}Ni_{4.15}S_8$	1.02	610 - 625	855 - 865

Table 5.1 Comparison of the extrapolated onset and offset temperatures for the major endothermic activity for the range of synthetic pentlandites under pyrolytic decomposition conditions of 10°C min^{-1} in an argon atmosphere using TG-DTA.

The onset temperature of the endothermic peak associated with the incongruent melting point of the high-temperature $(Fe,Ni)_{3\pm x}S_2$ phase also varied from 840°C to 850°C. For example, the onset temperature for the incongruent melting point occurred at 845°C for the iron-rich pentlandite, while for nickel-rich pentlandite a 5°C decrease was observed in the incongruent melting point occurring at 840°C. According to the isothermal section at 650°C, shown in Figure 5.1, the composition of the $(Fe,Ni)_{3\pm x}S_2$ phase will be similar for both the iron-rich and nickel-rich pentlandite samples. However, the composition of the mss will differ considerably between the two endmembers of the pentlandite series with the composition of the mss phase tending towards the iron-rich end of the mss stability field, while the nickel-rich pentlandite will tend towards the centre of the mss stability field. A comparison of the EPMA results obtained for the mss derived from iron-rich and nickel-rich pentlandite at 650°C gave compositions which ranged from $Fe_{0.82}Ni_{0.14}S$ to $Fe_{0.72}Ni_{0.25}S$ (Fe:Ni = 5.86-2.88) and $Fe_{0.75}Ni_{0.24}S$ to $Fe_{0.68}Ni_{0.41}S$ (Fe:Ni = 3.12-1.66) respectively. Hence, the mss phase will tend to vary depending on the pentlandite composition while the composition of the high-temperature $(Fe,Ni)_{3\pm x}S_2$ phase will vary to a lesser degree due to the limited solid solution formed by the phase.

Each of the pentlandite samples exhibited a small mass loss associated with the incongruent melting of the $(Fe,Ni)_{3\pm x}S_2$ phase and the formation of a central sulfide liquid phase. The extent of mass loss increased as the iron:nickel ratio decreased, with the iron-rich endmember exhibiting a mass loss of 1.50% (845-1000°C) compared with a loss of 7.50% (760-1000°C) for the nickel-rich endmember. The mass loss observed prior to the incongruent melting point for the nickel-rich pentlandite was attributed to the gradual conversion of mss to $(Fe,Ni)_{3\pm x}S_2$. All of the pentlandite samples continued to lose mass above 1000°C.

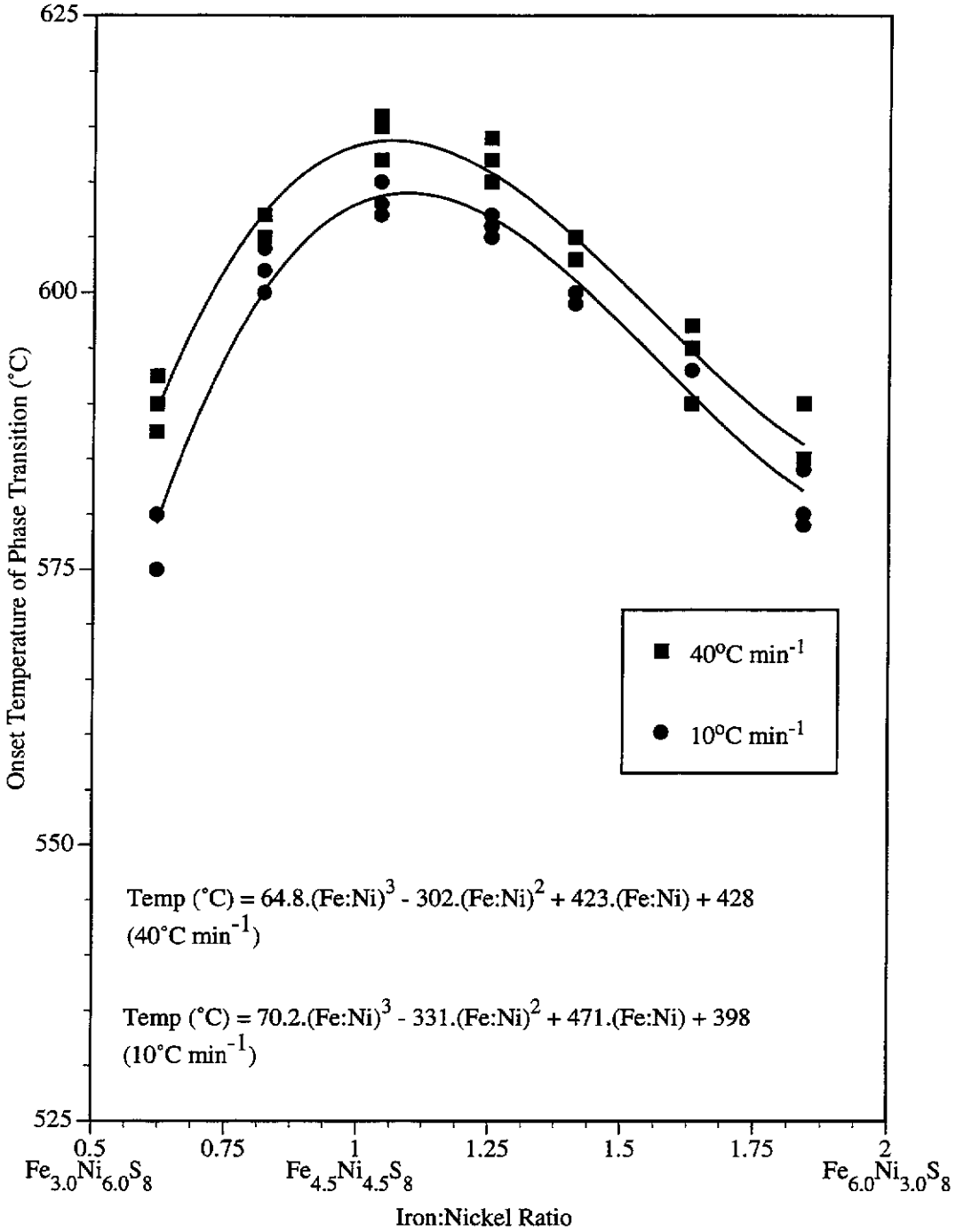

Figure 5.6 The effect of composition on the pyrolytic decomposition of synthetic pentlandite characterised by the onset temperature of the incongruent phase transition of pentlandite to mss and high-temperature $(Fe,Ni)_{3\pm x}S_2$. Each sulfide was analysed in triplicate.

5.1.4 The Effect of Metal:Sulfur Ratio on the Pyrolytic Decomposition of Synthetic Pentlandite.

The effect of the metal:sulfur ratio on the pyrolytic decomposition of synthetic pentlandite was also examined. A typical TG-DTA trace of a sulfur-rich pentlandite with a stoichiometry of $Fe_{4.20}Ni_{4.16}S_8$ is shown in Figure 5.5. The onset and offset temperatures of DTA events for $Fe_{4.20}Ni_{4.16}S_8$ and $Fe_{4.22}Ni_{4.15}S_8$ are shown in Table 5.1. The pyrolytic decomposition behaviour was identical for both sulfur-rich pentlandites. The TG-DTA trace for the sulfur-rich pentlandite ($Fe_{4.20}Ni_{4.16}S_8$) was similar to that recorded for ideal pentlandite ($Fe_{4.59}Ni_{4.43}S_8$). Both of these pentlandites have similar iron:nickel ratios, therefore the effect of the metal:sulfur ratio on the pyrolytic decomposition may be established by comparing the two TG-DTA traces.

The onset temperature of the incongruent phase transition of pentlandite to mss and $(Fe,Ni)_{3\pm x}S_2$ was not effected by a variation in the metal:sulfur ratio with the phase transition commencing at 610°C. There was no associated mass loss with the phase transition. Consequently the amounts of mss and $(Fe,Ni)_{3\pm x}S_2$ formed during the incongruent phase transition will be dependent on the metal:sulfur ratio with the amount of mss increasing as the metal:sulfur ratio decreases. The onset temperature of the incongruent melting point of $(Fe,Ni)_{3\pm x}S_2$ increased slightly from 845°C to 855°C between ideal pentlandite and sulfur-rich pentlandite respectively.

While the DTA events during pyrolytic decomposition mechanism were similar for both ideal and sulfur-rich pentlandite the loss of sulfur was significantly larger for the sulfur-rich pentlandite. Prior to the onset temperature of the incongruent melting point of $(Fe,Ni)_{3\pm x}S_2$ both pentlandites exhibited a mass loss between 780-845°C. A loss of 1.40% was observed for the sulfur-rich pentlandite compared to with a loss of only 0.2% for the ideal pentlandite sample. This mass loss was associated with the gradual

conversion of mss to $(Fe,Ni)_{3\pm x}S_2$. The conversion of mss to $(Fe,Ni)_{3\pm x}S_2$ can be attributed to an increase in the $(Fe,Ni)_{3\pm x}S_2$ stability field resulting in a shift in the equilibrium between the mss and $(Fe,Ni)_{3\pm x}S_2$. Therefore, the amount of $(Fe,Ni)_{3\pm x}S_2$ formed prior to the incongruent melting point transition by the conversion of mss increased as the metal:sulfur decreased.

The loss of sulfur decreased during the incongruent melting point transition of $(Fe,Ni)_{3\pm x}S_2$ with mass losses of 0.8% and 0.4% recorded between 845°C and 910°C for sulfur-rich and ideal pentlandite. The rate of sulfur loss increased again with losses of 2.20% and 1.40% observed between 910°C and 1000°C for the respective sulfide samples. This was associated with a broad endotherm due to the conversion of mss to the central sulfide liquid phase.

Therefore, the TG-DTA results indicate that thermal stability is not affected by a variation in the metal:sulfur ratio. However, as the metal:sulfur ratio decreases the amount of sulfur evolved increases when heated to 1000°C under an inert atmosphere. The effect of the metal:sulfur ratio on the loss of sulfur was not as large as that observed by the iron:nickel ratio for the range of synthetic pentlandites.

5.1.5 The Effect of Heating Rate on the Pyrolytic Decomposition

The TG-DTA trace for each synthetic pentlandite sample, heated at 40°C min^{-1} in an argon atmosphere, is shown in Figure 5.7. The extrapolated onset and offset temperatures of the DTA events are tabulated in Table 5.2.

The pyrolytic decomposition mechanism and particle morphology were unaffected by an increase in the heating rate. The onset and offset temperatures of the DTA events increased by only 5-10°C even though there was a fourfold increase in the heating rate, as is shown in Figure 5.6. The relationship was similar except for a 5-10°C offset

between the two curves obtained at 10°C and 40°C min^{-1}. The pyrolytic decomposition temperature of synthetic pentlandite heated at 40°C min^{-1} can be described by the following equation:

$$\text{Temp (°C)} = 64.8.(\text{Fe:Ni})^3 - 302.(\text{Fe:Ni})^2 + 423.(\text{Fe:Ni}) + 428$$

A similar increase was observed for the DTA peak associated with the incongruent melting point transition of $(Fe,Ni)_{3\pm x}S_2$. The melting point transition increased from 845°C to 855°C for iron-rich pentlandite as the heating rate was increased from 10°C min^{-1} and 40°C min^{-1}. The incongruent melting point transition also increased as the iron:nickel ratio increased (see Table 5.2). For example, the onset temperature increased from 840°C (nickel-rich pentlandite) to 855°C (iron-rich pentlandite) as the iron:nickel ratio increased from 1.63 to 1.84.

The broad endotherm following the incongruent melting point transition was more prominent in the DTA trace due to an increase in the response of the instrument. The endotherm coincided with the mass loss observed in the TG trace. The TG trace showed the greatest effect due to heating rate with the extent of mass loss decreasing as the heating rate increased. For example, iron-rich pentlandite exhibited a loss of 1.5% between 845-1000°C when heated at 10°C min^{-1} compared with a loss of only 0.5% between 855-1000°C when heated at 40°C min^{-1}. The decrease in mass loss was more evident as the iron:nickel ratio decreased with the observed mass loss decreasing from 7.5% (760-1000°C) to 2.5% (795-1000°C) for nickel-rich pentlandite. Hence, the loss of sulfur from pentlandite decreased as the heating rate was increased between the temperature range of 25-1000°C.

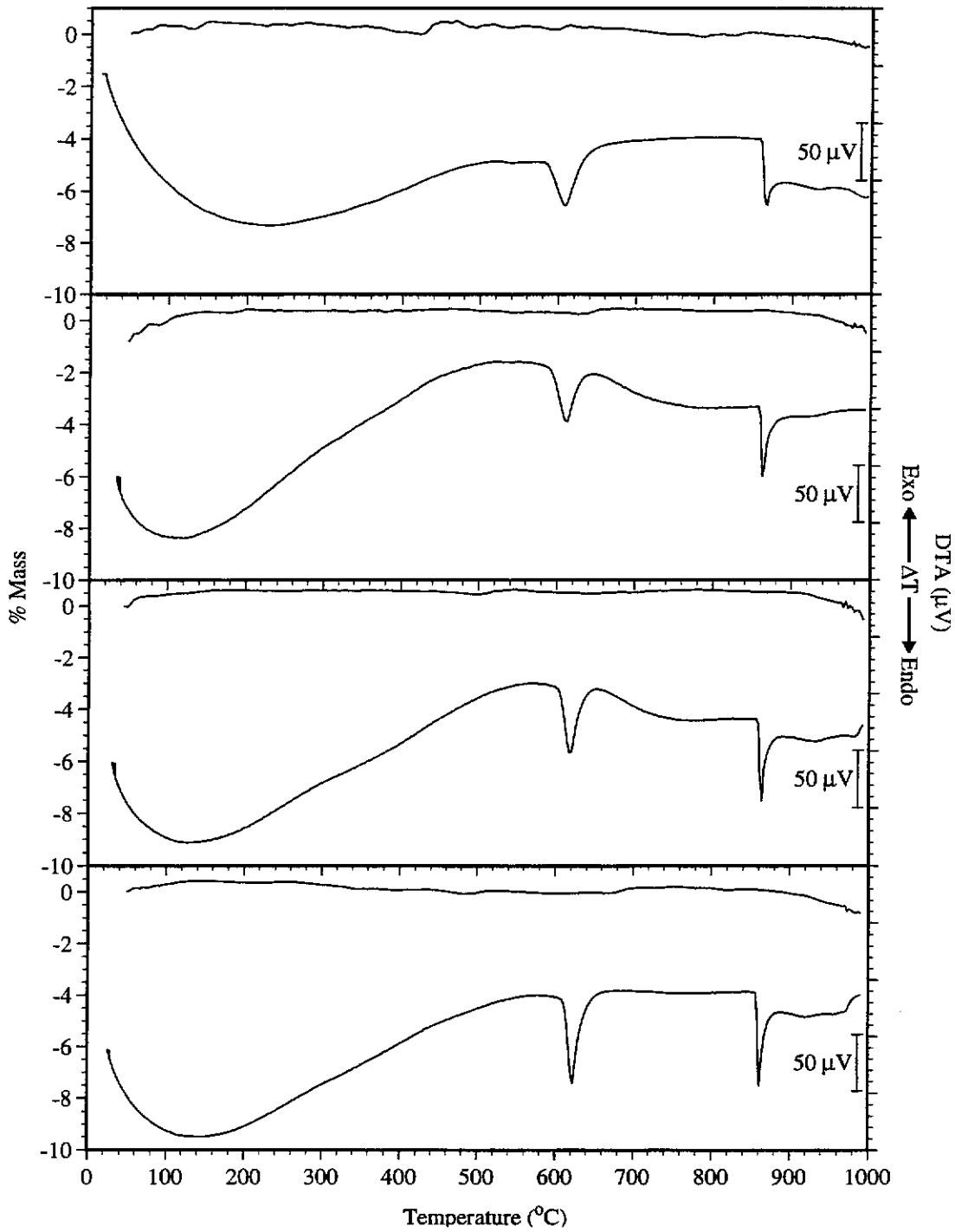

Figure 5.7 Typical TG-DTA traces for the entire range of synthetic pentlandite, heated at 40°C min^{-1} in an argon atmosphere. Approximately 5 mg of 63-45 μm particle size fraction was used. Starting from the top $Fe_{5.80}Ni_{3.15}S_8$ (iron-rich pentlandite), $Fe_{5.59}Ni_{3.42}S_8$, $Fe_{5.36}Ni_{3.79}S_8$, and $Fe_{5.08}Ni_{4.06}S_8$.

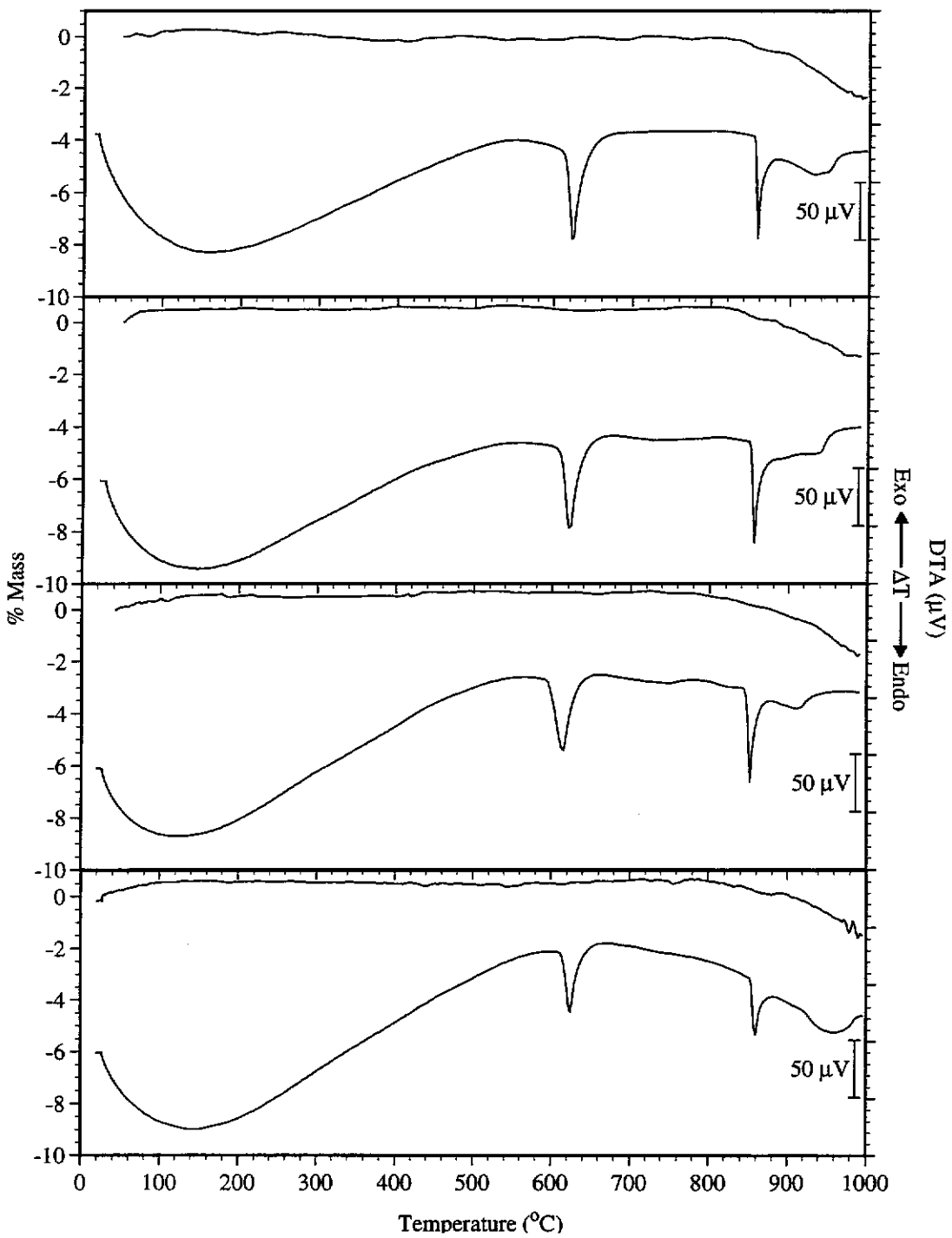

Figure 5.7 (con't) Starting from the top $Fe_{4.59}Ni_{4.43}S_8$ (ideal pentlandite), $Fe_{4.01}Ni_{4.89}S_8$, $Fe_{3.40}Ni_{5.55}S_8$ (nickel-rich pentlandite) and $Fe_{4.20}Ni_{4.16}S_8$ (sulfur-rich pentlandite).

Sulfide	Iron:Nickel Ratio	Temperature of Endothermic Events (°C)	
		Incongruent phase transition of pentlandite→mss and $(Fe,Ni)_{3\pm x}S_2$	Incongruent melting point transition of high temperature $(Fe,Ni)_{3\pm x}S_2$
$Fe_{5.80}Ni_{3.15}S_8$	1.84	585 - 635	855 - 870
$Fe_{5.59}Ni_{3.42}S_8$	1.63	590 - 630	855 - 870
$Fe_{5.36}Ni_{3.79}S_8$	1.41	605 - 640	855 - 875
$Fe_{5.08}Ni_{4.06}S_8$	1.25	610 - 640	855 - 875
$Fe_{4.59}Ni_{4.43}S_8$	1.04	610 - 645	855 - 870
$Fe_{4.01}Ni_{4.89}S_8$	0.82	605 - 640	850 - 865
$Fe_{3.40}Ni_{5.55}S_8$	0.61	595 - 630	840 - 865
$Fe_{4.20}Ni_{4.16}S_8$	1.01	610 - 645	855 - 870
$Fe_{4.22}Ni_{4.15}S_8$	1.02	610 - 645	855 - 870

Table 5.2 Comparison of the extrapolated onset and offset temperatures for the major endothermic activity for the range of synthetic pentlandites under pyrolytic decomposition conditions of 40°C min^{-1} in an argon atmosphere using TG-DTA.

5.2 Oxidation of Synthetic Pentlandite

Even though pentlandite is the predominant nickel bearing sulfide there has been limited studies performed on the oxidation mechanism (Thornhill and Pidgeon, 1957; Dunn and Kelly, 1980; Mackey, 1991). During the oxidation of pentlandite it has been reported that the pentlandite converts to a phase isomorphous with pyrrhotite (Thornhill and Pidgeon, 1957, p.993; Dunn and Kelly, 1980, p.151). Dunn and Kelly (1980) assigned the pyrrhotite like phase with the general formula of $Fe_{8\pm x}Ni_{8\pm y}S_{16\pm z}$. During the lower temperature region the iron is preferentially oxidised leaving a nickel-rich sulfide core. The nickel continues to be enriched in the sulfide core due to the oxidation of sulfur at the reaction interface resulting in the formation of $Ni_{3\pm x}S_2$ (Thornhill and Pidgeon, 1957). $Ni_{3\pm x}S_2$ is then oxidised between 775-805°C with the final products identified as Fe_2O_3, NiO and $FeNi_2O_4$ (Dunn and Kelly, 1980).

The oxidation mechanism of synthetic pentlandite was established under conditions of 10°C min^{-1} in an air atmosphere. Samples were quenched at preselected temperatures and characterised by the usual range of instrumental techniques. The thermal analytical results of iron-rich pentlandite will be discussed in detail and the effect of the iron:nickel ratio on the reaction mechanism will be established.

5.2.1 Oxidation of Iron-Rich Pentlandite

The oxidation of synthetic pentlandite was complex and proceeded in several stages. A typical TG-DTA trace of iron-rich pentlandite ($Fe_{5.80}Ni_{3.15}S_8$) with a particle size range of 63-45 μm, heated at 10°C min^{-1} in an air atmosphere, is shown in Figure 5.8. Evolved gas analysis was performed by a FTIR spectrometer coupled to the thermal analyser. Results indicated that sulfur dioxide gas accounted for all the peaks observed in the Gramm Schmidt chromatogram.

An initial mass gain of 3.85% was observed between 385-570°C. This was accompanied by a slight exothermic drift in the DTA baseline between 350-575°C. No sulfur dioxide was evident in the Gramm Schmidt chromatogram. XRD analysis of the oxidation product collected at 500°C revealed pentlandite and mss as the major phases with a minor amount of hematite and nickel oxide also detected (see Figure 5.9.). FTIR spectroscopy confirmed hematite as the major oxidation product with vibrational peaks identified at 558 and 470 cm^{-1}. There was only a minor trace of SO_4^{2-} detected in the infrared spectrum which appeared to be weakly associated to a metal cation indicated by the board vibrational peaks located at 1150 and 995 cm^{-1}.

SEM examination of the oxidation product quenched at 500°C confirmed pentlandite and mss as the two major sulfide phases surrounded by a small oxide rim (see Figure 5.11a). The average composition of the pentlandite and mss phases were $Fe_{4.68}Ni_{4.60}S_8$ and $Fe_{0.72}Ni_{0.25}S_{1.00}$ respectively. The iron:nickel ratio of the pentlandite had decreased from 1.84 to 1.02 between the temperature range of 400-500°C, while the metal:sulfur ratio showed an increase from 1.12 to 1.16.

Hence, as the temperature increases above 400°C the iron-rich end of the pentlandite solid solution decreases resulting in the iron-rich pentlandite falling within the divariant region formed between mss and pentlandite. Therefore, the iron-rich pentlandite thermally dissociates between 400°C and 500°C to form a more stable pentlandite phase with a composition close to the ideal composition of $Fe_{4.5}Ni_{4.5}S_8$, and an iron-rich mss phase close to the pyrrhotite endmember.

$$(Fe,Ni)_9S_8 \Leftrightarrow (Fe,Ni)_{1-x}S + \frac{7}{8}(Fe,Ni)_{\frac{8(8+x)}{7}}S_8$$

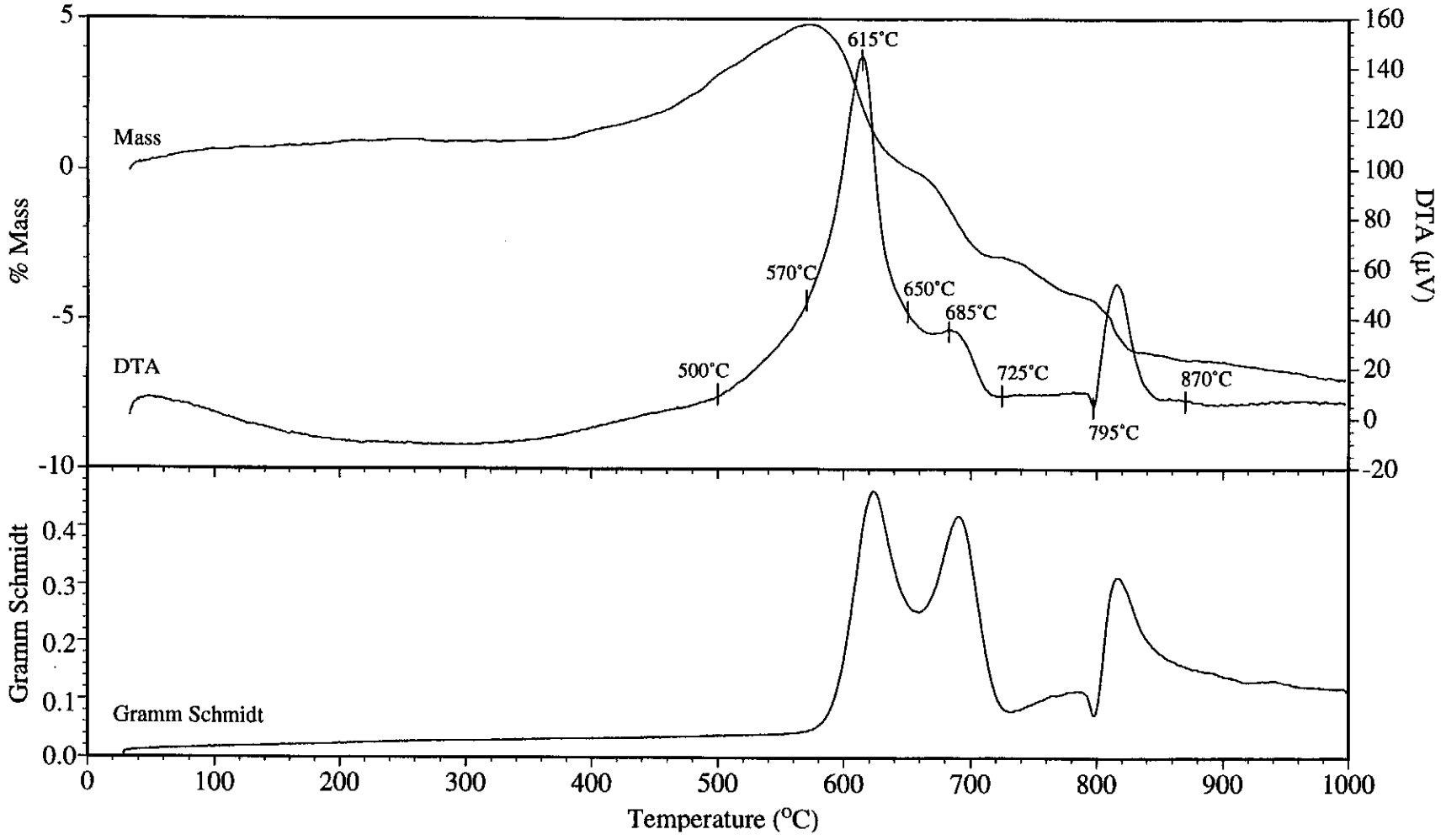

Figure 5.8 Typical TG-DTA profile for iron-rich pentlandite ($Fe_{5.80}Ni_{3.15}S_8$), 5.24 mg of sample heated at 10°C min^{-1} in an air atmosphere for the 63-45 µm particle size fraction. Oxidation products were collected at the indicated temperatures on the DTA profile. The Gramm Schmidt chromatogram is shown below.

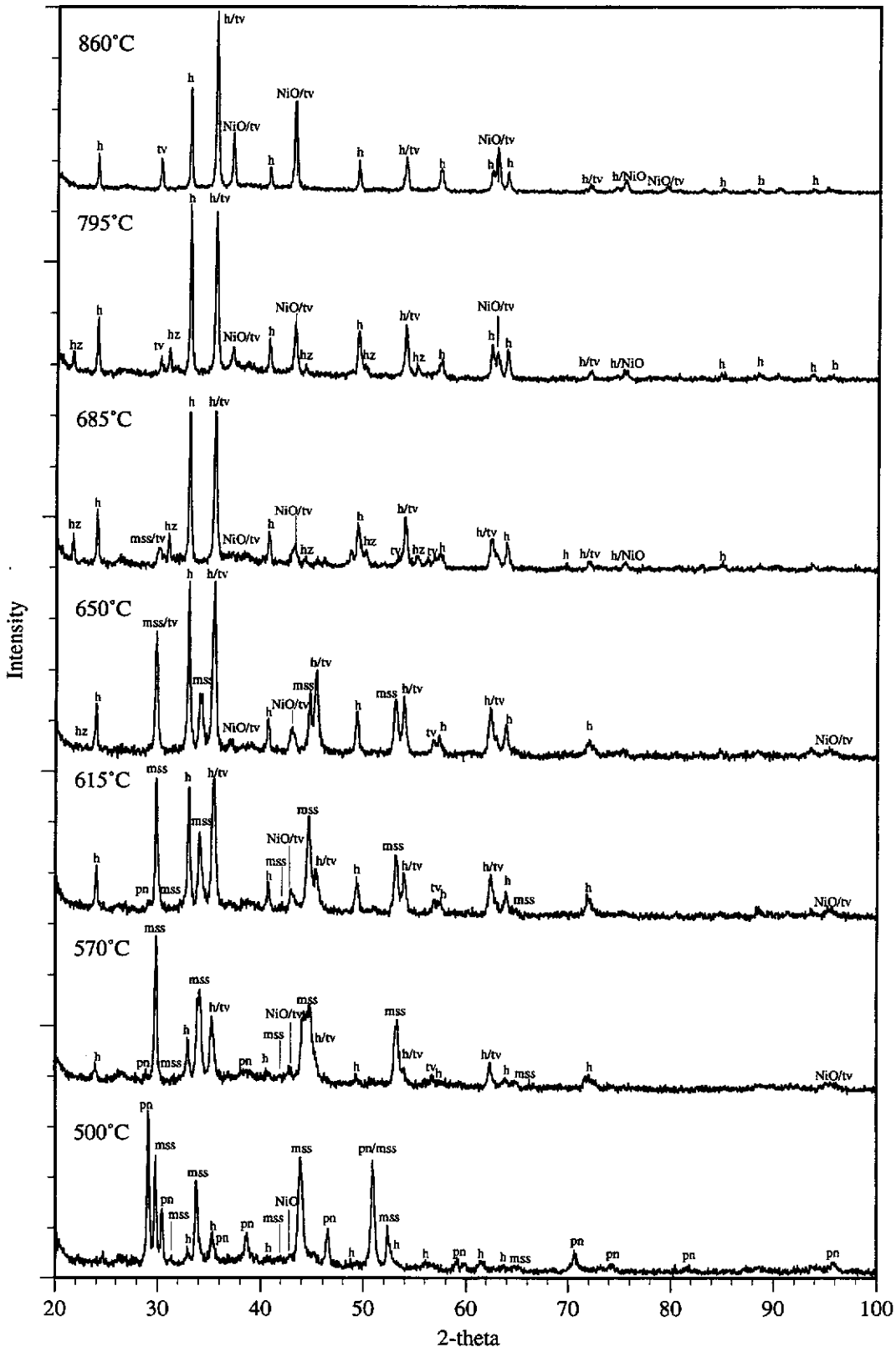

Figure 5.9 XRD patterns of oxidation products quenched at preselected temperatures in the TG-DTA trace for iron-rich pentlandite, heated at 10°C min^{-1} in air (pn - pentlandite, mss - monosulfide solid solution, h - hematite, tv - trevorite, NiO - nickel oxide, hz - heazlewoodite).

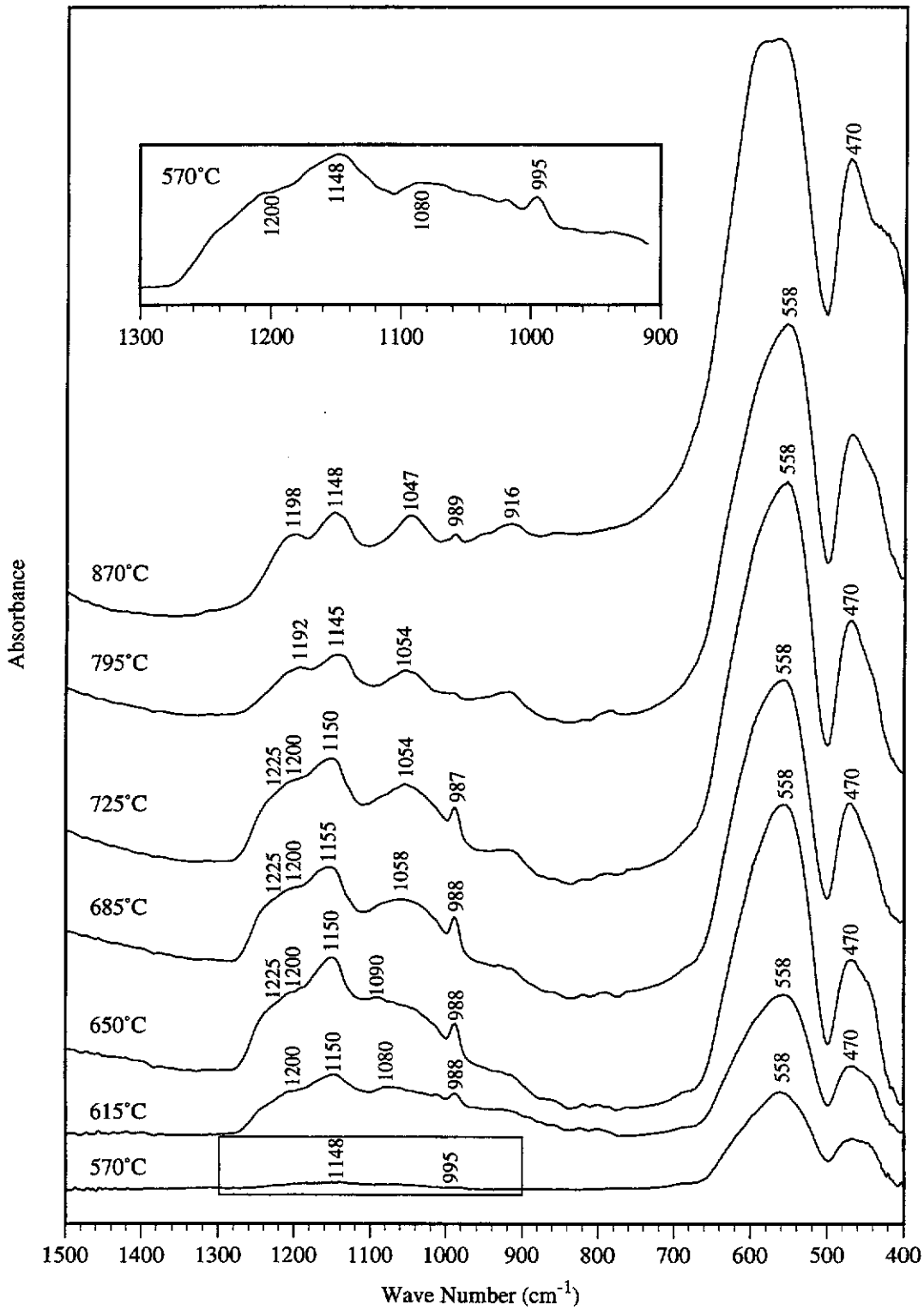

Figure 5.10 FTIR spectra of oxidation products quenched at preselected temperatures in the TG-DTA trace for iron-rich pentlandite, heated at 10°C min^{-1} in an air atmosphere.

XRD analysis of the oxidation product collected at 570°C showed mss as the major phase with only a minor trace of pentlandite remaining. There was also significant increase in the amount of hematite present according to the relative peak intensities. This was supported by the BSE micrograph of the oxidation product which showed the hematite present as oxide product layer approximately 2 μm in thickness surrounding the sulfide cores (Figure 5.11b). The pentlandite was visible as small thin remnants occurring along the grain boundaries of the mss within the sulfide cores. Table 5.3 shows the composition of the mss across the sulfide core as the temperature increases. EPMA of the sulfide core showed a decrease in the iron:nickel ratio from 1.41 to 1.29 coinciding with an increase in the metal:sulfur ratio from 0.94 to 0.96 from the centre of the mss core to the mss-oxide interface. There was also a minor trace of sulfate present in the oxidation product collected at 570°C. The sulfate appeared to be finely disseminated throughout the oxide rim and could not be resolved in the BSE micrograph (Figure 5.11b). Iron (II) sulfate was identified as the main sulfate product with infrared peaks identified at 1200, 1150, 1080 and 995 cm^{-1}. The sulfation of the mss phase can be described by the following reactions:

$$2(Fe_{1-x}Ni_{1-y})S + (16-8x-8y)O_{2\,(g)} \rightarrow (2-2x)FeSO_4 + (2-2y)NiSO_4 + (1-x-y)S_{2\,(g)}$$

$$(1-x-y)\,S_{2\,(g)} + (2-2x-2y)\,O_{2\,(g)} \rightarrow (2-2x-2y)\,SO_{2\,(g)}$$

Section Across Mss Core	Temperature (°C)		
	570°C	615°C	650°C
Centre	$Fe_{0.55}Ni_{0.39}S_{1.00}$	$Fe_{0.38}Ni_{0.63}S_{1.00}$	$Fe_{0.20}Ni_{0.83}S_{1.00}$
Middle	$Fe_{0.55}Ni_{0.40}S_{1.00}$	$Fe_{0.36}Ni_{0.65}S_{1.00}$	$Fe_{0.18}Ni_{0.84}S_{1.00}$
Edge	$Fe_{0.54}Ni_{0.42}S_{1.00}$	$Fe_{0.32}Ni_{0.70}S_{1.00}$	$Fe_{0.17}Ni_{0.88}S_{1.00}$

Table 5.3 The average composition of the mss core quenched at various temperatures, analysed by EPMA.

Therefore, the exothermic drift in the DTA curve and initial mass gain occurring between 385°C and 570°C can be attributed to the preferential oxidation of iron. This is supported by the EPMA results which showed the iron:nickel ratio had decreased from 1.84 to 1.29. Analysis of the sulfide core also showed the metal:sulfur ratio of the sulfide core had decreased from 1.12 to 0.94 between 385°C and 570°C due to the conversion of the iron-rich pentlandite to mss. Hence, the majority of the sulfur had been retained within the sulfide core. This was supported by evolved gas analysis which showed no evidence of sulfur dioxide evolved during the initial mass gain.

A mass loss of 4.60% was observed between 575°C and 645°C which coincided with the decomposition temperature of $FeSO_4$. A major exotherm associated with the mass loss had an onset and offset temperature of 575°C and 665°C respectively. Analysis of the oxidation product quenched at 615°C showed the pentlandite had completely decomposed (Figure 5.11c). Large holes were evident between the oxidation product layer and the mss core. These were due to a volume reduction in the sulfide core as the iron and sulfur were preferentially oxidised. Table 5.4 shows the change in volume for iron-rich pentlandite for a range of oxidation reactions. Optical micrographs taken of polished sections under polarised light exhibited distinctive red internal reflections characteristic of hematite around the outer oxide layer. XRD results showed a significant increase in the amount of hematite present according to the relative peak intensities in the diffraction pattern. This was supported by the EPMA results indicating the preferential oxidation of iron at the sulfide-oxide interface of the mss core continued with a significant decrease in the iron:nickel ratio from 1.28 to 0.46 between 570°C and 615°C. The metal:sulfur ratio exhibited an increase from 0.96 to 1.02. Under polarised light the mss cores displayed strong anisotropism, appearing yellowish-grey in colour, characteristic for both hexagonal pyrrhotite ($Fe_{1-x}S$) and millerite ($Ni_{1-x}S$) (Spry and Gedlinske, 1987). Oxidation of the mss appeared to occur along a preferred orientation of the mss lattice with some edges of the mss core exhibiting virtually no oxidation while others have undergone extensive

Reaction	Δ Mass %	Δ Volume %
$Fe_{5.80}Ni_{3.15}S_{8.00\,(s)} \rightarrow 8\,(Fe_{0.61}Ni_{0.39}S_{1.00})_{(s)} + 0.475\,Fe_2O_{3\,(s)}$ (iron-rich pentlandite) (mss) (hematite)	3.0	-9.6
$Fe_{0.61}Ni_{0.39}S_{1.00\,(s)} \rightarrow 0.39\,NiS_{(s)} + 0.61\,FeSO_{4\,(s)}$ (mss) (nickel-rich mss) (iron (II) sulfate)	43.6	69.8
$Fe_{0.61}Ni_{0.39}S_{1.00\,(s)} \rightarrow 0.39\,NiS_{(s)} + 0.30\,Fe_2O_{3\,(s)} + 0.61\,SO_{2\,(g)}$ (mss) (nickel-rich mss) (hematite)	-5.5	-11.8
$Fe_{0.61}Ni_{0.39}S_{1.00\,(s)} \rightarrow 0.13\,Ni_3S_{2\,(s)} + 0.30\,Fe_2O_{3\,(s)} + 0.74\,SO_{2\,(g)}$ (mss) (heazlewoodite) (hematite)	-10.7	-24.2
$Fe_{0.61}Ni_{0.39}S_{1.00\,(s)} \rightarrow 0.39\,NiO_{(s)} + 0.30\,Fe_2O_{3\,(s)} + SO_{2\,(g)}$ (mss) (nickel oxide) (hematite)	-12.6	-29.4
Overall Reaction		
$Fe_{5.80}Ni_{3.15}S_{8.00\,(s)} \rightarrow 3.15\,NiO_{(s)} + 2.90\,Fe_2O_{3\,(s)} + 8\,SO_{2\,(g)}$ (iron-rich pentlandite) (nickel oxide) (hematite)	-8.7	-20.7

Table 5.4 Theoretical changes in mass and molecular volume for range of oxidation reactions. Change in molecular volume was calculated from the measured and calculated densities for the individual mineral phases obtained from Roberts (1990).

oxidation. Previous oxidation studies performed on hexagonal pyrrhotite have shown that the sulfide is preferentially oxidised along the basal plains of the pyrrhotite lattice (Dunn and Chamberlain, 1991).

FTIR spectroscopy of the oxidation product collected at 615°C revealed $NiSO_4$ as the major sulfate phase with vibrational peaks identified at 1225, 1200, 1050 and 988 cm^{-1}. There was no evidence of $FeSO_4$ remaining at 615°C. Hence, the decomposition of $FeSO_4$ to FeO and subsequent oxidation to Fe_2O_3 at approximately 575°C can be represented by the following equation:

$$2\,FeSO_4 \rightarrow Fe_2O_3 + 2\,SO_{2\,(g)} + 0.5\,O_{2\,(g)}$$

The decomposition and oxidation of $FeSO_4$ is an endothermic process, however the reaction coincides with the preferential oxidation of the iron sulfide component of the mss between 575-665°C. This reaction is highly exothermic and the heat evolved is significantly larger in magnitude than that associated with the decomposition of the $FeSO_4$. Hence, the decomposition and oxidation of $FeSO_4$ is not evident in the DTA curve.

Further nickel enrichment occurred between 615°C and 650°C with the iron:nickel ratio ranging from 0.24 at the centre of the mss core to 0.19 at the mss-oxide interface of the mss core. Trevorite and hematite were detected as the major phases present at 650°C. The formation of trevorite was attributed to the direct oxidation of the iron and nickel associated with the mss. Examination of the oxidation products collected at 650°C were similar to the micrographs shown in Figure 5.11d. Trevorite can be clearly seen as a dark grey inner oxide layer in the optical micrograph surrounding the mss cores.

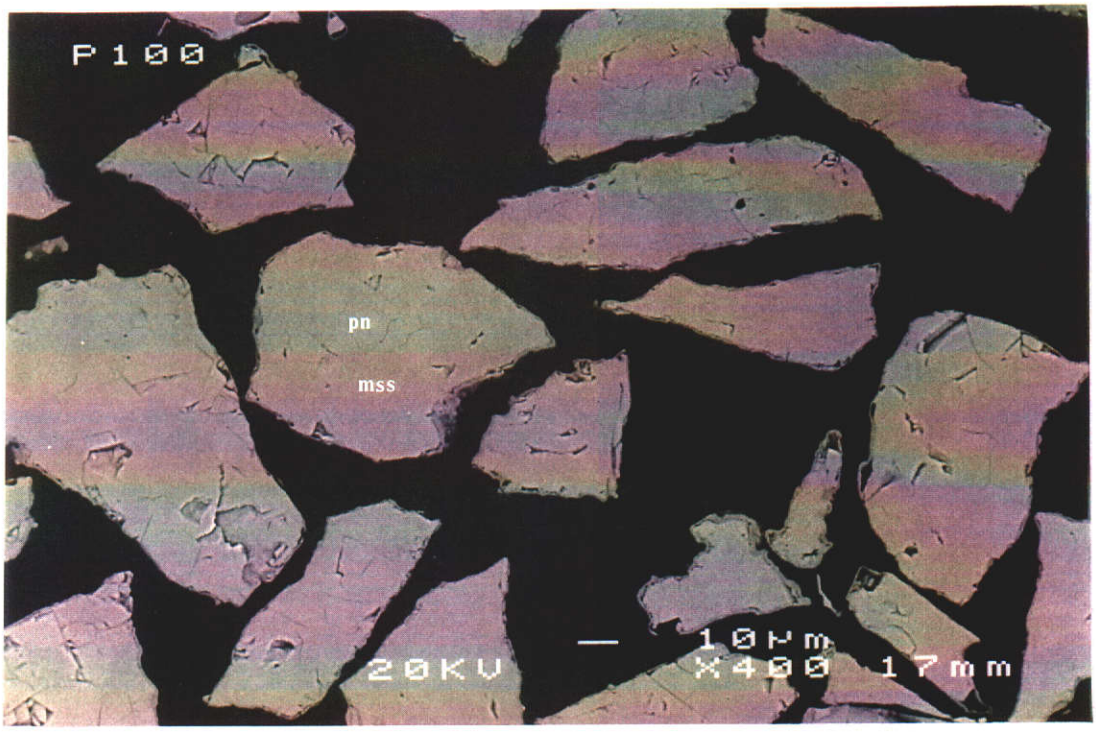

Figure 5.11a BSE micrograph of iron-rich pentlandite heated at 10°C min^{-1} in air and quenched at 500°C. Mss can be identified as the dark grey phase while the pentlandite phase is the light grey phase.

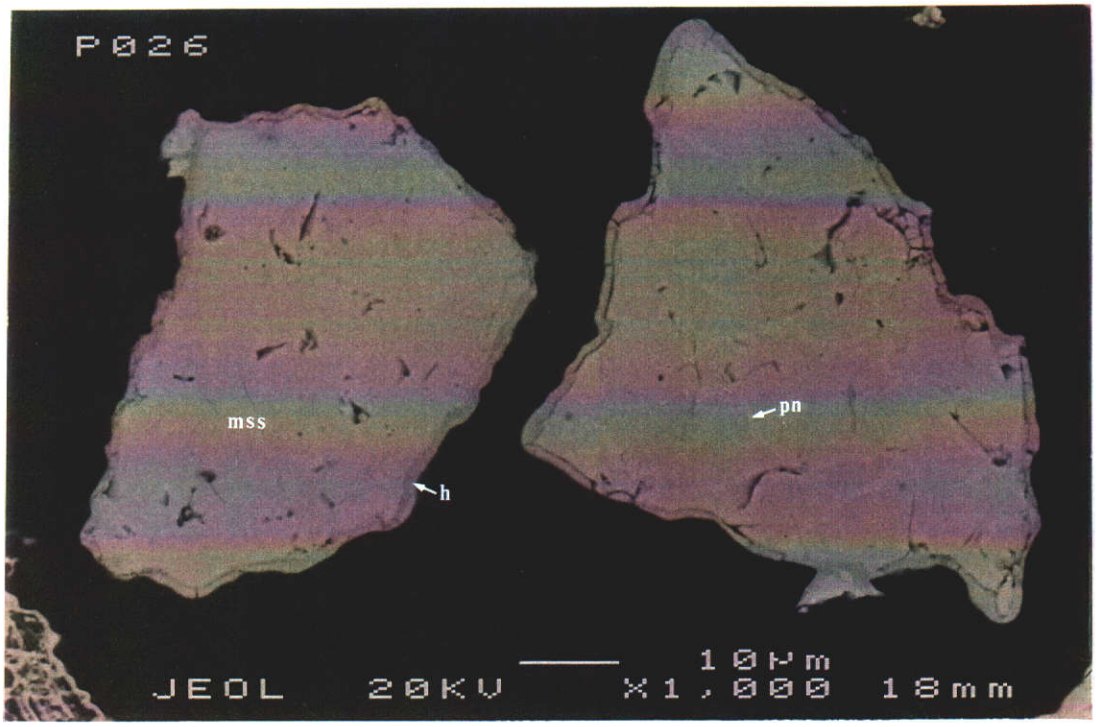

Figure 5.11b BSE micrograph of iron-rich pentlandite heated at 10°C min^{-1} in air and quenched at 570°C. There are minor remnants of pentlandite remaining in the mss cores. A oxide-sulfate rim surrounds the sulfide cores.

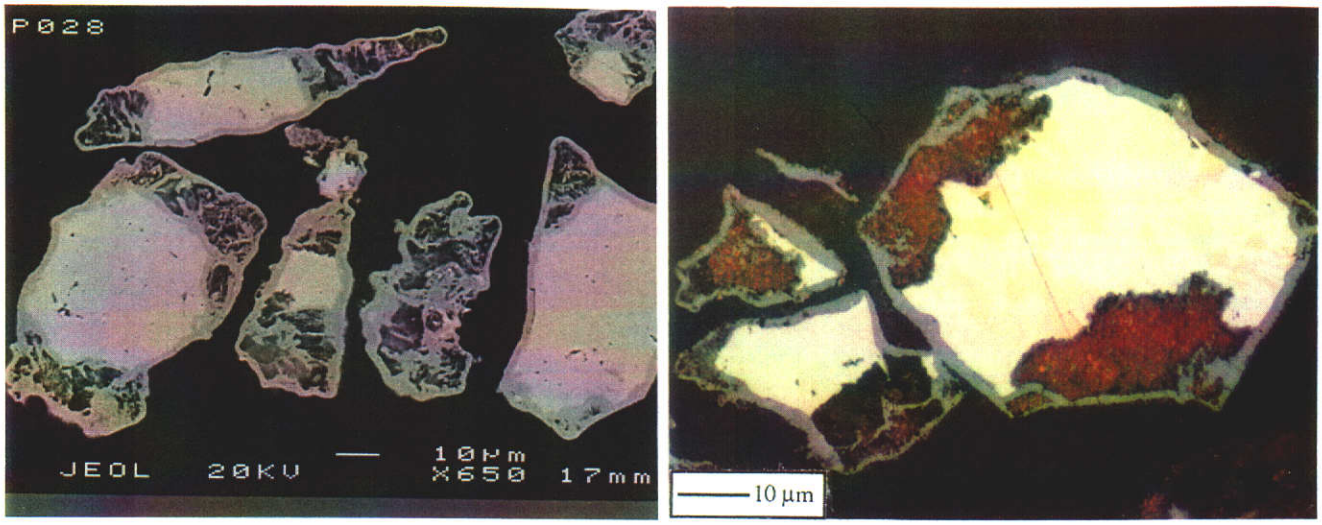

Figure 5.11c BSE (left) and optical (right) micrographs of iron-rich pentlandite quenched at 615°C. Hematite gives distinctive red internal reflections under polarised light.

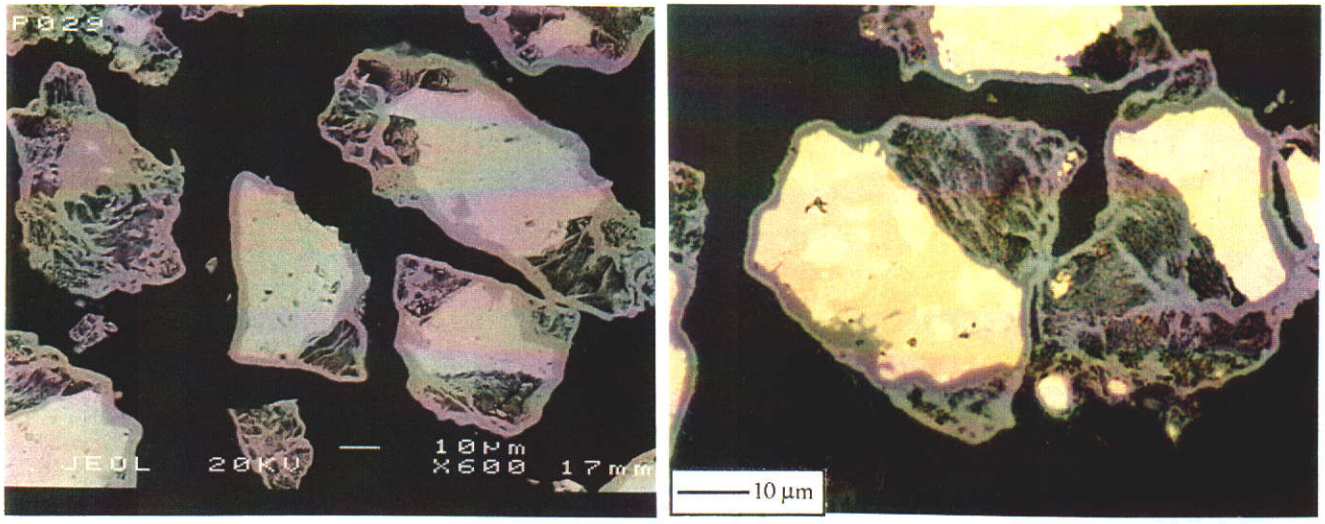

Figure 5.11d BSE (left) and optical (right) micrographs of iron-rich pentlandite quenched at 650°C. Trevorite appears as a dark grey inner oxide layer followed by a hematite oxide outer layer.

Therefore, the major exotherm can be attributed to the preferential oxidation of the iron sulfide component of the mss phase resulting in the formation of hematite. This is followed by the direct oxidation of the mss as the iron:nickel ratio decreases, forming an inner trevorite oxide layer during the later stages of the exothermic activity.

$$2\ Fe_{1-x}S + 7\text{-}3x\ O_{2\,(g)} \rightarrow (1\text{-}x)\ Fe_2O_3 + 2\ SO_{2\,(g)}$$

$$3\ (Fe,Ni)_{1-x}S + (5\text{-}2x)\ O_{2\,(g)} \rightarrow (1\text{-}x)\ (Fe,Ni)_3O_4 + 3\ SO_{2\,(g)}$$

As the temperature increases a small exothermic peak was observed between 675-725°C associated with a sharp mass loss of 3.10% between 645-710°C. XRD analysis of the oxidation product showed the formation of heazlewoodite between 650-685°C with a general formula $(Fe,Ni)_{3\pm x}S_2$. The BSE micrograph shows two distinctive sulfide phases in the core with the brighter phase identified as the high-temperature heazlewoodite phase and the dark phase as mss (Figure 5.11e). EPMA showed the average compositions of the two phases were $Fe_{0.12}Ni_{2.88}S_{2.00}$ and $Fe_{0.06}Ni_{1.13}S_{1.00}$ respectively. The iron:nickel ratio in the mss phase decreased from 0.24 to 0.05 while the metal:sulfur ratio increased from 1.03 to 1.19 as the temperature increased from 650°C to 685°C.

Therefore, between 650°C and 685°C the composition of the mss fell below the mss stability field into the divariant region formed between mss and the high-temperature heazlewoodite phase. This caused the high-temperature heazlewoodite phase to be exsolved within the mss. The formation of a high-temperature heazlewoodite phase resulted in a rapid loss of sulfur from the mss. The heazlewoodite phase forms a limited solid solution with iron resulting in further oxidation of iron and sulfur as the phase is formed. Therefore, the exothermic activity observed between 675-725°C associated with a rapid mass loss can be accounted by the preferential oxidation of sulfur, as the mss is converted to the high-temperature heazlewoodite phase.

The following reaction shows the conversion of mss to heazlewoodite with the loss of sulfur gas:

$$3\ (Fe,Ni)_{1\pm x}S \Leftrightarrow (Fe,Ni)_{3\pm x}S_2 + 0.5\ S_{2\,(g)}$$

A gradual mass loss of 1.25% was associated with no DTA activity observed between 710°C and 790°C. The mass loss can be assigned to the thermal decomposition of $NiSO_4$. FTIR analysis of the oxidation product collected at 725°C showed strong vibrational peaks at 1225, 1200, 1150, 1054 and 988 cm^{-1} due to the presence of $NiSO_4$. By 795°C the infrared spectrum showed only a minor trace of $NiSO_4$ remaining. Strong diffraction patterns were obtained for hematite and trevorite. There was a significant increase in the amount of nickel oxide detected as the temperature increased from 685°C to 725°C when the relative peak intensities were compared against the major oxide phases obtained for hematite and trevorite. The increase in nickel oxide confirms the decomposition of the $NiSO_4$ to nickel oxide during this temperature range. Therefore, the decomposition of $NiSO_4$ can be described by the following reaction above 710°C:

$$NiSO_4 \rightarrow NiO + SO_{2\,(g)} + 0.5\ O_{2\,(g)}$$

XRD analysis of the oxidation product quenched at 725°C showed heazlewoodite as the major sulfide phase with only a minor trace of mss remaining (see Figure 5.11e). EPMA of the mss showed the iron:nickel ratio decreased slightly from 0.053 to 0.050 while the metal:sulfur ratio increased from 1.19 to 1.24 with a composition of $Fe_{0.06}Ni_{1.13}S_{1.00}$ at 685°C and $Fe_{0.06}Ni_{1.18}S_{1.00}$ at 725°C. The solid solution formed by the high-temperature heazlewoodite expanded with both the iron:nickel ratio and metal:sulfur ratio increasing from $Fe_{0.12}Ni_{2.88}S_{2.00}$ (Fe:Ni = 0.042, M:S = 1.50) at 685°C to $Fe_{0.18}Ni_{3.09}S_{2.00}$ (Fe:Ni = 0.058, M:S = 1.64) at 725°C. Since the decomposition of $NiSO_4$ is an endothermic reaction, an exothermic reaction must also

be occurring simultaneously in order for there to be no DTA activity. The oxidation of sulfur as the mss continues to be converted to the high-temperature heazlewoodite phase would probably account for the exothermic activity in this temperature region.

A sharp endotherm was observed at 790°C prior to a large exotherm occurring between 800°C and 845°C. A mass loss of 2.30% coincided with the exotherm. The endotherm was associated with the incongruent melting point of the high-temperature heazlewoodite phase to form mss and a sulfide liquid. The exotherm observed between 800°C and 845°C was attributed to the oxidation of the resulting central sulfide liquid. This occurred over a relatively small temperature range due to a liquid-gas reaction being much more rapid than a solid-gas reaction. Samples collected during the endothermic peak showed both heazlewoodite and mss present in the cores with a composition of $Fe_{0.18}Ni_{3.09}S_{2.00}$ and $Fe_{0.06}Ni_{1.25}S_{1.00}$ respectively. Trevorite appears as a thick inner oxide layer at the sulfide-oxide interface while hematite and nickel oxide are present in the outer oxide layers (Figure 5.11f). Hematite, trevorite and nickel oxide were all detected in the XRD pattern.

$$(Fe,Ni)_{3\pm x}S_{2\,(s)} \Leftrightarrow (Fe,Ni)_{3\pm x}S_{2\,(l)}$$

$$(Fe,Ni)_{3\pm x}S_{2\,(l)} \Leftrightarrow (Fe,Ni)_{1\pm x}S_{\,(s)} + (Fe,Ni)_{1+x}S_{\,(l)}$$

$$(Fe,Ni)_{1+x}S_{\,(l)} \xrightarrow{O_2} Fe_2O_3 + NiO + (Fe,Ni)_3O_4$$

As the temperature was increased beyond 850°C the sulfide had completely oxidised to hematite, trevorite and nickel oxide (Figure 5.11f). The TG curve continued to lose mass up to 1000°C with a total mass loss of 8.15% observed between 25-1000°C. A theoretical mass loss of 8.75% should have been observed for iron-rich pentlandite if completely oxidised to hematite and nickel oxide.

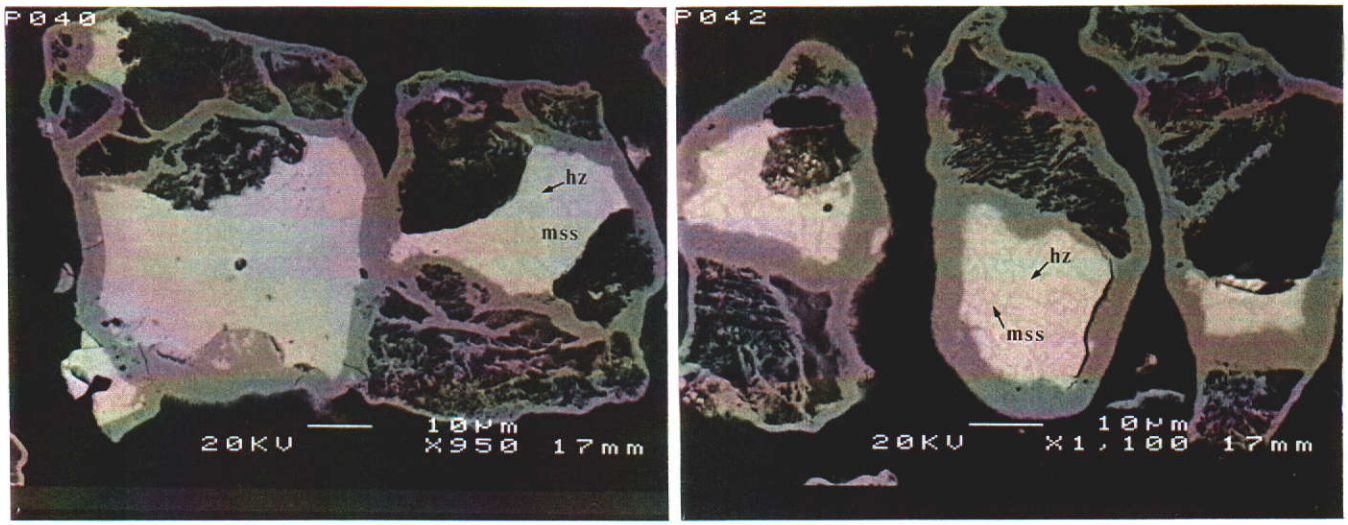

Figure 5.11e BSE micrograph of iron-rich pentlandite collected at 685°C (left) and 725°C (right). Mss can be identified as the dark grey phase while heazlewoodite as the light grey phase.

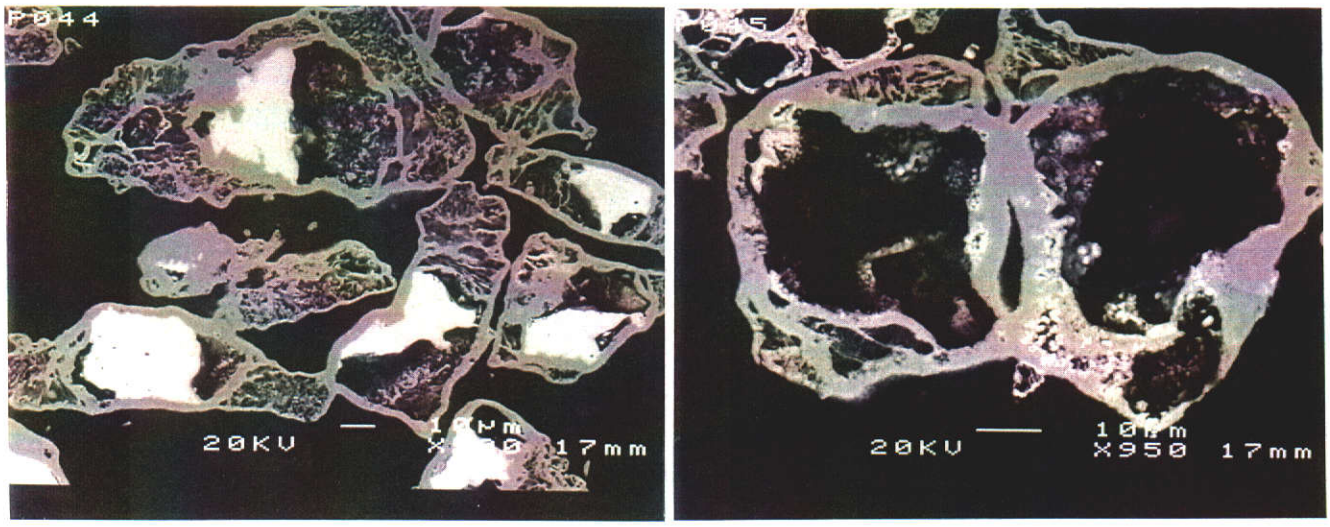

Figure 5.11f BSE micrograph of iron-rich pentlandite quenched at 795°C (left) and 860°C (right).

5.2.2 Summary

Table 5.5 summaries the phases identified during the oxidation of iron-rich pentlandite heated at 10°C min^{-1} in air. The iron-rich pentlandite thermally dissociated to form mss and a more stable pentlandite phase between 400°C and 500°C. By 570°C the remaining pentlandite had been converted to mss by the preferential oxidation of iron forming a mss core surrounded by an hematite product layer. Nickel enrichment of mss continued with the preferential oxidation of the iron sulfide component of the mss between 575°C and 665°C. The mss was then gradually converted to $(Fe,Ni)_{3\pm x}S_2$

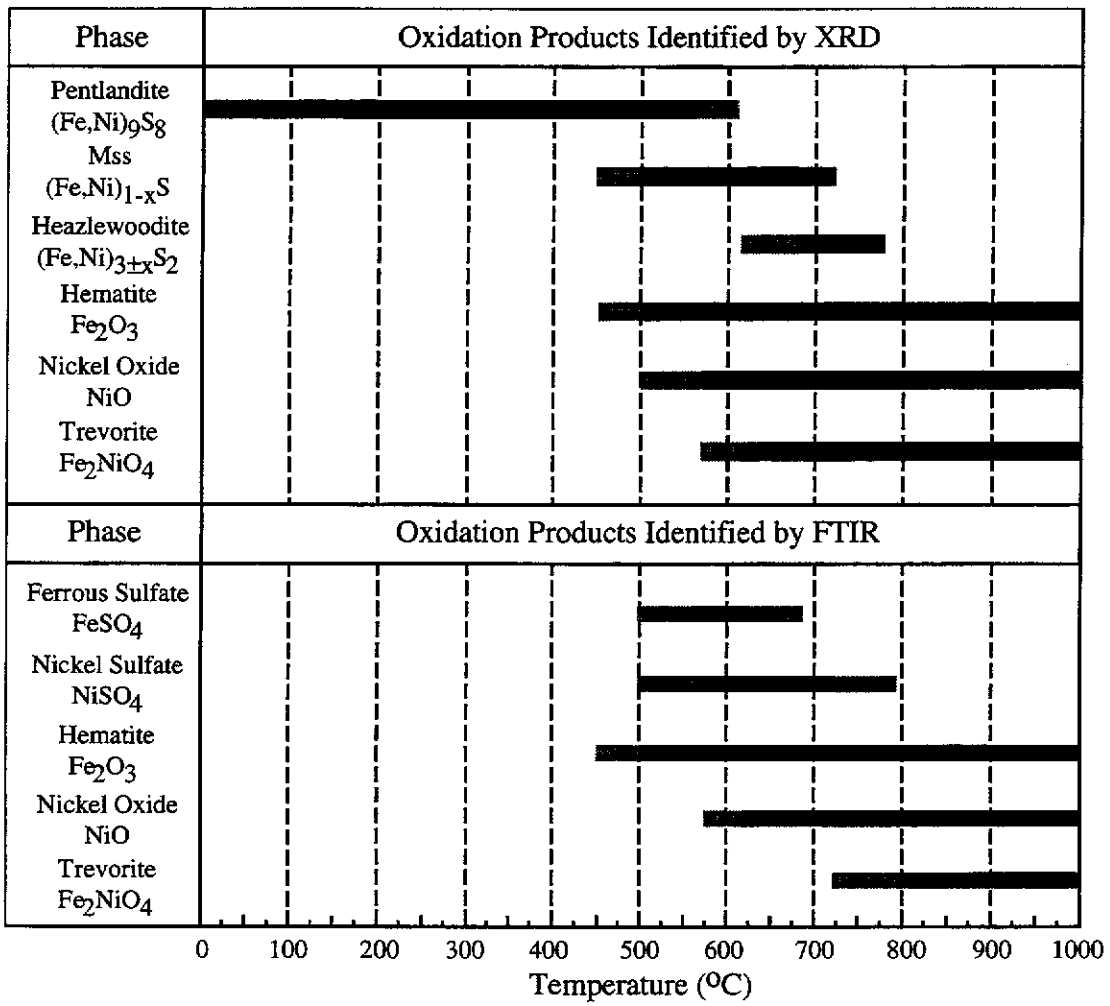

Table 5.5 Summary of the oxidation products identified by XRD and FTIR for iron-rich pentlandite between 25-1000°C. Minor phases are indicated by the shaded line and major phases by the dark line.

between 675°C and 795°C resulting in the loss of sulfur which was oxidised to sulfur dioxide. The remaining nickel sulfide did not oxidise until the incongruent melting point of the high-temperature heazlewoodite phase was obtained. Sulfur dioxide was evolved during the conversion of mss to a sulfide liquid phase. The sulfide liquid phase was then oxidised to completion forming nickel oxide via a liquid-gas reaction.

5.2.3 The Effect of Iron:Nickel Ratio on the Oxidation of Synthetic Pentlandite

A typical TG-DTA trace for each synthetic pentlandite sample heated at 10°C min^{-1} in air is presented in Figure 5.12. The reaction mechanism was unaffected as the stoichiometry varied from iron-rich pentlandite to nickel-rich pentlandite. This was reflected in their TG-DTA traces with the profiles being almost identical for each sample.

Mineralogical examination of oxidation products collected at 500°C for the two endmembers of the pentlandite series, iron-rich and nickel rich pentlandite, showed both samples thermally dissociated to form a metal-rich pentlandite phase and mss. The mss and pentlandite phases in the nickel-rich pentlandite sample were difficult to differentiate due to similar iron and nickel atomic ratios compared with the iron-rich pentlandite sample where there was a large difference in the atomic ratios between the mss and pentlandite (see Figure 5.13a). For example, the pentlandite and mss phases for the nickel-rich pentlandite sample showed only a minor deviation in the iron:nickel ratio with respective compositions of $Fe_{3.60}Ni_{5.82}S_8$ (Fe:Ni = 0.62, M:S = 1.17) and $Fe_{0.35}Ni_{0.66}S_{1.00}$ (Fe:Ni = 0.53, M:S = 1.01), compared to iron-rich pentlandite where the iron:nickel ratio of the mss was far greater than the pentlandite phase with respective compositions of $Fe_{0.72}Ni_{0.25}S_{1.00}$ (Fe:Ni = 2.88, M:S = 0.97) and $Fe_{4.68}Ni_{4.60}S_8$ (Fe:Ni = 1.02, M:S = 1.16).

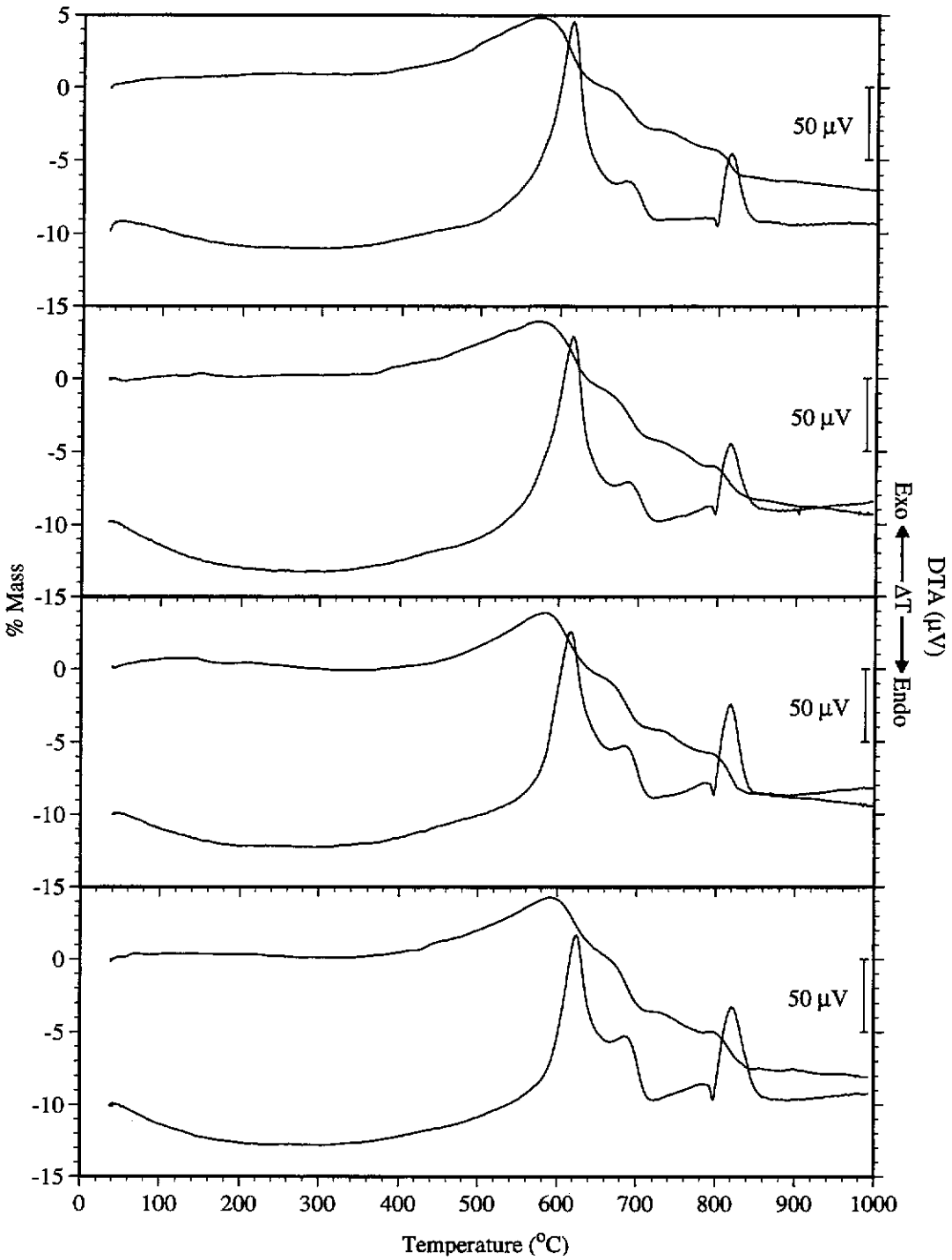

Figure 5.12 Typical TG-DTA traces for the entire range of synthetic pentlandites, heated at 10°C min^{-1} in an air atmosphere. Starting from the top $Fe_{5.80}Ni_{3.15}S_8$ (iron-rich pentlandite), $Fe_{5.59}Ni_{3.42}S_8$, $Fe_{5.36}Ni_{3.79}S_8$, and $Fe_{5.08}Ni_{4.06}S_8$.

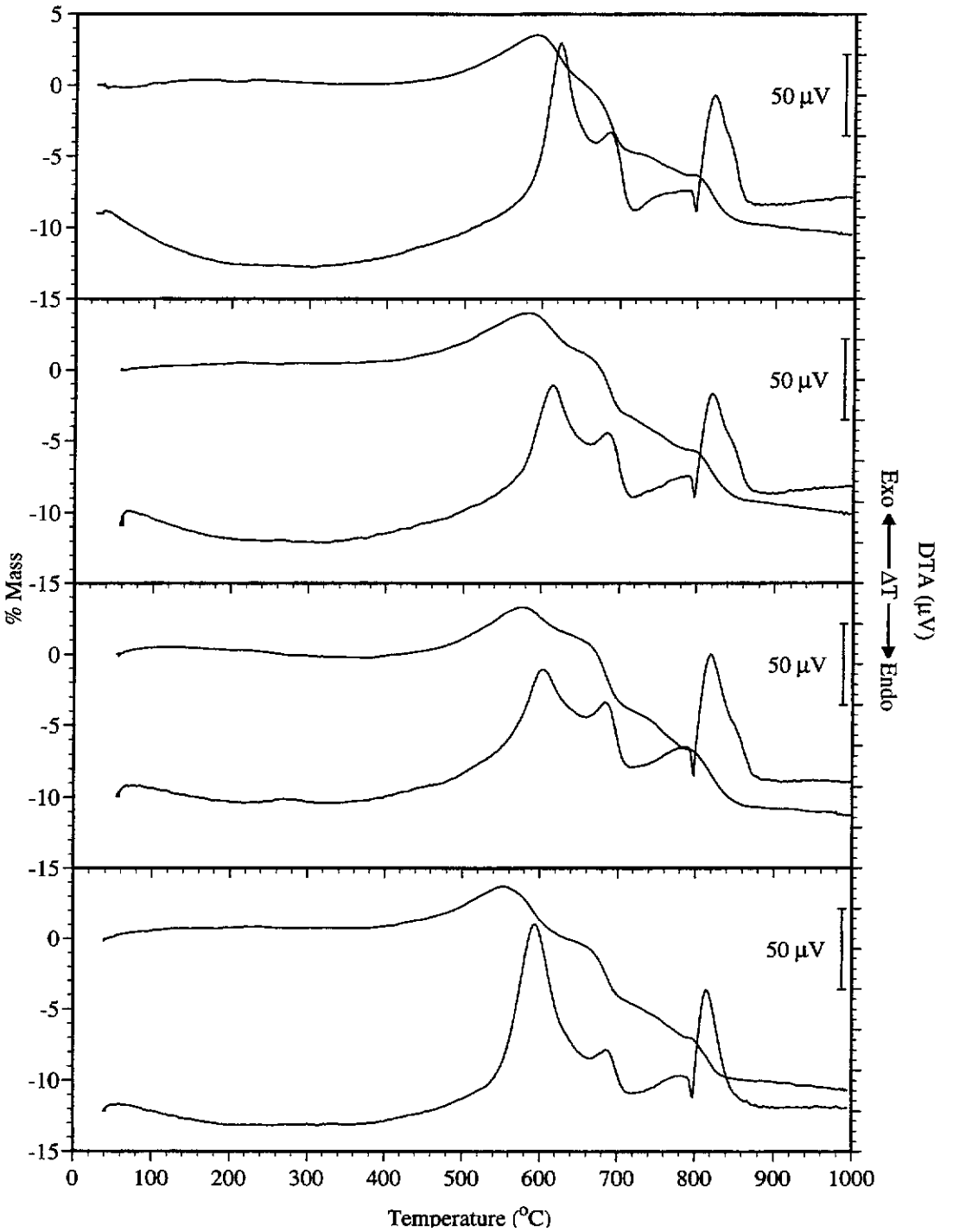

Figure 5.12 (con't) Typical TG-DTA traces for the entire range of synthetic pentlandites, heated at 10°C min^{-1} in an air atmosphere. Starting from the top $Fe_{4.59}Ni_{4.43}S_8$ (ideal pentlandite), $Fe_{4.01}Ni_{4.89}S_8$, $Fe_{3.40}Ni_{5.55}S_8$ (nickel-rich pentlandite), and $Fe_{4.20}Ni_{4.16}S_8$ (sulfur-rich pentlandite).

By 570°C both iron-rich and nickel-rich pentlandite had almost completely been converted to mss with only a minor trace of pentlandite remaining. The mass gain associated with the preferential oxidation of iron decreased as the iron:nickel ratio decreased, with iron-rich pentlandite gaining 3.85% between 380-570°C, while nickel-rich pentlandite gained 3.50% between 390-570°C. A minor amount of iron and nickel sulfate was also detected in the infrared spectrum at 570°C for both iron-rich and nickel-rich pentlandite.

Each sample commenced mass loss at 575°C coincided with the decomposition temperature of $FeSO_4$. A large exothermic peak coincided with the mass loss associated with the preferential oxidation of the iron sulfide component of the mss. The onset and offset temperatures of the DTA events were similar, however the intensity of the exotherm decreased as the iron:nickel ratio decreased from iron-rich to nickel-rich pentlandite. The preferential oxidation of iron was clearly evident in both the endmembers of the pentlandite solid solution. EPMA of the iron-rich and nickel-rich pentlandite showed a decrease in the iron:nickel ratio of the mss from the centre of the mss core to the mss-oxide interface. For example, at 570°C the iron:nickel ratio decreased from 0.51 ($Fe_{0.34}Ni_{0.67}S_{1.00}$) to 0.38 ($Fe_{0.27}Ni_{0.73}S_{1.00}$) for nickel-rich pentlandite. Similarly, for iron-rich pentlandite the iron:nickel ratio decreased from 1.41 ($Fe_{0.55}Ni_{0.39}S_{1.00}$) to 1.29 ($Fe_{0.54}Ni_{0.42}S_{1.00}$). By 650°C the iron:nickel ratios were similar for both nickel-rich and iron-rich pentlandites with the iron:nickel ratios ranging from 0.19 ($Fe_{0.16}Ni_{0.86}S_{1.00}$) to 0.12 ($Fe_{0.11}Ni_{0.94}S_{1.00}$) and 0.24 ($Fe_{0.20}Ni_{0.83}S_{1.00}$) to 0.19 ($Fe_{0.17}Ni_{0.88}S_{1.00}$) from the mss centre to the mss-oxide interface for the respective pentlandite samples. A comparison of the BSE micrographs of the endmembers of the pentlandite series quenched at 650°C both had similar particle morphology with a dark oxide rim surrounding a mss core (Figure 5.13b). The iron-rich pentlandite had undergone a greater extent of oxidation compared to the nickel-rich pentlandite due to the higher iron content.

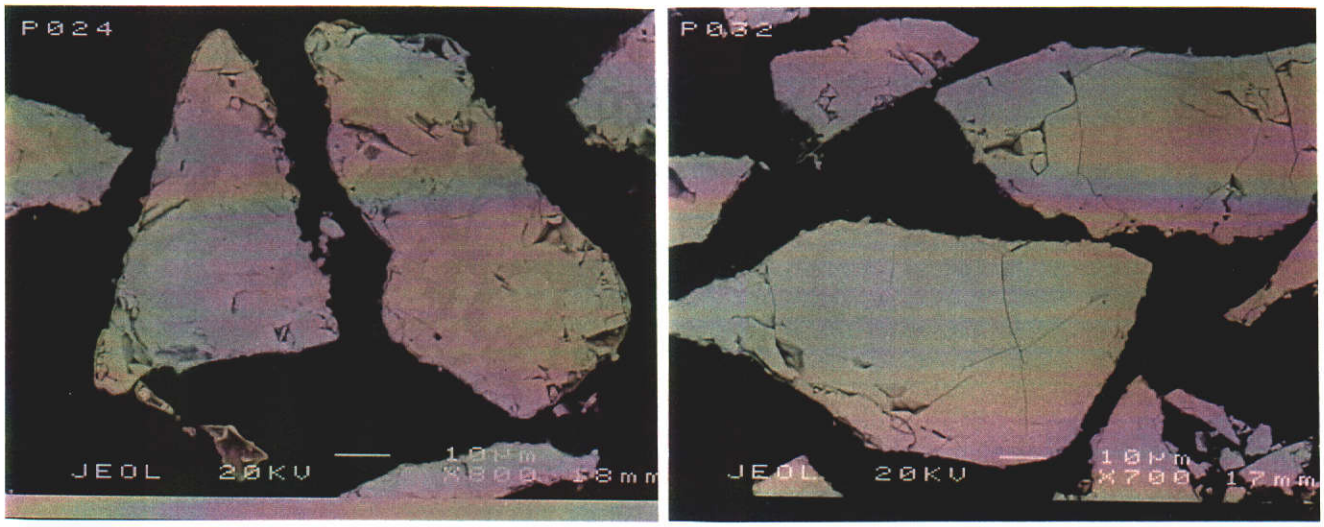

Figure 5.13a Comparison of BSE micrographs of iron-rich pentlandite (left) and nickel-rich pentlandite (right) quenched at 500°C.

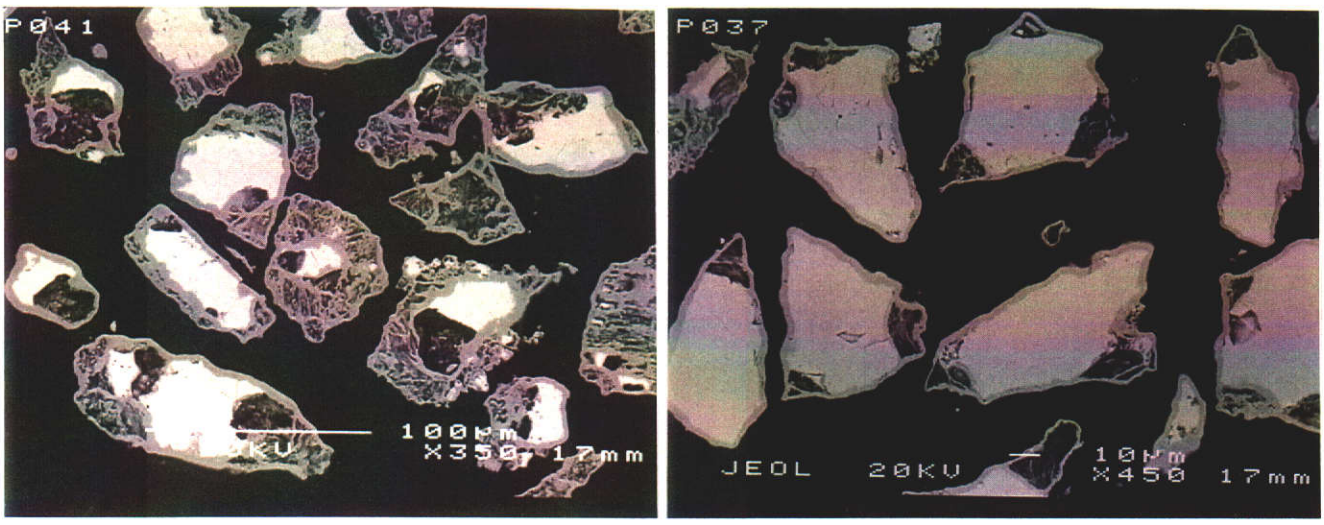

Figure 5.13b Comparison of BSE micrographs of iron-rich pentlandite (left) and nickel-rich pentlandite (right) quenched at 650°C.

The intensity of the exotherm, associated with the conversion of mss to $(Fe,Ni)_{3\pm x}S_2$ between the temperature range of 665-725°C, decreased as the iron:nickel ratio increased. This can be attributed to a reduction in the amount of mss remaining in the sulfide core after the preferential oxidation of the iron sulfide component of the mss. Hence, as the iron:nickel ratio increases the loss of sulfur and subsequent oxidation to sulfur dioxide during the conversion of mss to $(Fe,Ni)_{3\pm x}S_2$ will decrease. For example, nickel-rich pentlandite exhibited a mass loss of 5.20% between 620-700°C compared with only a 3.10% loss between 615-715°C for iron-rich pentlandite.

A comparison of the BSE micrographs of the oxidation products collected at 725°C for the two endmembers of the pentlandite series showed mss and heazlewoodite present in the sulfide cores (Figure 5.13c). Large holes were evident in both samples between the sulfide core and the oxide rim due to a reduction in volume as the mss was converted to heazlewoodite. Table 5.6 shows a comparison of the composition of mss and heazlewoodite for iron-rich and nickel-rich pentlandite samples. The iron:nickel and metal:sulfur ratios of the mss and heazlewoodite were similar for the two endmembers of the pentlandite series. At 710°C, $NiSO_4$ commenced decomposition to NiO with all of the pentlandite samples exhibiting a mass loss between 705-785°C.

Temperature	Iron-Rich Pentlandite		Nickel-Rich Pentlandite	
(°C)	$(Fe,Ni)_{1-x}S$	$(Ni,Fe)_{3\pm x}S_2$	$(Fe,Ni)_{1-x}S$	$(Ni,Fe)_{3\pm x}S_2$
685	$(Fe_{0.06}Ni_{1.13})S$	$(Ni_{2.88}Fe_{0.12})S_2$	$(Fe_{0.05}Ni_{1.09})S$	$(Ni_{2.93}Fe_{0.08})S_2$
725	$(Fe_{0.06}Ni_{1.18})S$	$(Ni_{2.96}Fe_{0.19})S_2$	$(Fe_{0.04}Ni_{1.15})S$	$(Ni_{2.94}Fe_{0.12})S_2$
790	$(Fe_{0.06}Ni_{1.25})S$	$(Ni_{3.09}Fe_{0.18})S_2$	$(Fe_{0.04}Ni_{1.18})S$	$(Ni_{2.96}Fe_{0.12})S_2$

Table 5.6 Composition of mss and heazlewoodite phases in the sulfide cores of iron-rich and nickel-rich pentlandite samples collected at various temperatures.

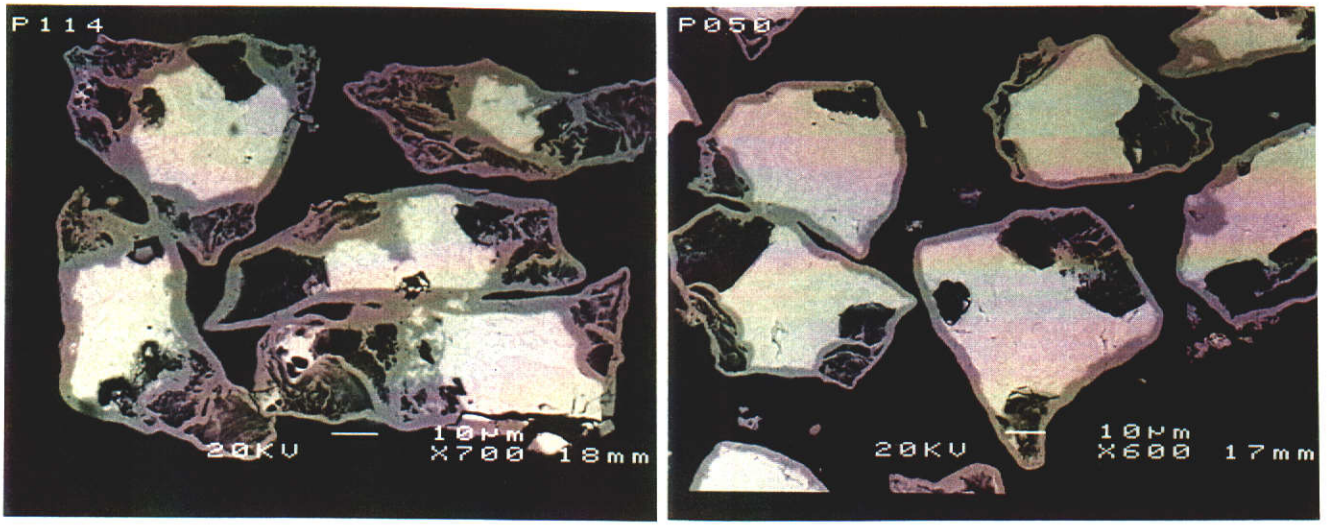

Figure 5.13c Comparison of BSE micrographs of iron-rich pentlandite (left) and nickel-rich pentlandite (right) quenched at 725°C.

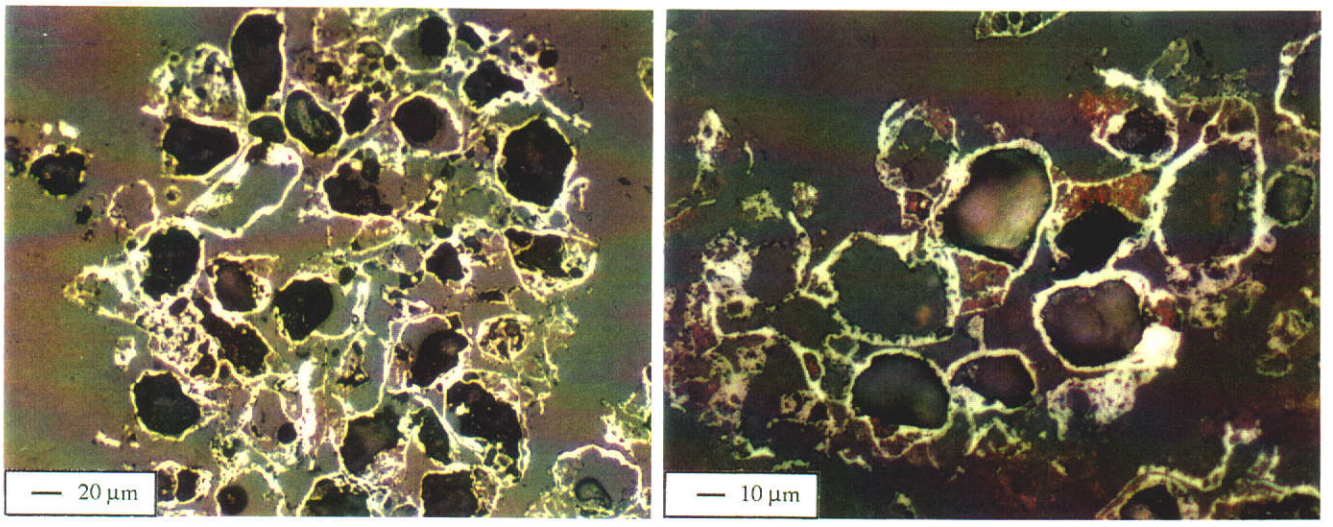

Figure 5.13d Comparison of optical micrographs of iron-rich pentlandite (left) and nickel-rich pentlandite (right) quenched at 860°C.

The onset temperature of the endothermic peak associated with the incongruent melting of heazlewoodite to mss and central sulfide liquid was observed at 790°C for the entire range of synthetic pentlandite samples. This was followed by a large exothermic peak and rapid mass loss. The intensity of the exotherm and the extent of mass loss increased as the iron:nickel ratio decreased. A mass loss of 4.00% between 790-860°C was observed for the nickel-rich pentlandite compared to only 2.30% mass loss for the iron-rich pentlandite sample between the temperature range of 775-845°C. By the offset temperature of the exothermic peak both endmembers had completely oxidised to hematite, trevorite and nickel oxide with an approximate 21% reduction in volume (see Figure 5.13d).

The total mass loss, observed between 25-1000°C, increased as the iron:nickel ratio decreased with iron-rich pentlandite exhibiting a mass loss of 8.15% compared to nickel-rich pentlandite with a loss of 11.25%. These were consistent with the theoretical mass losses of 8.75% and 11.50% calculated for the complete oxidation to hematite and nickel oxide.

5.2.4 The Effect of Metal:Sulfur Ratio on the Oxidation of Synthetic Pentlandite

A typical TG-DTA trace for sulfur-rich pentlandite heated at 10°C min^{-1} in air with a particle size range of 63-45 μm is shown in Figure 5.12. The oxidation mechanism was unaffected by a variation in the metal:sulfur ratio.

The initial mass gain associated with the preferential oxidation of iron due to the conversion of pentlandite to mss was lower for the sulfur-rich pentlandite than for the ideal pentlandite sample. For example, sulfur-rich pentlandite exhibited a mass gain of 2.90% between 380-555°C, while ideal pentlandite showed a mass gain of 3.40% between 405-590°C. This can be attributed to the lower metal:sulfur ratio of the

sulfur-rich pentlandite, and therefore less iron is required to be preferentially oxidised to decrease the metal:sulfur ratio sufficiently to convert all the pentlandite to mss.

Once all of the pentlandite had been converted to mss the iron sulfide component, $Fe_{1-x}S$, of the mss was preferential oxidised, with mass losses of 4.30% (555-665°C) and 4.20% (590-670°C) observed for sulfur-rich pentlandite and ideal pentlandite, respectively. This coincided with a major exothermic peak in the DTA trace in the temperature ranges of 550-640°C and 585-645°C. The onset temperature of the major exotherm was 35°C higher for the ideal pentlandite sample than for the sulfur-rich pentlandite sample. Therefore, as the metal:sulfur ratio increased from 1.04 to 1.13, there was a decrease in the relative reactivity of the pentlandite.

The onset and offset temperatures of the DTA events associated with the oxidation of the remaining nickel sulfide component were identical for both pentlandite samples. The observed mass losses for the sulfur-rich pentlandite sample were lower than for the ideal pentlandite sample due to less nickel present in the initial sample.

Total mass losses of 11.95% and 9.80% were found for sulfur-rich pentlandite and ideal pentlandite, respectively. These correlates well with the theoretical mass losses of 12.10% and 9.75% for the respective sulfides if they were oxidised to hematite and nickel oxide.

5.3 Oxidation of Synthetic Pentlandite Under Ignition Conditions

In this section the ignition behaviour of synthetic pentlandite will be examined using thermal analytical techniques. By increasing the heating rate from 10°C to 40°C min^{-1} and oxygen partial pressure by converting the atmosphere from air to oxygen, ignition conditions may be achieved. The effect of stoichiometry and particle size on the ignition behaviour will also be discussed.

5.3.1 Oxidation of Iron-Rich Pentlandite

The TG-DTA profile for iron-rich pentlandite, with a particle size of 63-45 μm, heated under conditions of 40°C min^{-1} and an oxygen atmosphere, is shown in Figure 5.14. The TG-DTA profile is similar to that recorded at 10°C min^{-1} in air (Figure 5.8) and so no significant effect on the reaction mechanism has occurred by an increase in the intensity of the oxidising conditions.

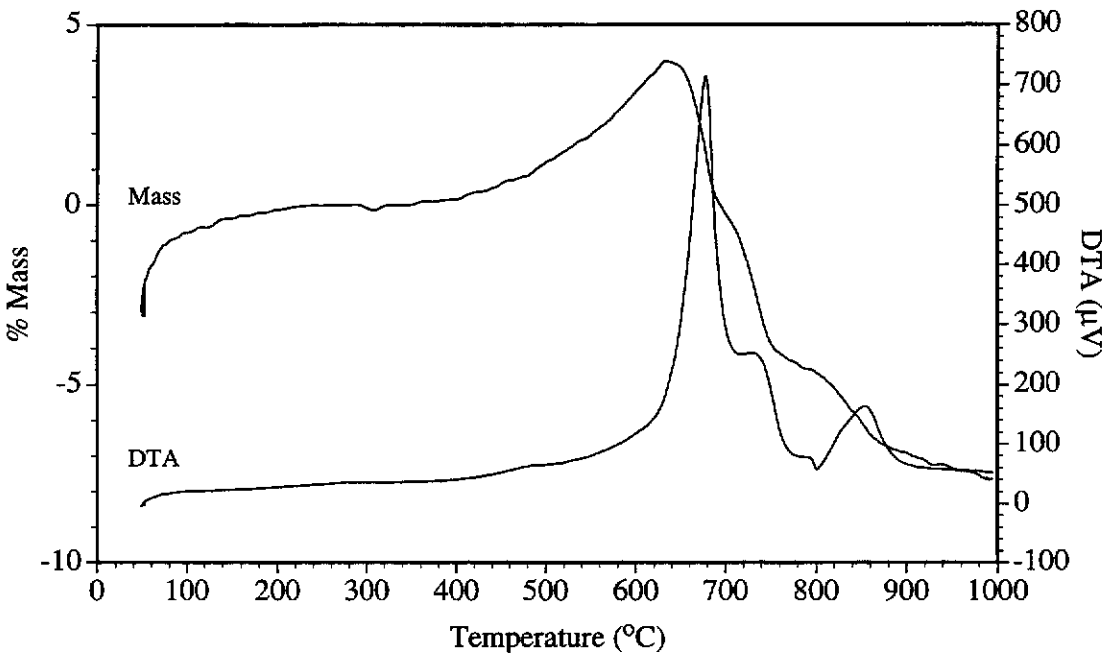

Figure 5.14 TG-DTA trace of iron-rich pentlandite ($Fe_{5.80}Ni_{3.15}S_8$), heated at 40°C min^{-1} in an oxygen atmosphere, 63-45 μm particle size fraction.

An initial mass gain of 4.00% was observed between 340-630°C associated with the preferential oxidation of iron as the pentlandite was converted to mss. This was followed by a sharp exothermic peak between 640-700°C coinciding with a rapid mass loss of 3.90% between 630-685°C. The exothermic activity was attributed to the preferential oxidation of the iron sulfide component in the mss phase. The onset temperature of the exothermic peak had increased by approximately 65°C due to an increase in the heating rate from 10°C min^{-1} to 40°C min^{-1}. There was a five-fold increase in the intensity of the exotherm when compared to the peak intensity of the major exotherm recorded under less vigorous oxidising conditions of 10°C min^{-1} in an air atmosphere.

The rate of mass loss decreased between 685-710°C with a loss of 0.90%. The conversion of mss to heazlewoodite resulted in the evolution of sulfur vapour which was oxidised at the sulfide-oxide interface to form sulfur dioxide gas. A 3.10% mass loss was associated with the loss of sulfur vapour from the mss between the temperature range of 710-750°C. This coincided with an exothermic peak with an onset and offset temperature of 710°C and 770°C.

The iron-rich pentlandite continued to lose mass with a loss of 0.55% observed between the temperature range of 750-805°C. The oxidation of the nickel sulfide component was initiated by the incongruent melting transition of $(Fe,Ni)_{3\pm x}S_2$ characterised by a sharp endothermic peak with an onset temperature of 790°C. This was immediately followed by a large exothermic peak between 800°C and 890°C and a 2.10% mass loss.

Although the oxidation of the iron sulfide component showed behaviour indicative of an ignition reaction the conditions were not sufficiently vigorous to oxidise remaining nickel sulfide. The sample temperature must exceed the incongruent melting point of $(Fe,Ni)_{3\pm x}S_2$ in order for the remaining nickel sulfide to be oxidised. Hence, the

oxidation of the nickel sulfide component occurred in a step wise reaction mechanism over a wide temperature range. Consequently a four-fold increase in the heating rate and an increase in the partial pressure of oxygen was not sufficient to completely ignite the iron-rich pentlandite sample.

5.3.2 Effect of Iron:Nickel Ratio on the Oxidation Behaviour of Synthetic Pentlandite

The TG-DTA profiles for the entire range of synthetic pentlandite, heated under conditions of 40°C min^{-1} in and oxygen atmosphere are shown in Figure 5.15. The profiles showed that there was no significant effect of stoichiometry on the oxidation behaviour of synthetic pentlandite as the iron:nickel ratio decreased from $Fe_{5.80}Ni_{3.15}S_8$ (iron-rich pentlandite) to $Fe_{3.40}Ni_{5.55}S_8$ (nickel-rich pentlandite).

Each of the synthetic pentlandite samples exhibited a mass gain between approximately 350-640°C. The mass gain was relatively constant as the iron:nickel ratio decreased. Analysis of oxidation products collected at 600°C for the two endmembers of the pentlandite series both revealed mss as the major sulfide phase and a minor amount of hematite. The incongruent phase transition of pentlandite to mss and $(Fe,Ni)_{3\pm x}S_2$ was evident in the DTA curve for the nickel-rich pentlandite sample between the temperature range of 580-605°C (Figure 5.15). The endothermic transition was not apparent in the DTA curves for the remaining pentlandite samples due to the transition coinciding with the onset of the main exothermic peak.

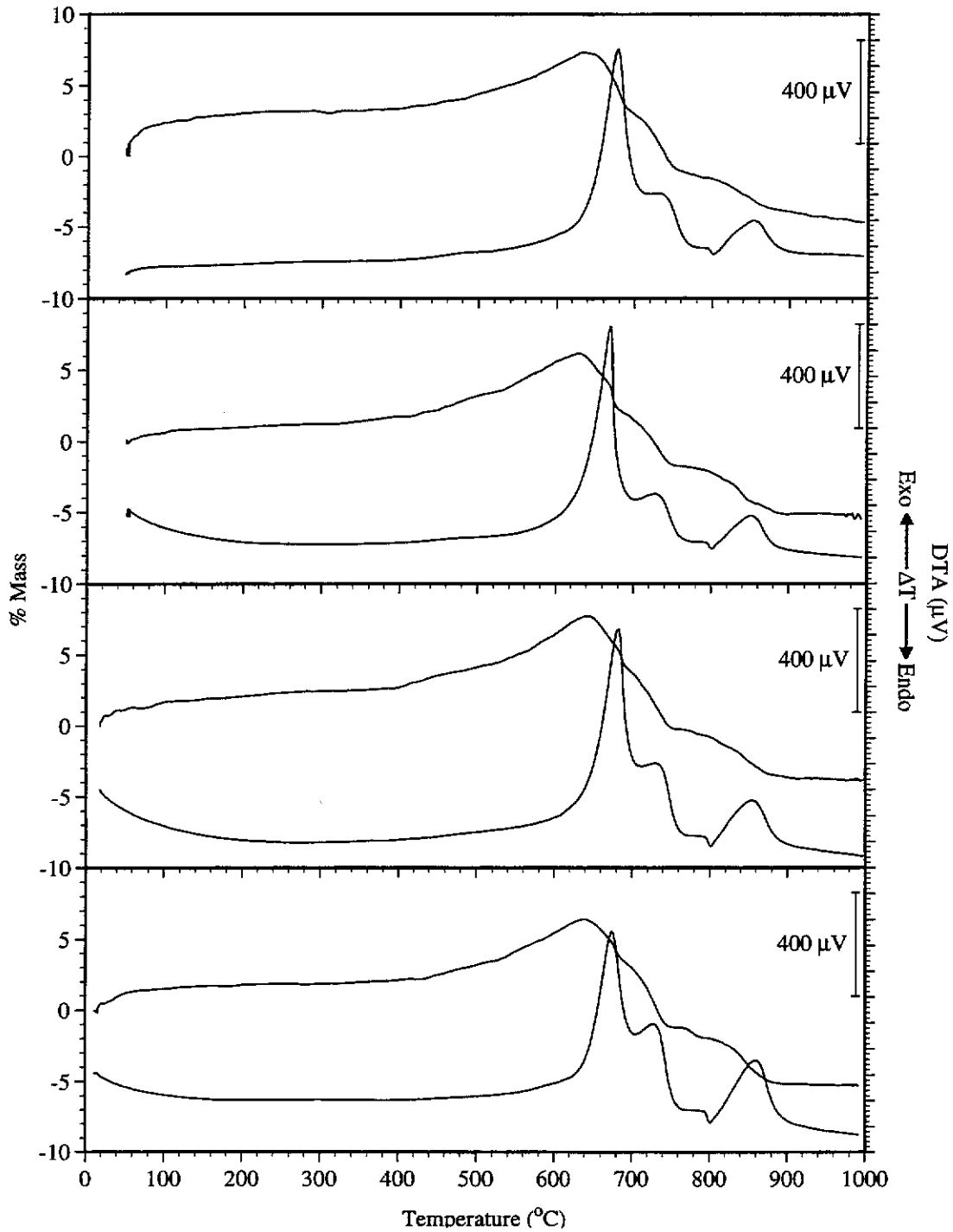

Figure 5.15 Typical TG-DTA traces for the entire range of synthetic pentlandites, heated at 40°C min^{-1} in an oxygen atmosphere. Starting from the top $Fe_{5.80}Ni_{3.15}S_8$ (iron-rich pentlandite), $Fe_{5.59}Ni_{3.42}S_8$, $Fe_{5.36}Ni_{3.79}S_8$, and $Fe_{5.08}Ni_{4.06}S_8$.

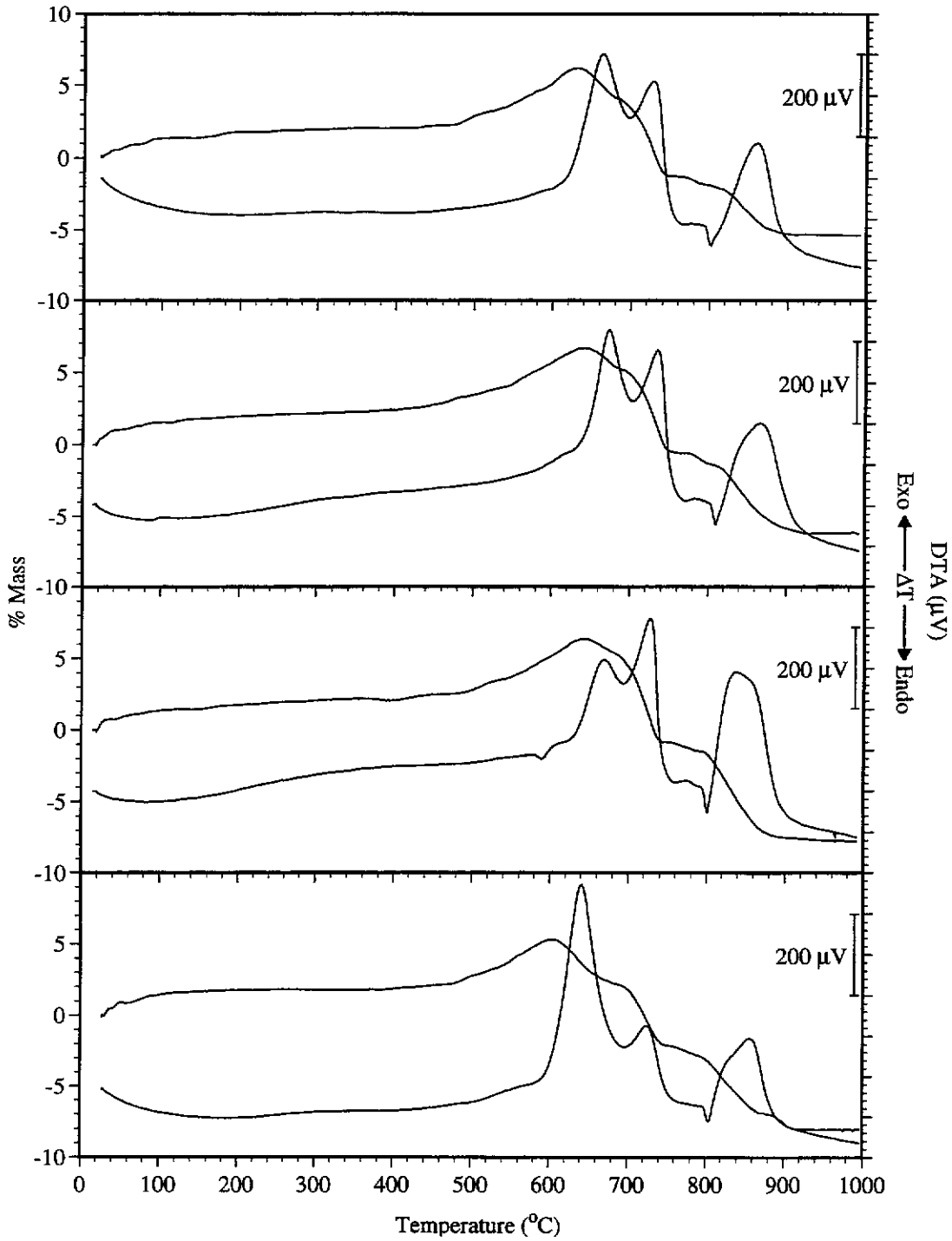

Figure 5.15 (con't) Typical TG-DTA traces for the entire range of synthetic pentlandites, heated at 40°C min^{-1} in an oxygen atmosphere. Starting from the top $Fe_{4.59}Ni_{4.43}S_8$ (ideal pentlandite), $Fe_{4.01}Ni_{4.89}S_8$, $Fe_{3.40}Ni_{5.55}S_8$ (nickel-rich pentlandite) and $Fe_{4.20}Ni_{4.16}S_8$ (sulfur-rich pentlandite).

Between 630°C and 685°C the synthetic pentlandites showed a sharp mass loss accompanied by a large exothermic peak associated with the preferential oxidation of the iron sulfide component of the mss. The extent of mass loss decreased as the iron:nickel ratio decreased with iron-rich pentlandite exhibiting a loss of 3.90% (630-685°C) compared with only 0.70% (640-670°C) for the nickel-rich pentlandite. The effect of the iron:nickel ratio on the preferential oxidation of iron was apparent by the intensity of the exotherm, with the iron-rich pentlandite peak being approximately four times greater than the nickel-rich pentlandite.

X-ray maps of partially oxidised samples collected prior to the exothermic activity for the iron-rich pentlandite showed the iron-nickel distribution to be relatively uniform across the sulfide core (Figure 5.16a). During the exothermic activity the iron diffuses towards the oxygen interface causing the iron to be depleted within the mss and concentrated in the oxide product layer (Figure 5.16b). This is clearly illustrated by x-ray line profiles of iron distribution across the sulfide particles (Figure 5.17). At 650°C, the x-ray line profile shows the iron was evenly distributed across the mss core. The intensity then increased sharply at the sulfide-oxide interface reaching a maximum across the oxide product layer before returning to the baseline at the outer rim of the oxide product layer (Figure 5.17a). By 750°C the iron remaining in the mss core had decreased substantially with the majority of the iron redistributed to the outer oxide product layer (Figure 5.17b). Similarly for the nickel-rich pentlandite, at 650°C the iron concentration decreased from the centre of the mss core to the sulfide-oxide interface where it then increased sharply in intensity across the oxide product layer (Figure 5.17c). By 750°C the iron has almost been completely preferentially oxidised with x-ray line profile showing the iron depleted across the mss core and redistributed to the oxide product layer (see Figure 5.17d).

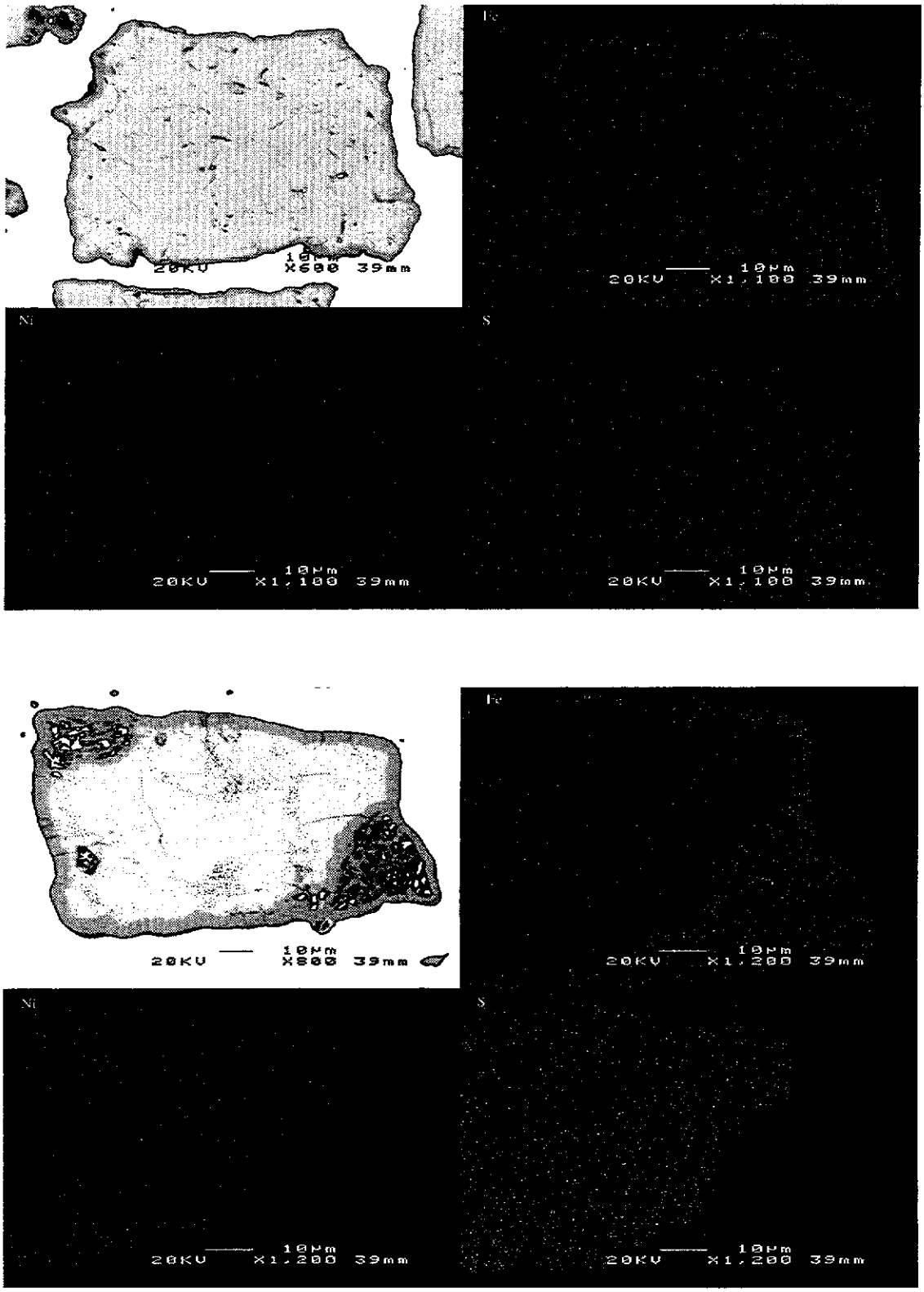

Figure 5.16a X-ray map of iron-rich pentlandite ($Fe_{5.80}Ni_{3.15}S_8$) quenched at 650°C (above) and 750°C (below) showing the distribution of iron, nickel and sulfur.

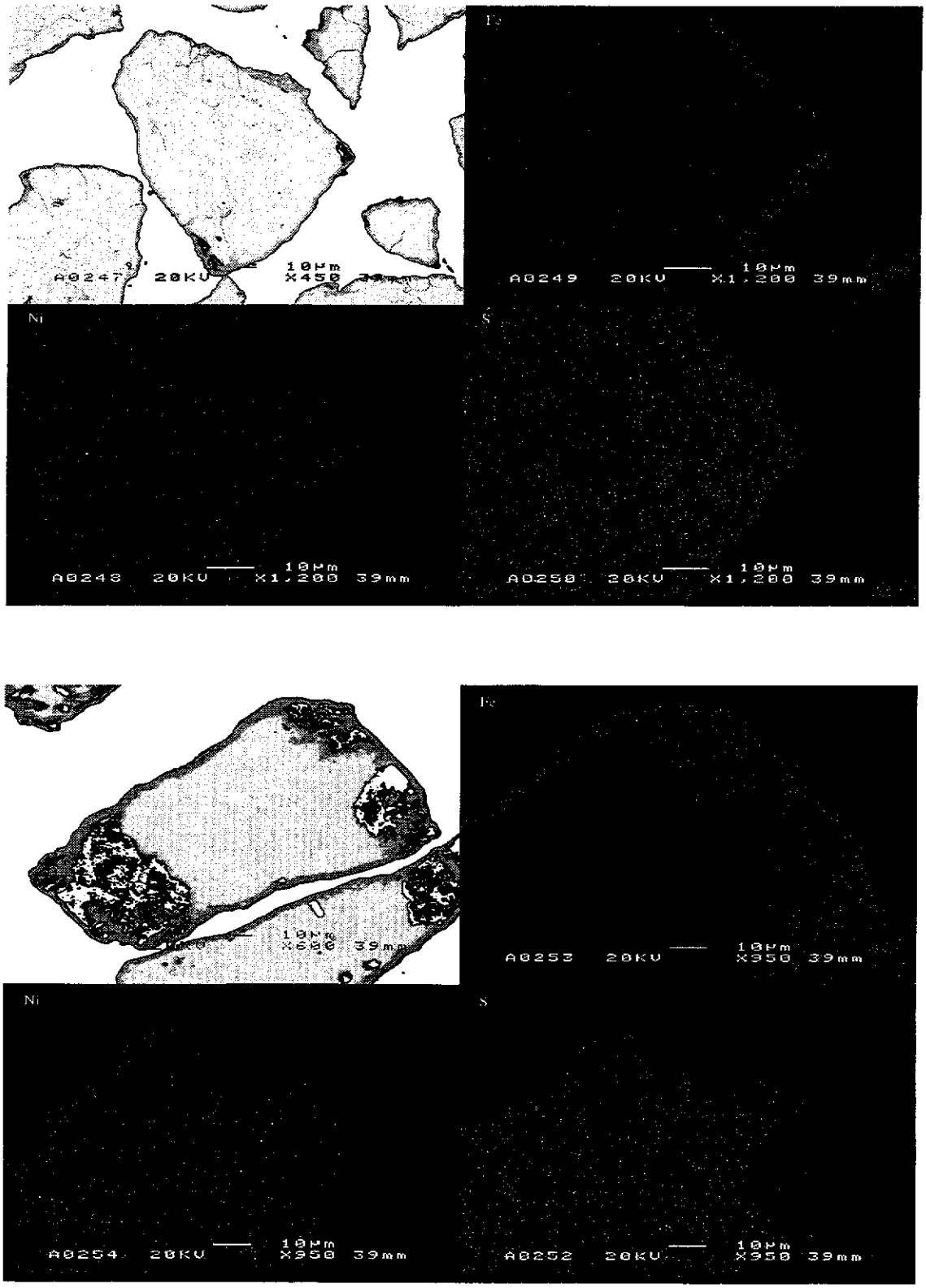

Figure 5.16b X-ray map of nickel-rich pentlandite ($Fe_{3.40}Ni_{5.55}S_8$) quenched at 650°C (above) and 750°C (below) showing the distribution of iron, nickel and sulfur.

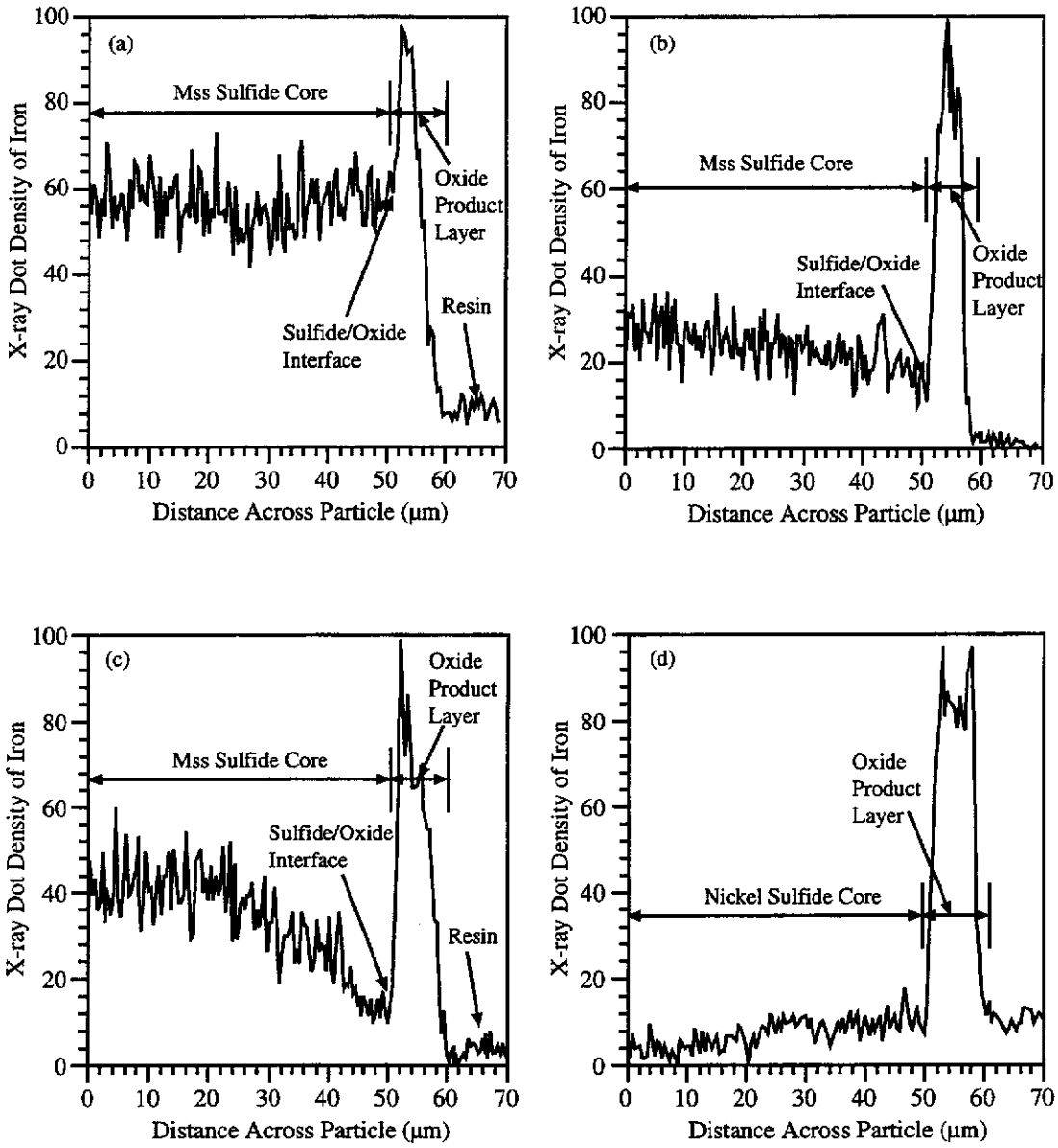

Figure 5.17 X-ray intensity of iron across partially oxidised samples of iron-rich pentlandite ($Fe_{5.80}Ni_{3.15}S_8$) collected at (a) 650°C and (b) 750°C, and nickel-rich pentlandite ($Fe_{3.40}Ni_{5.55}S_8$) collected at (c) 650°C and (d) 750°C, for the 125-90 μm particle size fraction.

The rate of mass loss decreased between 690-710°C and 670-685°C with mass losses of 0.90% and 0.45% observed for iron-rich and nickel-rich pentlandite respectively. The decrease in the rate of oxidation was due to the depletion of iron in the mss core. EPMA analysis of iron-rich and nickel-rich pentlandite quenched at 710°C and 685°C revealed mss as the major phase with an average composition of $Fe_{0.06}Ni_{1.14}S_{1.00}$ and $Fe_{0.04}Ni_{1.16}S_{1.00}$. There was also a minor amount of $(Fe,Ni)_{3\pm x}S_2$ detected with an average composition of $Fe_{0.16}Ni_{2.99}S_{2.00}$ and $Fe_{0.07}Ni_{3.04}S_{2.00}$ for iron and nickel-rich pentlandite respectively.

This was followed by a more rapid mass loss of 3.10% and 5.90% between 715-750°C and 685-740°C for iron and nickel-rich pentlandite, associated with the conversion of mss to $(Fe,Ni)_{3\pm x}S_2$ with the loss of sulfur vapour. The extent of the mass loss was dependent on the iron:nickel ratio with the nickel-rich pentlandite samples exhibiting an increase in mass loss as the nickel content increased.

The incongruent melting point transition of $(Fe,Ni)_{3\pm x}S_2$ occurred at 800°C for the entire range of synthetic pentlandites. The composition of the high-temperature heazlewoodite phase approached an ideal composition of Ni_3S_2. The intensity of the transition increased as the iron:nickel ratio decreased. The endothermic transition was immediately followed by the oxidation of the nickel sulfide core. The extent of mass loss increased as the iron:nickel ratio increased with iron-rich and nickel-rich pentlandite exhibiting a mass loss of 2.10% (800-870°C) and 5.90% (800-880°C) respectively.

The total mass loss observed between 25-1000°C increased as the nickel content of the synthetic pentlandite range increased with iron-rich and nickel-rich pentlandite exhibiting a mass loss of 6.40% and 9.60% respectively.

5.3.3 Effect of Metal:Sulfur Ratio on the Oxidation Behaviour of Synthetic Pentlandites

A typical TG-DTA trace of sulfur-rich and ideal pentlandite is shown in Figure 5.15, heated at 40°C min^{-1} in an oxygen atmosphere. There was no effect on the oxidation mechanism of synthetic pentlandite due to a variation in the metal:sulfur ratio. The onset temperature of the major exotherm was slightly lower for the sulfur-rich pentlandite compared to the ideal pentlandite. The intensity of the initial exotherm for the sulfur-rich pentlandite was approximately twice that of the ideal pentlandite sample. This was attributed to the higher sulfur content of the sulfur-rich pentlandite which is preferentially oxidised during the initial exothermic activity. The onset and offset temperatures of the DTA events associated with the oxidation of the nickel sulfide component were similar for both pentlandite samples.

5.3.4 Effect of Particle Size on the Oxidation Behaviour of Synthetic Pentlandite.

The effect of particle size on the oxidation behaviour of iron-rich and nickel-rich pentlandite, heated at 40°C min^{-1} in oxygen, is shown in Figure 5.18. As the iron:nickel ratio decreased the effect of particle size on the onset temperature of the initial exotherm, associated with the preferential oxidation of the iron sulfide component of the mss, increased. For example, the onset temperature decreased from 650°C to 605°C and from 700°C to 585°C between the 125-90 μm and 45-20 μm particle size fractions for iron-rich and nickel-rich pentlandite respectively. This represented a decrease of 45°C and 115°C in the onset temperatures as the particle size decreased. Similarly as the metal:sulfur ratio decreased the effect of particle size on the onset temperature of the initial exotherm decreased (Figure 5.19). For example, the onset temperature decreased from 700°C to 610°C and from 610°C to 595°C between the coarsest and finest particle size fractions for ideal and sulfur-rich pentlandite.

The effect of stoichiometry on the onset temperature of the exothermic activity decreased as the particle size decreased. For example, the 45-20 μm fraction for iron-rich and nickel-rich pentlandite only showed a difference of 20°C between the onset temperature of the exothermic activity, while the 125-90 μm particle size fraction showed a difference of 50°C. For ideal and sulfur-rich pentlandite the 45-20 μm showed a difference of only 15°C between the onset temperatures, whereas the 125-90 μm fraction showed a decrease of 90°C.

As the particle size decreased the increase in the relative reactivity of the pentlandite was insufficient to oxidise the remaining nickel sulfide component. The 45-20 μm fraction for iron-rich pentlandite exhibited a highly exothermic peak coinciding with a rapid mass loss and a temperature excursion of 20°C above the programmed furnace rate. The intensity of the exotherm was approximately 10 times greater than the intensity expected by a four-fold increase in the heating rate. Only 1.05% of a total mass loss of 6.50% was observed with the main exothermic activity. Hence, the heat generated by the oxidation of the iron sulfide component of the mss was insufficient to oxidise the remaining nickel sulfide to completion. The phase transition of nickel-rich mss to the high-temperature form of heazlewoodite and the subsequent incongruent melting and oxidation of the heazlewoodite phase was unaffected by a decrease in particle size.

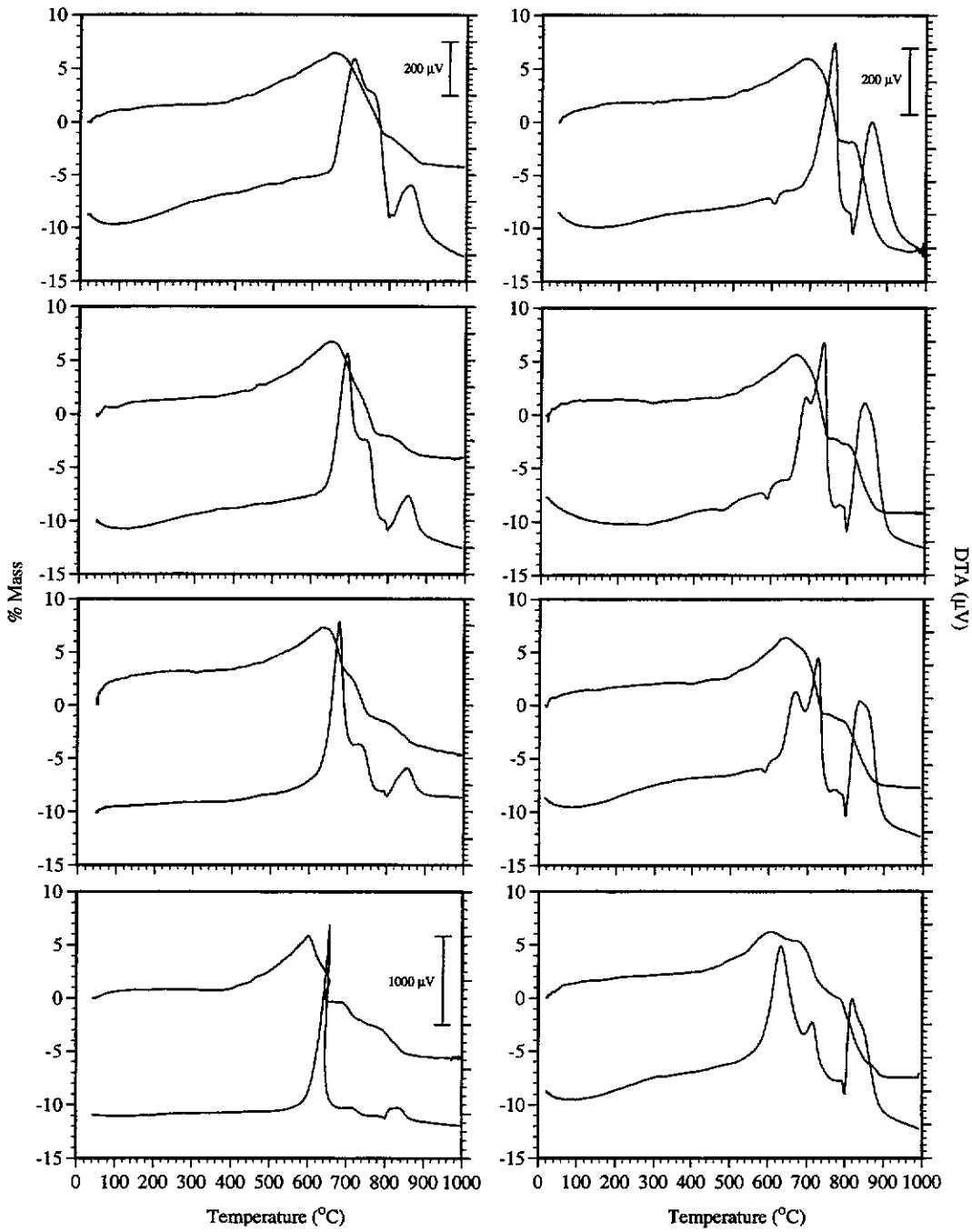

Figure 5.18 Typical TG-DTA traces for iron-rich pentlandite, $Fe_{5.80}Ni_{3.15}S_8$ (left), and nickel-rich pentlandite, $Fe_{3.40}Ni_{5.55}S_8$ (right), showing the effect of particle size when heated at 40°C min^{-1} in oxygen. In descending order 125-90, 90-63, 63-45 and 45-20 µm.

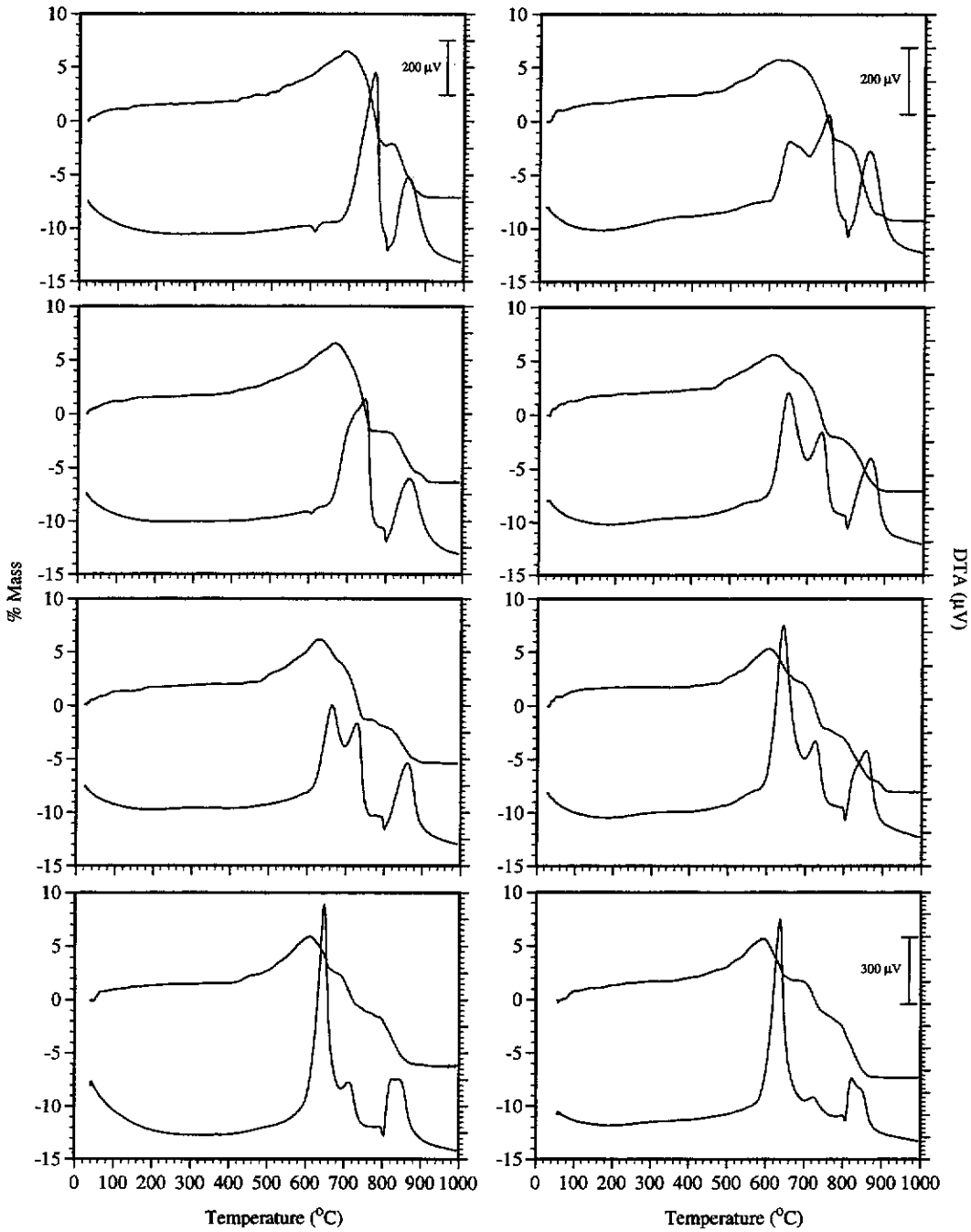

Figure 5.19 Typical TG-DTA traces for ideal pentlandite, $Fe_{4.59}Ni_{4.43}S_8$ (left), and sulfur-rich pentlandite, $Fe_{4.20}Ni_{4.16}S_8$ (right), showing the effect of particle size when heated at 40°C min^{-1} in oxygen. In descending order 125-90, 90-63, 63-45 and 45-20 μm.

5.4 Determination of the Ignition Temperature of Synthetic Pentlandite by Isothermal TG

The strategy used to study the ignition properties of synthetic violarite was used to study the ignition reactions of pentlandite. A range of pentlandites with varying stoichiometries were prepared between $Fe_{5.80}Ni_{3.15}S_8$ and $Fe_{3.40}Ni_{5.55}S_8$, and the effect of stoichiometry on their ignition behaviour examined using isothermal TG, as described in section 4.4.

5.4.1 Ignition of Synthetic Pentlandites

A typical isothermal TG curve for $Fe_{5.80}Ni_{3.15}S_8$ (iron-rich pentlandite) with a particle size range of 63-45 μm is shown in Figure 5.20. When the iron-rich pentlandite was heated at 705°C, just below its ignition temperature of 710°C, the sample exhibited a rapid mass gain of 3.5% due to the preferential oxidation of iron and sulfation of the pentlandite sample. This was followed by an equally rapid mass loss prior to a gradual mass loss over an extended period of time. The rapid mass loss was likely associated with the simultaneous thermal decomposition of iron (II) sulfate and direct oxidation of the sulfide core. A slight temperature excursion was associated with the rapid mass loss before returning to the preset temperature.

As the temperature was increased to 710°C this provided a sufficient increase in the heating rate in order for ignition conditions to prevail. During the induction period, where the sample is introduced into the preheated furnace, the mass of the sample rapidly increased. The gain in mass decreased as the iron:nickel and metal:sulfur ratio decreased for the series of pentlandite samples. After the sample had reached the programmed furnace temperature (710°C), the pentlandite ignited resulting in a rapid mass loss coinciding with a large temperature excursion. The temperature excursion increased in intensity as the iron:nickel ratio and the sulfur:metal ratio increased. The

iron-rich pentlandite sample ignited after approximately 16 seconds from being introduced into the preheated furnace, experiencing a heating rate of approximately 2700°C min^{-1}. The reaction reached completion after 36 seconds with an average mass loss of 4.0%. The ignition temperature of each synthetic pentlandite was reproducible to within ±5°C.

Therefore, the ignition temperature of synthetic pentlandite was characterised by the temperature at which a sharp mass loss coinciding with a temperature excursion from the programmed furnace temperature was observed. A sharp mass gain was always exhibited prior to the synthetic pentlandite igniting.

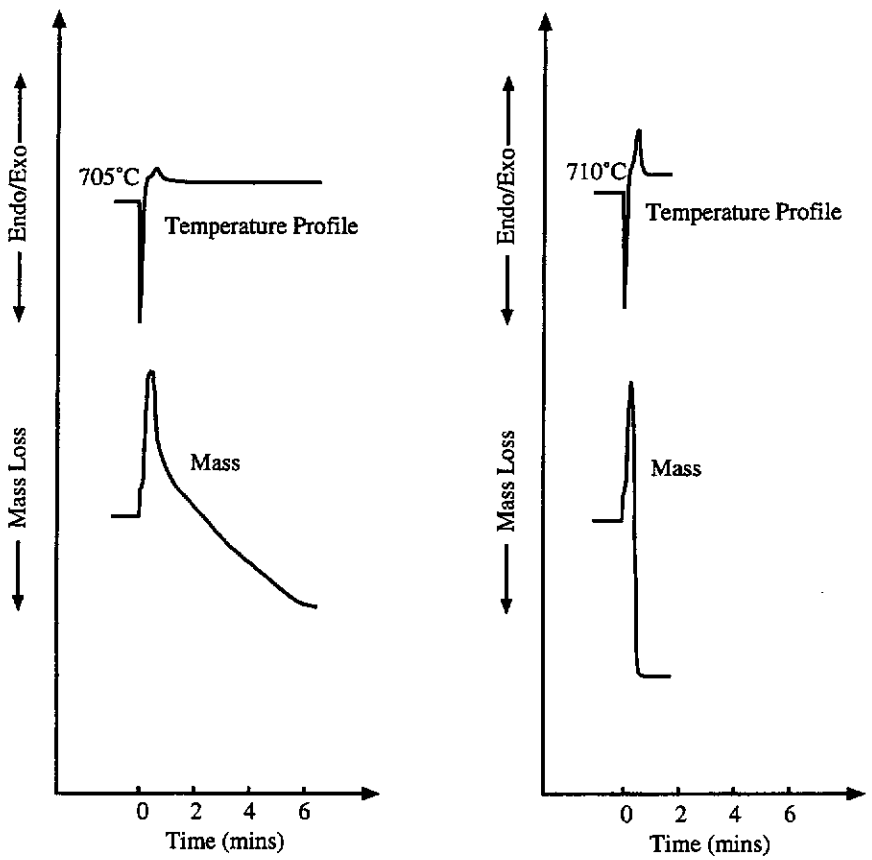

Figure 5.20 Schematic diagram of an isothermal TG trace for $Fe_{4.59}Ni_{4.43}S_8$ (63-45 μm fraction) prior to the ignition temperature (left) and at the ignition temperature (right). Heating rate approximately 2350°C min^{-1}, 5 mg sample in an oxygen atmosphere (25 ml min^{-1}).

5.4.2 Effect of Iron:Nickel Ratio on the Ignition Temperature of Synthetic Pentlandite

The ignition temperatures for the pentlandite samples for a range of particle sizes are given in Table 5.7. The bottom row in Table 5.7 shows the difference in the ignition temperatures between the two pentlandite endmembers for each particle size fraction. The effect of stoichiometry on the ignition temperature of synthetic pentlandite is illustrated in Figure 5.21. The ignition temperature of pentlandite was found to be linearly dependent on the iron:nickel ratio, with a decrease in the ignition temperature as the pentlandite composition tended towards the iron-rich endmember of the pentlandite solid-solution. For example, for the two endmembers of the pentlandite series, $Fe_{3.40}Ni_{5.55}S_8$ and $Fe_{5.80}Ni_{3.15}S_8$, the observed ignition temperatures for the respective samples were 720°C and 685°C, for the 63-45 μm particle size fraction. This represents a 35°C decrease in the ignition temperature as the iron:nickel ratio increased from 0.61 to 1.84.

Sample	Iron:Nickel Ratio	Particle Size Fraction (μm)			
		125-90	90-63	63-45	45-20
$Fe_{5.80}Ni_{3.15}S_8$	1.84	750	720	685	640
$Fe_{5.59}Ni_{3.42}S_8$	1.63	755	725	695	650
$Fe_{5.36}Ni_{3.79}S_8$	1.41	755	730	700	655
$Fe_{5.08}Ni_{4.06}S_8$	1.25	755	730	705	660
$Fe_{4.59}Ni_{4.43}S_8$	1.04	760	735	710	665
$Fe_{4.01}Ni_{4.89}S_8$	0.82	760	740	715	670
$Fe_{3.40}Ni_{5.55}S_8$	0.61	765	745	720	675
Difference (°C)		15	25	35	35

Table 5.7 The effect of the iron:nickel ratio on the ignition temperatures (°C) of synthetic pentlandite.

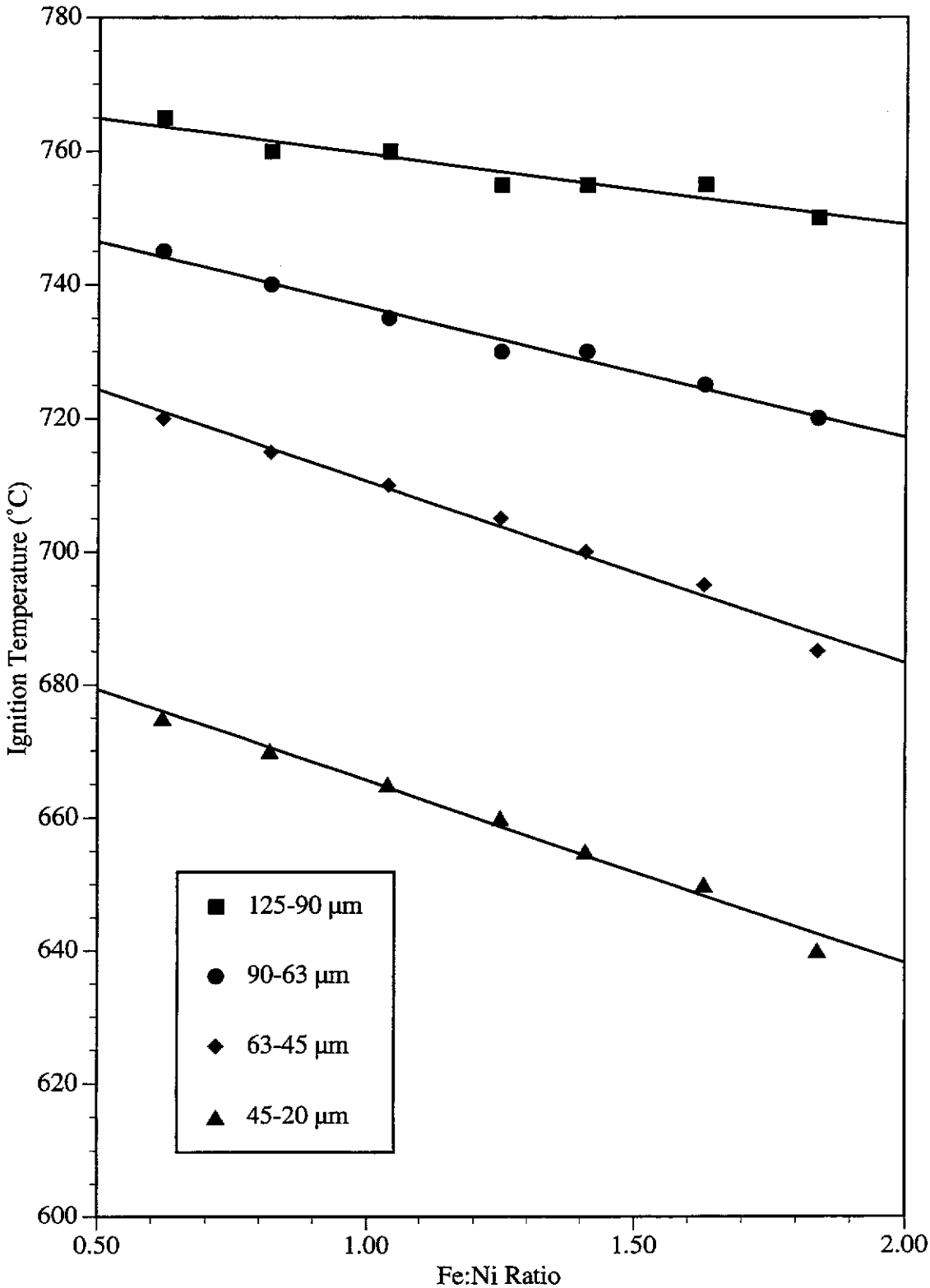

Figure 5.21 The effect of Fe:Ni ratio on the ignition temperature of synthetic pentlandite for a range of particle sizes.

Similarly, for the 125-90 μm particle size fraction, a decrease of 15°C was observed between the two respective pentlandite endmembers. Therefore, as the iron:nickel ratio of the synthetic pentlandite decreased the pentlandite became increasingly more difficult to ignite. The effect of stoichiometry on the ignition temperature diminished as the particle size increased.

The relative order of reactivity measured by the isothermal TG method was established as:

$$Fe_{5.80}Ni_{3.15}S_8 > Fe_{5.59}Ni_{3.42}S_8 > \ldots\ldots\ldots\ldots > Fe_{4.01}Ni_{4.89}S_8 > Fe_{3.40}Ni_{5.55}S_8$$

Increase in reactivity as iron:nickel ratio increases

5.4.3 Effect of Particle Size on the Ignition Temperature of Synthetic Pentlandite

The effect of particle size on the ignition temperature of synthetic pentlandite is presented in Table 5.8. The difference in ignition temperature between the 125-90 μm and 45-20 μm particle size fraction for each pentlandite sample is shown in the end column of Table 5.8. Figure 5.22 illustrates the effect of particle size on the ignition temperature of synthetic pentlandite.

A decrease of 90°C in the ignition temperature was observed for $Fe_{3.40}Ni_{5.55}S_8$ (nickel-rich pentlandite) between the particle size fractions of 125-90 μm and 45-20 μm. The effect of particle size increased as the iron:nickel ratio increased with the ignition temperatures converging as the particle size increased. The difference in the ignition temperatures between the respective particle size fractions increased from 90°C for $Fe_{3.40}Ni_{5.55}S_8$ (nickel-rich pentlandite) to 110°C for $Fe_{5.80}Ni_{3.15}S_8$ (iron-rich pentlandite).

Therefore, the effect of particle size on the ignition temperature of synthetic pentlandite increased in the following general order:

$$Fe_{5.80}Ni_{3.15}S_8 > Fe_{5.59}Ni_{3.42}S_8 > \ldots\ldots\ldots\ldots > Fe_{4.01}Ni_{4.89}S_8 > Fe_{3.40}Ni_{5.55}S_8$$

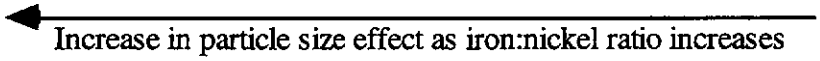

The ignition behaviour of ideal pentlandite ($Fe_{4.59}Ni_{4.43}S_8$) was comparable with previous results reported by Mackey (1991) for natural pentlandite with a stoichiometry of $Fe_{4.45}Ni_{4.90}S_8$ obtained from the Kambalda region in Western Australia (see Table 5.9). The ignition temperatures for the particle size fractions between the range of 125-45 μm correlated well. However, there was a difference of 30°C in the ignition temperatures between the natural and synthetic pentlandite samples for the 45-20 μm particle size fraction. This may have been caused by presence of fines in the natural sample, which would lower the ignition temperature. In the current study samples were ultrasonicated in a non-polar solvent, to disperse any fines adhering to larger particles, prior to being sieved through the 45 and 20 μm sieves.

Sample	Iron:Nickel Ratio	Geometric Mean Size (μm)				Difference (°C)
		106	75	53	30	
$Fe_{5.80}Ni_{3.15}S_8$	1.84	750	720	685	640	110
$Fe_{5.59}Ni_{3.42}S_8$	1.63	755	725	695	650	105
$Fe_{5.36}Ni_{3.79}S_8$	1.41	755	730	700	655	100
$Fe_{5.08}Ni_{4.06}S_8$	1.25	755	730	705	660	95
$Fe_{4.59}Ni_{4.43}S_8$	1.04	760	735	710	665	95
$Fe_{4.01}Ni_{4.89}S_8$	0.82	760	740	715	670	90
$Fe_{3.40}Ni_{5.55}S_8$	0.61	765	745	720	675	90

Table 5.8 The effect of particle size on the ignition temperatures (°C) of synthetic pentlandite samples.

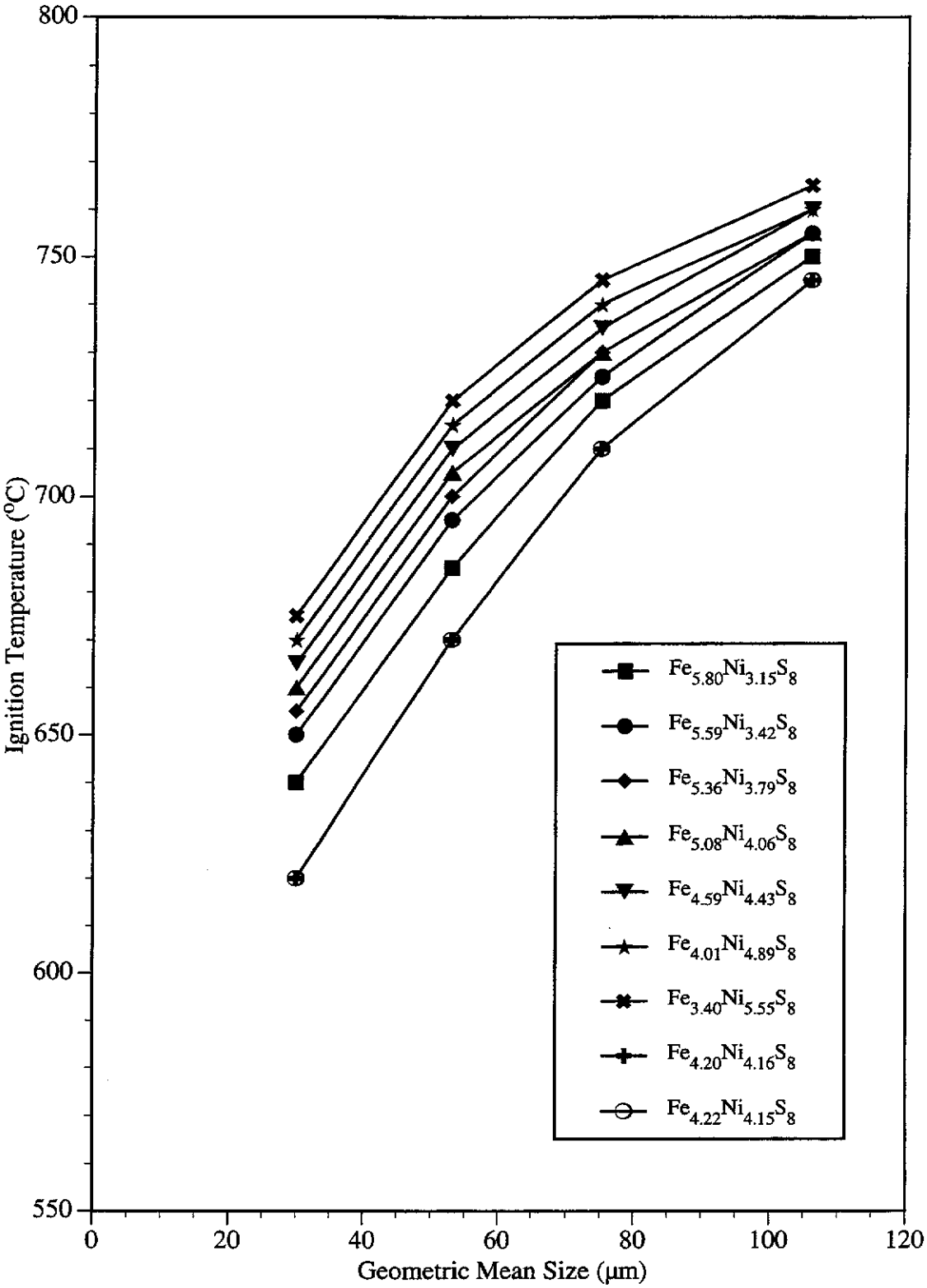

Figure 5.22 The effect of particle size on ignition temperature for the series of synthetic pentlandite samples.

Mackey (1991)		Present Study	
Particle Size Fraction (μm)	Ignition Temperature (°C)	Particle Size Fraction (μm)	Ignition Temperature (°C)
125-90	765-770	125-90	760-765
90-75	745-750	90-63	735-740
75-45	720-725	63-45	710-715
45-20	635-640	45-20	665-670

Table 5.9 A comparison of the ignition temperatures obtained for a natural pentlandite sample and ideal synthetic pentlandite using isothermal TG.

5.4.4 Effect of Metal:Sulfur Ratio of Synthetic Pentlandite on the Ignition Temperature

Two sulfur-rich pentlandite samples were synthesized with an iron:nickel ratio of approximately 1:1 to investigate the ignition behaviour of synthetic pentlandite as the metal:sulfur ratio was varied. The ignition temperatures for both of the sulfur-rich pentlandites are shown in Table 5.10 for a range of particle size fractions.

The ignition temperature of the 63-45 μm fraction of $Fe_{4.59}Ni_{4.43}S_8$ (ideal pentlandite), which has an iron:nickel ratio of approximately 1:1 and is slightly sulfur deficient compared with the ideal metal:sulfur ratio of 9:8, was found to be 665°C. In contrast, the ignition temperature of $Fe_{4.20}Ni_{4.16}S_8$ and $Fe_{4.22}Ni_{4.15}S_8$ (sulfur-rich pentlandites), for the same particle size was only 620°C. This represented a decrease of 45°C in the ignition temperature as the metal:sulfur ratio decreased from 1.13 to 1.05.

The sulfur-rich pentlandite samples also showed a significant decrease in the ignition temperature as the particle size decreased. For example, the ignition temperature decreased by 125°C from 745°C to 620°C between the particle size ranges of 125-90 μm and 45-20 μm, whereas ideal pentlandite only decreased 95°C from 755°C to 660°C between the coarsest and finest particle size fractions. Hence, as the pentlandite becomes more sulfur-rich the ignition temperature decreases and the effect of particle size increases.

The increase in the reactivity of sulfur-rich pentlandite compared to ideal pentlandite may be attributed to an increase in the loss of sulfur. A comparison of the TG-DTA of ideal and sulfur-rich pentlandite when heated at 40°C min^{-1} in argon showed that both pentlandites commence mass loss at approximately 780°C (Figure 5.5). However, the sulfur-rich pentlandite exhibited a larger mass loss between the temperature range of 780-1000°C. Hence, the increase in loss of sulfur from the sulfur-rich pentlandite may produce sufficient heat from the oxidation of the sulfur vapour to cause an ignition reaction at a lower temperature.

Sample	Metal:Sulfur Ratio	Iron:Nickel Ratio	Particle Size Fraction (μm)			
			125-90	90-63	63-45	45-20
$Fe_{4.59}Ni_{4.43}S_8$	1.128	1.04	755	730	705	660
$Fe_{4.20}Ni_{4.16}S_8$	1.045	1.01	745	710	670	620
$Fe_{4.22}Ni_{4.15}S_8$	1.046	1.02	745	710	670	620
Difference (°C)			10	20	35	40

Table 5.10 The effect of metal:sulfur ratio on the ignition temperature (°C) of synthetic pentlandite.

5.5 Determination of the Extent of Oxidation for Synthetic Pentlandites

The extent of oxidation was determined for the entire range of synthetic pentlandite samples using the isothermal TG method described in section 4.5. The TG profiles for ideal pentlandite at the ignition temperature of 710°C, and maximum furnace temperature of 900°C are illustrated in Figure 5.23. As the furnace temperature was increased above the ignition temperature the extent of oxidation increased. However, above 750°C the oxidation appeared to occur in two stages. This is evident in the TG profile for ideal pentlandite recorded at a furnace temperature of 900°C. The first stage was likely due to the preferential oxidation of iron while the second stage, which occurred over an extended period of time, may be attributed to the oxidation of the remaining nickel sulfide. After approximately 3 minutes the reaction had proceeded to completion with hematite, nickel oxide and trevorite identified as the final products.

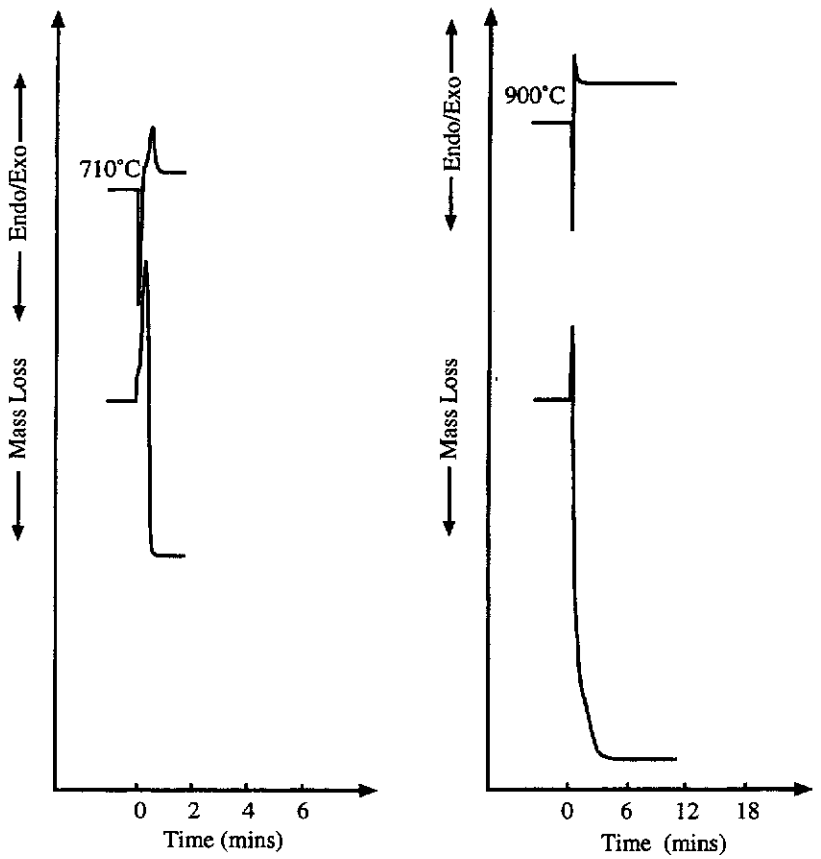

Figure 5.23 Typical isothermal TG trace of $Fe_{4.59}Ni_{4.59}S_8$ at 710°C and 900°C. Note the different time scales for each plot.

5.5.1 Effect of Iron:Nickel Ratio on the Extent of Oxidation of Synthetic Pentlandite.

The extent of oxidation for the entire pentlandite series with a particle size of 63-45 μm is presented in Table 5.11. Figure 5.24 shows the effect of iron:nickel ratio on the extent of oxidation for synthetic pentlandite. No oxidation was evident prior to the ignition temperature. Once the ignition temperature was reached the sulfide underwent rapid oxidation with a sharp mass loss associated with the preferential oxidation of iron. The extent of oxidation occurring at the ignition temperature was dependent on the stoichiometry of the sulfide, with an increase in the extent of oxidation as the iron:nickel ratio of the pentlandite increased. For example, the 63-45 μm fraction of $Fe_{5.80}Ni_{3.15}S_8$ (iron-rich pentlandite) had undergone 71% oxidation at its ignition temperature of 685°C, whereas $Fe_{3.40}Ni_{5.55}S_8$ (nickel-rich pentlandite) had only undergone 43% oxidation at its ignition temperature of 720°C. This is clearly evident in Figure 5.24 with the extent of oxidation increasing as the iron:nickel ratio tends towards the iron-rich endmember. The effect of stoichiometry becomes less significant as the temperature is increased above 800°C at which the remaining nickel sulfide is oxidised.

The results also showed there was a significant particle size effect on the extent of oxidation. Tables 5.12 and 5.13 give the extent of oxidation for the two endmembers of the pentlandite series for a range of particle size fractions. At 700°C, iron-rich pentlandite ($Fe_{5.80}Ni_{3.15}S_8$) had not commenced oxidation for the 125-90 μm particle size fraction, while the 45-20 μm fraction was 90% oxidised at the same temperature. A 50°C increase in the furnace temperature to 750°C showed the extent of oxidation for the coarsest particle size fraction had increased from 0% to 78% compared with the finest fraction which increased from 90% to 100%. Similarly for the nickel-rich pentlandite ($Fe_{3.40}Ni_{5.55}S_8$), at 750°C the 125-90 μm fraction had not oxidised,

Temperature (°C)	Percentage Extent of Oxidation								
	$Fe_{5.80}Ni_{3.15}S_8$	$Fe_{5.59}Ni_{3.42}S_8$	$Fe_{5.36}Ni_{3.79}S_8$	$Fe_{5.08}Ni_{4.06}S_8$	$Fe_{4.59}Ni_{4.43}S_8$	$Fe_{4.01}Ni_{4.89}S_8$	$Fe_{3.40}Ni_{5.55}S_8$	$Fe_{4.20}Ni_{4.16}S_8$	$Fe_{4.22}Ni_{4.15}S_8$
600	0.0	0.0	0.0	0.0	0.0	0.0	0.0	0.0	0.0
650	0.0	0.0	0.0	0.0	0.0	0.0	0.0	0.0	0.0
700	77.5	0.0	0.0	0.0	0.0	0.0	0.0	61.0	62.3
750	92.7	67.7	63.9	59.8	56.0	50.3	48.0	72.1	74.1
800	97.4	86.3	87.0	76.9	69.5	68.8	56.5	86.6	86.8
850	98.9	97.7	95.0	94.0	96.1	96.8	98.4	100.0	100.0
900	100.0	100.0	100.0	100.0	100.0	100.0	100.0	100.0	100.0

Table 5.11 Percentage extent of oxidation for the entire range of synthetic pentlandites for the particle size fraction of 63-45 μm.

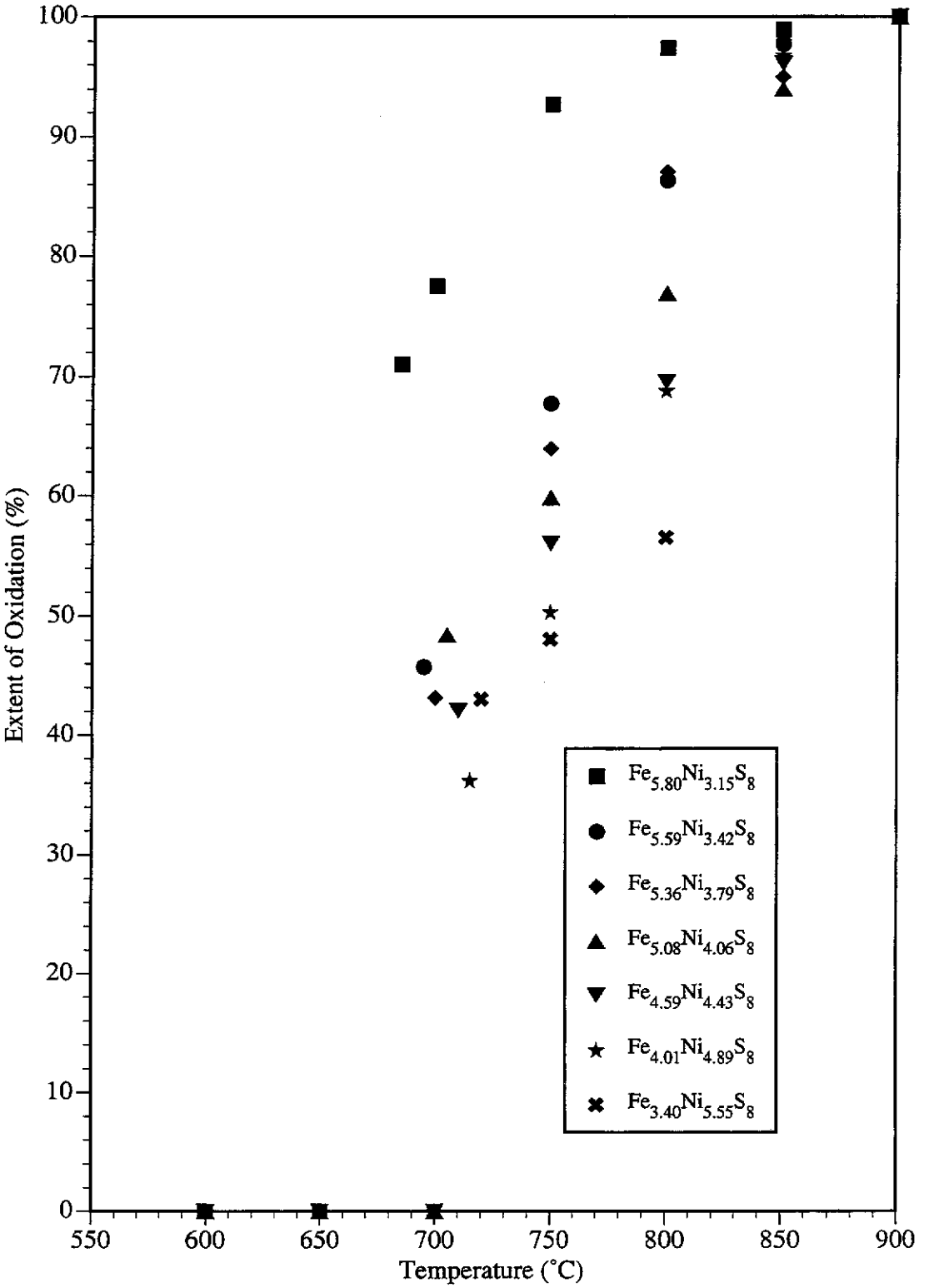

Figure 5.24 The effect of iron:nickel ratio on the extent of oxidation by isothermal TG for the 63-45 μm particle size fraction.

however the 45-20 μm fraction had oxidised by 58%. As the temperature was increased to 800°C the extent of oxidation had increased from 0% to 50% for the 125-90 μm fraction, while the 45-20 μm fraction increased from 58% to 95%.

Figure 5.25 shows the plot of extent of oxidation for the coarsest and finest particle size fraction for ideal pentlandite, iron-rich and nickel-rich pentlandite. If the iron-rich pentlandite sample is considered, the 45-20 μm particle size fraction was 100% oxidised at 750°C, but the 125-90 μm fraction was only 78% oxidised, and was not fully oxidised until the temperature of the furnace exceeded 850°C. Similarly, for the nickel-rich pentlandite sample, the 45-20 μm fraction was 95% oxidised at 800°C compared to only 50% oxidation for the 125-90 μm particle size fraction at the same temperature. Therefore, as the temperature of the furnace is increased the effect of particle size on the extent of oxidation decreases.

Temperature (°C)	Particle Size Fraction (μm)			
	125-90	90-63	63-45	45-20
600	0.0	0.0	0.0	0.0
650	0.0	0.0	0.0	84.7
700	0.0	0.0	77.5	89.6
750	77.7	71.5	92.7	99.8
800	86.7	93.5	97.4	100.0
850	98.7	91.0	96.9	100.0
900	100.0	100.0	100.0	100.0

Table 5.12 Percentage extent of oxidation for $Fe_{5.80}Ni_{3.15}S_8$ (iron-rich pentlandite) for each particle size fraction.

Temperature (°C)	Particle Size Fraction (μm)			
	125-90	90-63	63-45	45-20
600	0.0	0.0	0.0	0.0
650	0.0	0.0	0.0	0.0
700	0.0	0.0	0.0	42.8
750	0.0	47.0	48.0	58.3
800	49.7	56.2	56.5	94.7
850	100.0	100.0	98.4	97.4
900	100.0	100.0	100.0	100.0

Table 5.13 Percentage extent of oxidation for $Fe_{3.40}Ni_{5.55}S_8$ (nickel-rich pentlandite).

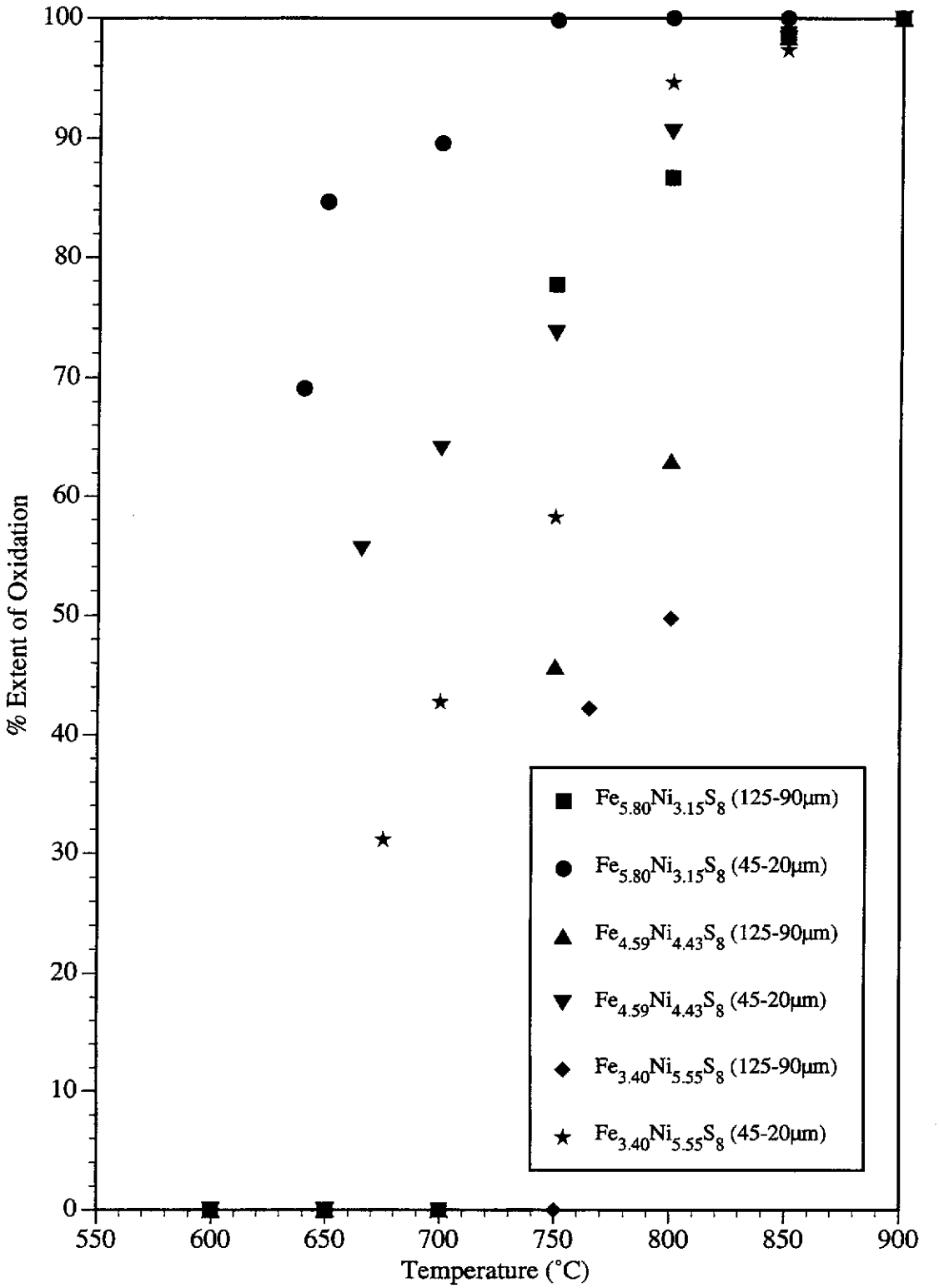

Figure 5.25 Extent of oxidation for iron-rich pentlandite ($Fe_{5.80}Ni_{3.15}S_8$), ideal pentlandite ($Fe_{4.59}Ni_{4.43}S_8$) and nickel-rich pentlandite ($Fe_{3.40}Ni_{5.55}S_8$). The graph shows a comparison between the two extreme particle size fractions.

5.5.2 Effect of Metal:Sulfur Ratio on the Extent of Oxidation of Synthetic Pentlandite

The extent of oxidation for both sulfur-rich pentlandites and ideal pentlandite are given in Tables 5.14 to 5.16. At the ignition temperature for the sulfur-rich pentlandite ($Fe_{4.20}Ni_{4.15}S_8$) of 670°C the 63-45 μm fraction had oxidised by 32%, whereas the ideal pentlandite ($Fe_{4.59}Ni_{4.43}S_8$) sample had not commenced oxidation. As furnace temperature was increase to 700°C the extent of oxidation for the sulfur-rich pentlandite had increased by 29% to 61%. The ideal pentlandite sample did not exhibit a mass loss until its ignition temperature, with 42% oxidation occurring at a temperature of 710°C. As the furnace temperature increased to 750°C the extent of oxidation for the ideal pentlandite increased from 42% to 56%, while the sulfur-rich pentlandite had undergone 72% oxidation. By 850°C both samples exhibited similar extents of oxidation as they approached completion. Therefore, the extent of oxidation was dependent on the metal:sulfur ratio, with the extent of oxidation increasing as the metal:sulfur ratio decreased. The effect of the metal:sulfur ratio on the extent of oxidation decreased as the furnace temperature was increased above 850°C.

There was also a significant particle size effect on the extent of oxidation as the metal:sulfur ratio decreased (Figure 5.26). At 700°C, sulfur-rich pentlandite had not commenced oxidation for the 125-90 μm particle size fraction, whereas the 45-20 μm was 85% oxidised at the same temperature. As the furnace temperature was increased to 750°C the extent of oxidation for the coarsest fraction had increased from 0% to 60% compared with the finest fraction which had oxidised to completion. The particle size effect was not as large for the ideal pentlandite sample. At 700°C the 125-90 μm had not commenced oxidation, while the 45-20 μm had undergone 64% oxidation. By 750°C the 125-90 μm fraction had increased from 0% to 49%, whereas the 45-20 μm had only increased by 10% with the extent of oxidation increasing from 64% to 74%. As the furnace temperature is increased above 800°C the effect of particle size on the extent of oxidation decreases.

Temperature (°C)	Particle Size Fraction (μm)			
	125-90	90-63	63-45	45-20
600	0.0	0.0	0.0	0.0
650	0.0	0.0	0.0	0.0
700	0.0	0.0	0.0	64.0
750	48.8	50.6	56.0	73.6
800	63.0	65.1	69.5	90.5
850	83.4	89.1	96.1	98.3
900	100.0	100.0	100.0	100.0

Table 5.14 Percentage extent of oxidation for $Fe_{4.59}Ni_{4.43}S_8$ (ideal pentlandite).

Temperature (°C)	Particle Size Fraction (μm)			
	125-90	90-63	63-45	45-20
600	0.0	0.0	0.0	0.0
650	0.0	0.0	0.0	83.0
700	0.0	0.0	61.0	87.2
750	60.6	71.5	72.1	100.0
800	72.0	86.4	86.6	100.0
850	94.9	98.5	100.0	100.0
900	100.0	100.0	100.0	100.0

Table 5.15 Percentage extent of oxidation for $Fe_{4.20}Ni_{4.16}S_8$ (sulfur-rich pentlandite).

Temperature (°C)	Particle Size Fraction (μm)			
	125-90	90-63	63-45	45-20
600	0.0	0.0	0.0	0.0
650	0.0	0.0	0.0	81.7
700	0.0	0.0	62.3	84.6
750	62.4	72.4	74.1	100.0
800	75.2	82.7	86.8	100.0
850	95.4	99.1	100.0	100.0
900	100	100.0	100.0	100.0

Table 5.16 Percentage extent of oxidation for $Fe_{4.22}Ni_{4.15}S_8$.

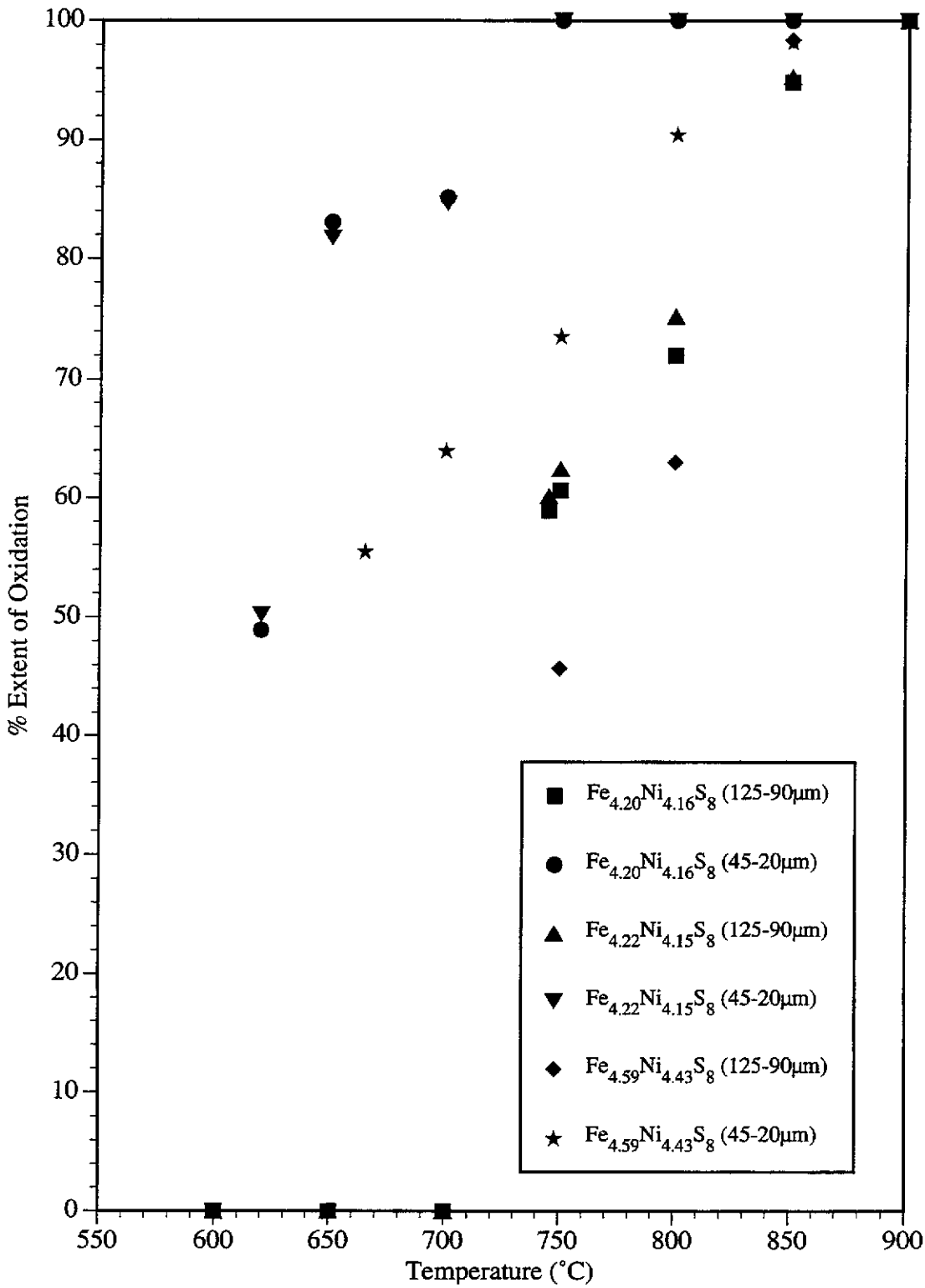

Figure 5.26 Extent of oxidation for both sulfur-rich pentlandites ($Fe_{4.20}Ni_{4.15}S_8$ and $Fe_{4.22}Ni_{4.16}S_8$) and ideal pentlandite ($Fe_{4.59}Ni_{4.43}S_8$). The graph shows a comparison between the two extreme particle size fractions.

5.6 Ignition Mechanism of Synthetic Pentlandite

The ignition mechanism of synthetic pentlandite was complex, and it was necessary to examine the ignition products at several temperatures in order to establish the mechanism. All samples were prepared using the isothermal TG method. Figure 5.27a shows the typical morphology of iron-rich pentlandite collected at 675°C, prior to its ignition temperature. The morphology of the oxidation products were similar to the partially oxidised products obtained at 40°C min^{-1} in oxygen (Section 5.3), with sulfate being formed in both instances followed by preferential oxidation of the iron. The heat evolved from the oxidation of the iron sulfide component appeared to be insufficient to oxidise the remaining nickel sulfide. The final product showed a thin (<5 μm) oxide rim around an unreacted sulfide core. The oxidation of the sulfide core appeared to have occurred along a preferred orientation of the sulfide lattice with large voids evident due to a reduction in the volume. XRD of the products revealed mss and hematite as the major oxidation products with a minor amount of trevorite present.

An optical micrograph of the oxidised product is shown in Figure 5.27a. The dark grey inner layer was identified as trevorite while the light grey outer layer, which displayed distinctive red internal reflections under polarised light, was identified as hematite. The sulfide core was strongly anisotropic, a characteristic of hexagonal mss. Analysis of the sulfide cores showed there was still a significant amount of iron remaining with an average composition of $Fe_{0.34}Ni_{0.65}S_{1.00}$. Therefore, at 675°C the particle morphology and oxidation mechanism was indicative of the reaction mechanism observed under less vigorous oxidising conditions (see Figure 5.11d).

Particles collected at the ignition temperature (680°C) for iron-rich pentlandite were significantly different from those collected at lower temperatures. The pentlandite sample exhibited an initial mass gain associated with the preferential sulfation of iron at the particle surface. As the sample temperature approached the decomposition

temperature of $FeSO_4$ the rate of sulfation decreased and the preferential oxidation of iron increased. Thermodynamic data suggests that the oxidation of FeS to Fe_2O_3 is more thermodynamically favourable than the of oxidation of NiS to NiO (Turnbull and Wadsley, 1992).

$$FeS + 1.75\ O_{2\,(g)} \Leftrightarrow 0.5\ Fe_2O_3 + SO_{2\,(g)} \qquad \Delta G^\circ = 137.07 \cdot T(K) - 610747 \quad (950\text{-}1273K)$$

$$NiS + 1.5\ O_{2\,(g)} \Leftrightarrow NiO + SO_{2\,(g)} \qquad \Delta G^\circ = 79.373 \cdot T(K) - 446893 \quad (670\text{-}1273K)$$

The formation of hematite results in an substantial reduction in the molecular volume of the oxidation product. The porosity of the oxide allows oxygen to diffuse through to the sulfide-oxide interface and the diffusion of sulfur dioxide away from the oxidation interface. The heat generated from the preferential oxidation of the iron sulfide component produces a sustainable oxidation reaction which proceeds to completion with hematite and nickel oxide as the final products.

Figure 5.27b shows a BSE micrograph of the ignition products collected at 680°C for iron-rich pentlandite with a particle size range of 63-45 μm. The ignition product consists of concentric layers of hematite and nickel oxide around a nickel-rich sulfide core. The majority of the particles had oxidised to completion (Figure 5.27c). Analysis of the ignition product indicated the outer oxide layers were iron-rich while the inner layers were nickel-rich with both nickel oxide and trevorite evident. Analysis of the sulfide core showed the stoichiometry ranged from $Fe_{0.07}Ni_{1.00}S_{1.00}$ to $Fe_{0.10}Ni_{1.15}S_{1.00}$.

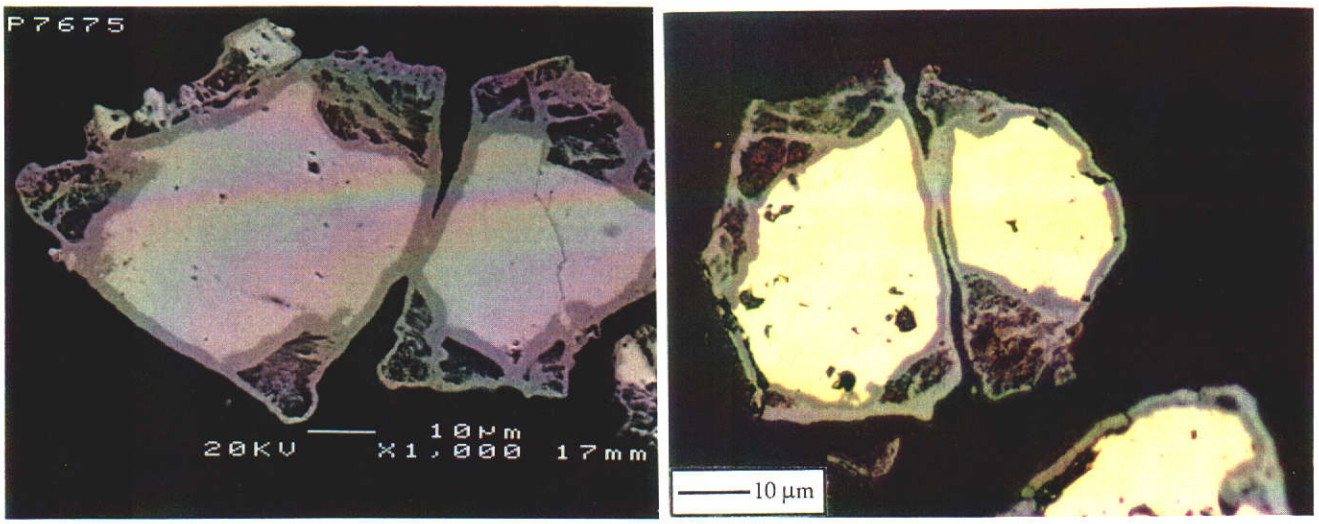

Figure 5.27a BSE (left) and optical (right) micrographs of iron-rich pentlandite collected at 675°C. Hematite may be identified by its red internal reflections under polarised light.

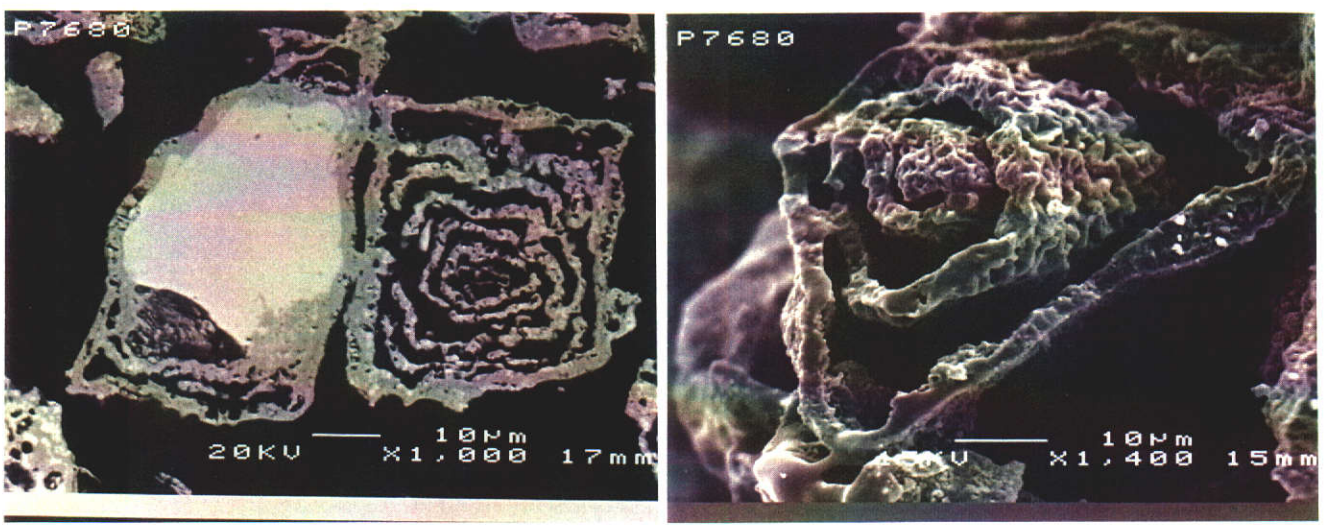

Figure 5.27b BSE (left) and SE (right) micrographs of iron-rich pentlandite collected at 680°C.

Ignition products collected at 725°C and 750°C for nickel-rich pentlandite exhibited similar particle morphology to iron-rich pentlandite prior to its ignition temperature (Figures 5.28a and 5.28b). Although the nickel-rich pentlandite displayed a temperature excursion from the preset furnace temperature the heat evolved from the preferential oxidation of the iron in the sulfide core was insufficient to oxidise the remaining nickel sulfide. Analysis of the nickel sulfide core showed millerite and heazlewoodite present with an average composition of $(Ni_{6.95}\ Fe_{0.23})S_6$ and $(Fe_{0.08}Ni_{2.95})S_2$ respectively. The micrographs show the particle temperature has not exceeded the melting point transition of heazlewoodite (795°C).

As the furnace temperature is increased to 800°C the heazlewoodite melts to form a molten mass (Figure 5.28c). The unreacted nickel sulfide phases were identified as

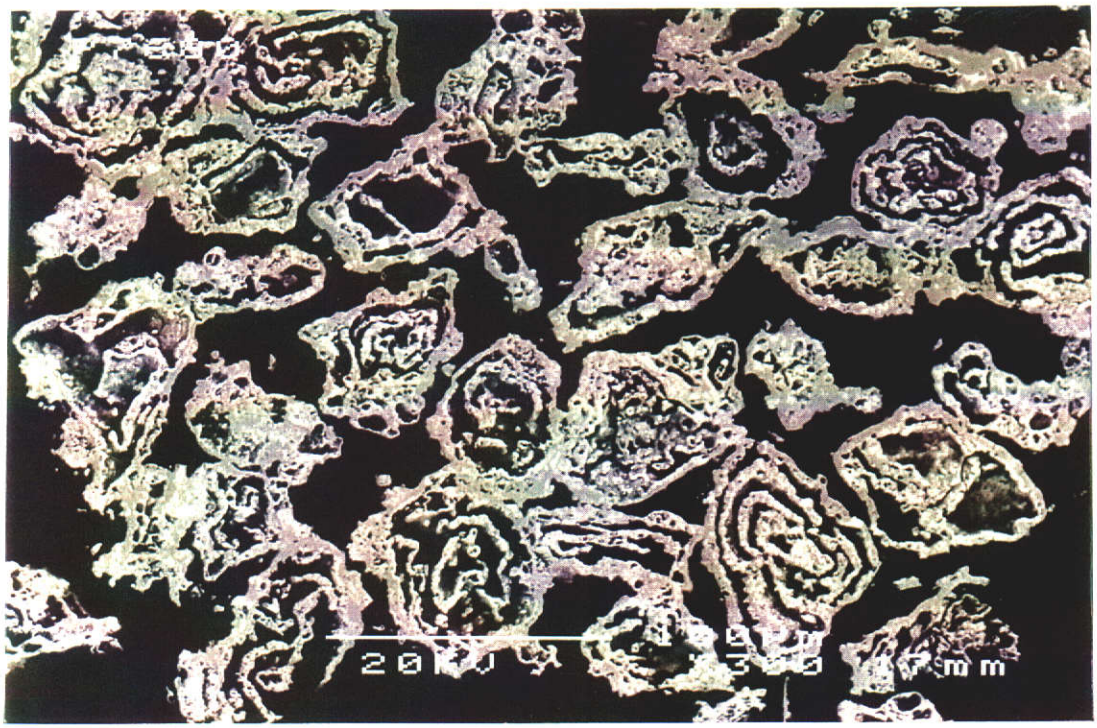

Figure 5.27c BSE micrograph of iron-rich pentlandite collected at 680°C. The oxide has formed concentric layers.

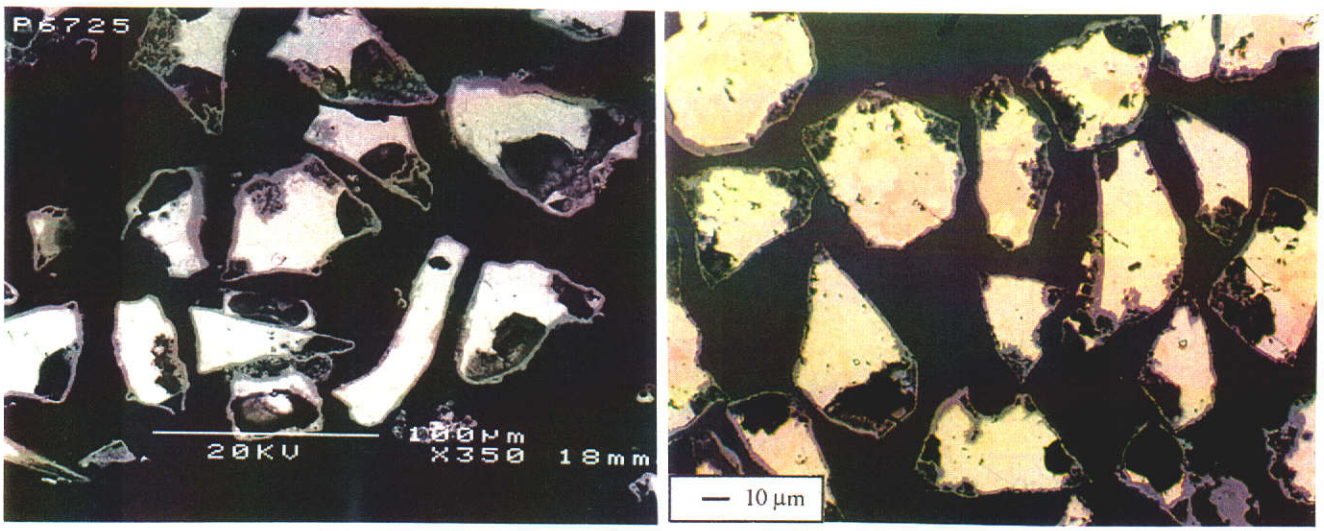

Figure 5.28a BSE (left) and optical (right) micrographs of nickel-rich pentlandite collected at 725°C.

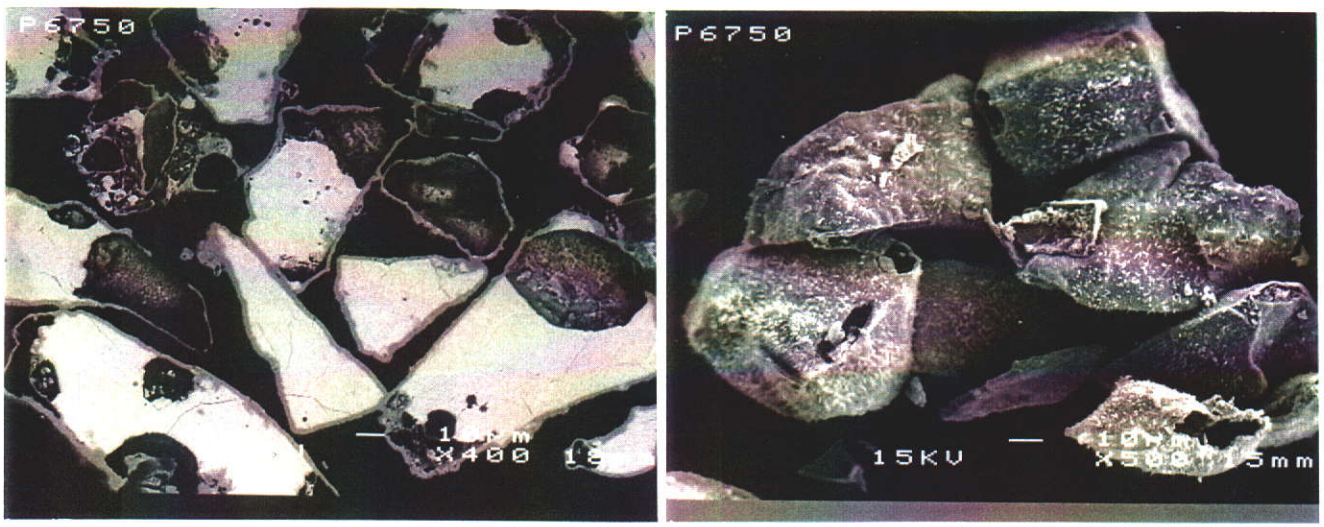

Figure 5.28b BSE (left) and SE (right) micrographs of nickel-rich pentlandite collected at 750°C.

mss and heazlewoodite with average compositions of $(Fe_{0.005}Ni_{1.38})S_{1.00}$ and $(Fe_{0.08}Ni_{3.00})S_2$. The bright crystals in the sulfide melt were identified as platinum from the crucible. The nickel sulfide melt did not oxidise to completion until the furnace temperature exceeded 850°C.

Similar particle morphology observed for iron-rich pentlandite at its ignition temperature has been reported for pyrite (FeS_2) and sphalerite (ZnS) (Nguyen,1990; Jorgensen and Moyle, 1981; Dimitrov and Bonev, 1986). Nguyen (1990) reported the formation of concentric layers of hematite around an unreacted pyrite core during roasting of pyrite between 400-500°C. The formation of these layers was explained by the strain produced between the sulfide-oxide interface due to a reduction in the molecular volume. The periodic formation of concentric cracks, separating consecutive oxide layers, was due to the critical growth of the interfacial strain. As the oxide separates this exposes a new sulfide surface for further oxidation. This process continues until the pyrite had completely oxidised to completion.

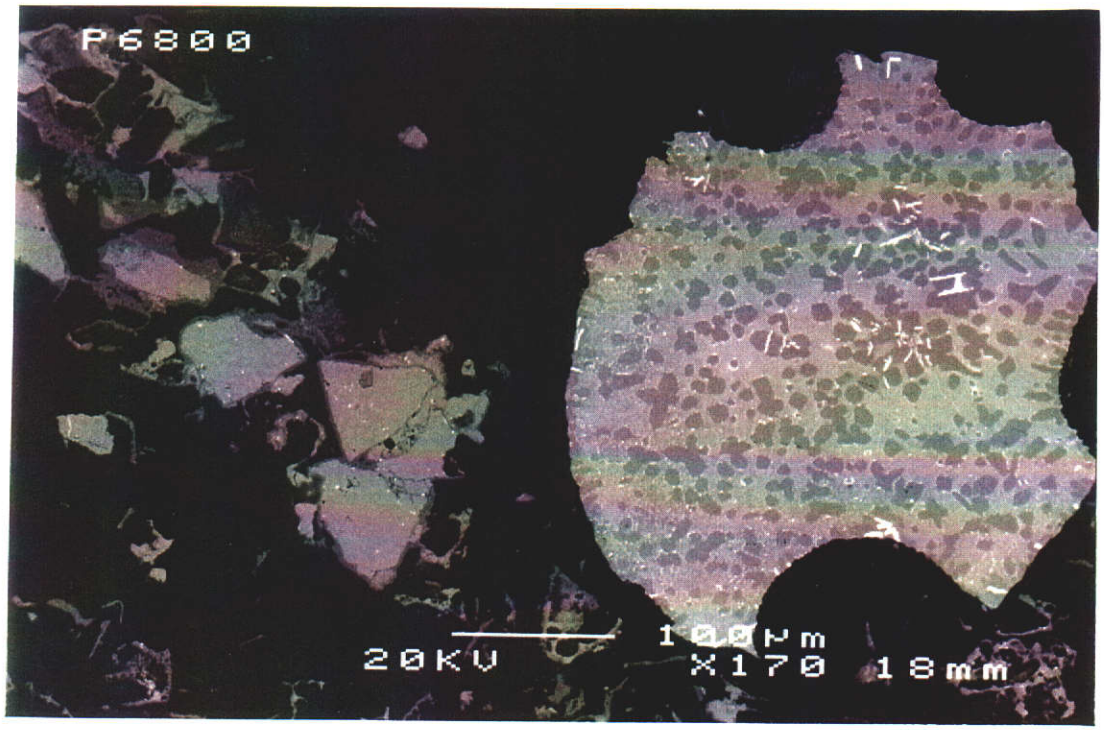

Figure 5.28c BSE micrograph of nickel-rich pentlandite collected at 800°C. The sulfide particles have formed a molten mass consisting of mss and heazlewoodite.

Dimitrov and Bonev (1986) proposed a similar reaction model during the oxidation of sphalerite between 800-1000°C. They suggested the following model for the oxidation:

(i) Oxidation of the sulfide surface:

- supply of oxygen to the sulfide surface,
- chemisorption of oxygen,
- oxidation with formation of sulfur dioxide,
- crystal growth of oxide,
- desorption of sulfur dioxide and
- separation of the surface oxide layer.

(ii) Oxidation of the subsequent sulfide core:

- supply of oxygen through to the surface of the oxide particle,
- diffusion of oxygen through the pores and cracks towards the moving reaction front,
- chemisorption of oxygen on the unreacted sulfide,
- oxidation of the sulfide,
- desorption of the sulfur dioxide from the reaction front,
- diffusion of sulfur dioxide from the reaction front,
- diffusion of sulfur dioxide through finely porous outer oxide layers and
- separation of the new oxide layer.

The model suggests that the initial rate of oxidation is controlled by a topochemical reaction at the surface, while the subsequent layers are controlled by diffusion of the gaseous reactant and product through the porous oxide. Therefore, the rate of oxidation will decrease as the diffusion path of the gases increases. This phenomenon is described by the "Shrinking-Unreacted Core" model (Mohan, Mckinley and Douglas, 1979). The model implies that as oxidation proceeds a thickening product layer is formed around a shrinking core. In order for the reaction to proceed gaseous oxidant must diffuse through the product layer to the unreacted core. The oxidation reaction will be significantly influenced by the surface area of the particle. Therefore,

the rate of oxidation of larger particles will be slower due to their lower surface area. This would explain the particle size effect observed for synthetic pentlandite shown in Figure 5.25.

An alternative mechanism for the formation of concentric oxide layers was reported by Thornhill and Pidgeon (1957). They proposed that during the oxidation of low sulfur minerals such as FeS, Cu_2S and pentlandite the rate of oxidation of the metal and sulfur does not take place simultaneously even after the conversion of the sulfide to its high temperature equilibrium defect structure. For example, during the oxidation of triolite (FeS), the Fe:S ratio decreases due to the preferential oxidation of iron at the reaction interface. The depletion of iron within the sulfide core near the oxidation interface results in an increase in the sulfur concentration. The sulfur may increase to the point where the sulfur pressure between the sulfide-oxide interface may cause localised disruption of the oxide layer. The preferential oxidation of sulfur would cause the iron concentration at the reaction interface to increase and a new oxide layer to form. The process is repeated until the rate of iron and sulfur oxidation reach equilibrium.

The morphology of the ignition products seem to be consistent with the "Shrinking-Unreacted Core" model. The following reaction mechanism is proposed for the ignition of synthetic pentlandite:

(i) Topochemical oxidation.

During the induction period iron (II) sulfate and nickel sulfate are formed by a topochemical reaction at the surface of the particle. The sulfates are oxidised to hematite and nickel oxide as the sample temperature exceeds the decomposition temperature of the respective sulfides.

(ii) Decomposition of pentlandite to mss and heazlewoodite.

It appears the ignition reaction is initiated by the decomposition of synthetic pentlandite to mss and heazlewoodite between the temperature of 580°C to 610°C. No sulfur loss occurs during the decomposition of pentlandite. The formation of mss enables the iron to migrate from the sulfide core to the reaction interface where it is preferentially oxidised. Concentric oxide layers are formed as the interfacial strain between the sulfide core and oxide rim increases. The oxidation of the iron sulfide component causes the particle temperature to increase causing the rate of iron diffusion to the reaction interface to increase. The oxidation product appears not to inhibit the diffusion of oxygen to the reaction interface. The extent of oxidation increases as the iron:nickel ratio increases.

(iii) Oxidation of nickel sulfide component.

The oxidation of the remaining nickel sulfide increases as the temperature increases. The reaction proceeds to completion when the particle temperature exceeds the incongruent melting point of $(Fe,Ni)_{3\pm x}S_2$. In the case of the iron-rich pentlandite sufficient heat was generated from the preferential oxidation of the iron to oxidise the remaining nickel-sulfide. As the iron:nickel ratio decreases the nickel sulfide component does not ignite but rather oxidises by a shrinking core or oxygen diffusion process as the furnace temperature is increased. This accounts for the greater temperature dependence for the nickel-rich pentlandites on the extent of oxidation.

CHAPTER 6

CONCLUSIONS

6.0 CONCLUSIONS

The primary purpose of this work was to study the effect of stoichiometry on the ignition properties of violarite and pentlandite, which are the two major nickel bearing minerals found in Western Australia. These minerals, with a range of stoichiometries, were synthesised and characterised.

The effect of stoichiometry on the pyrolytic decomposition and oxidation mechanisms of violarite and pentlandite was only minor, with slight temperature shifts observed in the onset and offset temperatures of the TG-DTA events.

However, the stoichiometry of the sulfide had a marked effect on the ignition temperatures of violarite and pentlandite as determined using the isothermal TG technique. For violarite, the ignition temperature was found to increase as the iron:nickel ratio decreased. For the 63-45 μm particle size fraction, an increase of 20°C was observed in the ignition temperature, from 415°C to 435°C, as the iron:nickel ratio decreased from 0.49 (ideal violarite) to 0.07 (nickel-rich violarite). For pentlandite the ignition temperature was found to be linearly dependent on the iron:nickel ratio, with the ignition temperature increasing as the iron:nickel ratio decreased. For the 63-45 μm fraction, there was a 35°C increase in the ignition temperature, from 685°C to 720°C, as the iron:nickel ratio decreased from 1.84 (iron-rich pentlandite) to 0.62 (nickel-rich pentlandite). Hence there was a decrease in reactivity of the minerals as the iron content decreased. The effect was less evident for violarite relative to pentlandite. The pentlandite became more reactive as there was a decrease in the metal:sulfur ratio, with a decrease in the ignition temperature of 45°C as the ratio changed from 1.13 to 1.05. The range of compounds that could be prepared with variation in metal:sulfur ratio was limited, and only this one result was possible.

Investigation of the effect of particle size on relative reactivity revealed that the ignition temperatures of the two minerals decreased as the particle size decreased. The magnitude of the effect varied with the iron:nickel ratio. The ignition temperature for the nickel-rich violarite ($Fe_{0.20}Ni_{2.72}S_4$) showed the largest decrease of 50°C between the coarsest and finest particle size fractions, compared with a 40°C decrease for $Fe_{0.97}Ni_{1.96}S_4$ (ideal violarite). The effect of particle size on the ignition temperature of synthetic pentlandite was approximately twice the magnitude compared to violarite, with the ignition temperature decreasing by approximately 100°C between the 125-90 and 45-20 μm fractions for any given stoichiometry .

Isotheral TG was also used to determined the extent of oxidation for the two minerals. The violarite samples reacted in two distinct stages. A rapid increase in the extent of oxidation was observed as the furnace temperature was increased beyond the ignition temperature. Between 650-800°C the extent of oxidation remained constant . As the temperature was increased beyond 800°C, the remaining sulfide was oxidised to completion. The effect of particle size on the extent of oxidation was significant in the lower temperature ranges from 350-450°C with the extent of oxidation increasing as the particle size decreased. In the mid temperature range of 400-750°C the effect of stoichiometry was more significant. A decrease in the extent of oxidation was observed as the iron:nickel ratio tended towards the nickel-rich endmember of the violarite series. Both particle size and stoichiometry had a limited effect on the extent of oxidation above 800°C.

The extent of oxidation for pentlandite was also shown to occur in two stages with the extent of oxidation increasing as the iron:nickel ratio increased. For the 45-20 μm fraction of $Fe_{5.80}Ni_{3.15}S_8$ (iron-rich pentlandite), 90% oxidation had occurred at 700°C, whereas for $Fe_{3.40}Ni_{5.55}S_8$ (nickel-rich pentlandite), only 43% oxidation had occurred at the same temperature. The extent of oxidation increased significantly as the particle size decreased.

The ignition of synthetic violarite and pentlandite occurred via two different mechanisms. The ignition of violarite was linked to its ability to generate sulfur vapour through the decomposition of vaesite. This sulfur vapour reacted with oxygen forming a rapid and highly exothermic gas-phase reaction. This generated heat causing the particle temperature to rapidly escalate well above the temperature of the surroundings. As a consequence of the rapid evolution of sulfur and a reduction in volume, due to the conversion of vaesite to mss, the sulfide particle develops a porous internal structure. As the partial pressure of sulfur evolved from the particle decreases, oxygen may diffuse through the gas boundary layer to the unreacted sulfide resulting in the preferential oxidation of iron. The remaining nickel sulfide core does not ignite, but rather oxidises at a higher temperature. Hence, the gas-phase oxidation of sulfur vapour in the boundary layer surrounding the particle and a change in the morphology of the particle are fundamental to the ignition process.

Like violarite, pentlandite decomposes to form an iron sulfide species and a nickel sulfide species but with no associated loss of sulfur. The iron migrates to the reaction interface where it is preferentially oxidised, forming an oxide product layer. The preferential oxidation of iron is thermodynamically favourable due to the sulfide-oxide exchange reaction between nickel oxide and iron sulfide shown below:

$$FeS_{(s)} + NiO_{(s)} \Leftrightarrow NiS_{(s)} + FeO_{(s)}$$

where, $\Delta G^{\circ} = -0.63058 \cdot T(K) - 20980$ in the temperature range of 400-1000°C (Turnball and Wadsley, 1992). The nickel sulfide will remain in its sulfide form until the iron sulfide component has been completely oxidised. Consequently, the ignition process relies upon the diffusion of oxygen and iron to the reaction interface. The ignition reaction proceeds as a solid-gas reaction consistent with the shrinking-unreacted core model. The ignition reaction for pentlandite will be highly dependent

on the surface area of the particle. Hence, this explains the greater dependence of ignition temperature on the particle size for pentlandite compared to violarite.

The objective of this work was to assess the ease of flash smelting of violarite and pentlandite. Ideal violarite with an iron:nickel ratio of 0.49 and a particle size of 45-20 μm was more readily smelted, igniting at 400°C, than nickel-rich violarite with an iron:nickel ratio of 0.07 and a particle size of 125-90 μm, which ignited at 465°C. Hence, violarites with a small particle size and high iron composition are more readily smelted than those with larger particle sizes and higher nickel contents. Similar conclusions can be made about pentlandite, with the iron-rich pentlandite, of particle size of 45-20 μm, igniting at 640°C compared to a value of 675°C for the nickel-rich pentlandite. For the particle size range 125-90 μm, the ignition temperatures for the iron-rich and nickel-rich pentlandites were not significantly different. Hence, pentlandites with a small particle size and high iron composition are more readily smelted than those with larger particle sizes and higher nickel contents. In addition, it has been demonstrated that a sulfur-rich pentlandite was more reactive than any of the other pentlandites.

A knowledge of the mineralogical composition of the smelter feed stock alone is not sufficient to assess the smelting behaviour. The stoichiometry of the mineral must also be considered when determining the relative ease with which a mineral may be flash smelted.

REFERENCES

REFERENCES

Albers, W. and Rooymans, C. J. M. (1965). High Pressure Polymorphism of Spinel Compounds. *Solid State Communications*, 3, pp.417-419.

Anderson, B. Hanniala, P. and Harkki, S. (1982). Use of Oxygen in the Outokumpu Flash Smelting Process, *Canadian Institute of Mining and Metallurgy Bulletin*, 75 (845), pp.172-177.

Annamalai, K. and Durbetaki, P. (1977). A Theory on Transition of Ignition Phase of Coal Particles. *Combustion and Flame*, 29 (2), pp.193-208.

Armstrong, J. J. (1988). *CITZAF-Microprobe/SEM Data Correction Program, Version 3.04.* California Institute of Technology, Pasadena.

Asaki, Z., Matsumoto, K., Tanabe, T. and Kondo, Y. (1983). Oxidation of Dense Iron Sulfide. *Metallurgical Transactions B*, 14B, pp.109-116.

Asaki, Z., Tosa, M., Tanabe, T. and Kondo, Y. (1984). Oxidation Kinetics of Mixed Copper-Iron Sulfide at 1173K. *Transactions of the Institute of Metals*, 25 (7), pp.487-496.

Asaki, Z., Mori, S., Ikeda, M., and Kondo, Y. (1985). Oxidation of Pyrrhotite Particles Falling Through a Vertical Tube. *Metallurgical Transactions B*, 16B, pp.627-638.

Banerjee, A. C. (1976). Mechanism of Oxidation and Thermal Decomposition of Iron Sulfides. *Indian Journal of Chemistry*, 14A, pp.845-850.

Barin, I. and Sauert, F. (1980). Thermodynamics and Kinetics of Cyclone Smelting of Sulphidic Copper Concentrates, in Jones, M. J. (ed.) *Complex Sulfide Ores*, pp.193-198. The Institute of Mining and Metallurgy, London.

Barin, I., Modigell, M. and Sauert, F. (1983). Thermodynamics and Kinetics of Cyclone Smelting of Metal Sulfides, in Sohn, H. Y., George, D. B. and Zunkel, A. D. (eds.) *Advances in Sulfide Smelting Volume 1. Basic Principles*, pp.257-273. The Metallurgical Society of AIME, Pennsylvania.

Biswas, A. K. and Davenport, W. G. (1994). *Extractive Metallurgy of Copper.* Pergamon Press, Oxford.

Bouchard, R. J. (1967). Spinel to Defect NiAs Structure Transformation. *Materials Research Bulletin*, 2, pp.459-464.

Chaubal, P. C. (1986) *The Reaction of Chalcopyrite Concentrate Particles in a Flash Furnace Shaft.* PhD Dissertation, The University of Utah, Salt Lake City.

Craig, J. R. (1971). Violarite Stability Relations. *The American Mineralogist*, 56, pp.1303-1311.

Cutifani, M. (1994). Nickel in Australia - An Overview, in Grimsey, E. J. and Stockton, N. D. (eds) *Nickel in Australia - Mineral to Market, Kalgoorlie, Australia, December 2*, pp.1-15. The Australasian Institute of Mining and Metallurgy, Kalgoorlie.

Davenport, W. G. and Partelpoeg, E. H. (1987). *Flash Smelting: Analysis, Control and Optimization.* Pergamon Press, Oxford.

Desborough, G. A. and Czamanske, G. K. (1973). Sulfides in Eclogite Nodules from a Kimberlite Pipe, South Africa, with Comments on Violarite Stoichiometry. *American Mineralogist*, 58, pp.195-202.

Dimitrov, R. and Bonev, I. (1986). Mechanism of Zinc Sulphide Oxidation. *Thermochimica Acta*, 106, pp.9-25.

Dunn, J. G. and Kelly, C. E. (1977). A TG/DTA/MS Study of the Oxidation of Nickel Sulphide. *Journal of Thermal Analysis*, 12, pp.43-52.

Dunn, J. G. (1983). The Flash Smelting of Nickel Sulfide Concentrates. *Western Australia Mining and Petroleum Research Institute*, Report No. 1, pp.1-53.

Dunn, J. G. and Smith, T. N. (1984). Flash Smelter Shaft Operations. *Western Australian Mining and Petroleum Research Institute*, Report No. 7, pp.B1-B39.

Dunn, J. G., Jayaweera, S. A. and Davies, S. G. (1985). Development of Techniques for the Study of Flash Smelting Reactions Using Differential Thermal Analysis and Thermogravimetry. *Proceedings of the Austalasian Institute of Mining and Metallurgy*, 290 (4), pp.75-82.

Dunn, J. G., De, G. C. and O'Connor, B. H. (1989a). The Effect of Experimental Variables on the Mechanism of the Oxidation of Pyrite: Part 1. Oxidation of Particles <45 μm in Size. *Thermochimica Acta*, 145, pp.115-130.

Dunn, J. G., De, G. C. and O'Connor, B. H. (1989b). The Effect of Experimental Variables on the Mechanism of the Oxidation of Pyrite: Part 2. Oxidation of Particles of Size 90-125 μm. *Thermochimica Acta*, 155, pp.135-149.

Dunn, J. G., Davies, S. G. and Mackey, L. C. (1989). The Effect of Mineralogical Composition and Particle Size on the Relative Ignition Reactivities of Nickel Sulfide Concentrates. *The Australasian Institute of Mining and Metallurgy Bulletin and Proceedings*, 294 (6), pp.57-62

Dunn, J. G. and Mackey, L. C. (1991). The Measurement of Ignition Temperatures and Extents of Reaction on Iron and Iron-Nickel Sulfides. *Journal of Thermal Analysis*, 37, pp.2143-2164.

Dunn, J. G. and Chamberlain, A. C. (1991). The Effect of Stoichiometry on the Ignition Behaviour of Synthetic Pyrrhotites. *Journal of Thermal Analysis*, 37, pp.1329-1346.

Dunn, J. G., Mackey, L. C., Stevenson, I. R. and Smith, T. N. (1991). Pilot-Scale Study of Effect of Mineralogy and Particle Size on Flash Smelting of Nickel Sulphide Concentrates. *Transactions of the Institute of Mining and Metallurgy, Section C*, 100, pp.C105-C109.

Dunn, J. G. and Mackey, L. C. (1992). The Measurement of the Ignition Temperatures of Commercially Important Sulfide Minerals. *Journal of Thermal Analysis*, 38, pp.487-494.

Dunn, J. G., Gong, W. and Shi, D. (1992). A Fourier Transform Infrared Study of the Oxidation of Pyrite. *Thermochimica Acta*, 208, pp.293-303.

Dunn, J. G. and Mackey, L. C. (1993). TG-DTA Studies of Pyrite, Pyrrhotite, Pentlandite, and Violarite Under Ignition Conditions. *Journal of Thermal Analysis*, 39, pp.1255-1271.

Dunn, J. G., Mackey, L. C., Smith, T. N. and Stevenson, I. R. (1993). A Mineralogical Study of the Products Collected Following Pilot Scale Smelting of some Western Australian Nickel Sulfide Concentrates, *Transactions of the Institute of Mining and Metallurgy, Section C*, 102, pp.C75-C82.

Dunn, J. G. and Howes, V. L. (1994). A TG-DTA Study of the Oxidation of Violarite: Determination of Sulfate Phases by FTIR. *Book of Abstracts of the 6th European Symposium on the Analysis and Calorimetry*, p140. ESTAC, Italy.

Essene, J. E. (1996). Geological Sciences, University of Michigan. Private Communication.

Ewers, W. E. (1973). Nickel-Iron Exchange in Pyrrhotite. *Proceedings of the Australasian Institute of Mining and Metallurgy*, 241, pp.19-26.

Farmer, V. C. (1974). The Anhydrous Oxide Minerals, in Farmer, V. C. (ed), *The Infra-red of Minerals*, pp.183-204. The Mineralogical Society, London.

Francis, C. A., Fleet, M. E., Misra, K. and Craig, J. R. (1976). Orientation of Exsolved Pentlandite in Natural and Synthetic Nickeliferous Pyrrhotite. *American Mineralogist*, 61, pp.913-920.

Griffin, B. J., Muhling, J. R., Carroll, G. W. and Rock, N. M. S (1991). RECALC2 - A Package for Processing Mineral Analyses Produced by Electron Microprobe. *American Mineralogist*, 76, pp.295-298.

Hagni, R. D. and Vierrether, C. B. (1988). Sulfide and Oxide Mineralogy, Textures, and Reactions in Suspended Particles from Experimental and Production Flash Furnace Reaction Shafts, in Robertson, D. G. C., Sohn, H. Y. and Themelis, N. J. (eds.) *Flash Reaction Processes, Centre for Pyrometallurgy Conference, University of Utah, June 15-17*, pp.245-262. The Centre for Pyrometallurgy, Missouri-Rolla.

Hagni, R. D., Vierrether, C. B. and Sohn, H. Y. (1988). Process Mineralogy of Suspended Particles from a Simulated Commercial Flash Smelter. *Metallurgical Transactions B*, 19B (5), pp.719-729.

Hahn, Y. B. and Sohn, H. Y. (1987). Mathematical Modelling of the Combined Turbulent Transport Phenomena, Chemical Reactions, and Thermal Radiation in a Flash-Furnace Shaft, in Szekely, J. et al. (eds.) *Proceedings of the Symposium on Mathematical Modelling of Materials Processing Operations*, pp799-834. The Metallurgical Society of AIME, Pennsylvania.

Hahn, Y. B. and Sohn, H.Y. (1990). Mathematical Modelling of Sulfide Flash Smelting Process: Parts I and II. *Metallurgical Transactions B*, 21B (6) pp.945-966.

Harkki, S., Aaltonen, O. and Tuominen, T. (1976). High Grade Matte Production with Oxygen Enrichment by the Outokumpu Flash Smelting Method, in Agarwal, J. C. and Yannapoulous, J. C. (eds) *Extractive Metallurgy of Copper*. The Minerals, Metals and Materials Society, Pennsylvania.

Harris, D. C. and Nickel, E. H. (1972). Pentlandite Compositions and Associations in Some Mineral Deposits. *Canadian Mineralogist*, 11, pp.861-878.

Harrowfield, I. (1996). CSIRO Division of Minerals, Port Melbourne. Private Communication.

Henderson, C. E. (1996). Electron Microbeam Analysis Laboratory, University of Michigan. Private Communication.

Howard, J. B. and Essenhigh, R. H. (1966). Mechanism of Solid-Particle Combustion with Simultaneous Gas-Phase Volatiles Combustion. *Eleventh Symposium (International) on Combustion, [Proceedings]*, pp.399-408.

Hudson, D. R. and Groves, D. I. (1974). The Composition of Violarite Coexisting with Vaesite, Pyrite, and Millerite. *Economic Geology*, 69, pp.1335-1340.

Huffman, G. P., Huggins, F. E., Lavasseur, A. A., Chow, O., Srinivasachar, S. and Mehta, A. K. (1989). Investigation of the Transformation of Pyrite in a Drop-Tube Furnace. *Fuel*, 68, pp.485-490.

Jorgensen, F. R. A. and Segnit, E. R. (1977). Copper Flash Smelting Simulation Experiments. *Proceedings of the Australasian Institute of Mining and Metallurgy*, 261, pp.39-46.

Jorgensen, F. R. A. (1978). The Ignition Temperature of a Nickel Concentrate From Kambalda Under Simulated Flash Smelting Conditions. *Proceedings of the Australasian Institute of Mining and Metallurgy*, 268, pp.47-55.

Jorgensen, F. R. A. (1979). Heat Transfer Mechanism in Ignition of Nickel Sulfide Concentrate Under Simulated Flash Smelting Conditions. *Proceedings of the Australasian Institute of Mining and Metallurgy*, 271, pp.21-25.

Jorgensen, F. R. A. (1980a). Cenosphere Formation During the Combustion of Pyrite. *Proceedings of the Australasian Institute of Mining and Metallurgy*, 276, pp.41-47.

Jorgensen, F. R. A. (1980b). Combustion of Chalcopyrite, Pyrite, Galena and Sphalerite Under Simulated Suspension Smelting Conditions. *Australia-Japan Extractive Metallurgy Symposium, Sydney, Australia*, pp.41-50.

Jorgensen, F. R. A. (1981). Combustion of Pyrite Concentrate Under Simulated Flash-Smelting Conditions. *Transactions of the Institute of Mining and Metallurgy Section C*, 90, pp.C1-C9.

Jorgensen, F. R. A. and Moyle, F. J. (1981). Periodic Thermal Instability During the Isothermal Oxidation of Pyrite. *Metallurgical Transactions B*, 12B, pp.769-770.

Jorgensen, F. R. A. and Moyle, F. J. (1982). Phases Formed During the Thermal Analysis of Pyrite in Air. *Journal of Thermal Analysis*, 25, pp.473-485.

Jorgensen, F. R. A. (1983). Single-Particle Combustion of Chalcopyrite. *Proceedings of the Australasian Institute of Mining and Metallurgy*, 288, pp.37-46.

Jorgensen, F. R. A. and Moyle, F. J. (1984). Periodic Thermal Instability During the Differential Thermal Analysis of Pyrite. *Journal of Thermal Analysis*, 29, pp.13-17.

Jorgensen, F. R. A. (1986). Ignition Testing of Materials from the Kalgoorlie Nickel Smelter. *The Metallurgical Society of AIME, TMS Paper Selection*, No. A86-21, pp.1-13.

Jorgensen, F. R. A. (1987). Investigation of Shaft Reactions in Nickel Flash Smelting at 0.5 kg min^{-1} Scale. *Pyrometallurgy '87, Papers presented at the "Pyrometallurgy'87" Symposium, 1st, London, September 21-23*, pp.627-645. The Institute of Mining and Metallurgy, London.

Juntgen, H. (1977). The Course of Combustion of the Individual Coal Particle. *EPE, Revue Energie Primaire*, 12 (3-4), pp.11-23.

Juusela, J. T., Harkki, S. and Anderson, B. (1975). Outokumpu Flash Smelting and Its Energy Requirement in Efficient Use of Fuels in Metallurgical Industries, in White, J. and Sprague, R. (eds.) *Institute of Gas Technology, Chicago*, pp.555-575.

Kang, J. S., Steinhauser, J., and Wuth, W. (1983). Oxidation Kinetics of Chalcopyrite in a Dispersed High Temperature Reaction System. *Prace Instytutu Metali Niezelaznych*, 12(1-2), pp.64-77.

Kang, J. S. and Pyun, S. (1988). High-Temperature Oxidation Processes in a Dispersed Particle Jet System of Cu-Fe-S Mineral-Bearing Concentrates. *Radex-Rundschau*, 1, pp.520-535.

Keele, R. A. and Nickel, E. H. (1974). The Geology of a Primary Millerite Bearing Sulfide Assemblage and Supergene Alteration at the Otter Shoot, Kambalda, Western Australia. *Economic Geology*, 69, pp.1102-1117.

Kellogg, H. H. (1964). A Critical Review of Sulfation Equilibria. *Transactions of the Metallurgical Society of AIME*, 230, pp.1622-1634.

Kemori, N., Ojima, Y., Mori, Y., and Yasukawa, M. (1987). Simulation of Oxygen Pressure Profile Along the Reaction Shaft, in Szekely, J., Hales, L. B., Henein, H., Jarrett, N., Rajamani, K. and Samarekera, I. (eds) *Mathematical Modelling of Materials Processing Operations*. The Metallurgical Society, Inc., Pennsylvania.

Kemori, N., Ojima, Y. and Kondo, Y. (1988). Variations of Composition and Size of Copper Concentrate Particles in the Reaction Shaft, in Robertson, D. G. C., Sohn, H. Y. and Themelis, N. J. (eds.) *Flash Reaction Processes Centre for Pyrometallurgy Conference, University of Utah, June 15-17*, pp.47-54. The Centre for Pyrometallurgy, Missouri-Rolla.

Kim, Y. H. and Themelis, N. J. (1986). Effect of Phase Transformation and Particle Fragmentation on the Flash Reaction of Complex Metal Sulfides, in Gaskell, D. R., Hager, J. P., Hoffmann, J. E. and Mackey, P. J. (eds.). *The Reinhardt Schumann International Symposium on Innovative Technology and Reactor Design in Extraction Metallurgy, Proceedings of a Symposium, Colorado Springs, November 9-12*, pp.349-369. The Metallurgical Society, Inc., Pennsylvania.

Kim, Y. H. (1987). *Studies of the Rate Phenomena in Particulate Flash Reaction Systems: Oxidation of Metal Sulfides*. PhD Dissertation, Columbia University, New York.

Kimura, T., Ojima, T., Mori, Y. and Ishii, Y. (1986). Reactions Mechanism in a Flash Smelting Reaction Shaft, in Gaskell, D. R., Hager, J. P., Hoffmann, J. E. and Mackey, P. J. (eds.) *The Reinhardt Schumann International Symposium on Innovative Technology and Reactor Design in Extractive Metallurgy, Proceedings of a Symposium, Colorado Springs, November 9-12*, pp.403-418. The Metallurgical Society, Inc., Pennsylvania.

Knop, O., Ibrahim, M. A. and Sutarno (1965). Chalcogenides of the Transition Elements. IV. Pentlandite, A Natural π Phase. *The Canadian Mineralogist*, 8, pp.291-316.

Kullerud, G. (1962). Thermal Stability of Pentlandite. *The Canadian Mineralogist*, 7 (1), pp.353-366.

Kullerud, G. and Yund, R. A. (1962). The Ni-S System and Related Minerals. *Journal of Petrology*, 3 (1), pp.126-175.

Kullerud, G. (1963). The Fe-Ni-S System. *Carnegie Institute of Washington Year Book*, 62, pp.175-189.

Kullerud, G. (1968). Cubic-Hexagonal Inversions in Some M_3S_4-Type Sulfides. *Carnegie Institute of Washington Annual Report*, 67, pp.179-182.

MacKenzie, R. C. (1970). *Differential Thermal Analysis Volume 1: Fundamental Aspects*. Acedemic Press Inc., London.

Mackey, L. C. (1991). *The Ignition Properties of Pyrite, Pyrrhotite, Pentlandite and Violarite*. Ph.D. Thesis. Curtin University of Technology, Perth, Western Australia.

Marston, R. J., Groves, D. I., Hudson, D. R. and Ross, J. R. (1981). Nickel Sulfide Deposits in Western Australia: A Review. *Economic Geology*, 76, pp.1330-1363.

Medard, L. A. (1989). *Accidental Explosions Volume 1: Physical and Chemical Properties*. Ellis Horwood Limited Chichester, West Sussex.

Merril, L. S. Jr. (1973). The Coal-Oxygen Reaction Near the Ignition Temperature. *Fuel*, 52, pp.61-65.

Misra, K. C. and Fleet, M. E. (1973). The Chemical Compositions of Synthetic and Natural Pentlandite Assemblages. *Economic Geology*, 68, pp.518-539.

Misra, K. C. and Fleet, M.E. (1974). Chemical Compositions and Stability of Violarite. *Economic Geology*, 69, pp.391-403.

Mohan, R., Mckinley, M. D., and Douglas, G. W. (1979). Reaction of Coke Particles with Air: Effect of Diffusion on Reaction Rate. *Proceedings of the Underground Coal Conversion Symposium, 5th, Alexandria, Virginia, June 18-21*, pp. 419-428.

Munroe, N. D. H. (1987). *Simulation of Flash Smelting Phenomena in a Laboratory Reactor*. PhD Dissertation. Columbia University, New York.

Nakomoto, K. (1987). *Infrared and Raman Spectra of Inorganic and Coordination Compounds*. 4th ed. John Wiley and Sons, Brisbane.

Nettleton, M. A. and Stirling, R. (1967). The Ignition of Clouds of Particles in Shock-Heated Oxygen. *Proceedings of the Royal Society of London. Series A, Mathematical and Physical Sciences*, 300 (1460), pp.62-77.

Newhouse, W. E. (1927). The Equilibrium Relations of Pyrrhotite and Pentlandite. *Economic Geology*, 22, pp.288-299.

Nguyen, G. H. (1990). *Micro-Textural Changes to Pyritic Concentrates During Roasting and Their Effect on Gold Extraction*. M.Sc. Thesis. Curtin University of Technology, Perth, Western Australia.

Nickel, E. H. (1973). Violarite - A Key Mineral in the Supergene Alteration of Nickel Sulphide Ores. *Paper presented at the Western Australia Conference, The Australasian Institute of Mining and Metallurgy*, pp.111-116.

Nickel, E. H., Ross, J. R. and Thornber, M. R. (1974). The Supergene Alteration of Pyrrhotite-Pentlandite Ore at Kambalda, Western Australia. *Economic Geology*, 69, pp.93-107.

Otsuka, K. and Soma, T. (1980). Suspension Roasting of Pyrite and Copper Concentrate. *Australia/Japan Extractive Metallurgy Symposium, Sydney, Australia*, pp.233-243.

Rajamani, V. and Prewitt, C. T. (1973). Crystal Chemistry of Natural Pentlandites. *Canadian Mineralogist*, 12, pp.178-187.

Roberts, W. L. (1990). *Encyclopedia of Minerals*. 2nd ed. Van Nostrand Reinhold, New York.

Sainsbury, R. B., Yellow, P. C., Badzioch, S. and Hawksley, P. G. W. (1966). Thermal Decomposition of Pulverised-Fuel Particles, Part 1: Apparatus and Experimental Procedure. *The British Coal Utilisation Research Association, Members' Information Circular*, No.309, pp.1-24.

Shadman, F. and Cavendish, J. C. (1980). An Analytical Model for the Combustion of Coal Particles. *The Canadian Journal of Chemical Engineering*, 58 (4), pp.470-475.

Shewman, R. W. and Clark, L. A. (1970). Pentlandite Phase Relations in the Fe-Ni-S System and Notes on the Monosulfide Solid Solution. *Canadian Journal of Earth Sciences*, 7, pp.67-85.

Spry, P. G. and Gedlinski, B. L. (1987). *Tables for the Determination of Common Opaque Minerals*. Economic Geology, New Haven.

Stevenson, I. R., Culshaw, P. C., Watkins, S. T., Messner, S. and Park, L. J. (1994). Operations at the Kalgoorlie Nickel Smelter-Past, Present and Future, in Grimsey, E. J. and Stockton, N. D. (eds) *Nickel in Australia - Mineral to Market, Kalgoorlie, Australia, December 2*, pp.72-92. The Australasian Institute of Mining and Metallurgy, Kalgoorlie.

Stromberg, S., Nurmi, P., Lilius, G., Jyrkonen, S. and Jokilaakso, A. (1995). Oxidation of Nickel Concentrates and Crushed Nickel Matte Under Simulated Flash Smelting Conditions, in Warren, G. W. (ed) *EPD Congress 1995*, pp.207-222. The Minerals, Metals and Materials Society, Pennsylvania.

Themelis, N. J. and Kellogg, H. H. (1983). Principles of Sulfide Smelting, in Sohn, H. Y., George, D. B. and Zunkel, A. D., (eds.) *Advances in Sulfide Smelting Symposium and the Extractive and Process Metallurgy Meeting of The Metallurgical Society of AIME, Volume 1. Basic Principles*, pp.1-29. The Metallurgical Society of AIME, Pennsylvania.

Themelis, N. J., Mackinen, J. K. and Munroe, N. D. H. (1985). Rate Phenomena in the Outokumpu Flash Smelting Reaction Shaft, in Kudryk, V. and Roa, Y. K. (eds) *Physical Chemistry of Extractive Metallurgy, Proceedings of the International Symposium*, pp.289-309. The Metallurgical Society of AIME, Pennsylvania.

Themelis, N. J., Wu, L. and Jiao, Q. (1988). Some Aspects of Mathematical Modelling of Flash Smelting Phenomena, in Robertson, D. G. C., Sohn, H. Y. and Themelis, N. J. (eds.) *Flash REaction Processes, Centre for Pyrometallurgy Conference, University of Utah, June 15-17*, pp.263-285. The Centre for Pyrometallurgy, Missouri-Rolla.

Thornber, M. R. (1975). Supergene Alteration of Sulphides, 1. A Chemical Model Based on Massive Nickel Sulfide Deposits at Kambalda, Western Australia. *Chemical Geology*, 15, pp.1-14.

Thornhill, P. G. and Pidgeon, L. M. (1957). Micrographic Study of Sulfide Roasting. *Journal of Metals*, 9, pp.989-995.

Tressler, R. E., Hummel, F. A. and Strubican, V. S. (1968). Pressure-Temperature Study of Sulfospinels. *Journal of the American Ceramic Society*, 51, pp.648-651.

Tsukada, H., Asaki, Z., Tanabe, T. and Kondo, K. (1981). Oxidation of Mixed Copper-Iron Sulfide. *Metallurgical Transactions B*, 12B, pp.603-609.

Turnball, A. G. and Wadsley, M. W. (1992). *CSIRO-Monash Thermochemistry System Vesion 1.0 Software*. CSIRO, Division of Mineral Products.

Vaughan, D. J. and Craig, J. R. (1978). *Mineral Chemistry of Metal Sulfides*. Cambridge University Press, Melbourne.

Vaughan, D. J. and Craig, J. R. (1985). The Crystal Chemistry of Iron-Nickel Thiospinels. *American Mineralogist*, 70, pp.1036-1043.

Vilyunov, V. N. and Zarko, V. E. (1989). *Ignition of Solids*. Elsevier Science Publishers, Amsterdam, The Netherlands.

Wall, T. F., Gupta, R. P., Gururajan, V. S. and Zhang, D. (1991). The Ignition of Coal Particles. *Fuel*, 70, pp.1011-1016.

Ware, N. G. (1981). Computer Programs and Calibration with the PIBS Technique for Quantitative Electron Probe Analysis using a Lithium-Drifted Silicon Detector. *Computers and Geosciences*, 7, pp.167-184.